



A 3D-PRINTABLE COMPOSITE FOR BONE-REGENERATION IMPLANTS FOR PAEDIATRIC MAXILLOFACIAL RECONSTRUCTION

CARLOS AMNAEL OROZCO-DÍAZ

January 2019

Supervisors: Dr Cheryl Miller, Dr Robert Moorehead, Dr Gwendolen Reilly, Dr Fiona
Gilchrist

Bioengineering and Health Technologies

School of Clinical Dentistry

Faculty of Medicine, Dentistry and Health

The University of Sheffield

SR No. 15024754

Thesis submitted in total fulfilment of the requirements of The University of
Sheffield for the Degree of Doctor of Philosophy

ACKNOWLEDGMENTS

*“What fear or would could ever still this last defiant cry
As I stand against the Shadow, ‘neath the endless, burning sky?”
From ‘Long Road’s End’ by C. V. Metzner*

Dreadful as I find the occasion to conjure up all the names upon which gratitude I would like to rain – out of fear of the indelible sin of omission the task will inevitably entail –, I wholeheartedly take these humble lines to honour this dark duty (under no premeditated hierarchy):

This entire work would not have even started without the nearly blind faith of my supervisors, who took me in for this project with barely two years of funding and little more insurance than my word: I hope my time here lived up to it. I even more certainly hope the nice people at the Dental School and the INSIGNEO lab will excuse the intermittency of my social engagements, and receive this appreciation for their counsel and acquaintance – especially Rob and Zena, who took care of most all of my training. On that note, I also extend my gratitude to Le Ma, Caroline Fry, and Rob Hanson, for their service and help in the production of my ever-so-seductive SEM, μ CT, GPC data.

These acknowledgments must also include my parents, my comrades from the 201st B.O.W., as well as my family and friends departed since I embarked on this solemn quest. Lastly, this goes dedicated to Lilith and my lovely Kitteh.

FUNDING DISCLOSURE

This research and degree were made possible through co-funding by the National Council for Science and Technology of Mexico (CONACYT), and The University of Sheffield; as well as by the contributions made by the School of Clinical Dentistry, and the INSIGNEO Institute of In-silico Medicine.

ABSTRACT

Autografted cancellous bone is the current gold-standard for maxillofacial reconstruction surgery (MRS), where it is used to fill in small defects. These grafts still pose several drawbacks, including the need for an additional surgical wound at the grafting site, and inadequate bone density at the repaired site. Both situations can have chronic medical and surgical implications, especially in paediatric patients since they are still growing. Cancellous bone, additionally, is not structural, so its applications are limited to non-load bearing sites.

This research aimed to developing a bone regeneration material for 3D-printing, which could potentially address these issues. A polylactic acid (PLA) and hydroxyapatite (HA) composite was developed, which is usable in commercial-grade Fused Filament Fabrication (FFF) 3D-printers. FFF allows for the reproduction of any geometry necessary to treat a given bone lesion. PLA provides a biocompatible and resorbable structure for the material, while HA works as a functionalisation agent to induce a cellular response.

These composites were studied for mechanical, chemical, thermal, and degradation properties as per ISO-10993-13-2010. *In vitro* biocompatibility for the material included cell-viability and extracellular-matrix deposition using the MG-63 cell line. The composite behaved as expected during characterisation, and was also found to perform equivalent to tissue-culture plastic in regards to *in vitro* biocompatibility. Degradation results showed that 3D-printing of these materials will likely result in faster *in vivo* resorption than current PLA implants, and a mathematical model was proposed from these results. This research suggests that 3D-printable PLA-HA composites are a viable material for therapeutic implants for bone-regeneration.

GLOSSARY OF ACRONYMS

Term	Definition
3DP	3D-printing
ADT	Accelerated degradation test
AM	Additive manufacturing
ANN	Annealed
ARS	Alizarin red staining
ASCII	American standard code for information exchange
BFB	Bits from bytes
CAD	Computer-assisted design
CAE	Computer-assisted engineering
CAE	Computer-assisted engineering
CLP	Cleft lip and palate
CNS	Central nervous system
CP	Cleft palate
CPX	X-linked cleft palate
Cr	Crystallinity
CT	Computer-assisted tomography, computed tomography
DSC	Differential scanning calorimetry
DTA	Differential thermal analysis
DTA/TGA	Differential thermal analysis/Thermogravimetric analysis
E	Elastic modulus
EDS	Energy dispersive spectroscopy
EM	Expansion medium for cell culture
EOS	Ethylene oxide sterilisation

FDA	United States's Food and Drug Administration
FFF	Fused-filament fabrication
FFF3DP	Fused-filament fabrication 3D-printing
GPC	Gel permeation chromatography
mADT	Modified accelerated degradation test
MRP	Medical rapid prototyping
MRS	Maxillofacial reconstruction surgery
Mn	Number-average molecular weight
Mw	Weight-average molecular weight
NADH	Nicotinamide adenine nucleotide
NADPH	Nicotinamide adenine nucleotide phosphate
NIST	National Institute of Standards and Technology
NSCP	Non-syndromic cleft palate
PBS	Phosphate-buffered solution
PDLA	Poly-D-lactide
PLA	Polylactic acid
PLLA	Poly-L-lactide
PRP	Platelet rich plasma
ReSKY	Revised Smith-Hernahan striped "Y" classification system
RRA	Resazuring reduction assay
RSET	Real-time simulated environment test
SEM	Scanning electron microscopy
SLM	Selective laser melting
SLS	Selective laser sintering
SM	Mineralisation-supplemented medium for cell culture
SRS	Siruis red staining
STL	Standard tessellation language

TCP	Tissue culture plastic
Tf	Fusion temperature
Tg	Glass-transition temperature
TGA/DTA	Thermogravimetric analysis/differential thermal analysis
UTS	Ultimate tensile strength
VWS	Van der Woude syndrome
VB	Verbatim
w	Weight

TABLE OF CONTENTS

Acknowledgments	2
Funding Disclosure	2
Abstract	3
Glossary of Acronyms	4
Table of Contents	7
1. Introduction	12
2. Literature Review	16
2.1. Clinical Need: Maxillofacial Bone Reconstruction	16
2.1.1. A Brief History of Organ Repair and Replacement	16
2.1.1. An Overview of Bone Lesion Repair	18
2.1.2. Biomaterials in Historic Skull Repair	22
2.1.3. Anatomical features and Function loss on Cleft-Palate Lesions	27
2.1.4. Risk factors: Genetics and Teratogenicity	29
2.1.5. Palatogenesis and its Disruption	32
2.2. Surgical Repair of Bone Defects Clefts	36
2.2.1. Aims and techniques	36
2.2.2. General Treatment Sequence Layout	38
2.2.3. Post-repair Complications	40
2.2.4. Bone Grafting: Issues, outcomes, and Secondary Morbidities	42
2.3. Fused Filament Fabrication for CranioFacial Reconstruction Applications	45
2.3.1. Stereolithography and the Basic Principles of 3D Printing	45
2.3.2. 3D Printing Technologies	49
2.3.3. Fused Deposition Modelling, its Issues and Limitations	51
2.3.4. Prosthesis manufacture and Maxillofacial Reconstruction	53
2.3.5. Application-Specific Considerations on materials and FFF	56
2.4. Lactide Polymers: Properties, Processing, and Application in FFF	59

2.4.1.	Lactide Polymers	59
2.4.2.	Compositing and Self-REinforcing of Lactide Polymers.....	61
2.4.3.	Degradation and Enhancement of LActide Polymers: Annealing and Self-Reinforcing 64	
2.4.4.	Degradation Profiles: Real-Time Simulated-Environment Test and Modified accelerated Degradation TEst	67
3.	Aims and Objectives.....	72
4.	Materials and Methods.....	75
4.1.	Determining the printer’s resolution limit and Printing Accuracy	75
4.2.	Accelerated degradation of FFF PLA.....	77
4.2.1.	Mass Change	82
4.2.2.	Crystallinity and Thermal analysis.....	82
4.2.3.	Mechanical Properties and Visual Inspection	83
4.2.4.	Molecular Weight.....	84
4.3.	Processing of 3DP Materials and Samples.....	84
4.3.1.	Annealing.....	85
4.3.2.	PLA-HA Composite Filament Production.....	86
4.4.	Geometric Design And Sample Production	87
4.4.1.	Design of a base geometric unit.....	87
4.5.	<i>In Vitro</i> Material Biocompatibility	90
4.5.1.	Tissue Engineering Cell-Line Preparation	90
4.5.2.	Sample Production and Preparation	91
4.5.3.	MG-63 Cell Viability.....	93
4.5.4.	Cell Attachment.....	94
4.5.5.	Cellular Matrix Deposition.....	95
4.6.	Composite Characterisation	97
4.6.1.	Composite Formulation Selection	97
4.6.2.	Composite HA content Measurements.....	97
4.6.3.	3DP Composite Mechanical Properties.....	98
4.6.4.	Composite Accelerated Degradation Test.....	99

4.7.	Mathematical Modelling for Polymer Degradation	99
4.7.1.	Modelling from Molecular weight Before Mass-Loss	99
4.7.2.	Modelling from Molecular weight After Mass Loss	103
5.	Results.....	104
5.1.	Determining the printer’s resolution limit and Printing Accuracy	104
5.2.	Accelerated degradation of FFF PLA.....	106
5.2.1.	Mass Change	106
5.2.2.	Crystallinity.....	109
5.2.3.	Mechanical properties and visual inspection	112
5.2.4.	Thermal Analysis	115
5.2.5.	Molecular Weight.....	121
5.3.	Processing of 3DP Structures and Materials	122
5.3.1.	Annealing.....	122
5.3.2.	PLA-HA Composite Filament	130
5.4.	Implant Geometric Design.....	132
5.5.	<i>In Vitro</i> Material Biocompatibility	134
5.5.1.	3D-Printed PLA Sterilisation	134
5.5.2.	Initial MG-63 Cell Viability Study.....	136
5.5.3.	MG-63 Cell Viability Study in SM.....	139
5.5.4.	Effects of Osteogenic Supplements in MG-63 Culture in PLA and PLA-HA composites 143	
5.5.5.	<i>In Vitro</i> Cell Culture in Three-Dimensional 3D-Printed Structures	145
5.6.	Composite Characterisation	150
5.6.1.	Composite HA Content Measurement and Distribution	150
5.6.2.	3DP Composite Mechanical Properties	157
5.6.3.	Composite Accelerated Degradation	158
5.6.4.	Mass change.....	158
5.6.5.	Crystallinity.....	159
5.6.6.	Mechanical Properties	160

5.6.7.	Thermal Analysys	160
5.6.8.	Molecular Weight.....	162
5.7.	Mathematical Modelling for Polymer Degradation	163
5.8.1.	Modelling for Molecular Weight before Mass-Loss	164
5.8.2.	Modelling for Molecular WEight after Mass-Loss	167
6.	Discussion.....	174
6.1.	Determining the printer’s resolution limit and Printing Accuracy	174
6.2.	Accelerated degradation of FFF PLA.....	177
6.2.1.	Mass Change	177
6.2.2.	Crystallinity.....	181
6.2.3.	Thermal Analysis	183
6.2.4.	Mechanical properties and visual inspection	185
6.3.	Processing of 3DP Composite Materials and Structures	189
6.5.1.	Annealing.....	189
6.5.2.	PLA-HA Composite Filament Production and Characterisation	193
6.4.	Implant Geometric Design.....	197
6.5.	<i>In Vitro</i> Material Biocompatibility	198
6.5.1.	3D-Printed PLA Sterilisation	198
6.5.2.	MG-63 Cell Viability Study.....	199
6.5.3.	<i>In-Vitro</i> Cell Culture in Three-Dimensional 3D-Printed Structures.....	202
6.6.	Composite Accelerated Degradation	204
6.7.1.	Mass Change	204
6.7.2.	Crystallinity, Mechanical, and Thermal Properties	205
6.7.3.	Thermal Properties.....	208
6.7.	Mathematical Modelling for Polymer Degradation	209
6.7.1.	Modelling for Molecular Weight before Mass-Loss	209
6.7.2.	Modelling for Molecular Weight After Mass-Loss	211
7.	General Conclusions.....	216
8.	Further work	223

9.	Publications Arising from the Thesis	225
9.1.	Peer-Reviewed Publications In Preparation	225
9.2.	Conferences.....	225
10.	References.....	226

1. INTRODUCTION

Craniofacial reconstruction, perhaps more than any other discipline within healthcare, has been actively taking advantage of overall developments in biomaterials and manufacturing processes. Such developments have been aimed towards producing therapeutic implants, since bioactive bone substitutes are a relatively straightforward and well-studied means of implementing tissue regeneration technologies [1–8]. The patients dealt with in this context are exposed to a wide range of secondary morbidities, including a potential toll on their psychological health due to the origin of their injuries – usually traumatic – and the impossibility of concealing them from others [9]. The impact of the aesthetic outcomes of these treatments has also been noted and frequently listed as one of the key points to improve upon in the development of new reconstructive surgical implementations. In this regard, healthcare professionals who treat congenital deformities and lesions of the skull – and their iatrogenic secondary ailments – emphasise attention on improving the final aesthetic results of new techniques. These particular outcomes have been a gradually growing concern, since aesthetic consequences for young patients happen to align with active anatomical and social developmental stages [9–14].

Although a plethora of conditions can require skeletal reconstruction early in childhood, cleft palate is an excellent benchmark for the challenges that development of artificial implants must overcome. Reconstruction of an infant's growing skull has the explicit drawback of requiring implants and procedures that are adapted for the rapid growth of young tissues [15,16]. Any

solid inert implant substituting missing bone tissue can have detrimental and life-long effects on craniofacial growth [17–20]. An especially vulnerable age range is found around 8 and 12 years of age [15], when skull bones tend to grow fastest. For these reasons, and due to its high incidence in the general population, Cleft Lip and Palate (CLP) was used as a reference clinical application to guide the development of the basic science established in this project.

Craniofacial clefts are the most common congenital deformity of the skull worldwide [21,22], with an incidence rate ranging around 0.2-1.9 per 1000 live-births. These incidences depend on several environmental factors but are also well correlated with pathologic and race-related genetic heritage [23–30]. In the European Union, this range narrows down to 0.5-1.4 per 1000 live births, with the United Kingdom ranking at the higher end [31,32]. Notably, defects of this kind outnumber cardiovascular ones – globally the most common [33] – in the general Mexican population, although with wide variations in between the Republic's states [22,23,34]. The former is expected given the wide region-dependent genetic diversity within the country [35]. The treatment of these patients is lengthy – spanning over probably a third of their lifetime – involves high costs, longitudinal follow-up, and usually more than two surgical interventions, where most of the surgical time will focus on the reconstruction of the bone defects inherent to this clinical entity [25,32,36].

This disorder is reflective of the broader challenge posed by bone reconstruction in paediatric patients. Depending on local CLP treatment guidelines, most reconstruction surgeries happen at any time from the first

year of life to 16 years of age – even later in some cases –, posing a unique challenge for the development of artificial grafts that must take in account their effect on bone-growth (especially between ages 8 to 12) [15]. Artificial grafts have the potential to produce functional bone on the injured site while avoiding the side-effects and costs of grafting surgery [14,25,37]. The mainstay of treatment for the maxillary malformations commonly found in these patients is autologous grafting of cancellous bone from the iliac crest [14,25,38]. This procedure in itself raises some concern regarding extended surgery times, secondary morbidities (lifelong chronic pain at the donor site, weakening of the harvested pelvic bone at the ilium, surgical wound infection, or scarring), and variable clinical outcomes – in regards to density of the regenerated bone at the treated site, which tends to be low, and can even require a second graft [14,32,38].

The present research is concerned with implementing the still-growing field of Fused Filament Fabrication (FFF) 3D-printing (3DP) technologies into addressing the unique challenges posed by alveolar reconstruction for CLP patients. Implementing advanced manufacturing technologies could allow for improvement of this treatment through the production of patient-specific, image-study-based custom implants [8,13,39,40]. Since the introduction of the first stereolithography techniques in 1988 by Charles Hull, medical rapid prototyping has looked into its potential for developing new treatments and devices [41]. FFF systems launched in the last decade of the last century – coupled with their commercial availability and affordability being improved during recent years – have had their role in medical research and applications become commonplace [41,42]. Their use in conjunction with medical imaging

– namely computed tomography – has a potential that is just beginning to be explored for the production of long-awaited patient-specific devices and implants [13,40,43–48].

The need for this research arises from the relatively recent introduction of consumer-level 3D-printing. There are few data available the literature on the potential adverse effects of FFF as a medical manufacturing process. These are concerns in terms of medical materials regulation, since well-evidenced good-manufacturing practices are as necessary for clinical application as medical-grade raw material [49]. The main points of consideration for this work are focused on the effects of FFF on the mechanical, molecular, and biocompatibility properties of lactide polymers, and specifically polylactic acid (PLA), which is widely used in medical implants. Additionally, a compositing method was developed for integrating hydroxyapatite (HA) as a bioactive ceramic into PLA FFF 3D-printing materials. Both objectives were addressed through mechanical, thermal, chemical testing, as well as through *in-vitro* degradation and biocompatibility studies. Finally, drawing from the data produced, a final proposal documented the development of general guidelines for the production of absorbable maxillofacial reconstruction materials for implant production through 3D printing, which allows for patient-specific solutions in the context of both CLP and craniofacial reconstruction in general. A literature review of the scientific basis for this research follows.

2. LITERATURE REVIEW

2.1. CLINICAL NEED: MAXILLOFACIAL BONE RECONSTRUCTION

2.1.1. A BRIEF HISTORY OF ORGAN REPAIR AND REPLACEMENT

Organ replacement has been a long-standing dream for humanity (and engineers), probably since the advent of any notion of healthcare some 10,000 years ago, just after the establishment of sedentary settlements birthed the millennia-long age of infectious disease that would – in turn – culminate on our modern medical practice [50]. Along with the much-expected animal-mauled and battle-wounded amputees, classical texts were among the first to recount anecdotal resection procedures, as well as wood-crafted prosthetic limbs with fixation arrays and straps of varying complexities and materials to allow for everyday use [51] (though Greeks were not the first to implement a rough form of prosthetics [52,53]). These very set-ups would then be referred to as *cork legs* as they were implemented throughout the 19th century [54], reflecting just how little net advance this particular *techné* made throughout two millennia [51,55].

The former is but an example of successful anatomy replacement at its simplest possible iteration, yet one must bear in mind that less than two human lifetimes ago that was the only instance of it we could aspire to. This is by no means a random timeframe, since many of the now-given scientific advances were just emerging through the 1800's, and modern medical practice – roughly recognised as such with the start of asepsis, microbiology, and biochemically-

based pharmacology – is currently just halfway through its second century of existence [50,56,57].

As physiological functions and anatomical structures were more widely understood (and understood to be heavily intertwined) during the 20th century, it became clear that the recently-born field biomedical engineering would be tasked with implementing and capitalising on such advances for the benefit of the niche of medical technologies. It also became obvious that those physiological functions were a lot more complex to mimic than mere structural features, and even harder it would be to match *Nature's* efficiency at it [58].

The scientific and technological expertise that goes into creating a replacement organ – under the modern expectations of the regenerative medicine field – is predictably broad [55], posing a challenge for research and development groups in that they require large, flexible, and multidisciplinary teams to effectively keep track and assess the impact of emerging – and especially of disruptive – technologies [42,45]. Achievements in this respect, thus, have advanced side by side with the knowledge-base on the broad fields of physiology, electronics, manufacturing, and materials up to its current achievements: artificial substitutes for renal, circulatory, and pulmonary functions, as well as cardiopulmonary bypass devices, and implantable artificial kidneys and hearts [59]. Further still, these accomplishments have moved onto future goals as proposed by the American Society for Artificial Internal Organs on their 2005-2055 Phase 2 aims, which refocuses their view towards therapeutic artificial organs, addressing cardiac therapeutics, and immunological and metabolic regulators [60,61]. These objectives align very

well with current healthcare research trends heavily embracing regenerative medicine and tissue engineering.

2.1.1. AN OVERVIEW OF BONE LESION REPAIR

Osseous tissue is one of the few instances in humans – and higher-order vertebrates – of naturally-regenerating organs. Commonplace examples of other such tissues include the skin, which is highly specialised in the process of wound-healing since its main function is protection of other organ systems from the environment [62]. The endometrium is similarly differentiated towards constant regeneration, albeit from cyclical decay driven by the hypothalamic-pituitary-gonadal axis [63]. Less obvious cases of extensive regeneration occur in the liver, where remaining tissue can respond to even catastrophic organ damage by replication and repopulation of lost volume with functional tissue [64]. The myth of Prometheus is frequently quoted at this point on tissue-regeneration pieces, but it is worth noting that archaeological and historical evidence suggests his immortal liver is likely a coincidence rather than a reflection of ancient Hellenic physiological awareness [65]. Notably, distal hand phalanxes have also been reported to completely regenerate after avulsion, even in adult patients [66–68].

This phenomenon of natural organ reconstruction can be broadly understood under the concept of tissue-healing, and it encompasses a vast array of sub-processes where a common feature is the involvement of connective tissue

and stem-cell lines [62,66,69,70]. Healing is highly dependent on paracrine signalling and chemotactic markers released by damaged cells from the tissue in distress, as well as by platelets and other blood cells as they stream out of broken capillaries and onto exposed collagen of injured connective tissue [67,69,70]. Given their crucial role in coagulation as an initiation of damage-control measures at injury sites, platelets and other blood-borne products are thought to be central to any healing effort [62,69]. This is the reason why Platelet-Rich Plasma (PRP) has been of consistent interest as an agent for injury healing in general [71–73], for treatment of chronic tissue damage [71,74–76], and for bone regeneration in particular [25,77,78].

As part of this cascade of responses, pro-inflammatory factors are released by damaged tissue and vasculature, as well as by local tissue-resident immunological cells from the surrounding sites [79,80]. These cells – most from the phagocytic macrophage and neutrophil varieties, along with some myeloid-line cells – are activated via two routes: through damage/danger-associated molecular patterns [80,81], and through pathogen-associated molecular patterns [81–83]. Their release of numerous cytokines (such as interleukins 1, 6, and 8, and tumour necrosis factor α) mediates the initial vasodilation and further recruitment of immunological cells, along with the complement system [82,84], and coagulation processes [85,86].

Appropriate coagulation marks one of the milestones of healthy injury-response [85,86]. As the formation of platelet-mediated thrombi and fibrin clots stabilise homeostasis and mechanics at injured site, they also further signal the recruitment of fibroblasts with subsequent differentiation to myofibroblasts [87]. These undertake the generation of replacement connective-tissue

collagen, which restores the structure of the damaged site. Being contractile, myofibroblasts are also involved in approximation of injury-separated tissue, and alignment of collagen fibres [88].

The rate and extent to which myofibroblasts manage to secrete collagen matrix seems to affect the degree of regenerated and scarred tissue achieved during the repair [62,70,89]. All non-regenerating tissues in humans undergo some degree of scarring during healthy healing – which implies that at least some of the lost tissue is replaced by non-functional fibrous patches. Rapid and extensive secretion of collagen is thought to be linked with the scarring process, as is the density of differentiated myofibroblasts at the injured tissue [88]. Research on animal models suggests that foetal wounds – which heal without scarring – do so in the absence of myofibroblasts [88].

Healing of osseous injuries is dependent on similar factors to the above, since an important part of the functional aspects of the skeleton depends on its extracellular matrix – apart from its metabolic and haematopoietic activities [90,91]. By weight, this extracellular matrix is up to 70% bone-mineral, comprised of hydroxyapatite (HA): a form of calcium phosphate organised in both an amorphous phase, and a crystalline phase of carbonate-apatite [91–93]. Though analogous to geological calcium-apatites, biological crystalline HA follows a different synthesis pathway, dependent on acidic phosphate and carbonate precursors [92]. The formula for HA is usually written as: $\text{Ca}_5(\text{PO}_4)_3(\text{OH})$, but it should be noted that this refers to the repeating molecular unit [92,94]. In contrast, the crystal unit cell is actually pairs of these, thus some sources report it as $\text{Ca}_{10}(\text{PO}_4)_6(\text{OH})_2$. The remaining mass of bone extracellular matrix is given almost entirely by aligned type I collagen fibres.

These tend to orient themselves parallel to the direction of usual mechanical load of a given bone – commonly along its longest axis [91].

Osseous, endometrial, and dermal tissues undergo constant loss of functional tissular mass, while maintaining a balanced rate of replenishing of such loss. Relying mostly on epithelial tissue, the endometrium and dermis achieve this through a highly-mitotic basal layer [62,63,89]. In contrast, healthy bones are subject to *remodelling*: a cell-mediated process balancing resorption of existing mineralised tissue, and ossification (generation of new extracellular matrix with subsequent mineralisation) [90,91].

This on-going remodelling process in bones allows for the repair of microfractures that occur due to normal locomotion and interactions with the environment [91]. This adaptation is one of the mechanisms that allow bone to heal as often and as effectively as it does. It must be noted that most of the load-bearing tissue of bone is non-cellular, and this fact also contributes to the relative ease with which osseous tissue achieves true regeneration [91].

Even though there is some evidence of involvement of stem cells in post-embryologic skeletal development [95], bone remodelling is mainly driven by differentiated cell-lines. Pre-osteoclasts are distributed in the outermost layers of bones in structures known as lacuane of Howship, while osteoblasts are evenly scattered through the tissue. Damage and inflammation signals trigger pre-osteoclasts to become osteoclasts, and osteoblasts near the injury site to activate [91]. Osteoclasts then degrade and resorb the tissue around the damaged site, while active osteoblasts secrete a new collagen matrix to fill in lost tissue volume. The process is finally completed as osteoblasts trigger

mineralisation of this protein matrix, and deactivate while embedded inside it [91,96,97]. Harnessing and directing these former processes is the ultimate goal of bone-regeneration materials and devices.

2.1.2. BIOMATERIALS IN HISTORIC SKULL REPAIR

Just as the *techné* around organ replacement grew, so did the knowledge regarding materials for this purpose. Beyond functional limb prosthetics, there is evidence of dental replacements, and even full-thickness skull implants documented archeologically for civilisations as far back as seven millennia from now [52,53,98–100]. Not only does this speak highly of the resourcefulness of human minds – even amidst the darkness of vast scientific naivety –, but it is also humbling to think that prosthetics of these sorts would be amongst the very – very – few pre-modern medical interventions that actually solved the problem they treated [50]. This would hold true until surprisingly recent times: somewhere around the 19th century [51,54,55]. Even so, the current concept of “biomaterial” as part of the collective scientific *imaginarium* did not really emerge until halfway through the 20th century [101].

Though the nuances of physiology and pathology remained beyond understanding during the process, trial and error (and coincidence) helped establish the usefulness of several commonplace materials as adequate for implants or prosthetics. As for most other manufacturing applications of old, wood was one of the recurrent materials – and probably one of the first – to be implanted for medical purposes [52]. Though wooden prostheses became commonplace for limbs, the material has also seen use in contact with mucosal tissue in ocular prosthetics and dentures, and even cases of

attempted limb fracture stabilisation have been found documented as treatment procedures – using wooden blocks fixed directly in contact with bone [52]. This is just an instance of how early prosthetics and implants must have been developed: not as a discipline within healthcare, but as one more task for craftsmen – who used whatever material they were skilled at working [101].

It is likely that the most common site for ancient bone-repair was the skull. Trepanation appears to be the main reason for development of early cranioplasty, though that remains open for interpretation, since in many cases implants could have been scavenged *post-mortem*, making a successful skull repair appear archeologically like a peri-operative death [100,102,103]. This trend led to other plant-based materials becoming widely popular [52,53,100,104]. Dried shells of *Curcubitaceae* plants and coconuts were employed for cranioplasty in several parts of the world, most frequently in treatment for common folk [53,100,103,105], which may hint at some success in their application.

The higher, richer classes, in contrast, founded a trend that still stands today: the use of metallic bone substitutes. Precious metals saw a lot of use in bone repair, with silver and gold skull-implanted plates appearing consistently all the way from Incan exhumed skeletons (**Figure 2.1**), to proper surgical texts during the 14th century [100,101,105]. These have clear advantages over any presentation of cellulose or lignin in that the so-called *noble metals* (classified on corrosion resistance and/or d-shell *nobility*) are chemically more stable than organic compounds, and display some antibacterial properties. Recently, these have fallen out of use within medical materials due to their price, high malleability, and relatively high toxicity, with favour going towards more

complex metallic alloys with titanium, steel, and aluminium. The main advantages of metals come from their large tensile and compressive strengths when compared to bone, and from them being bioinert (eliciting little to no immune response at the implantation site) [47,106–109].

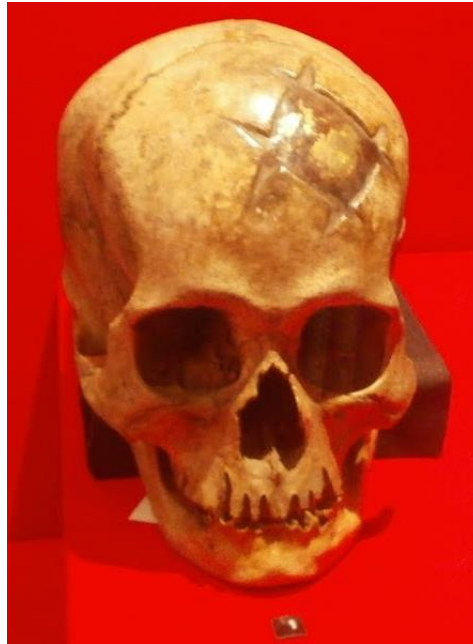


Figure 2.1. Gold plate in frontal bone-trepanation repair. Notice the smooth edges at the transition between bone and implant: these suggest adequate post-operative osteointegration. The subject must have survived several months post-operatively for this to be observable. Skull on display at *Museo del Oro* at Lima, Peru [109].

Along with treatments for the cranial vault, dental and maxillofacial repair procedures have been a constant through virtually every early civilization. Metals were also prominent in these applications, as were some polisheable minerals like quartz. Similarly, pre-colonial Latin-American cultures were no strangers to using xenografts on these kinds of repairs. Human remains throughout this large region have been discovered with intricate dental-work using seashells, as well as other animal osseous tissue and dentine (ivory).

As one could expect, these materials were also a logical choice in Europe, Asia, Africa, and the islands of the Pacific [100,110].

Even later, formal medical practice experimented with bone from readily-available mammals and birds for reconstruction of the skull [100,111]. In one of the more bizarre treatment protocols documented, a 14th Century text recommends a chicken-breast graft – freshly harvested and bleeding – for cleft lip and palate repair [112]. The author of this recommendation – a Catholic archbishop – appears to have been inspired by contemporary superstitions surrounding birth defects [113]. This position on animal tissues apparently was reversed by the 15th century, when the Dutch physician Meekeren used dog bone for a skull implant, much to the dislike of his church [111]. Xenografts may still pose a viable option for some types of grafting in humans, but immunological limitations remain a challenge to be consistently overcome by research [114]. Cases of successful xenografting of bone are not unheard of, but the clinical outcome is limited by severe immune rejection – as happens with other tissues –, and rapid resorption of the graft – a problem particular to osseous grafts [105,111].

Regarding polymers, pre-Columbian Mexican cultures are well known to have used *Castilla elastica*-derived rubber balls for their ceremonial *juego de pelota*, and production of other goods like rubber bands; no direct medical use is currently reported [115]. This kind of natural rubber was virtually the only type used for most of human history, until 1865, when Alexander Parkes developed parkesine: the first synthetic polymer [116]. He was followed by John Hyatt in 1870, who patented the material originally known as *celluloid* – a stabilised nitrocellulose polymer [117]. This is considered the first modern plastic, since

it was the first to achieve widespread adoption in several branches of industry. Just as the eventual creation of medical polymers aimed to replace hard-to-secure natural materials, celluloid was developed initially as an affordable (and less regulated) substitute for ivory.

Since then, countless different synthetic polymers have been created with ever more application-specific adjustments to their properties for every branch of industry [118]. Unlike medical-grade metals, medical polymers have a natural tendency to degrade when exposed to biological systems – a property so-called biodegradability. This follows from the fact that their molecular superstructures are held in place by the same types of bonds that biological materials share. In the case of polymers (both biological and petrochemical), polymerisation occurs either via several types of carbon-carbon bonds, or some weaker carbon-oxygen bonds (as polyesters), or carbon-nitrogen bonds (as polyamides) [49,119–121]. Biodegradability, while being an industrial disadvantage for early plastics, proved to be useful in medical devices. By 1962, polyglycolic acid absorbable sutures were already implemented in clinical practice, soon followed by others made with polylactic acid (PLA) [121].

A variety of polymeric medical devices are currently used for surgical reconstruction, including that of the head and face bones, in the form of surgical instruments, guides, fixtures, and bone implants [122–128]. The different polymers currently in use for surgical purposes would fill a list too long to detail in this review. Some of the most common examples include medical-grades of familiar commodity plastics (such as polyvinyl chloride, polyethylene terephthalate, polyurethane, and silicone) [118,129]. Some others are popular choices for implants, like methacrylate polymers (used in intraocular lenses,

bone fillers, blood-contact coatings, dermal fillers, and dental crowns [130]), polyamides – especially Nylon – (used in sutures, hernia-repair meshes, and recently in additive manufacturing [131]); and polytetrafluoroethylene (used in vascular grafts, orthopaedic devices, and some dermal implants [132–134]).

Of interest of the present project is PLA, which has also been used in the manufacture of bone implants and fixtures, as well being a standard material for commercial Fused Filament Fabrication (FFF) [135–138]. Its role in this form of 3D-printing, coupled with its history of application as a resorbable implantable material, make it a natural choice for this research on resorbable bone-repair and regeneration materials. As a benchmark of sorts, Cleft Lip and Palate (CLP) – and specifically the maxillary bone-defects associated with it – was used in this work as a reference in terms of its clinical bone-repair needs.

Alveolar bone-defect repair for CLP has been attempted with a variety of materials through history [14,139–141], with one of the earliest recorded being gold plates, back in the 14th century [53,105]. However, non-degrading rigid bone-implants are incompatible for current standards of care for CLP. The fact that most maxillary-cleft repairs are done in children is largely to blame, and the evidence leading to this – and eventually relating to the present research – is discussed in the following sections.

2.1.3. ANATOMICAL FEATURES AND FUNCTION LOSS ON CLEFT-PALATE LESIONS

The structure and location of the palate make it important for two processes: language production, and deglutition. Its essential functions derive from it being a barrier between the nasal and oral cavities [142], and its barrier and support functions enable – along with the tongue, lips, respiratory system, vocal chords – for manipulation of matter (liquids, and edible items), as well as pressure gradients within the cavity, and between the respiratory and digestive systems. While the hard palate provides a passive barrier between the oral and the nasal cavities, the soft palate allows for managing of pressure waves during speech by means of the velopharyngeal valve and its muscular bundle (the palatopharyngeal muscles). Unfortunately, a palate with compromised integrity usually fails in performing at least one of its intended tasks, with various degrees of dysfunction depending on the portions of it involved, as well as the severity and extent of the lesions (though, admittedly, some instances of CP are asymptomatic) [143,144].

CP can appear in a variety of ways, with affected structures ranging from the upper lip (sometimes with nasal involvement), maxilla, hard palate, and soft palate all the way back to the uvula [145]. These lesions, in turn, can range in width, depth, length, and location, manifested at any point along the fusion borders of the primary and secondary palates and their neighbouring soft-tissue. The involvement of these numerous structures results in the geometrically complex lesions which are relevant for the clinical application of this project (**Figure 2.3**).

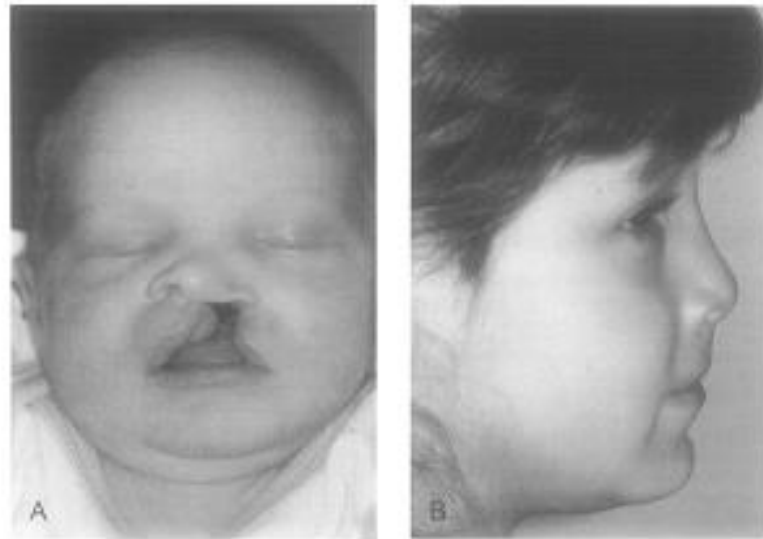


Figure 2.2 Facial growth after primary bone grafting. A, perioperative view of unilateral complete cleft patient. B, Eight-year postoperative result. Alveolar defect is evident on the perioperative presentation of the patient. Treatment including grafting resolves the bony lesion, but some degree of midface retrusion is observable in the patient's postoperative profile. Reprinted with permission from Elsevier [159].

2.1.4. RISK FACTORS: GENETICS AND TERATOGENICITY

Palatoschisis, more often referred to as cleft palate (CP), covers a range of congenital orofacial deformities that arise from faulty fusion of the pharyngeal arches during embryonic development [146]. These result in fissures that are classified together as they affect the primary and secondary palates, leading to a diverse array of subsequent complications that depend on the type and extent of these defects. Traditionally, there are two main groups of factors thought to be responsible for this kind of abnormal development of the palate: teratogenic substances and genetic defects [21]. Even though a range of genetic alterations and defects have been hypothesised to contribute or

decisively lead to CP [27,146–150], research has led to a modern consensus in that the underlying genetics of CP are a complex and multifactorial predisposition [21,147,151–154], and its ultimate mechanisms have yet to be described [27]. This predisposition, in turn, is accentuated – or maybe enabled – by the developmental environment of the embryo [26,152–155], the sum of which culminates in the aforementioned palatine fissures. It is noteworthy that these deformities are linked (through some shared risk and preventive factors, such as maternal diet) to neural tube defects, which have also been widely studied and are equally complex in aetiology [26,154,155].

Some presentations of CP are mostly genetically-driven. In studies of cases of X-linked cleft palate (CPX), for instance, the malformation was found to have an autosomal-recessive inheritance pattern [27], while CPX with ankyloglossia has been described as an autosomal-semidominant mutation [156]. CPX is a type of non-syndromic cleft palate (NSCP), meaning it does not appear concomitantly with more than two additional malformations as a consistent entity [27,151]. The most recent research has shed light about the TBX22 T-box transcription factor gene and its promoter to be the most direct causal agents known of so far [27,149,156]. In cellular terms, alterations to these genes are theorised to interfere with mesoderm growth, migration, and apoptosis, thus altering normal palatogenesis [156]. Syndromic CP variants, on the other hand, occur within a given set of deformities, the most common of these being the van der Woude syndrome (VWS), which was found to be an autosomal-dominant condition. It is also linked to a single gene defect in the transcription factor IRF6 [150]. Several other syndromes that feature CP exist and are described in genetic mechanism with varying degrees of certainty

[157–159]. CP itself, however, manifests similarly within syndromes as it does as an isolated entity.

There is a group of *environmental factors* that mostly encases teratogens related to orofacial clefting. It must be noted that not all of these are causally linked to such malformations, but have been found to contribute to their overall occurrence risk when used during pregnancy or near conception [151]. Some heavily teratogenic drugs are capable of inducing CP or CLP amongst their spectrum of deformities; such is the case of anticonvulsants like phenytoin, valproic acid and oxazolidinones [160]. Other substances are less strongly implicated with CP, like tobacco and benzodiazepines, and might also depend upon genetic predisposition to yield their full effects [161–164]. Maternal alcohol use and steroids are dose-dependent and well-documented causal agents for CP [165,166].

Maternal nutrition encompasses a noteworthy set of factors balancing the risk of CP and other such abnormalities [148]. Folic acid has been prescribed for decades now as a nearly mandatory prescription for pregnant women, as studies have found it to reduce the overall risk of birth defects when used in doses well above the average dietary intake [167]. It was shown to reduce the incidence of CP and CLP in mothers with increased risk when taken as part of multivitamin supplements [24]. In contrast, however, increased vitamin A intake might also facilitate the appearance of CP [153], as do abnormally low erythrocyte zinc levels [154]. Glucose has been theorised as a teratogen [168], but thus far the evidence is inconclusive at best [154], but more likely pointing towards metabolic circumstances – such as maternal diabetes and/or obesity

– as the actual culprits, as their presence accompanies an increased risk for congenital anomalies, including CP [26,155].

Palate clefting can be also acquired from lesions secondary to bacterial infection: this has been observed in both humans [169] and mice [170]. Trauma, naturally, can also lead to structural damage that mimics congenital CP. Other mechanisms are known, such as chronic cocaine use, which necroses palatal tissue and eventually erodes a deep lesion that requires surgical treatment [171]. However, in these cases the aetiology is relatively simple to explain, and their literature focuses on procedures for repair derived from those developed for congenital CP.

2.1.5. PALATOGENESIS AND ITS DISRUPTION

Development of the palate can be understood in three broad phases: proliferation, elevation, and fusion. It is worth noting that these processes occur simultaneous to the development of the rest of the structures in the head, neck, and central nervous system (CNS), from around the fourth to the twelfth week of gestation [153,172,173]. All these structures are very close by and many – namely the oral cavity, middle and inner ear, neck, and face – derive mostly from the pharyngeal arches and the frontal process: this is partly why any deviation from normal cellular mechanics, local genetics, or local growth factors can lead to a plethora of craniofacial malformations, and why several forms of CLP occur within a syndrome along with other anomalies [153,155,172,174]. Less specific mutations, however, can result in CP or CLP along with defects at more distant sites, as is the case for popliteal pterygium syndrome, to name an instance [150].

The proliferation phase of palatogenesis starts around the end of the 5th gestational week. By this moment, the pharyngeal arches are eight bilateral collections of tissue protruding inferior to the cephalic structures, closely packed along the lateral margins of the ventral portion of the embryo (**Figure 2.4**). These arches are composed of a mesoderm core covered by an ectoderm layer on the outer surface, and an endoderm one on the inner side. Portions of the core differentiate into nervous, vascular, and cartilaginous tissue, which will give rise to skull vasculature, bones, and cranial nerves [172,175].

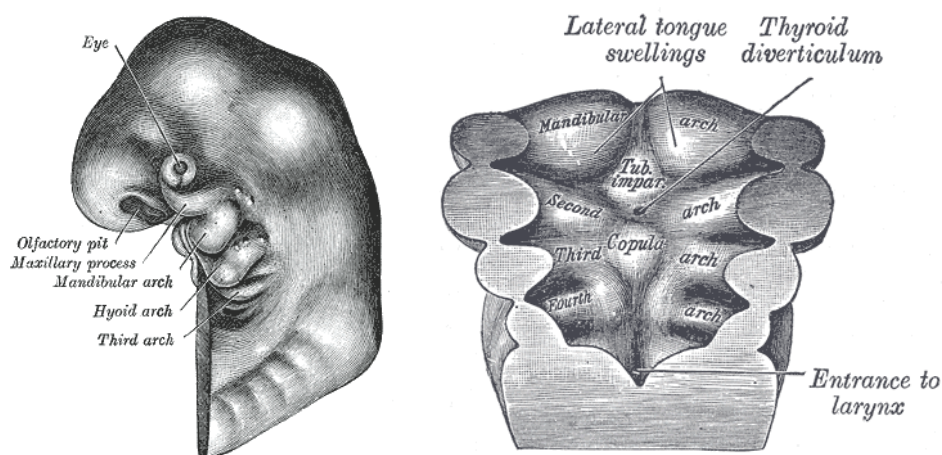


Figure 2.3. Diagram of early development of the pharyngeal arches. Lateral (left) and anterior (right) views of a developing embryo near the fifth gestational week [175].

Any alteration on tissue and cellular growth factors – genetic or environmental – will necessarily affect this process, as well as the later ones since all happen as every structure of the head is beginning to form [153,172]. Shortly after the 6th gestational week, the mandibular processes on either side of the first pharyngeal arch meet at the medial plane of the foetal skull and start ossification. Around this time, the medial nasal processes – coming from the first pharyngeal arch – have similarly extended medially, forming the

intermaxillary process which will start to ossify by the 7th gestational week. The intermaxillary process, in turn extends posteriorly to form the premaxilla [176].

Notably, this previous step is a crucial point where alveolar clefts can commence, as precise coordination in cell proliferation, death, and differentiation is needed to achieve healthy tissue architecture. Molecular signals on cell growth, migration, extracellular matrix production, and death (like those of the TGB- β superfamily) are at play along with nutrients derived from maternal intake (like vitamin A, zinc, myoinositol, or folic acid), and have been studied as linked to CP when they suffer alterations on their balance [24,153,154,167,174,177]. Teratogens, as mentioned in the previous section, are thought to affect such balance to varying extents [147,161,162,177,178].

Around the end of the 12th to 14th developmental week, the elevation phase is complete, and the base of the tongue differentiates into the genioglossus muscle and its supporting structures, and these help pull the tongue down into its final (horizontal) position [28], moving out of the way of the recently-formed shelves. Several other mechanisms are thought to be involved in the reorientation of the palatal shelves, but tongue withdrawal – which coordinates with mouth opening – is considered a crucial event as it preludes the observation of horizontal shelves which then grow medially towards fusion [28,153,172]. Whether these movements themselves or the physiological and mechanical events around them are directly involved in palatine shelf elevation remains unknown, but their disruption has been shown to impair this stage of palatogenesis and thus lead to CP [28,153,154].

Palatine shelf fusion is a rather complex phenomenon (**Figure 2.5**), since it occurs late relative to organ genesis and tissue on the shelves themselves is already vastly differentiated at this point: their integration becomes less straightforward. Even though this process shares some of the regulatory conditions that dictate primary palate fusion, additional mechanisms become necessary for their successful integration into a single continuous structure. This is likely why fissures on the lip, alveolus, and palate are closely associated, but also why CP is such a common craniofacial malformation [21,22,28,142,173].

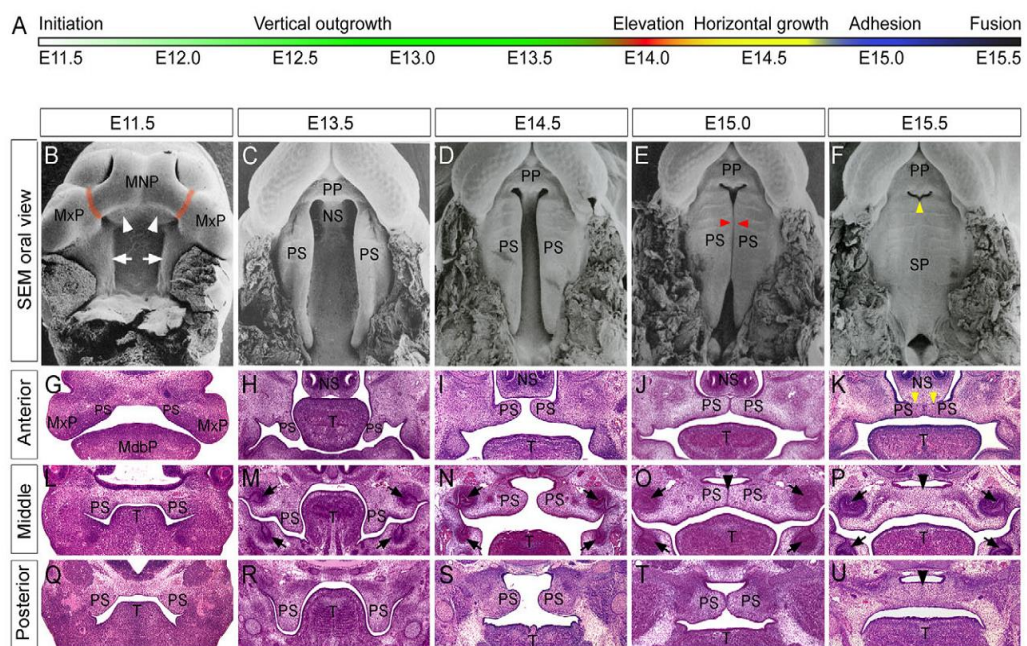


Figure 2.4. Scanning electron microscopy (top row) of mouse palatal development. Progress in time (A) depicted from left to right (B to F), corresponding to human 4th through 13th weeks of development (mouse E11.5 to E15.5). Letters G through U are corresponding histologic coronal sections of the SEM images. MxP: maxillary process; MNP: medial nasal process; PS: palatal shelves; MdbP: mandibular process; NS: nasal septum; PP: primary palate; SP: secondary palate. Reprinted with permission [173].

Not only is apoptosis of the epithelium at the medial edge of the shelves needed for their mitotically active inner layers to contact, but selective adhesion of these layers to each other is also imperative for successful fusion [142,172]. Fusion begins in the central portion of the shelves, and the process is then completed at the frontal and dorsal portions, with the former also fusing with the primary palate [172]. Subsequently, further differentiation occurs at the epithelial surfaces of the complete palatal shelf, with distinct epithelial types appearing at the lower and upper sides of it, formally separating the nasal and oral cavities [177]. The relatively high incidence of CP is probably also due to the fact that ossification of the cranial structures is already underway when fusion is completed [172], which usually signifies the end of differentiation for the internal tissue of the palatine shelves as the final anatomical structures and geometries are close to be achieved: any fissure or fistula that is still unclosed after this point will remain part of the embryo's anatomy.

2.2. SURGICAL REPAIR OF BONE DEFECTS CLEFTS

2.2.1. AIMS AND TECHNIQUES

There are three aspects that cleft palate repair should take into account: speech development, deglutition capacity (together comprising velopharyngeal function), and cosmetic facial features (including dentition) [21,152,179]; all of it in the context of continuing craniofacial growth, since most patients will not be fully developed during their treatment [180–182]. Four

structures are primarily involved in this type of malformation: the lip, the alveolar bone, the soft palate, and the hard palate. Secondary structures affected vary from case to case, but most commonly include the Eustachian tubes, the nose, and the velopharyngeal muscles [21,172]. It is evident that these functions and structures are affected differently depending on location, extent, and severity of a given fissure. In virtually all its presentations, treatment of CP and CLP is comprised of an extended series of medical and surgical interventions all the way through the teen years of the patient (when treatment starts during the first months of life) [25,181,183,184]. Breathing alterations, nasal deformities, and middle ear anomalies and infections are also amongst the possible and common side effects of some clefts [185–187].

Early CP repair procedures as described by Dieffenbach [188], Warren [189], LeMonnier [190,191], and von Langenbeck [192] were later revised by Veau [193]. All such procedures follow a straightforward objective: to reconstruct the palatal anatomy with the tissues actually present on-site – exclusively soft tissues. These surgeries eventually integrated a bone autograft to close down the alveolar gap while trying to prevent maxillary retrusion [194,195]. Currently, grafting is performed from ages 10 to 14, though some studies recommending the eruption of the central incisors as a timing indicator [38,196]. Closure of the alveolar gap was at first done with gingivoperiosteal tissue; similarly, mucoperiosteal flaps and reorientation of the vault were also used for hard palate lesions [25,196,197]. Although the main objective is achieved through these means, they only accomplish successful function restoration to some degree due to excessive scarring, infections, tissue contraction, insufficient posterior reach of the soft palate, or due to inconsistent results on different CP

presentations [198,199], adding to abnormal development of facial features into adulthood [20,200].

The need to overcome these limitations furthered experimentation and the creation of the V-Y incision techniques and their variants – namely the Veau-Wardwill-Kilner one – that were predominant through the 20th century and are still are used today [25,171,180,183,198,199,201]. More modern takes on this treatment were developed by Bardach (two-flap palatoplasty) [202] and later Furlow (double-opposing Z-plasty) [197], with divergence on what soft tissues to manipulate and how to handle them for better healing and overall outcome. These techniques are presently the most commonly reported [25,36,180,203], though, as often happens, slight variations and preferences appear amongst healthcare centres and surgeons, and sometimes even depending on case-specific circumstances, including call-backs to Veau's and Lagenbeck's methods (usually in the form of their respective revised versions) [36,183,184].

2.2.2. GENERAL TREATMENT SEQUENCE LAYOUT

Though the surgical treatment of soft tissues (lip and soft palate) takes care of most of the immediate aesthetic and functional issues, closing the hard palate and alveolar fissures plays a decisive role on patients' post-surgical evolution [20,36,184,200,204], as well as in how post-closure treatment will be handled (which mainly involves orthodontic interventions, plastic surgery, and attention to closure-derived complications) [184]. The treatment outcome has to be balanced between development of speech and compromise of craniofacial growth, with earliness on hard palate repair – closure performed between two and five years of age – leading to maxillary hypoplasia later in life [20,183,205–

208], since the shape of the hard palate is usually narrowed medially during reconstruction [184,197]. Current consensus on an optimal age for alveolar and hard palate defect repair can range from 18 months to 14 years, since previous closure of the soft tissues (at 6 or 18 months) already reduces the width of bony tissue fissures [28,196,209], though this age will vary according to local practice [208,210]. If delayed until dentition has ensued, facilitation of eruption of the lateral incisors and/or canines is a reliable indication for alveolar repair through grafting, so this helps narrow down the timeframe for treatment of bone fissures as, in some cases, it can be convenient to perform this procedure along with the hard palate closure. This is currently performed from ages 10 to 14 in the United Kingdom [32,36,38,184,196,211].

The two-stage repair protocol was envisioned to address the above issues, with the more immediate aesthetic and soft-tissue features repaired during the first year of life, and the bony defects treated once the patient's development has progressed [19]. Hard palate closure under this scheme was delayed to ages between 12 and 14, and even later in some patients [19,212]. This timeframe allows for normalisation of palatal anatomy, but comes at the expense of speech proficiency unless speech therapy is included in the treatment regime [196]. It is remarkable that, even though analysis shows that two-stage repair yields better overall results [196], a recent report found that only about 14% of (non-syndromic) CP and CLP patients in the US receive treatment in two stages, with most practices looking towards avoiding multiple surgical interventions [36]. This is also a tendency in developing countries where the monetary burden – personal or public – of chronic treatment poses a major limitation [183]. Centres practising one-stage closure for CP and CLP

do not seem to report any adverse long term problems, but studies on this respect do not advocate for this protocol [20,184,196,200,205,213,214].

2.2.3. POST-REPAIR COMPLICATIONS

Adverse events as consequence of surgical repair of CP have motivated the study and development of the techniques up to the current state-of-the art. The gradual refinement of the main objective from closing the fissures to recreating the normal architecture of the oral, nasal, ear, and pharyngeal complexes has improved the overall outcome of the treatment and reduced secondary complications. Such complications can be divided into two broad groups: immediate and long-term, though it is evident that they can also be understood in terms of functional and structural compromise [183].

The most common serious functional complication is post-surgical respiratory problems, which arise from either perioperative airway management, inflammation of the involved tissues, persistent bleeding into the nasal cavity, haematomas, or secondary to wound infection [183]. It is worth mentioning that otitis media and upper respiratory infections are even more common, albeit much less serious [215]. These can result in anything from pulmonary infections to respiratory obstruction [183,216]. On the same line, other common structural issues derive from surgical wound complications, with failure of repair being caused by necrosis of manipulated tissue, graft or prosthesis failure, as well as infections [183,216]. Some have even reported death as a possible complication, most likely as a result of perioperative management, but at least one study hypothesises patient intraoperative positioning as a possible cause for a brain infarction [217].

Formation of oronasal fistulae [183,216,218], and mucoperiosteal flap detachment (hanging palate) [219] are possible structural complications that become evident in the following weeks as the patient recovers from surgery; both are caused by faulty surgical wound healing. Incidence for this complication has been estimated between 5.4% and 23% [180,218]. These happenings are considered an indicator for repair success [216], and they require additional medical and/or surgical intervention. It is known that most fistulae develop at the border between hard and soft palates [180], though decisive measures to prevent post-palatoplasty fistulae formation remain elusive at present [218]. One case report suggests that injections of human platelet-rich plasma (PRP) around the areas to be operated might reduce the chances of tissue failure and fistula formation through hyperplasia and hypervascularisation of the zone [25]. Though healing adjuvants might be a possible solution to this issue, surgical wound healing has been found to be more complex than just biological factors, with even the psychological state of the patient playing a prominent role in effective healing [220,221].

Long-term complications are all related to how the surgery affects normal craniofacial anatomy and development. Maxillary hypoplasia and speech abnormalities have drawn the most attention during development of surgical techniques for CP and CLP repair, but others are also relevant – albeit less dramatic in presentation – such as velopharyngeal dysfunction, recurrent otitis media, obstructive sleep apnoea, and dental alignment disruption [20,183,222]. Although lip and alveolar deformities are alarmingly obvious in new-borns, these do not worsen with normal craniofacial growth [17,19,184,196,205,214]; as such, palatoplasty is implicated as the main

cause of aberrations on facial skeleton development in these patients [20]. The maxillary and the mandibular bones are almost exclusively affected [17,20] due to tissue contraction and scar formation lowering the palatal height after repair. In turn, all of this leads to abnormal facial features due to maxillary retrusion, especially affecting its vertical proportion [184,223].

2.2.4. BONE GRAFTING: ISSUES, OUTCOMES, AND SECONDARY MORBIDITIES

Applied to alveolar repair for CP patients, autologous grafting was first documented by Schmid in the middle of the 20th century [224], and this early approach harvested tissue from the ribs [208]. Bone grafts, in virtually any surgical context, are indicated with the aim of establishing a normal architecture of the skeleton which could have been disrupted due to a variety of reasons (**Figure 2.6**). From this perspective, it was only logical that autologous bone became the reference material to fill in any gaps, resections, and fractures, since it should naturally comply with the patient's immunological requirements [159,195,225] – arguably the harshest limitation for an implantable material. Once past biocompatibility issues, five types of properties determine if a material is suitable for a given bone reconstruction application: manufacturing, mechanical, osteogenic (viability of intrinsic bone formation within the material), osteoinductive (capacity for mesenchymal stem cell recruitment and differentiation), and osteoconductive (capacity to support angiogenesis) [195]. Bioresorbability is desirable as well, as the ultimate goal is full integration of the tissues surrounding the implants [8].

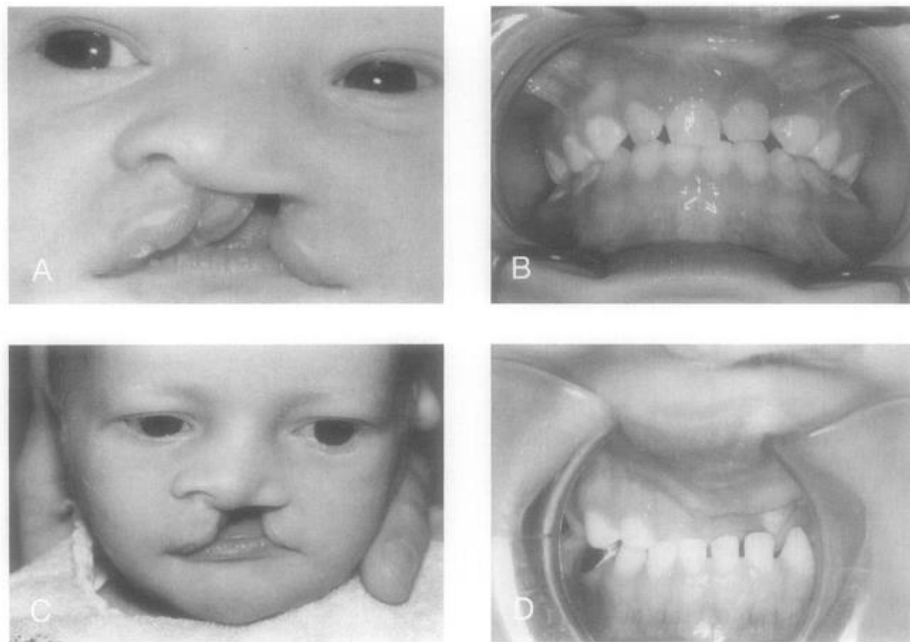


Figure 2.5. Postoperative (6 year) maxillary arch form. A, Initial unilateral cleft deformity. B, Postoperative maxillary aspect with grafting. C, Initial unilateral cleft deformity. D, Postoperative maxillary aspect with complete crossbite after treatment without grafting. Reprinted with permission from *Elsevier* [159].

Cancellous bone is the most used form of autograft, though not without the limitation of lacking mechanical integrity [90,195]. It does excel at all other characteristics; though in applications like those requiring a fixation or load-bearing device, cortical bone is preferred, since a cancellous graft is not at all structural [195], and it is simply applied by packing it into a defect and soft tissue is sutured around it [226]. A cancellous graft integrates readily with the host site's tissue, with resorption and bone neogenesis occurring as soon as one month after grafting, completing integration after one year [90]. Cortical implants, on the other hand, have adequate mechanical properties to begin with, but will start being resorbed around the second week after being implanted, which is usually faster than the rate at which the surrounding bone will be able to integrate it, as its compact internal structure makes it unsuitable for angiogenesis and osteoblast recruitment [90,195]. By the sixth month after

grafting, cortical implants will have weakened beyond the mechanical performance of surrounding bone, with this problem persisting for years [90].

Secondary morbidity of a grafting site is harvested-volume dependent, with as high as 25% of patients presenting persisting severe pain following tricortical full-thickness iliac grafts (**Figure 2.7**) [227]. Depending on individual surgical circumstances, major secondary morbidity rates range from 8.6 to 17.9%, including requirement of additional surgery, haematomas, chronic pain, deep infections, chronic paraesthesia, and additional wound treatment [228]. About 20.6% of patients, in turn, develop minor complications which include superficial infections, and non-chronic paraesthesia and pain. Chronic pain, being one of the most disrupting complications, ranges in reported incidence rate from 3% to 26% [225,227–229]. Additional complications of grafting are linked to the surgical circumstances of each case, where the Veau-Wardwill-Kilner technique has been implicated in higher incidences of persistent bleeding and post-operative fistulae [215,230], although other studies claim there is no clear rate-to-technique correlation [218]. One possible and serious side-effect of cancellous grafts on alveolar fissures, for instance, is dental root resorption, which normally requires extraction [194]. Synthetic implants have been explored as an alternative to address the issues highlighted in this section, for which 3D printing is a promising manufacturing option.

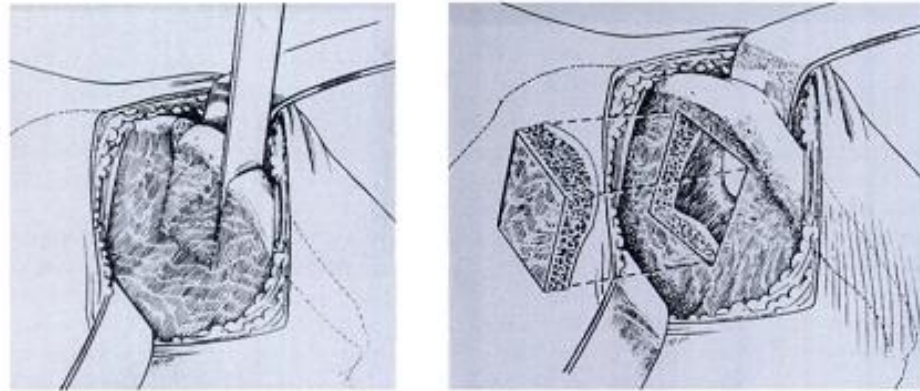


Figure 2.6. Autografting from iliac bone. Left, operative removal of a tricortical graft including the iliac crest. Right, a bicortical graft preserving the crest. Reproduced with permission and copyright © of the British Editorial Society of Bone and Joint Surgery [227].

2.3. FUSED FILAMENT FABRICATION FOR CRANIOFACIAL RECONSTRUCTION APPLICATIONS

2.3.1. STEREOLITHOGRAPHY AND THE BASIC PRINCIPLES OF 3D PRINTING

All 3D printing techniques started as derivatives of the stereolithography technology developed by Charles Hull in 1983 [41]. This method relies on photo-curing powdered resins through focused UV-lasers in order to generate flat plastic shapes [41]. This patterning process introduced many of the now-familiar elements of a 3D printer: the resin was laid out in a flat and levelled printing bed, with a movable toolhead suspended on top of it (or a movable bed in some setups). In the case of stereolithography, the toolhead houses the lasers, which it then focuses along the areas to be cured in the intended shape. Once one such layer of resin has been polymerised, a new layer of resin is

laid on top and cured, stacking these flat projections until the final volume is obtained [45].

Arguably the most important piece of technique from the early days of stereolithography is the standard tessellation language (STL) used for programming the process. This programming language stores a standardised representation of coordinates that make up a given volume and shape [231]. These coordinates are further processed by a 3DP system – through a so-called slicing software – to generate a series of contours and cross-sectional surfaces that will form a desired geometry when stacked on top of each other. Not only do 3DP systems rely on STL coding, but most computer-assisted engineering (CAE) and computer-assisted design (CAD) software packages are able to work with its file extension (*.stl) to this day [231]. This part of the whole method is key and common to all modern 3DP techniques: in principle any STL file can be turned into a real model through this technique.

Tessellation procedures convert a modelled 3D shape into a mesh of triangular polygons warped around the surface of the model in question [232]. This processing step is crucial in that it allows for a mathematical parametrisation of any given geometry in a standardised, scale-independent way. Mathematically, this mesh is broken down to a matrix of coordinates and vectors that provide enough information to locate any single triangle within the whole arrangement, while also locating them in reference to other adjacent polygons. Each individual triangle is represented by a vector normal to its surface, as well as the coordinates for each of its vertices, such that:

$$f = \begin{bmatrix} v_i & v_j & v_k \\ p_{1x} & p_{1y} & p_{1z} \\ p_{2x} & p_{2y} & p_{2z} \\ p_{3x} & p_{3y} & p_{3z} \end{bmatrix} \quad \text{Equation 2.1}$$

Where f is a given triangle (or facet), and v values stand for vector magnitudes parallel to the i , j , and k unit vectors, while p values stand for vertex coordinates along the designated axes. Coordinates and magnitudes are formally floating-point variables, and are expressed as significands followed by signed exponents: it follows that each coordinate can only assigned a positive value by definition [233], though vector magnitudes can naturally be negative. In terms of coding, a given geometry A consisting of the single f facet just described can be written in American Standard Code for Information Interchange (ASCII) as follows:

solid A

facet normal v_i v_j v_k

outer loop

vertex p_{1x} p_{1y} p_{1z}

vertex p_{2x} p_{2y} p_{2z}

vertex p_{3x} p_{3y} p_{3z}

endloop

endfacet

endsolid A

It is noteworthy that it is possible and correct to represent any n -vertex polygon in this fashion by describing its corresponding number of vertices but, traditionally and for practical reasons, STL files deal exclusively with triangles [232,234]. In regards to this, modern digital modellers usually avoid working with triangular polygons in the initial stages of the creation of a solid, in favour of quadrangular polygons. This is owed to the fact that many digital processing methods – especially those involving deformation of a solid – will complicate calculations when dealing with triangles, and often yield unpredictable results. Errors in meshing are a common issue and have been subject to study as digital modelling technologies have evolved [232,235,236]. Loading digital models into rendering software, for instance, will triangulate their surfaces, resulting in unnecessarily increased polygon counts. This happens as their procedural algorithms divide the model's polygons. This is optimal on quadrangular ones – which will usually be divided in two triangles –, but redundant and detrimental in triangular ones – which will be only divided into smaller triangles. Broadly speaking, a higher polygon count usually means smoother surfaces closer to real curved shapes. This comes, however, at the expense of longer processing times [234]. This is but one issue of the many that can arise when triangulating surfaces, and modern 3D printing software will generally have built-in functions to deal with mesh correction and optimisation [232–234].

In general, the processing of a model prior to additive manufacturing (AM) suffers from loss of information on two stages: during the surface triangulation processing, and at the cross-section slicing step [233,235,237]. Slicing is usually undertaken by a proprietary software that ultimately translates the

inputted geometry into a program cycle for a given AM device. The contour of a given cross-section can be derived from the definition of its STL facets, and reproduced in terms of displacements from a point on the printer bed. It becomes evident that any curved shape along the vertical direction of the construction process will only be as smooth and accurate as the resolution of the given AM technique and device allow [233].

2.3.2. 3D PRINTING TECHNOLOGIES

Section 2.3.1 illustrates the driving principles behind all modern 3DP technologies: that the intermediate steps between CAD and a final product can be cut down to a minimum through adequate implementation of technological advances. These AM processes aim to remove the need of indirect methods like casting, and subtractive ones like tooling, which were virtually the only options for industrial manufacturing up to the beginning of stereolithography. This preference was reflected on the role AM methods held as rapid prototyping technologies through most of their existence in industrial applications, since the quality they could provide was not up to the standard of finished parts made through other means [41,42,45]. It has only been in recent years that finished (or near-finished) products have been producible through AM methods, likely through the affordability and proliferation of consumer-level devices [42].

Shortly after the introduction of stereolithography, research from the University of Texas resulted in the selective laser sintering process (SLS), which is very similar to the former [238]. In this form of AM a layer of polymer powder on a printer bed is also used, but it is instead heated beyond its glass transition

temperature in order to bond the polymer particles without melting the material. As in stereolithography, a laser patterns a given layer into the required shape, with more powder added on top at the end; the process also bonds each layer to the previous one. Once all layers have been laid, the part is subject to thermal treatment to consolidate the bonding between particles. Selective laser melting (SLM) follows the same logic, but employs a high-power laser to fuse the powder. This technique is only applicable to materials with sharp melting ranges, which makes it suitable for ceramics and metals [231].

Ink-jet 3D printing relies on the same basic technology as standard ink-jet paper printing, and was developed at the Massachusetts Institute of Technology during the early 90's. Its procedure is also based around a powder bed, with an ink-jet actuator delivering a binder solution on the desired cross-sectional shape. More powder is added on top after each layer is finished, and the process is repeated throughout the desired volume. This method is naturally limited by the existing suitable combination of powdered materials and liquid binding agents, though it makes it possible to introduce different materials into the production of a single part [45,231].

At the turn of the century, 3D plotting techniques were introduced by the Freiburg Materials Research Center, which integrate hydrogels and high-viscosity liquids into a process similar to ink-jet 3D printing [239]. The main difference from the former is that 3D plotting delivers the whole of its materials in the liquid phase. This method was specifically developed for use in construction of tissue engineering scaffolds made from naturally-occurring materials such as fibrin, collagen, agar, or gelatin [45,239]. These materials cannot be processed in the high-temperature settings of the formerly

discussed methods, but can be argued to be the best choices for tissue scaffolding, since they most closely resemble the make-up of an extracellular matrix. This technique allowed for the eventual development of bioprinting, which refers to the integration of live cells to the printing process with the aim of recreating tissues more accurately, though with limits on its resulting geometries [239].

The present research is based around fused deposition modelling (FFF) since this method allows handling of plastics without intervening chemical agents that could complicate biocompatibility. Polymeric implants are best suited for maxillofacial reconstruction since they allow for good control over the desired complex shapes. The major limitation of this technology is that the material must be a thermoplastic, but this also opens up other possibilities for thermal processing of the input materials and finished parts. A detailed review on this manufacturing technique follows.

2.3.3. FUSED DEPOSITION MODELLING, ITS ISSUES AND LIMITATIONS

FFF was introduced shortly after stereolithography by Scott Crump, and patented in 1992 [240]. As with the methods already described, FFF follows on the same layer-by-layer construction protocol, but it does so using molten polymers extruded into thin fibres that form a given contour [241]. As a general reference frame, the *X* and *Y* axes in most 3D printers are commonly those parallel to the printer bed, while the *Z* axis would be perpendicular to it. The toolhead in FFF devices usually consists of an extrusion system movable on the *XY* plane, whereas the printer bed can be adjusted along the *Z* axis [240]. Some exceptions integrate vertical positioning to the toolhead with a static

printer bed. Currently, the preferred input material for these devices is purpose-specific cylindrical plastic filament, commonly found packed into a spool of a given weight. Most commercially available FFF printers are standardised towards either 1.75 mm or 3 mm filaments, with some requiring proprietary brands that might deviate from these measurements [237,241]. This filament is driven by means of a press or worm drive into a heating chamber that is set above the melting point of the material in question [237]. The softened plastic accumulates at the bottom of the extruder and is finally forced through a nozzle with typical diameters ranging from 0.4 mm to 1 mm [240].

As with any iterative process, it is bound to be subject to inaccuracies arising from its practical resolution limits. The ideal AM device would be capable of differential increments along any reference axis, as well as differential deposition of material. In the case of FFF, it is evident that its resolution is inherently anisotropic: one limit is given by precision and accuracy on positioning of the extruder on the XY (horizontal) plane, while the other depends on the printer-bed's controlled movement along the Z (vertical) axis relative to the extruder [233,242]. The resolution on the horizontal plane is directly dependent on the drive motors and positioning mechanism of the toolhead. The type and quality of these elements translates to the smallest displacement in the X or Y direction that the toolhead is capable of achieving [233,240]. It can also be argued that the control loops and electronics in place can make the system drift from its theoretical highest resolution. Similarly, the resolution along the Z axis depends on the setup of its respective drive motors, mechanisms, and controls.

Even though the system for vertical positioning is simpler — in that it handles movement in a single dimension — it has been pointed out that the Z axis is further limited on its delivered resolution by the thickness of the deposited plastic fibre [233]. Commercial FFF printers control fibre widths through the separation of the nozzle from the printer bed, with most models being calibrated to work under settings of 0.125 mm, 0.25 mm, or 0.5 mm [233,243]. The larger fibre widths are used to speed up printing while sacrificing vertical resolution, since the number of layers forming the geometry — and therefore construction time — is directly proportional to this value. Nozzle diameter must also contribute to variations in resolution, as it will alter the rate at which material can flow through the extruder, all other settings being equal [242,243]. In practice, however, little can be done to enhance a printer's performance in this respect without modifying it. Some control can be achieved through detailed characterisation, since a number of other variables are programmable through printer-specific software [240,242], ranging from extrusion rate, filament feed rate, density of fibres in the internal geometry of the cross-sections, extrusion temperature, toolhead displacement speed, printer bed offset, amongst several other predetermined by each manufacturer.

2.3.4. IMPLANT MANUFACTURE AND MAXILLOFACIAL RECONSTRUCTION

Since the advent of Rapid Prototyping (RP) in the early 80's, its potential for medical applications was evident, eventually sprouting the term medical rapid

prototyping (MRP) as a catch-all category for custom models produced for clinical use [42,125,244]. As the technology evolved, its potential within the field of tissue engineering was also expanded and explored in applications ranging from surgical guides [245], orthopaedic prosthetics [246] to regenerative medicine [247]. Maxillofacial surgery and facial reconstruction have certainly been identified as an area to benefit from modern MRP techniques. There is much room for improvement on problems that have been identified on current practices, which rely on metallic implants and surgical plates of standardised shapes which can only be deformed intraoperatively to reasonably match the required anatomy. In terms of geometric accuracy of the final product, quality can be greatly improved by FFF techniques [40,47,125,248], which themselves are a subset of RP technologies.

Maxillofacial reconstruction applications tend to deal with very complicated geometries where standardisation is complicated – and many times impractical – [45], and where an intraoperative stage for implant adaptation becomes necessary, increasing surgical times [39]. Advances in manufacturing technologies throughout the last century widened the reach of bioengineering in prosthetic devices, which has been of interest for MRP and has made possible to reproduce geometries straight from medical imaging studies [125]. Research on this respect has proved computed tomography (CT) scans to be accurate enough on reproducing bone anatomy for surgical planning [48,249] and tools [48], as well as for facial-bone-reconstruction implants [39,40,246,248,250].

Tissue engineering has also found AM to be of great interest for production of clinically sound implants to improve upon bone autografts: the current standard-of-care for CP and many orthopaedic applications [108,180]. Common issues in terms of implant biocompatibility, biodegradation, and biomimetic activity are looking to be addressed and resolved through advances in tissue engineering [45,247,251]. The use of scaffolds for the purpose of cellularisation (or functionalisation) is nowadays the preferred method to apply tissue engineering to regenerative medicine [3]. These techniques, however, are still in development and would pose significant complications and additional costs to the manufacturing of an implant for clinical use. New polymers and AM methods – which are now commonplace in scaffold construction – have led to the development of current medical 3DP technologies and bioprinting: bringing the promise of organ replacement closer to reality [3,45,252]. By themselves, however, a polymeric bioactive implant could be an adequate solution for some applications, since it cuts out on the fore-mentioned complications and costs of *ex vivo* culture and growth of adequate quality and quantity of tissue(s) on a given scaffold [37]. Moreover, cell or tissue culture on a three-dimensional structure is possible, and recent research has shed light on the application of MRP implants for craniofacial reconstruction [103], [114], [115], as well as on the paradigms of using plastic implants [8].

It is worth noting that dimensional error would be a concern to manage during design for FFF. Given the slicing algorithms used for production of the base code necessary for FMD printers to operate – which breaks down a digital model into a series of cross-sections similar of those of CT scans [45,236,254]

–, it is expected that the scale of the printed structure affects the precision of the printing, as it is expected that the printer performs with varying accuracies depending on this same factor. Error on CT scans is reported around 0.9 to 2.16% on linear measurements to reproduce anatomical bone structures [254–256]. These are to be considered while deciding the geometry for an implant based on CT images and produced by FFF, as errors in manufacturing will add up to those of the scans. The principles used for modular designs for scaffolds have proven to be an efficient way to tackle scaffold design through 3DP [108]. By introducing a repeating pattern or subunit, it is possible to more closely control some of the parameters of the printed structure, while allowing to flexibly adapt the geometry to the shape of any given defect – while also avoiding scale-dependent variations to a certain extent. In the case of the present design guidelines, applying this idea will focus on handling void content, material porosity, and accuracy of printed measurements. For these reasons, it was considered that FFF was a viable line of research for addressing this clinical need.

Additive manufacturing techniques (like FFF, selective laser sintering, and bioprinting) have found applications as a production method for regenerative medicine plastic implants in research on reconstruction of cranial bones and bone regeneration in general [1,7,262–265,44,123,138,257–261]. For clinical use, it is far more common to find metallic implants – usually titanium based – made through other additive manufacturing techniques, such as selective laser melting [135,250] or 3D-fiber deposition [266]. Powder-based techniques tend to be more accurate in reproducing geometries since their resolution is limited in principle by the particle size of the powder used [254]. In contrast

FFF is limited in this respect by nozzle calibre, which for desktop 3D-printers is usually 0.4 mm (referring to the diameter of the opening of the extruder) [243], with other commercially-available choices being 0.25 mm and 0.6 mm. This limits the amount of small details that can be accurately reproduced by FFF from a 3D-model – especially in the sub-millimetre range. However, one of the strong advantages of FFF over selective laser sintering/melting is that the technique is not as material-intensive. This is due to the fact that FFF only requires material within the geometry being printed, while selective laser sintering/melting need to fill up the entire print-volume with powder. This makes these techniques less suitable for testing new developed materials, since large batches must be prepared for each single print-run. In contrast, FFF can produce single, small-sized samples, and material tests only require the production of some dozens of grams a time.

Recently, implants made through additive manufacturing specifically for reconstruction of the alveolus – from either CLP or other diseases – are also found in the literature. Patryk, et al. report a preliminary clinical study on five patients who received 3D-printed titanium scaffolds for alveolar reconstruction [267]. Berger et al developed a 3D-printing process for calcium phosphate using powdered ceramic with a liquid binding agent to produce a porous scaffold in custom fitted to a sample CT-scan [268]. Hixon et al described a method for using 3D-printed moulds used to cast a chitosan-gelatin hydrogel [269]. Coelho et al. published an animal study on rabbits with a surgically-created alveolar cleft that was repaired using a 3D-printed bioceramic scaffold [270]. Reports on alveolar cleft repair using FFF-produced implants are not available at time of writing.

2.3.5. APPLICATION-SPECIFIC CONSIDERATIONS ON MATERIALS AND FFF

The FFF device selected for the initial phase of this project is the BFB-3000 Triple Head Clear Case (3D Systems) manufactured by Bits from Bytes from 2002 to 2012. It is configured and tuned to extrude PLA out of the box, and runs on proprietary build files (*.bfb) generated through the Axon 2 slicer software provided, which are in turn based upon STL files from CAD or CAE models [41]. This machine is considered to be reliable and overall sturdy [246]. More modern printers might prove more accurate and better at reproducibility and resolution, but the present application does not require high-precision machinery-like components as much as organically shaped and reproducible geometries. Though the materials usable for scaffold construction are varied and rather diverse, FFF 3D printing has the obvious disadvantage of requiring a thermoplastic, as well as an innate incompatibility with bioprinting methods that use live cells [45]. A list of thermoplastics – alone, as composites, or as co-polymers – that have been reported for FFF in regenerative medicine is detailed on **Table 2.1**.

As is, the BFB-3000 should be able to handle any of the listed materials given proper calibration, while still being customisable and troubleshoot in-house if needed. This particular printer has seen very little use in the literature, as a single article reports its application on geometric evaluation for orthopaedic implants [246], though another model from the same manufacturer has been documented for tissue engineering scaffold production [271]. Its merits are remarked in this publication, as well as in the manufacturer's forums by long-

time users. It is regarded as being highly reliable, having a sturdy platform, as well as being easily repairable and modified while running in low upkeep costs. Support for this equipment, however, has been discontinued as of 2012, though third-party spares are available on-line.

The printer was considered to be accurate and precise enough for an initial approach to this application. One of the main disadvantages of this model comes from its use of induction sensors for positioning. The “zeroed” position of the printer tends to drift slowly from calibration each time it resets the extruder to its home position – this is likely to interference from the magnetic field of the motors and fans on the extruder, which are very close to the sensors. Modern printers avoid this issue by using mechanical end-stop switches. Many of the printing parameters (such as printing speed, infill speed, outer walls speed, flow rate, jerk, and retraction) are not configurable from its proprietary software, which limits configurability for different situations and materials. Relative to more modern FFF printers, this device prints faster, but at cost of print-quality, probably due to excessive vibrations from sudden deceleration of its heavy triple-extruder head. These disadvantages were considered minor given the sturdiness of construction of the printer, the availability of components and ease-of-access to its internal systems if in-house repairs were necessary during the project, and its good track record within the laboratory.

Given that a material is biocompatible and otherwise suitable for scaffold or implant fabrication, porosity becomes one of them main concerns when designing such a structure. Past publications [8,250,266,272–275] suggest a

range of an adequate porosities, on average of about 0.4 mm in diameter, in order to allow bone regeneration. Meanwhile, 0.3 mm is suggested to facilitate angiogenesis [8,276], which is relevant since its deficiency is certain to limit tissue growth and viability, as observed to happen with non-vascularised cortical bone grafts [90]. Moreover, adequate vascular supply is essential for clearing metabolic waste anywhere in the anatomy, and especially at implant sites where degradation by-products will build up. Even though all lactide polymers degrade into metabolically-occurring lactic acid, the compound is capable of inducing chronic inflammatory response when implanted, and build-up of degradation products is likely to blame [277].

With a bone regeneration implant, tissue growth is sought after within a three-dimensional space, and cells and their extracellular matrix should be able to infiltrate down to the innermost part of the geometry. Taking cortical bone grafts as a reference, low vascularisation and high density cause the graft to fail from the inside out, and the extracellular matrix to be slowly removed, with the zones furthest in from the graft's surface becoming an expanding necrotic core [90]. Both in culture and upon implantation, cells tend to prefer attachment to the surface of the any material rather than infiltration into its internal structure or porosity network [273]. Maximising surface area and accessibility to the inner spaces of the material have been taken in account for the design guidelines proposed as part of this project.

Table 2.1. Published thermoplastics applied through additive manufacturing techniques in regenerative medicine

Material	Authors	Year	Application
PLGA with type II collagen	Yen, <i>et al</i> [257]	2009	FFF hybrid scaffold chondrogenicity testing
PCL/PLGA	Kim and Cho [258]	2009	Multi-head FFF printer characterisation
PCL/tricalcium phosphate	Probst, <i>et al</i> [1]	2010	Calvarial reconstruction implant
PMME	Espalin, <i>et al</i> [44]	2010	Anatomical and mechanical evaluation of FFF printed implant
PCL	Teo, <i>et al</i> [259]	2011	Drug delivery device
PCL	Kang, <i>et al</i> [260]	2012	Seeded scaffold for critical-size defect in animal model
PCL and alginate hydrogel	Shim, J. H., <i>et al</i> [261]	2012	Proof of concept for bioprinter
PCL/PLGA/tricalcium phosphate	Shim, J., <i>et al</i> [262]	2012	Non-seeded implant for critical-size defect in animal models
PCL	S. Van Bael, <i>et al</i> [263]	2013	Biocompatibility testing
PCL composite with bioactive glass, PCL/PLA, PLA	Korpela, <i>et al</i> [271]	2013	FFF 3D printer characterisation
PLA/HA	Esposito, <i>et al</i> [264]	2017	FFF PLA/HA composite
PLA/HA	Esposito, <i>et al</i> [265]	2018	FFF PLA/HA composite
ABS, PLA	Rosenzweig, <i>et al</i> [138]	2015	FFF scaffold osteogenicity testing

PCL, polycaprolactone; PLA, polylactic acid; ABS, acrylonitrile butadiene styrene; PLGA, Poly(D,L-lactide-co-glycolide); PMME, polymethylmethacrylate.

2.4. LACTIDE POLYMERS: PROPERTIES, PROCESSING, AND APPLICATION IN FFF

2.4.1. LACTIDE POLYMERS

As shown in **Table 2.1**, polylactic acid polymers and its isomers present a more than viable and convenient choice – namely the L-isomer poly-L-lactide (PLLA), preferred for implantable devices due to its slower degradation profile (probably due to higher crystallinity). The 3D printer used for this study was

calibrated to use PLA (with PLLA having similar thermal properties), and virtually all commercial printers are factory-compatible with it. It has also been extensively documented in the literature regarding implantable-device production [11,138,247,278–282], as well as characterization as a degradable biomaterial [283–285]. These include techniques and reports on the material's relevant characteristics such as crystallinity [286,287], porosity [44,108,257,288], molecular weight [283,285,289], and calorimetric values [283,284,289,290], and processing [49,282,291,292]. Moreover, lactide polymers have been found to arguably be the most biocompatible of all printable thermoplastics due to their monomer being a common metabolic by-product [271].

It must be noted that PLA usually refers to the D isomer of the molecule (PDLA), while its enantiomer is designated PLLA. These and the L-D composite, known as PDLLA, differ in mechanical properties and degradation rates – probably due to differences in crystallinity [49,293,294]. Their biocompatibility and degradation products are nonetheless equivalent [137]. Medical grade PLA and PLLA are commercially available, and cleared by the FDA for use in implantable devices, though concerns might arise about new regulations required for FFF medical applications, as the process might have unexpected effects on the materials [295]. Though, in principle, much of the data on this respect could be extrapolated and deduced from previous research regarding other manufacturing techniques [49], the impact of FFF on the polymer's initial properties remains largely undocumented in the literature.

To this author's knowledge, the present work is the first formal attempt at doing this kind of characterisation for FFF specimens, which follows the challenges perceived by industry and research alike [296,297]. A need for further testing dealing with thermal and molecular properties has been pointed out by the National Institute of standards and Technology (NIST) of the US Department of Commerce, for instance [297]. There are currently no official standards specifically issued for the evaluation of 3D-printed parts and devices. Many of the ASTM and ISO procedures deal already with measurement, processing, and evaluation of the materials suitable for the diverse forms of 3D printing currently available, and these should reasonably apply and be followed [297]. PLA is one of the most widely-available printing materials, and virtually all commercial 3D printers are pre-configured to work with it. Additionally, PLA has been successfully composited with HA in published literature [136,283,298], with positive results relevant for bone-regeneration. It is being taken in account that the proposed battery of tests must be achievable in relatively brief time-windows, since custom geometries may not reflect testing done on standardised models — which is the current industry norm —, and applicable standards suggest device-specific dismantling properties is convenient, and is likely crucial on load-bearing implantable devices.

2.4.2. COMPOSITING AND SELF-REINFORCING OF LACTIDE POLYMERS

In general, biodegradable polymers are less resistant to mechanical stress – by a wide margin – than bone and other stress-bearing-implantable materials (mostly metals), although they are comparable or superior to other bone substitutes in all other relevant aspects [293]. Bone tissue exhibits tensile

strength in the range of 5-15 GPa, while tensile resistances of 7-30 GPa (in the direction parallel to the load) are desirable for bone implant purposes [247]. High-molecular weight lactide polymers yield an average of 2-3 GPa [136], with a maximum of 7 GPa for very high molecular weight (>1,000,000 g/mol) [136,247]. There are several documented techniques to improve tensile properties of lactide polymers – and polymers in general – [247], and, two are of relevance to the present application: compositing with hydroxyapatite (HA), and Self-Reinforcing (SR).

HA-PLA composites have been explored to address the mechanical resistance issue in applications where bone regeneration – as opposed to orthopaedic reconstruction – is the main priority. These require the implanted device to be biodegradable and its degradation products to be physiologically safe. Moreover, the implant is meant to fulfil the roles of an extracellular matrix, providing support, tissue scaffolding, osteoconduction, and osteoinduction, while still maintaining the adequate geometry and placement to bear the mechanical load the repaired tissue is supposed to withstand [247]. This last point, although it might not be instinctively evident, is one of the main variables to ensure the newly formed tissue develops under the right conditions to withstand its nominal load [299,300].

Integrating HA crystals into a PLA matrix has yielded an increase in tensile strength up to ~12 GPa [136,298]. The use of nano-scale hydroxyapatite (nHA) seems to allow for similar results in other polymers, but at the expense of ductility and impact strength [301]. Additionally, functionalisation of materials with HA has been studied due to its role in osteoblast differentiation

and new-bone formation [250,302–307]. In-house production of nHA through a simple and reproducible precipitation pathway is possible [308,309], and was explored in this research. SR, on the other hand, is achieved through the manufacturing and/or machining processes the polymer undertakes. The macroscopic and microscopic alignment of the polymer matrix and the nanocrystals enhance the mechanical properties parallel to them; the former is achieved through the controlled deformation of the material during processing [282,291,292], which FFF intrinsically does. Both processes have been successfully tried in implants, and HA by itself has FDA clearance for this application, though some production processes of nHA might be of concern in this regard due their use of hazardous solvents [247,282,292].

It is notable, however, that mechanical considerations arise from the demands of orthopaedic implants, which usually deal with the repair of long bones and other load-bearing sections of the skeleton which would require an implant due to a compromised structure: after fractures, resections, or neoplastic destruction, for instance [45,310], where the implant also acts as a fixation device [12]. Cleft palates should not be treated as such, since the missing tissue is *not* compromising the load-bearing duties of the maxillae, as evidenced by the fact that alveolar fissures can be left untreated for more than a decade in some schemes [196,211]. Mechanical strength of PLLA is a very valid concern in load-bearing applications, since studies show that *in vivo* tensile strength of bone fixation plates deteriorates more rapidly than both *in vivo* plates implanted without load, and *in vitro* PBS degradation setups [126,311,312]. Velopharyngeal function, on the other hand, is very restricted by clefting, and much of it is restored after successful – and appropriated –

closure of the palatal shelves, where grafts are not currently indicated [25,198,222,313].

2.4.3. DEGRADATION AND ENHANCEMENT OF LACTIDE POLYMERS: ANNEALING AND SELF-REINFORCING

Polymer breakdown is a concern that comes along with the use of plastics. Implementing polymeric biomaterials requires that this issue is given importance as it arises from the conditions within a given host organism, which tend to favour polymer erosion: the main mechanism of breakdown on plastic degradable biomaterials [314]. Bone illustrates the complexity of this issue, as organic molecules are intrinsically fragile, and only exist within a limited range of environmental conditions, exhibiting their biological activity through an even narrower range of these [294,315]. This is why all connective tissues – which are naturally-occurring polymers and composites – require constant upkeep processes, and why bone physiology responds and relies heavily on being subjected to constant mechanical stress [90]. Bodily fluids and immune-response-molecules – both humoral and cellular – are chemically aggressive: this adds a complex physiological component on top of every polymer's variable molecular arrangement and their tendency to lyse when exposed to solvents, radiation, heat, and mechanical stress [311,312,314–316].

Manufacturers state a range of degradation periods of PLLA and other lactides above 24 months [317,318]. *In vivo* testing shows high-crystallinity remnants persisting for almost six years [279,283,319,320], with *in vitro* data suggesting very long water penetration periods along with a slow initial scission of long chains – lasting from several months to a year –, which afterwards is to fuel

autocatalytic hydrolysis due to the release of oligomers and pH-lowering monomers [321]. This results in early degradation through surface erosion (causing the geometry to shrink from the outside), followed by later stages of bulk degradation (which eventually causes dismantling). Degradation is highly dependent on crystallinity, and amorphous regions are thought to fail first and, moreover, the first stage of degradation of these polymers predominantly involves reduction of molecular weight and increases in crystallinity [137,283,321]. By the end of this stage, further oligomer breakdown will eventually yield soluble monomers, as well as effective loss of mass on the structure with deterioration of its mechanical properties [283,321]. Molecular weight reduction during the first stage of degradation can be linearly related to molecular weight at a given time during degradation (Mn_t) such that:

$$\ln(Mn_t) = -kt + \ln(Mn_0) \quad \text{Equation 2.2 [284,321,322]}$$

Where Mn_0 is the initial (number average) molecular weight and k is the degradation rate constant for a given experimental setup, and t is time. For semi-crystalline lactides like PLLA, several studies place this threshold roughly after the material's mechanical strength drops below 70-80% of its original value during *in vitro* degradation [2,283,323,324]. Furthermore, an estimated dismantling period for medical-grade-PLLA ($Mw \sim 400$ kg/mol) is clocked at three to six months [317].

During this subsequent phase, monomers can accumulate in cavities and other such low-recirculation spaces inside a specimen, locally reducing pH and catalysing further hydrolysis from within the geometry [283,289,294]. It is generally accepted that, under physiological and simulated conditions, surface

erosion accounts for the very first stages of polymer degradation, with bulk degradation taking place as water infiltrates and accumulates through small-scale defects on a specimen's topology [137,294]. Polymer chains in the crystalline region are more tightly packed, fixed in place by intermolecular forces, and arranged in a lower flexibility superstructure, where water will not penetrate easily [319]. Amorphous regions, however, are less dense, smaller in size, randomly oriented, and more free to displace – therefore easier to infiltrate by water and able to harbour a larger amount of it – [2], contributing to the aforementioned degradation pattern [49], and the ultimate prevalence of high-crystallinity remnants in long-term studies [319,320].

Annealing and SR of FFF parts can help tailor – to a certain extent – the degradation and dismantling profile of an implant, in a similar way as how crystallinity and polymer blends are used for drug-delivery purposes – where amorphous PDLLA is preferred amongst lactides [137,321]. Thermal processing at 120 °C for 4 hours after machining yields increases in crystallinity and mechanical strength at the expense of elastic modulus [49]. Treatment at 200-250 °C of a very high molecular weight PLLA coating (Mw 1000 kg/mol) on cell-culture plates also proved to stimulate osteoblast differentiation, apparently by facilitating monomer release from lowered molecular weight sections during the early stages of degradation [325]. Self-reinforcing, on the other hand, is achieved through aligning polymer chains into macroscopic structures through processing of the material [12,326], with best results – doubling or even tripling tensile strength – achieved with different drawing techniques, as well as high-pressure moulding of heat-softened plastic above its glass transition temperature (T_g), but below its melting point

(T_m) [327]. FFF, in principle, can be used as a SR process, since it complies with the requirements of the technique. More than improving the material mechanically, aligned structures on small scales also increase degradation times by easing water flow along the surfaces, directing shearing into causing erosion, and thus presumably retarding infiltration [283,290].

2.4.4. DEGRADATION PROFILES: REAL-TIME SIMULATED-ENVIRONMENT TEST AND MODIFIED ACCELERATED DEGRADATION TEST

Lactide polymers are well documented to be bioresorbable and widely used in implantable devices and absorbable sutures [127,280,283–285,289,290]. *In vivo*, implants made out of these polymers take anywhere from two years to five or more to degrade completely, while *in vitro* tests and manufacturers' specifications place that time in over three years [279,280,285]. This is dependent on factors like implantation conditions, with fixation devices holding a fracture together, for instance, deteriorating overall faster than controls implanted on healthy bone [126]. However, for resorbable *devices* – as opposed to the material itself – in accordance with *ISO-10993-13-2010* [328], testing can be conducted up to the point where the implant's structure is compromised: its dismantling point. This is suitable for the present research, since degradation data for PLA is available, and the current focus lies around the effects of FFF on the manufactured parts. After implantation, the implant's mechanical characteristics become irrelevant once its structural features break down. Given that, the main interest in these experiments is how long the implant will hold its shape and function. After that point, biologically speaking,

it is safe to assume that degradation will proceed as expected, in theory with healthy bone growth happening around its debris [8].

Resorbable materials have been extensively studied in regards to their breakdown both *in vitro* and *in vivo*. The *in vitro* procedure is addressed by the *ISO-10993-13-2010* standard, with an emphasis on identifying rates of mass loss, molecular structure deterioration, and potential accumulation of degradation products. It is noteworthy that, though the procedure focuses on determining the amount of time it takes for a material specimen to completely dissolve into a medium, it also recognises the relevance of functional breakdown of a resorbable device. This can apply to a number of current applications, such as resorbable sutures and drug delivery devices, but as well to bone-fixation mechanisms and implants, which have been reported to exhibit drastically different chemical and mechanical degradation profiles when implanted as compared with *in vitro* data, likely due to mechanical wear [2,137,284,329]. These discrepancies show up despite the protocol using phosphate-buffered solution (PBS) at 37 °C as its degradation medium in its real-time simulated environment test (RSET) iteration to introduce part of the effects of bodily fluids on the material.

RSET, moreover, takes over a year to complete when following the *ISO* standard, but polymers like lactides, taking over three years to degrade *in vitro*, have brought attention to the accelerated degradation test (ADT) variant also listed within the standard. In ADT, the reaction rate is sped up by holding the experiments at a higher temperature, which should be decided in accordance to the thermal properties of the material in question so as to prevent thermal

decomposition [294]. Studies done in this respect found, as expected, that degradation tests of lactides above their T_g (which, at around 60 °C, is relatively near the physiological temperatures on the RSET setting) induce a much faster decay of all measured variables, probably due to thermal degradation [283,290], setting a limit to the applicability of this option for lactides.

Most published degradation tests for PLA follow the procedure described in *ISO-10993-13-2010*, or some variation of the methods thereby described [2,283–285,289,290,314,325,330]. However, many of these publications pre-date the standard, and others are not completely detailed regarding methodologies when not directly citing it as the procedure followed. At least one study [2] has compiled and compared degradation profiles for lactides *in vivo* and *in vitro*, but direct comparison is questionable given such methodological variations. Notwithstanding, the overall patterns registered are similar, and they seem to follow the expected sequence of events for polymers degraded in exposure to aqueous media. It becomes clear that *in vitro* degradation data does not directly mimic the effects of devices *in vivo*, especially for mechanical testing since implants' geometries and chemical exposure are very far from standardised specimens and conditions. In short, their testing results should be compared with caution as factors such as implantation site and load-bearing affect their deterioration, speeding it up to as little as six months [126,137,331]. Since crystallinity is observed to relate closely to the degradation behaviour of polymers, it follows that promoting further crystallisation through an appropriated annealing process (posterior to 3DP) would affect degradation properties of the printed specimens, as well as

their mechanical resistances. The effects of annealing in degradation tests of compression-moulded lactides has been studied by past research [49,290].

FFF might have unexpected effects on the materials being used, as the fusion of each layer of polymer happens from seconds to hours apart, and stochastic factors can vary unforeseeably during the whole process. Moreover, layers on asymmetric structures are allowed to cool down differently as the succeeding softened polymer is added on top, usually well above their T_g , transferring heat to the lower levels. While most applications are likely to disregard the resulting intermolecular disturbances these processes can cause, these might be significant in settings sensitive to crystallinity (C_R) and molecular weight (M_W) changes, such as biocompatibility cell cultures, or *in vitro* and *in vivo* degradation tests, as others have pointed out [49,137,247,283]. Additionally, mass-transfer devices which operate in high heat-transfer-to-mass ratios have been found to be prone to errors due to hysteresis, and, depending on their severity, sometimes might require built-in temperature regulators, or even closed-loop temperature and extrusion controls [225]. Implementation of these kinds of advanced automatic control systems might eventually prove to be necessary to improve the quality and reproducibility of FFF manufacturing.

PLA components manufactured through other means, for instance, suffer deterioration on mechanical and molecular properties upon ethylene oxide sterilisation (EOS), or even simple oven-drying: processes regarded as *mild* for most plastics and other materials [49]. Keeping these facts in mind, the effects FFF must have on thermoplastics – and particularly on lactide polymers –, have not been documented in detail in published media to this author's

knowledge, and are mostly extrapolated from other bulk extrusion techniques [297]. As the technology becomes ubiquitous thanks to consumer-grade products lowering the overall price of 3D printers, new ways for standardisation will have to be developed to keep quality control on products, as well as to promote scientific rigour and allow for directly-comparable results. The following procedure is presented so as to fulfil the aforementioned objectives, but as well as a proposal for a standardised approach to evaluate and characterise 3DP technologies in regard to dimensional accuracy, as the method allows for most variables to be controlled so as to make reasonably quantifiable the effects of varying the FFF device, its settings, or the material used.

Given the fact that degradation tests are lengthy and provide information on the bulk properties of standardised samples, a modified accelerated dissolution test (mADT) will be explored in this work, which aims to provide a fast way to retrieve mode-of-breakdown (meaning the way in which a given geometry suffers structural failure) data by introducing acetone as a test medium to replace PBS without modifying the testing temperature. Acetone has been used in past research to determine molecular weight deterioration of PLA [2], as it readily dissolves it at environmental temperature. In the absence of water, pure acetone attacks the material immediately, without the need for reduction of its molecular weight: this reveals the sites for weakest intermolecular interaction. An accompanying series of ADT is also presented so as to attempt correlation mADT data and past publications. The experimental procedures on this project are also designed to assess the effects on ADT degradation and mADT dissolution (namely in regards to

Ultimate Tensile Strength (UTS), E, Cr, and mass loss) of annealing and hydroxyapatite (HA) compositing on specimens produced through FFF.

3. AIMS AND OBJECTIVES

There are several basic considerations kept in mind before tackling the design and guidelines for the production of CP implants through FFF. One of the main issues to be addressed is the fact that patients receiving these prosthetics will still be growing [200], and that the repair process itself disrupts normal craniofacial development [18,20,204]. This problem is present even with autografting – at least for alveolar defects –, which is the current standard of care [25]. It is reasonable that it can be addressed through FFF by selecting a lactide polymer for construction of the implant, since they are estimated to suffer structural failure (their dismantling point) about six months after implantation [2,126,331], which coincides well with the required time for new bone formation to be well on its way [90].

Recent research has focused on the application of AM techniques and lactide polymers for the fabrication of implants and other orthopaedic devices, and most of it envisions a double function for the implant as a fixation means, as well as a bone regeneration scaffold [8,36,333,43,46,48,77,107,126,245,303]. Promising results have surfaced from such projects, and both the technique and material have potential clinical significance. Furthermore, compositing lactides with hydroxyapatite has been shown to positively affect the adhesion, proliferation, and differentiation cellular responses on *in vitro* tests [298,334]. PLA by itself has been used successfully on resorbable devices for implantation, and integration of HA can potentially enhance bone growth, and therefore the overall therapeutic performance of a bone implant.

The aim of this project was to investigate the production process for PLA-HA composites suitable for FFF-based bone-regeneration applications and to explore FFF as a manufacturing technique for therapeutic implants for complex lesions such as those found in CP.

The following objectives were identified in order to accomplish these aims:

- To develop a practical method for assessing dimensional reproducibility and precision of 3DP devices.
- To measure effects of the FFF process on PLA parts, in terms of mechanical properties, temperature-dependent phase changes, molecular weight, and biocompatibility.
- To develop a production method for a PLA-HA composite filament usable on FFF devices.
- To characterise such composite filament in regards of mechanical properties, temperature-dependent phase changes, and molecular weight.
- To determine the potential for bone-regeneration of this composite material by exploring the optimal PLA-HA ratio for *in vitro* cell response, while taking in account manufacturing limitations.
- To measure the *in vitro* response of MG-63 cell-lines to FFF surfaces as an initial approach to assessing their bone-regeneration potential, both in PLA and PLA-HA variants.
- To propose general guidelines and considerations for the design of FFF-compatible patient-specific resorbable implants for complex geometries.

- To determine the degradation profile of 3DP parts in relation to current published data on parts manufactured through other methods.
- To propose alternative abridged degradation test for rapid evaluation of the degradation characteristics of FFF-produced geometries.
- To produce a mathematical model of molecular weight degradation for PLA.

The knowledge gained upon completion of this project was condensed into practical recommendations for the production of clinically relevant FFF-compatible composites. This research hoped to highlight the convenience and relative simplicity of producing new blends of materials for FFF. This can be done in low volumes and allows for quick iterations. Methods for evaluating relevant mechanical and molecular parameters of structures fabricated through FFF, as well as detailed information on the effects of FFF on inputted materials were developed. The potential of FFF-processed PLA-HA composite blends for bone regeneration applications was also documented and compared to pure PLA. Practical guidelines for digital design of FFF-compatible geometries – to be subsequently implemented to implant design based on imaging studies – were produced. The viability and osteogenicity of this composite material in 3D cell-culture scaffolds was also be tested *in vitro*.

4. MATERIALS AND METHODS

4.1. DETERMINING THE PRINTER'S RESOLUTION LIMIT AND PRINTING ACCURACY

Tests were performed comparing specimens made from two FFF PLA filaments of the colourless (*natural*) variety. Samples made from the first material are labelled BFB-PLA (purchased from *3D Systems Inc.*, UK), and those from the second are referred as VB-PLA (purchased from *Verbatim*, UK). The molecular weight of these polymers was determined through gel-permeation chromatography (GPC, as shown in section **4.2.4**), their crystallinity through differential thermal analysis (DTA, as detailed on section **4.2.2**), their tensile strength and elasticity modulus were measured according to *ASTM D638-03* (detailed on section **4.2.3**). Their properties are listed in **Table 5.1**.

The FFF device selected for this project is the BFB-3000 Triple Head Clear Case (3D Systems, USA) manufactured by Bits from Bytes from 2002 to 2012. It is configured and tuned to extrude PLA out of the box, and runs proprietary build files (*.bfb) generated through the Axon 2 slicer software. No formal characterisation of this particular printer could be found on the literature.

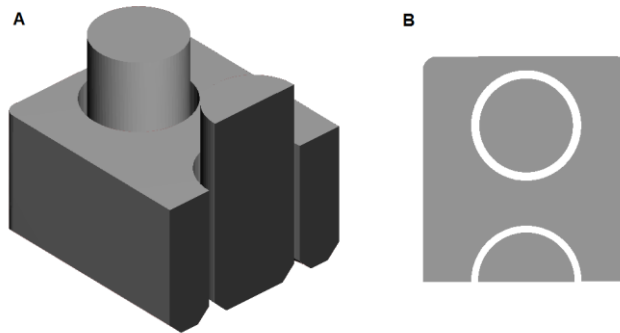


Figure 4.1. Negative space tolerance test model. Isometric (A) and top view (B). Model file modified from *3D Printer Shoot Out Test Models byMAKE*, licensed under the Creative Commons - Attribution - Share Alike license, 2015, retrieved from www.thingiverse.com.

Figure 4.1 shows negative space tolerance model used for characterisation of the printer. Each inner cylinder in the model is an independent geometry, as well as concentric with its surrounding rim: scaling down the model will eventually cause both structures to fuse during printing, obliterating the gap between them, and marking an approximate resolution limit for the printer. The separation between the pieces is 10% the length of the cylinder's diameter.

Note also that this particular test is designed so that orientation variability on the horizontal axes is cancelled out by the circular geometries. Ten BFB-PLA samples of this model were printed. These and all subsequent tests are done under the highest fill setting (95%). Consequently, a tolerance test formally characterised the accuracy and precision of the equipment, as well as its smallest feature resolution. Measurements done with Draper Digital Metal Callipers (Part No. PDVC150M) and weights measured with Mettler-Toledo Mettler BB2400 digital balance. Volumes were computed in accordance to ASTM F2450-04 and **Equation 4.5**. Expected volumes for error calculation were derived from CAM models. The models used are depicted in **Figure 4.2**,

Table 5.2 and **Table 5.3** compile these findings on the 20 samples of each printed for this experiment.

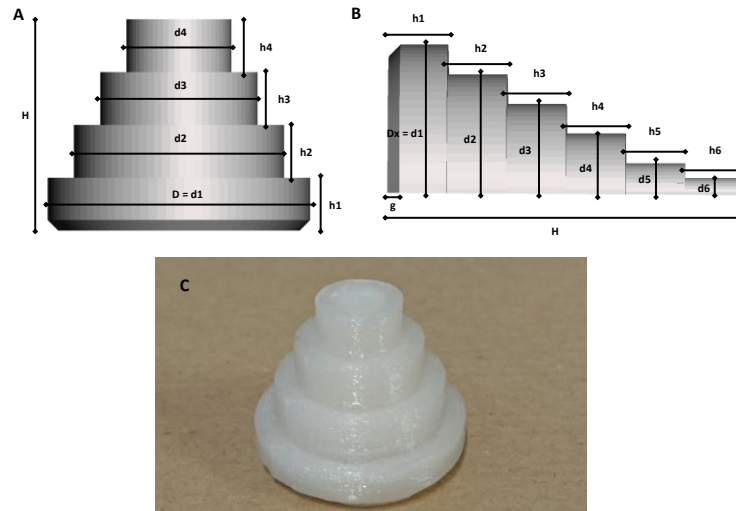


Figure 4.2. Dimensional accuracy test models. **A**, vertical pyramid dimensional test model, and **B**, horizontal half-pyramid dimensional test model. Model file modified from *3D Printer Shoot Out Test Models* by MAKE, licensed under the *Creative Commons - Attribution - Share Alike license, 2015*; retrieved from www.thingiverse.com.

4.2. ACCELERATED DEGRADATION OF FFF PLA

In vitro degradation tests are meant to simulate the chemical (and by extension thermal) stresses implanted polymers and polymeric devices undertake upon integration to an organism. For PLA, the main degradation mechanism is chain scission through random ester-group hydrolysis along the main polymer chain [2,12,137]. This reaction is spontaneous in aqueous medium, such that at a given ester bond along the polylactide chain (R):



The spontaneous cleavages through this route result in a net decrease of ester groups, implying an increase in carboxyl end-groups, which are prone to ionisation in aqueous solution, becoming a source of hydronium ions [137]:



Free hydronium ions, in turn, are capable of protonating carbonyl groups at ester bonds, further facilitating hydrolysis: these phenomena comprise the mechanism for autocatalysis of ester polymers.

In an aqueous solution, the surplus of water molecules drives the main reaction forward, while temperature increases the reaction rate [137]. For these reasons, degradation tests according to the *ISO-10993-13-2010* [328] standard control for these reaction rate variations and autocatalysis by requiring constant pre-defined temperatures and the use of phosphate-buffered solution as degradation medium.

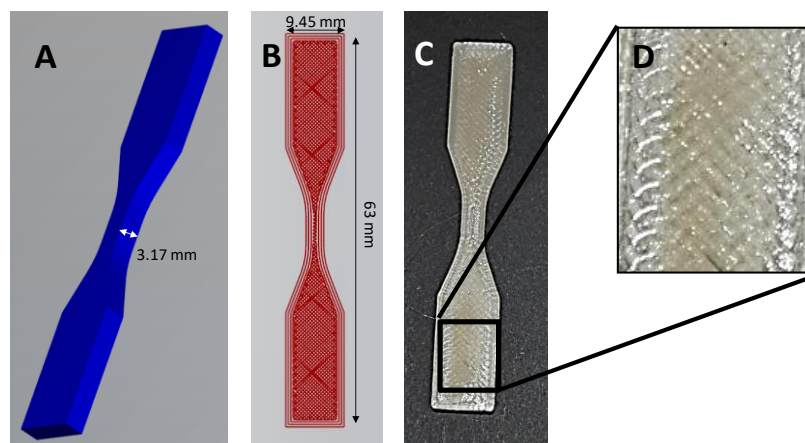


Figure 4.3. Specimens used for ADT and mADT procedures. Tensile specimen type V model designed on *Blender 2.76b*, according to specifications under *ASTM D638-03* standard. (A) The solid CAD model (B). G-code sliced file represented as toolpaths. (C) Fill patterns are readily visible on finished prints (D), and very likely contribute to lowering the apparent density of a 3DP geometry, as visible variations in opacity throughout the prints suggest (D).

Tests were run in 3DP tensile bars made of BFB-PLA, VB-PLA and composites based on VB-PLA as noted (**Figure 4.3** and **Figure 4.4**). Samples for testing were spread in triplicates throughout eight time (at 1, 3, 5, 9, 14, 18, 21, and 23 days, based on previous reports [283,290]) of controlled-temperature incubation, accounting for 24 samples per instance of the experiment. In every instance of Real-time Simulated Environment Test (RSET) and Accelerated Degradation Test (ADT), each specimen is put inside an individual vial where it must be completely submerged in test medium on a ratio of at least 10 ml per gram of material. The temperature suggested by the standard for RSET is 37 °C, with any different value selected properly justified: by this definition, ADT runs take place at temperatures >37 °C. For the present research, molecular weight deterioration, drops in crystallinity, mass change, and melting range alterations are sought after quantitatively, as they reflect effects on the material's intermolecular organisation. Qualitatively, mode of structural breakdown is also of interest in the context of exploring the effects of FFF on implant fabrication so as to derive design guidelines from these observations.

Prior to degradation, every specimen is dried at 50 °C for 24 hours so that any humidity trapped within the material is removed to prevent it from interfering with the test [290,318]. Manufacturers recommend 80+ °C for 2-4 hours [318], and other polymer drying schemes have been published with higher temperatures [320], but the 50 °C figure poses better conditions for lactides since it is well under their expected T_g range of ~58-65 °C [294,335]. This assures intermolecular interactions remain reasonably undisturbed, especially since oven drying at higher temperatures – and even ethylene oxide

sterilisation [49] – is reported to lower molecular weight and overall mechanical integrity on polymers [282,283,294,320]. Once dried, sample weight was recorded (Mettler Toledo Mettler BB2400 digital balance) as their initial value (w_0).

ADT data presented for this project used a testing temperature of 70 °C, which has previously been shown to enhance the degradation reaction rate while still correlating well with tests performed under the T_g of lactides [283,290]; it is also well below the average melting point and annealing temperatures of these materials. ADT was performed on VB-PLA.

Test periods of 2 days and 60 days were required for ADT by the standard, and additional 24 hours and 2 week periods help monitor structural decay. However, previous research suggests that the above ADT conditions reach the dismantling point for PLA within 23 days [290], while preliminary testing for the purpose of the present study found the specimens reached it within the first 48 hours. In light of this, the ADT tests done in the interest of correlating with mADT were done in triplicate through 23 days, with testing periods based on previous reports [283,290]. The periods chosen for mADT were 0.5, 1, 1.5, 2, 24 and 48 hours, based on preliminary tests (which yielded an approximate dismantling time of 2 or 3 days). Based on the overall behaviour of degradation tests on PLA [283,289,290,329,336], these periods would allow to survey the overall shape of the degradation curve, and determine the need for additional time periods. Each period was run with triplicate samples, with each of the three specimens set apart in independent vials and each analysed separately.

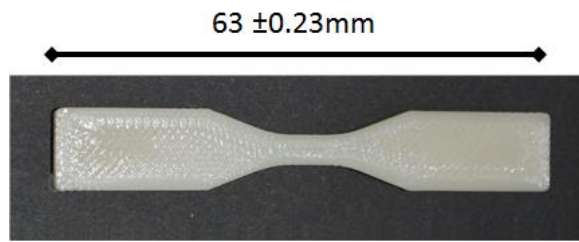


Figure 4.4. **3D-printed tensile specimen used for degradation tests.** The off-whitish aspect of the material is characteristic of semicrystalline PLA, with amorphous blends being colourless and transparent. The corresponding 3D model used is detailed in Figure 4.3. Standard deviation based on dimensional testing.

After each test period was concluded, its respective specimens were taken out of the test medium, dried again on the above conditions, and measurements were taken. Weight was once again recorded as the specimen's final value (w_f). Tensile strength (S_t) and elastic modulus (E) were measured according to *ASTM D638-03*. Thermogravimetric Analysis (TGA) was used to determine both thermal behaviour [283,284,289,290] and crystallinity (Cr) [286,287,337,338]. Molecular weight (M_w) was determined through gel permeation chromatography (GPC) [137,247,280,281,293,298,328,339]. These methods were selected so as to keep in line with the most common techniques reported in the literature, as well as those recommended in the appropriated standards.

Data gathered through several time points (such as mass-loss or melting points) was compared through Two-Way ANOVA with Sidak hypothesis testing for multiple comparisons. Data gathered on a single time point (such as initial crystallinity or mechanical testing) was compared through One-Way ANOVA with Tukey hypothesis testing for multiple comparisons.

4.2.1. MASS CHANGE

The main stages of polymer degradation were measured through mass loss, as bulk degradation and erosion ensue and large polymer chains are broken down along with the structure of the device or specimen in question [294,314,340]. Mass change (Δm) was reported as a per-cent of the starting specimen weight (w_0) when compared to the final weight after the degradation period (w_f), and computed as:

$$\Delta m = \frac{w_f - w_0}{w_0} \% \text{ Equation 4.7 [2,283,285,290]}$$

All values were taken as averages of triplicate samples for each time period, as weighed on a Mettler Toledo Mettler BB2400 digital balance. The results of this comparison were then plotted over the time periods studied, so that any trend can become noticeable, as reported in the literature and recommended on *ISO-10993-13-2010*.

4.2.2. CRYSTALLINITY AND THERMAL ANALYSIS

The preferred method for determining crystallinity (Cr) for polymers in the literature – which is also the one recommended in *ISO-10993-13-2010* – is differential scanning calorimetry (DSC), which can be derived from Differential Thermal Analysis/Thermogravimetric Analysis (DTA/TGA) data [286,287,337,338]. Through this method, heat flow curves can be used both for analysing the thermal properties, and for estimating the relative crystalline-amorphous mass ratio from the crystallisation (ΔH_c) and fusion (ΔH_f) enthalpies [341]. This was accomplished by comparing those enthalpies with

known values for fusion of a 100% crystalline sample of PLA (ΔH_{100}): reportedly 91.3 J/g [293,341]. From TGA data-derived enthalpies, the degree of crystallinity (Cr) was calculated as:

$$Cr = \frac{\Delta H_f - \Delta H_c}{\Delta H_{100}} \% \quad \text{Equation 4.8 [137,286,287,338]}$$

For this study, samples were analysed in a *Diamond TG/DTA* (Perkin Elmer). Aluminium sample pans with a 40 μ l capacity held ~10mg of polymer for each analysis. Sampling on the specimens took the form of a transversal cut perpendicular to the *X-Y* printing plane, so as to include equal proportions of material from all layers of the printed specimen. Similarly, samples from FFF filaments consisted of a ~10 mg cut perpendicular to the length of the filament itself. For every test run, the sample was held at 40° C for one minute to stabilise the system, and then thermal scanning took place at 10° C/min up to 350° C. Reported values for crystallinity with standard deviation are averaged from samples studied in triplicate.

4.2.3. MECHANICAL PROPERTIES AND VISUAL INSPECTION

After their respective degradation period, specimens were oven-dried at 50°C and then subjected to tensile testing on a *Lloyd Instruments LRX* tester, as described in *ASTM D638-03* in order to determine their tensile strength (St) and elastic modulus (E). An elongation rate of 1 mm/min was applied to the specimens along their longitudinal axis up to their point of mechanical failure. The data points are automatically recorded by the instrument, and values for

tensile strength and elastic modulus are also calculated automatically. For each time period on the degradation tests, three specimens were subjected to tensile testing.

4.2.4. MOLECULAR WEIGHT

Molecular weight measurements were outsourced to the Department of Chemistry at The University of Sheffield. The measurements were done through Gel-Permeation Chromatography (GPC), in a *1090 HPLC with UV-Vis and Differential Refractive Index Detectors* (Hewlett-Packard). Measurements were made in triplicate per time period, as laid out in the ADT experimental setup. Samples were dissolved in chloroform to a concentration of 0.10 mg/ml before being injected into the system. The measurements were calibrated against a polystyrene reference, and results are thus reported with respect to this equivalence.

4.2.5. ACCELERATED DISSOLUTION TEST

Tensile bars made from BFB-PLA and VB-PLA were used for the mADT protocol here proposed. This protocol is also based upon *ISO-10993-13-2010* [328] recommendations, with the main difference being that at least 12.5 ml of acetone per gram of sample replaces the test medium, thus maintaining the 1:1 weight ratio described in the standard. The temperature was kept at 37 °C to make the results relatable to RSET and ADT settings. Measurements on mass loss, crystallinity, mechanical properties, and thermal properties were carried out through the same methods described earlier in this section.

4.3. PROCESSING OF 3DP MATERIALS AND SAMPLES

Thermal treatments and compositing are frequently resorted to in order to enhance desirable properties on medical polymers. Unfortunately, many of these processes can detriment the molecular qualities of a polymer, and some others involve the use of solvents that would rise concern about their safety for clinical use or animal testing [136,325,327,334,342]. Annealing of samples is used in this research as a means to enhance the crystallinity of 3DP structures in order to assess the relevance of this parameter in the manufacturing and biocompatibility characteristics of PLA. This is considered relevant as 3DP requires melting of the polymer, which could have some effect in variables like crystallinity and molecular weight. Similarly, a solvent-free method for compositing PLA with hydroxyapatite (HA) and extruding it into 3D-printable filament was developed as part of this project. This compositing procedure also involves repeated melting of the material – hence annealed samples were deemed relevant for comparison.

Data gathered from these methods on a single time point was compared through One-Way ANOVA with Tukey hypothesis testing for multiple comparisons.

4.3.1. ANNEALING

The annealing protocol used in this research requires the specimens to be heated to 120 °C for 4 hours in a pre-heated oven. It has been previously reported to yield consistent results for lactide polymers [49]. Pre-heating of

the oven to the treatment temperature proves to be essential, since gradual heating of the polymer along with the oven might cause printed parts to soften too drastically and deform. Samples were cooled by powering down the oven and letting it reach uncontrolled environmental temperature while sealed, typically taking under three hours. A total of 18 specimens were annealed for each material, accounting for the eight degradation time periods that were ran in triplicate. Degradation and measurements for mass loss, C_r , St , and E were conducted as described formerly for mADT in **Section 4.2**.

4.3.2. PLA-HA COMPOSITE FILAMENT PRODUCTION

Compositing PLA and HA into an usable FFF filament was achieved in a three-step process. VB-PLA filament was first pelleted into <5 mm pieces. These were then mixed with Captal S hydroxyapatite powder (sintered, $D_{50} = 3.59 \mu\text{m}$) (Plasma Biototal Ltd, UK) in a PTFE container to distribute the HA powder as uniformly as possible on the surface of the pellets. The mixture was then molten in a drying oven at 185 °C over 3 hours with overnight cooling to ambient temperature inside the closed oven.

The composite disc obtained is finally pelleted into pieces smaller than 5x5 mm, which are in turn fed to a *Filabot Original Filament Extruder* (Filabot). The unit used for this work was modified with an external extrusion-rate regulator, as it was found that the factory-set rate was too high for the PLA-HA mixture. The composite filament was processed at 190 °C, with a variable air-cooling system fitted at the output nozzle of the extruder.

The output filament from this setup was set to 2.85 to 3 mm in thickness, which is suitable for the *BFB-3000* printer used. For this research, three HA concentrations were trialled: 5%, 10%, and 20% weight by weight in proportion to PLA. The filament was manually pulled from the extruder's nozzle and spooled in order to ensure consistency in its quality, curvature, and diameter.

4.4. GEOMETRIC DESIGN AND SAMPLE PRODUCTION

4.4.1. DESIGN OF A BASE GEOMETRIC UNIT

Given the intrinsic limitations of FFF 3DP (such as wall-fill disparity in printing settings, overhang limits of 45° , and overall better performance on printing highly geometric shapes), a modular design protocol was developed to tackle these challenges in the reproduction of complex geometries of the craniofacial bone structures. The idea revolves around generating a repeating unit that can be stacked into any 3D shape. Additionally, making these units macroscopically porous increases their surface area, while reducing the amount of material required to fill the required space; this could facilitate cell attachment, as well as post-implantation degradation of a device.

The overall procedure to generate the proposed units is based on generating a mesh's geometry. The overall stages of this method are depicted in **Figure 4.5**. A 50 mm cube was used as the base for the generation of a 3D lattice. This lattice consisted of 1.5 mm diameter cylinders, with a 2 mm separation from centre to centre of each cylinder. Starting out perpendicular to the faces of the original cube, the lattice was tilted 45° around every axis, and it was then subtracted from the cube to form the internal channel system of the resulting mesh. The mesh's 45° inclination allows for at least one printing orientation in which there are no cantilever structures parallel to the printing bed, which would require the printer to lay material in mid-air and are commonly accomplished using additional support structures foreign to the

desired print. The desired geometry for this test was a 11x15x22 mm prism-like structure with the frontal surface arbitrarily substituted with a 50 mm sphere section to emulate an organic shape (**Figure 4.5B**). This desired shape is used to cut a section of the base cube to produce a meshed version of itself. This new meshed geometry was enclosed within a more geometric frame. The frame's pillars are within the 2mm limit described in **Section 5.1**, which is congruent with scale of the mesh so that their porosities are similar to those of the internal mesh.

The test geometry trialled was created taking in account adult average measurements of the maxillary bone around the root of adult incisors [343,344] such that most child alveolar clefts would fit within the test mesh's volume. The volume selected was 11x15x22 mm, corresponding to a prism which can fit the volume of alveolus around the root of an adult incisor tooth. The present design was implemented in *Autodesk Meshmixer V. 11.0.544* by realising the mesh pattern and then subtracting it from a desired geometry. The *desired shape* used here represents the maximum limits that can be expected to contain a cleft (11x15x22 mm), with the frontal face of that prism replaced with a spherical section with 50 mm diameter. This was chosen arbitrarily to include a more organic shape into the prototype, and to roughly approximate the proportions of a maxillary bone section.

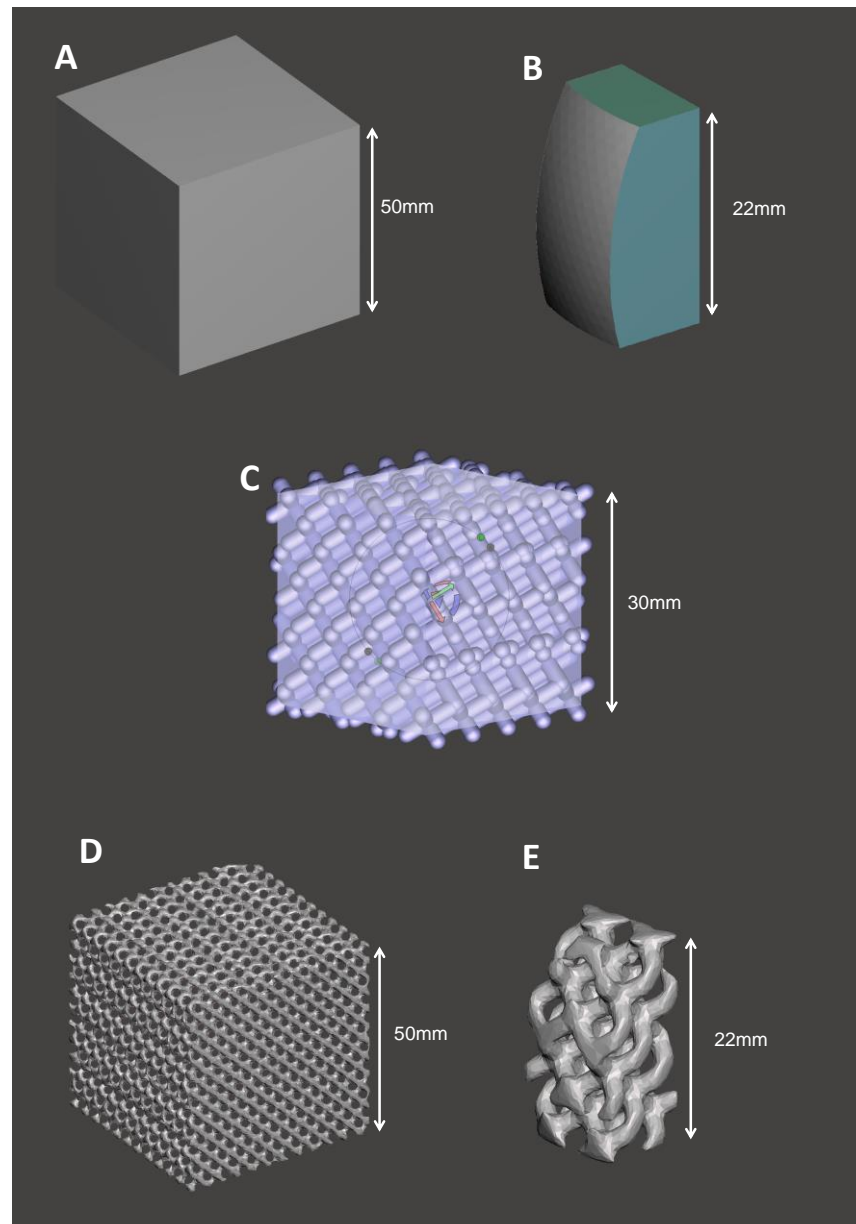


Figure 4.5. stages of base-3D mesh procedure. A. 50 mm cube used as the base for the generation of the 3D lattice. B. The test geometry: an 11x15x22 mm prism-like structure with the frontal surface arbitrarily substituted with a 50mm sphere section to emulate an organic shape. C. Closeup to material to be subtracted in the form of a cylinder lattice with 1.5 mm diameter and 2 mm separation. The lattice was tilted 45° around every axis. D. Resulting mesh from subtracting the lattice from the base cube. E. The desired shape is used as a pattern to cut out a portion of the 3D-lattice. Models generated in *Autodesk Meshmixer V. 11.0.544*.

4.5. COMPOSITE CHARACTERISATION

4.5.1. COMPOSITE FORMULATION SELECTION

Data gathered from biocompatibility studies was taken in account to select the optimal HA concentration to use for the remainder of this study. These observations were coupled with practical issues found when handling each of the three candidate concentrations during compositing and 3D-printing. This led to the selection of the 10% HA by-weight formulation as the most adequate for our processing and manufacturing setup.

Material	Brittleness	Ease of extrusion into 3 mm filament	Ease of printing	Printing quality	Printer clogging
BFB-PLA	*	N/A	*	*****	*
VB-PLA	**	N/A	****	*****	*
VB-PLA Annealed	***	N/A	**	**	*
VB-PLA + 5% HA by weight	****	****	***	****	**
VB-PLA + 10% HA by weight	****	***	***	****	**
VB-PLA + 20% HA by weight	*****	*	**	*	*****

Qualitative rating from one star to five stars. Brittleness referring to how likely the material is to break during normal use.

4.5.2. COMPOSITE HA CONTENT MEASUREMENTS

Data from TGA analysis was used to determine the concentration of HA found throughout each step of the compositing process: pre-extrusion, composite filament, and composite 3D-printed parts. The procedure used was as described in **Section 4.2.2**, but with the upper temperature changed to 500 °C so that the polymer would undergo full decomposition. The remaining

measured weight was taken as the mass of HA in the sample, and this value was compared to the sample's initial weight. For each stage of the compositing process, this test was run in triplicate.

Additionally, Scanning Electron Microscopy (SEM) was done on samples of the different stages of the production process to scrutinise the distribution of HA particles within PLA matrix. These images were generated on an *FEI Inspect F50* scanning electron microscope, and then analysed via Electron Dispersive Spectroscopy (EDS). SEM was performed at 20 kV, with a spot size of 4.0, and at a magnification of 200X in order to survey a reasonably wide area. Samples for these experiments consisted all on cuts performed with a circular saw that allowed for imaging of their fractured face, in order to determine HA distribution within the volume of the composite. These faces were manually flattened and polished with silicone carbide sand paper as best as the material allowed.

Finally, 3D-printed 1 cm disc samples and 3D-mesh structures (made from the 10% HA composite) were analysed with Micro-Computed Tomography (μ CT), using a Skyscan 1172.High Resolution Micro-CT (Bruker microCT). These samples were scanned at a source voltage of 50 kV, with 180° rotation, and 1210 ms of exposure. This experiment was run to further characterise the distribution of HA within the polymer matrix's volume.

4.5.3. 3DP COMPOSITE MECHANICAL PROPERTIES

Ultimate Tensile Strength (*UST*) and elastic modulus (*E*) were determined following the same procedure outlined in **Section 4.2.3**. Tensile bars were

produced through 3D-printing the PLA-HA10% in accordance to *ASTM D638-03*; the printer's settings used were its standard factory settings for PLA. The composite-filament used was produced through the procedure described in **Section 4.3.2**. Five tensile bars were then subject to pull-to break testing in a *Lloyd Instruments LRX Universal Tester*.

4.5.4. COMPOSITE ACCELERATED DEGRADATION TEST

Tensile bars made with the PLA-HA10% composite were subject to accelerated degradation as described for ADT in **Section 4.2** in order to compare the results with those for pure VB-PLA. A total of 24 samples were arranged in triplicates and subjected to degradation through eight testing periods at 1, 3, 5, 9, 14, 18, 21, 23 days as per *ISO-10993-13-2010*. The test was performed on individual vials with PBS at 70 °C, and the samples were measured for mass change, crystallinity, thermal properties, mechanical properties, and molecular weight was described in **Section 4.2**.

4.6. IN VITRO MATERIAL BIOCOMPATIBILITY

4.6.1. TISSUE ENGINEERING CELL-LINE PREPARATION

In order to assess if the various processing steps of sample production were affecting the biocompatibility of PLA, surface biocompatibility tests were performed using the human osteosarcoma MG-63 cell line. This cell-line – although arguable – is considered an acceptable initial approach for human biocompatibility testing, and it is thus widely used for *in vitro* testing of novel medical materials. These cells are also well documented in regards to their interactions with both PLA and composites containing PLA and/or HA in the context of orthopaedic implant development, and are an accepted and widely used model for initial biocompatibility testing [345–347].

MG-63 cells with passage number 24 were cultured in a T-75 flask pre-treated with a 0.1% weight-to-volume gelatin solution for 30 minutes prior to seeding. They were fed with α -modification Eagle's Minimum Essential Medium (α -MEM) with added 10% foetal bovine serum (FBS), 10,000 units of penicillin, 10 mg/ml of streptomycin, and L-Glutamine at 200mM, and incubated at 37 °C in 5% CO₂ until confluent. This expansion medium (EM) preparation was also used to prepare supplemented medium (SM) by adding 50 μ g/mL of ascorbic acid and 10 mM β -glycerophosphate to stimulate extracellular matrix mineralisation [348–350]. These cells were used for 21-day viability studies on the different versions of the PLA material studied. For experiments using SM, cells were kept in EM during the 24 hours after seeding.

Data gathered through several time points (such as 23-day cell-viability) was compared through Two-Way ANOVA with Sidak hypothesis testing for multiple comparisons. Data gathered on a single time point (such as collagen and calcium deposition) was compared through One-Way ANOVA with Tukey hypothesis testing for multiple comparisons.

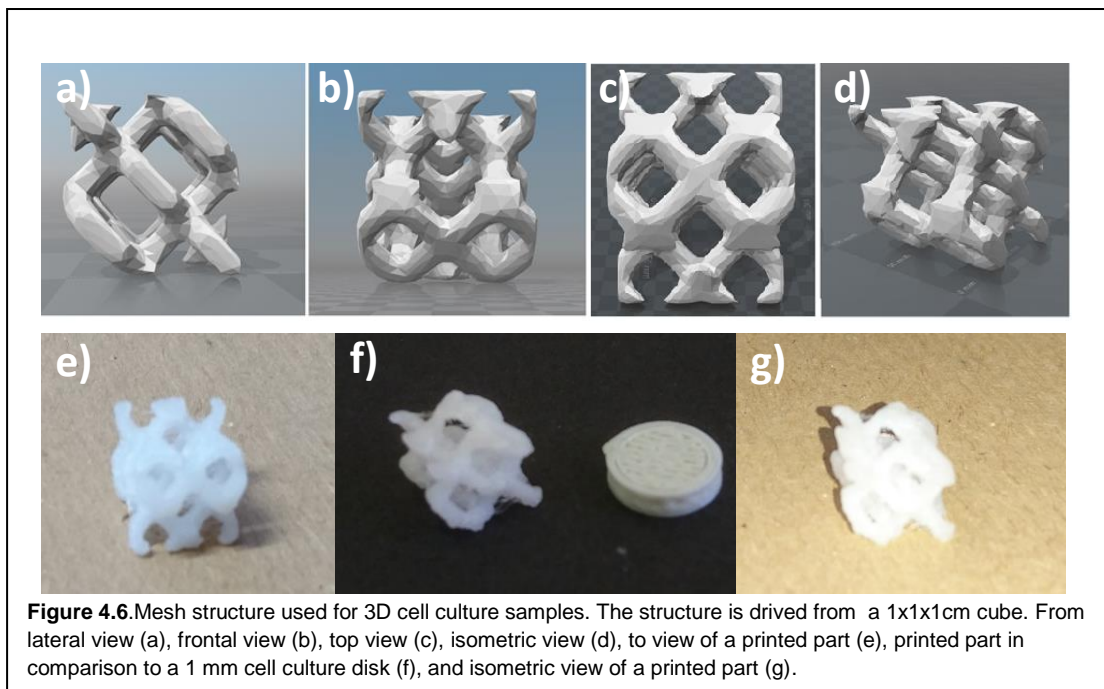
4.6.2. SAMPLE PRODUCTION AND PREPARATION

As BFB-PLA was discontinued by the time of these experiments, only VB-PLA was used as raw polymer for the materials used in the cell culture work presented from this section on. Sample discs of 1 cm in diameter and 2 mm in thickness with flat surfaces were 3D-printed for this experiment. These discs were produced in the following materials for this study: pure 3DP-PLA (3DP-PLA), annealed-3DP PLA (PLA-ANN), and 5%, 10%, and 20% PLA-HA composites (PLA-HA5%, PLA-HA10%, and PLA-HA20%, respectively). Additionally, 1x1x1 cm cube models were produced following the meshing procedure described in **Section 4.4**. Such meshed cubes were then 3D-printed as samples for cell culture in 3D (**4 4.7**). This type of sample was studied in SM in the following material versions: 3DP-PLA, PLA-ANN, and PLA-HA10%

Prior to cell culture, all samples were chemically sterilised in 2 ml of a 70% ethanol solution for 24 hours, and incubated at 37 °C. Additionally, a 5% ethaneperoxoic acid (peracetic acid) solution for 30 minutes, or a 70% propan-2-ol (propanol) solution for 15 minutes were also tested as sterilisation methods for these experiments. These three solutions were prepared as volume by volume ratios. The samples were subsequently washed twice with

PBS, and then further incubated in 2 ml of PBS for 1h to leach off residual sterilising solution.

Disc samples were used for surface biocompatibility testing by placing sets of 4 discs in a 12-well plate (three samples plus one blank control), with one sample per well. The discs were laid flat and then 50 μ l of EM with 5000 MG-63 cells were seeded on their up-facing side. These samples were then incubated at 37 °C for 45 minutes to allow for cell attachment, and then 2 ml of EM were added to each well, leaving each sample completely submerged. The plate was then incubated at 37 °C in 5% CO₂ for the duration of the experiment. Two runs of this experiment were completed under this setup, each including all the materials tested (totalling n=6). An additional total of 6 wells (3 per run) were seeded without samples for control measurements on tissue-culture plastic (TCP). This experimental setup was also repeated replacing EM with SM.

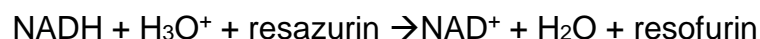


The setup for mesh cube samples was modified in regards of seeding technique. In this case, the samples were put into their respective well oriented

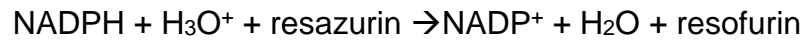
as shown in **Figure 4.7**, and 2500 MG-63 cells were then seeded from above in 25 μ l of EM. After incubating at 37 °C for 45 minutes, the samples were flipped upside down and an additional 25 μ l of EM with 2500 cells were added from above. After a 45 minute incubation period, 2 ml of SM were added to each well, submerging each sample completely. The rest of the experiment proceeded as previously described (ran twice for n=6, with empty wells as TCP controls), except that it was only run using SM.

4.6.3. MG-63 CELL VIABILITY

In vitro testing for biocompatibility of the polymer and composites in this research was carried out by extrapolating cellular metabolic activity to cell population numbers via Resazurin Reduction Assays (RRA). RRA reflects mitochondrial metabolic activity through indirect detection of nicotinamide adenine nucleotide (NADH) and nicotinamide adenine nucleotide phosphate (NADPH). Being one of the main outputs of catabolic degradation of caloric molecules through the citric acid cycle, NADH is the substrate for the cellular oxidative phosphorylation process, and has therefore direct influence on the process's initiation rate. On the other hand, NADPH is a high-demand co-enzymatic factor for synthesis of biomolecules – including nucleic acids. This fact makes its presence indicative of anabolic activity, especially during cellular division – where nucleic acid synthesis is a metabolic priority. Both NADH and NADPH promote the reduction of resazurin to resofurin via their respective dehydrogenase enzymes, such that:



and:



Where resazurin acts as an electron acceptor. While being reversible through their dehydrogenases, abundance of NADH and NADPH drives these reactions forward. Extrapolation is then possible given that resofurin is a fluorophore and can be detected through its fluorescence to green light (~500-580 nm), which can be measured at ~590 nm [351,352].

For these assays, EM (or SM) was drained from each sample's well, and they were then stained with 2 ml of EM with added 27.9 µg/mL resazurin sodium salt, and were incubated at 37 °C for 4 hours. Afterwards, fluorescence measurements were taken in triplicate at an excitation of 540 nm and emission of 590 nm using an Infinite 200 Pro plate reader (Tecan Trading AG). The samples were finally washed twice in PBS to remove leftover RRA staining, and their 2 ml of medium were replenished. RRA measurements were taken at days 1, 4, 7, 14, and 21. Fluorescence measurements were compared to a standard curve to extrapolate an approximated cell-count.

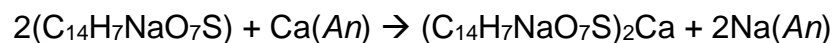
In order to produce such a standard curve, wells of MG-63 cells were seeded in triplicate with 5, 10, 20, 25, 50, 100, 150, and 200 thousand cells (as counted via an hemacytometer), incubated for 24 hours, then measured for 590 nm fluorescence as per the procedure described in this section. A correlation of fluorescence readings with cell counts was then produced through linear regression in *Graphpad Prism 7.03*.

4.6.4. CELL ATTACHMENT

Cell attachment to both the disc and mesh samples was determined after the first day of the viability study. At this point, the samples were transferred to a new well-plate, and RRA was run on the wells where the samples had been seeded. These measurements were then compared to those of day 1 of the viability study to estimate the proportion of cells that had remained attached to the sample after that period of incubation.

4.6.5. CELLULAR MATRIX DEPOSITION

The cells' production of extracellular-matrix compounds related to osteogenic differentiation was assessed through measuring the deposition of calcium and collagen after day 21 of the viability study. Alizarin Red S Assay (ARS) was used to measure calcium deposition. Alizarin red S stains calcium-salt containing tissues through the general substitution reaction:



Where *An* is an anion ionically bonded to calcium. Calcium is able to bond with the sulphonic acid group in the staining. This reaction allows for detection of early-stage mineralisation on otherwise calcium-free tissue. Though calcium ions react readily with alizarin red S, their salts are precipitated and washed off during the staining procedure described below. Thus, only extracellular-matrix-bound calcium should be stained and finally measured at spectroscopy, exhibiting absorbance at 405 nm [353].

Collagen deposition was measured using Sirius Red Staining (SRS). This staining reacts mainly with strongly basic sections of the collagen polymer – likely with histidine, arginine and lysine residues. As for ARS, de-staining and

washing of the treated samples allows for only matrix-bound collagen to remain along with its staining. This red staining is also known to show absorbance at 405 nm [354].

Once RRA for day 21 was completed, the samples were washed twice in PBS and then fixed in a 37% formaldehyde solution for 15 minutes. The fixing solution was removed and the samples were washed twice with deionised water (DI). They were then stained using 2 ml of a 1% weigh-by-volume ARS solution for 30 minutes. DI was then used to wash the excess staining solution along with 5-minute intervals of orbital shaking at 50 rpm, changing the DI after each interval until the dye was cleared from each well. Each sample was finally de-stained in 2 ml of 5% perchloric acid for 15 minutes in orbital shaking at 100 rpm. Absorbance was then measured in triplicate in an Infinite 200 Pro plate reader at 405 nm, and compared to a concentration standard curve for ARS.

An SRS staining solution was produced with a 1% weight-by-volume solution of Direct Red 80 in 1.3% picric acid (2, 4, 6-trinitrophenol). After completing ARS measurements, the samples were washed with DI twice, and then put in 2 ml of SRS solution for one hour in an orbital shaker at 100rpm. Orbital shaking at 50 rpm was once again used to wash the excess staining solution with DI in 5 minute intervals, changing the DI after each interval until it appeared clear. The samples were de-stained using 2 ml of a 0.2 M NaOH:methanol solution, with orbital shaking at 100 rpm for 20 minutes. Triplicate absorbance measurements were then made in an Infinite 200 Pro plate reader at 405 nm, and the results were compared to a standard curve for SRS.

4.7. MATHEMATICAL MODELLING FOR POLYMER DEGRADATION

4.7.1. MODELLING FROM MOLECULAR WEIGHT BEFORE MASS-LOSS

Molecular weight data from the ADT experiments performed during this study was processed through *Microsoft Excel 2010* and *GraphPad Prism 7.03* to look for mathematical relationships among the measured parameters. Although number-average molecular weight (M_n) has been found to best correlate with degradation parameters in experiments on lactide polymers [290,355], calculations were also performed using weight-average molecular weight (M_w) to look in to further evidence in that regard. Both measurements are carried out during the same GPC run.

Two probable models were explored for modelling of the initial phase of the polymer's degradation reaction: one assuming ester-bond hydrolysis of the polymer chains undergo autocatalysis, and one assuming hydrolysis proceeds without autocatalysis. Both models assume that the concentration of end-group carboxyl groups remains relatively high in the solid phase of a given sample. The autocatalysed model is then described as:

$$\frac{dC(t)}{dt} = k \cdot C(t) \cdot S(t) \cdot W(t) \quad \text{Equation 4.10 [356]}$$

Where k is a generalised reaction rate constant, $C(t)$ is the concentration of carboxylic-acid end-groups as a function of time (t), $S(t)$ is the concentration of ester groups as a function of time, and $W(t)$ is the concentration of water molecules as a function of time. The experimental set up of ADT allows for

control of the polymer and water quantities available for reaction, at least during the phase before the sample starts to experience mass-loss. The cutoff point for this section of the data was determined by fitting a plateau-exponential decay model to the mass-loss data for each experiment: the cutoff point being the time after which the exponential curve-segment of the function starts. This is referred as the *tipping point* (t_p) of the mass-loss plot in the literature [357]. Thus, a simplification of **Equation 4.10** under these conditions can be rewritten as:

$$\frac{dC(t)}{dt} = k_1 \cdot C(t) \quad \text{Equation 4.11 [108,355,356]}$$

Where k_1 is a case-specific reaction rate constant. From this point, it becomes evident that:

$$C(t) = A \cdot e^{k_1 t} + B \quad \text{Equation 4.12}$$

Where the integration constants A and B must be constrained by the boundary conditions of the experiment. A must therefore be initial concentration of carboxyl-end groups (so $A = C(0) = C_0$). Under these experimental conditions and before t_p , it has been noted that $C(t)$ keeps an inverse relation to M_n as a function of time (so $C(t) = M_n(t)^{-1}$) [290,355,356]. Substituting and rearranging the former equation, it can be then shown that:

$$\frac{1}{M_n(t)} = \frac{1}{M_{n0}} \cdot e^{k_1 t} + B \quad \text{Equation 4.13}$$

Where M_{n0} will then be the initial value for the sample's M_n . It can then be proven that $B = 0$, which – in this experimental context – is in accordance to the asymptotic tendency to 0 that could be expected of the function as time

approaches infinity. In turn, this reflects the practical decrease in polymer-chain size, and its theoretical and eventual fall to a negligible value. It can then be understood that:

$$M_n(t) = M_{n0} \cdot e^{-k_1 t}; t \leq t_p \quad \text{Equation 4.14 [108,355,356]}$$

Notably, a linear relationship can be established from this equation as follows:

$$\ln M_n(t) = -k_1 t + \ln M_{n0}; t \leq t_p \quad \text{Equation 4.15 [284,290]}$$

If a process is indeed autocatalysed, data will correlate well with this linear behaviour [355,356]. It can also be thought of k_1 as a degradation constant in the context of ADT. Moreover, it could be feasible to predict such constant with two M_n measurements: one of the initial value, and one at a time t_a before mass-loss ensues (before t_p is reached):

$$k_1 = -\frac{\ln\left(\frac{M_n(t_a)}{M_{n0}}\right)}{t_a}; t_a \leq t_p \quad \text{Equation 4.16}$$

The Anderson statistical model would describe this degradation phenomenon in the case that autocatalysis is negligible [358]. Such model would describe de time-dependent process as:

$$\frac{1}{M_n(t)} = k_2 t + \frac{1}{M_{n0}}; t \leq t_p \quad \text{Equation 4.17 [358]}$$

Where the rate constant k_2 could be then computed from experimental data as:

$$k_2 = \frac{\left(\frac{1}{M_n(t_a)} - \frac{1}{M_{n0}}\right)}{t_a}; t_a \leq t_p \quad \text{Equation 4.18}$$

Molecular weight data can further be utilised to predict mechanical behaviour during degradation experiments through the Flory relationship [359]:

$$S_t(t) = S_\infty - \frac{D}{M_n(t)}; t \leq t_p \quad \text{Equation 4.19 [359]}$$

Where $S_t(t)$ is the tensile strength of the polymer as a function of time, S_∞ is the theoretical tensile strength of the polymer as its molecular weight approaches infinity, and D is a polymer-specific constant that relates number-average molecular weight with tensile strength through time. If experimental data are available, the gradient of this function is also useful, since it does not require a value for S_∞ :

$$\frac{dS_t(t)}{dt} = \frac{d\left(-\frac{D}{M_n(t)}\right)}{dt}; t \leq t_p \quad \text{Equation 4.20}$$

Which leads to two possible models for prediction of the rate of tensile strength deterioration during ADT. One if the initial stage of the process is autocatalysed, such that:

$$\frac{dS_t(t)}{dt} = -\frac{D \cdot k_1}{M_{n0}} e^{k_1 t}; t \leq t_p \quad \text{Equation 4.21}$$

Alternatively, if the degradation happens not to be autocatalysed, the relevant model would be:

$$\frac{dS_t(t)}{dt} = -D \cdot k_2; t \leq t_p \quad \text{Equation 4.22}$$

Extra-sum-of-squares F-test was used to compare suitable non-linear regression models that satisfied two or more data sets.

4.7.2. MODELLING FROM MOLECULAR WEIGHT AFTER MASS LOSS

Molecular weight data from the ADT experiments performed during this study were processed through *Microsoft Excel 2010* and *GraphPad Prism 7.03* to look for consistent mathematical relationships that arose during the experiment. Non-linear regression was favoured, and segmented functions were also sought after, since – as mentioned in the previous section – variables are expected to behave differently during progressive stages of ADT when measured against degradation time. Additionally, data for M_n and M_w were plotted against mass loss, crystallinity, and melting temperature in order to look for trends that could be useful for describing degradation behaviour.

Extra-sum-of-squares F-test was used to compare suitable non-linear regression models that satisfied two or more data sets.

5. RESULTS

5.1. DETERMINING THE PRINTER'S RESOLUTION LIMIT AND PRINTING ACCURACY

Properties for the two different brands of PLA used are listed in **Table 5.1**. Under the conditions mentioned in section 4.1, the printer was unable to successfully resolve features under 2 mm: this can be considered its resolution limit. Results for this testing are listed in **Table 5.2** showing that the vertical (*Z*) was the least consistent (measurements *H*, *h1*, *h2*, *h3*, *hb*), with deviations in accuracy ranging from 0.56% to 18.18% (average 3.83%) from the inputted (expected) value. This axis has also the lowest precision, with deviations in reproducibility from ± 0.10 to ± 0.35 mm (± 0.23 mm on average). In light of these findings, a second test for the resolution limits of the *X* and *Y*-axes is summarised in **Table 5.3**. This test showed increased variability on the dimensions of the printed parts in all directions, with overall higher values along the *Z* axis of the printer.

Table 5.1 Properties of PLA FFF filaments used for this project.

	BFB-PLA Filament	BFB-PLA 3DP	VB-PLA Filament	VB-PLA 3DP
Mw[kg/mol]	91.08 \pm 0.90	*	118.50 \pm 3.80	97.08 \pm 1.39
Mn[kg/mol]	46.88 \pm 0.62	*	53.46 \pm 7.75	46.98 \pm 1.39
Polydispersity	1.93 \pm 0.02	*	2.25 \pm 0.27	2.04 \pm 0.03
Crystallinity [%]	21.38 \pm 1.01	15.89 \pm 0.51	29.26 \pm 0.55	24.04 \pm 1.84
Tensile strength [MPa]	-	31.39 \pm 2.58	-	48.46 \pm 3.23
Elastic Modulus [MPa]	-	88.65 \pm 10.98	-	181.30 \pm 7.95

*This material was discontinued before measurements could be taken.

Table 5.2. Vertical Pyramid Dimensional Tolerance Test

Meas.	Dx	Dy	H	d1x	d1y	d2x	d2y	d3x	d3y	h2	h3	h4	h1	w[g]
Expected[mm]	25.0	25.0	20.0	20.0	20.0	15.0	15.0	10.0	10.0	5.0	5.0	5.0	5.0	4.2
Average	25.1	25.3	20.8	20.0	20.2	15.1	15.1	9.88	9.93	4.92	4.96	4.97	5.91	4.63
SD	0.14	0.12	0.28	0.34	0.09	0.11	0.11	0.06	0.06	0.11	0.10	0.10	0.35	0.14
%error	0.67	1.06	3.83	0.15	0.91	0.49	0.61	-1.18	-0.68	-1.53	-0.78	-0.56	18.2	10.06

Expected values are as defined on the digital model. Measurements done in a sample of 20 specimens. Measurement labels reference to model in Figure 4.2A. Dimensions labelled x and y as measured parallel to that respective printer horizontal axis. Percent error (%error) is reported as the average percent difference from the expected value.

Table 5.3. Horizontal Pyramid Dimensional Tolerance Test

Meas.[mm]	Dx	H	d1x	d2x	d3x	d4x	d5x	h1	h2	h3	h4	h5	h6	w[g]
Expected[mm]	12.50	15.00	10.00	7.50	5.00	2.50	1.25	2.50	2.50	2.50	2.50	2.50	2.50	0.38
Average	12.36	15.58	9.85	7.48	5.13	2.71	1.42	2.93	2.70	2.49	2.52	2.45	2.51	0.44
SD	0.08	0.38	0.14	0.05	0.12	0.13	0.10	0.24	0.12	0.11	0.11	0.08	0.22	0.02
%err	-1.09	3.89	-1.50	-0.29	2.57	8.57	13.60	17.09	8.06	-0.29	0.91	-2.02	0.29	15.41

Expected values are as defined on the digital model. Measurements done in a sample of 20 specimens. Measurement labels reference to model in Figure 4.2B. Dimensions labelled x as measured parallel to that respective printer horizontal axis. Percent error (%error) is reported as the average percent difference from the expected value.

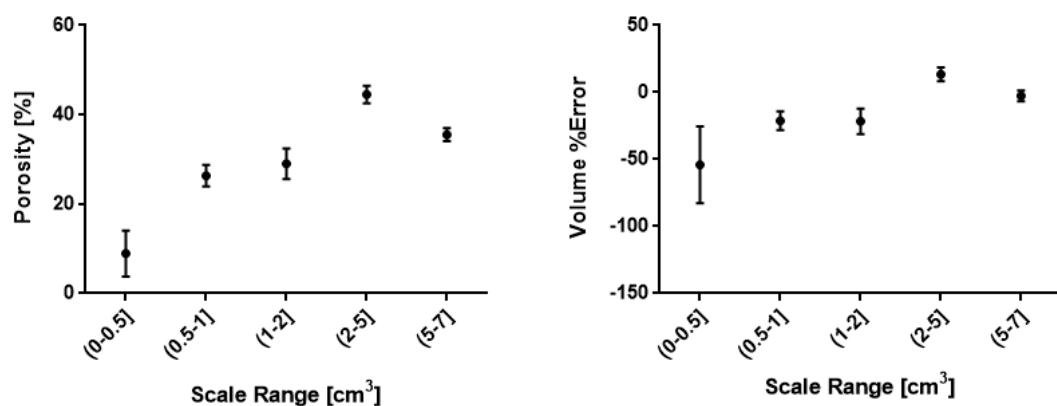


Figure 5.1. Scale-Porosity dependence and expected volume percent error on 3DP PLA geometries. Points correspond to means with standard deviation bars. Brackets on ranges denote inclusiveness.

Semicrystalline PLA density of 1.27 g/cm^3 [137,251,293,318,331,334] was taken in account when calculating the microporosity of the dimensional specimens. Under the setting of 95% material fill on the printer's software configuration, the observed density of the prints was scale-dependent, with a highest density of roughly 1.14 g/cm^3 on the smallest end of the printed range, from where it gradually drops to 0.63 g/cm^3 . This trend stabilises around a 40% porosity value for apparently solid prints. Corresponding porosity measurements are available in **Figure 5.1**.

5.2. ACCELERATED DEGRADATION OF FFF PLA

5.2.1. MASS CHANGE

Mass loss measurements for ADT are shown in **Figure 5.2** on VB-PLA specimens over the course of 23 day. The plot can be fitted to an exponential decay model. In these experiments, the point where mass loss ensues was sharply evident between the 9th and 14th day of degradation, with non-linear regression to a plateau-exponential decay model setting it at 8.82 days ($R^2 = 0.9789$, **Figure 5.2**). The infiltration period appears to happen during the first two days of the experiment, with the plateau phase noticeable before mass loss starts. The small slope observed could correspond to surface erosion happening in parallel to this process [360]. The final measurements were consistent with other studies in that they appear to be heading for a second plateau phase, corresponding to the degradation of the remaining crystalline phase [290,361]. This is in line of what could be expected for bulk erosion of

a poly-ester such as PLA, as the whole of the geometry undergoes degradation roughly simultaneously after infiltration [360].

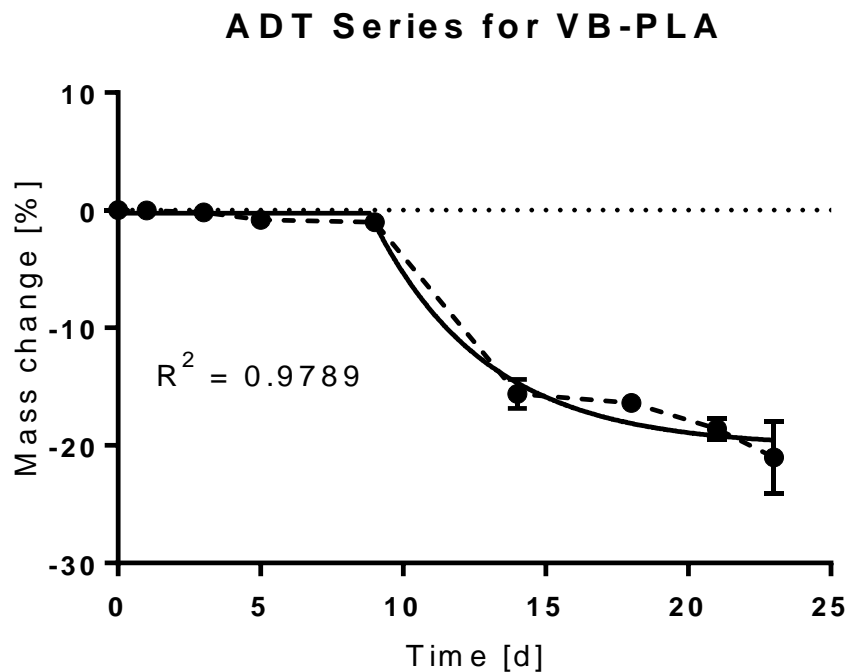


Figure 5.2. Mass change measurements from ADT specimens. Data from degradation on PBS at 70 °C. Points correspond to means with standard deviation bars. Solid line denotes a non-linear fit to an exponential curve; point-connecting line is shown dashed.

5.2.2. CRYSTALLINITY

The first crystallinity measurements for degradation experiments were made to determine the initial values for the materials as filaments and after undergoing 3DP. An immediate change in crystallinity was induced by the printer's FFF process, with both tested filaments experiencing a significant ($p < 0.05$) loss of crystalline mass with respect to their filament form. These observations are depicted in **Figure 5.3**. Both polymers are largely amorphous

(~70-80% by weight), since the filament presentation benefits from a more plastic behaviour. Notably, both PLA brands exhibit statistically significant differences among them when compared as filaments, as well as after 3DP ($p < 0.05$).

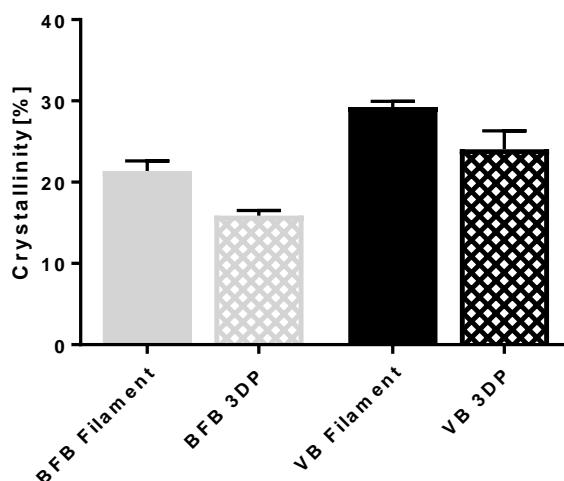


Figure 5.3. FFF-induced crystallinity loss. Filament values are measured on PLA filaments for FFF as provided by their respective manufacturers, and the same plastic after FFF.

These data were used as initial values for the mADT (**Section 5.26**) and ADT experiments. ASTM tensile specimens (**Figure 4.4**) were subject to *in vitro* degradation, as described in section 4.2. Crystallinity changes during ADT experiments are shown in **Figure 5.4**. An exponential trend was well identifiable, without reaching a point of crystallinity loss within the span of the time periods selected. An increase from 28.16% to 87.83% was recorded for

these tests, corresponding to the crystallinity surge observed for mADT specimens.

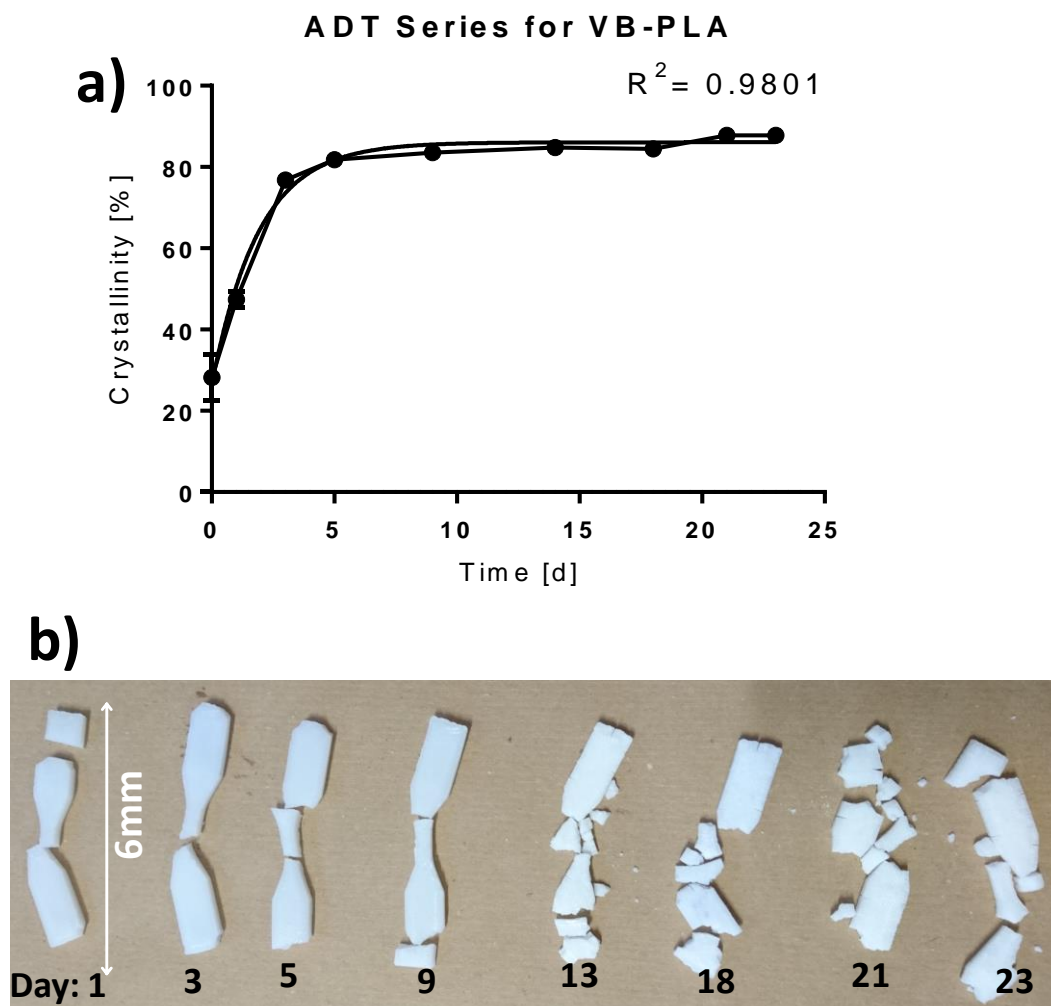


Figure 5.4. (A) Crystallinity loss and (B) detail photograph of resulting structural deterioration during ADT. Data from degradation on PBS at 70 °C. Points correspond to means with standard deviation bars.

5.2.3. MECHANICAL PROPERTIES AND VISUAL INSPECTION

For ADT specimens, mechanical testing was impossible after the first day of degradation. Though geometrically intact, the specimens became too brittle to

be loaded into the tester. Averaging the only two specimens that were testable from the repeats of the 1 day test period, an UTS of 1.06 MPa and an E of 422.8 kPa were found. As can be seen in **Figure 5.4**, the samples break down while on their degradation vials from the first time point, and lose structural integrity as degradation progresses.

5.2.4. THERMAL ANALYSIS

Data from DTA brings forward further confirmation for the role of crystallinity on *in vitro* degradation of PLA. Though there were only slight differences between the measurements for the filament and the post-3DP polymer, some of these were illustrative of what previously-discussed data has suggested. **Figure 5.5** shows a comparison between the thermal properties of BFB-PLA and VB-PLA in filament form and after being processed through FFF. Changes were evidently less dramatic for VB-PLA, which was reflected in a drop in *crystallinity* proportionally smaller decrement from 29.26% to 24.04%, when

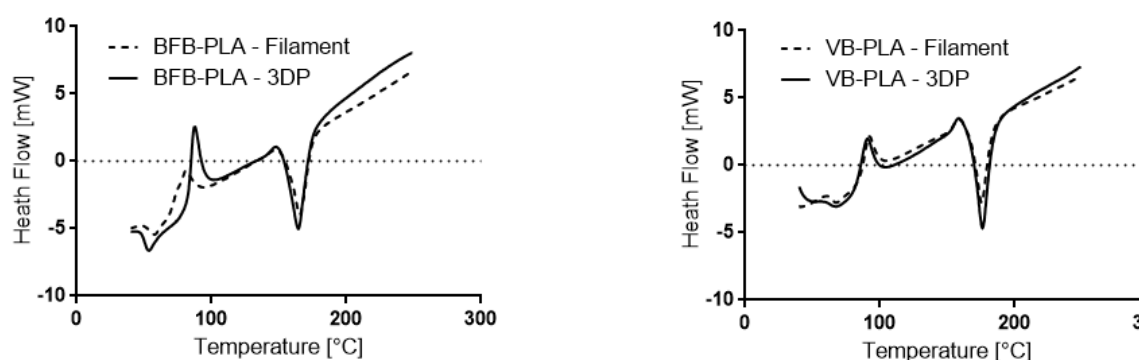


Figure 5.5. Thermograms for BFB-PLA and VB-PLA as FFF filament and after 3DP. The curves for both materials are very similar, with that of VB-PLA displaying a smaller crystallisation peak, and a slightly higher fusion peak, consistent with higher crystallinity. Endothermic processes are arbitrarily depicted downwards.

compared to BFB-PLA dropping from 21.38% to 15.89% (**Figure 5.3**). T_g for both filaments was found to be higher than for the material after 3DP: 59 °C against 46 °C for BFB-PLA, and 64 °C against 55 °C for VB-PLA. This change can be attributed to the drop in crystallinity itself. T_g was undetectable throughout degradation tests.

For ADT experiments, DTA data were collected in **Figure 5.6**. Relatively little change was observed throughout the course of the time periods. One of the most noticeable was the increase in size and overall area of the fusion peak from 1 day to 3 days. After that event, the smaller variations were noted in the fusion peak, with some displacement of the fusion point from an initial 176 °C to 159 °C, as seen on **Figure 5.7**.

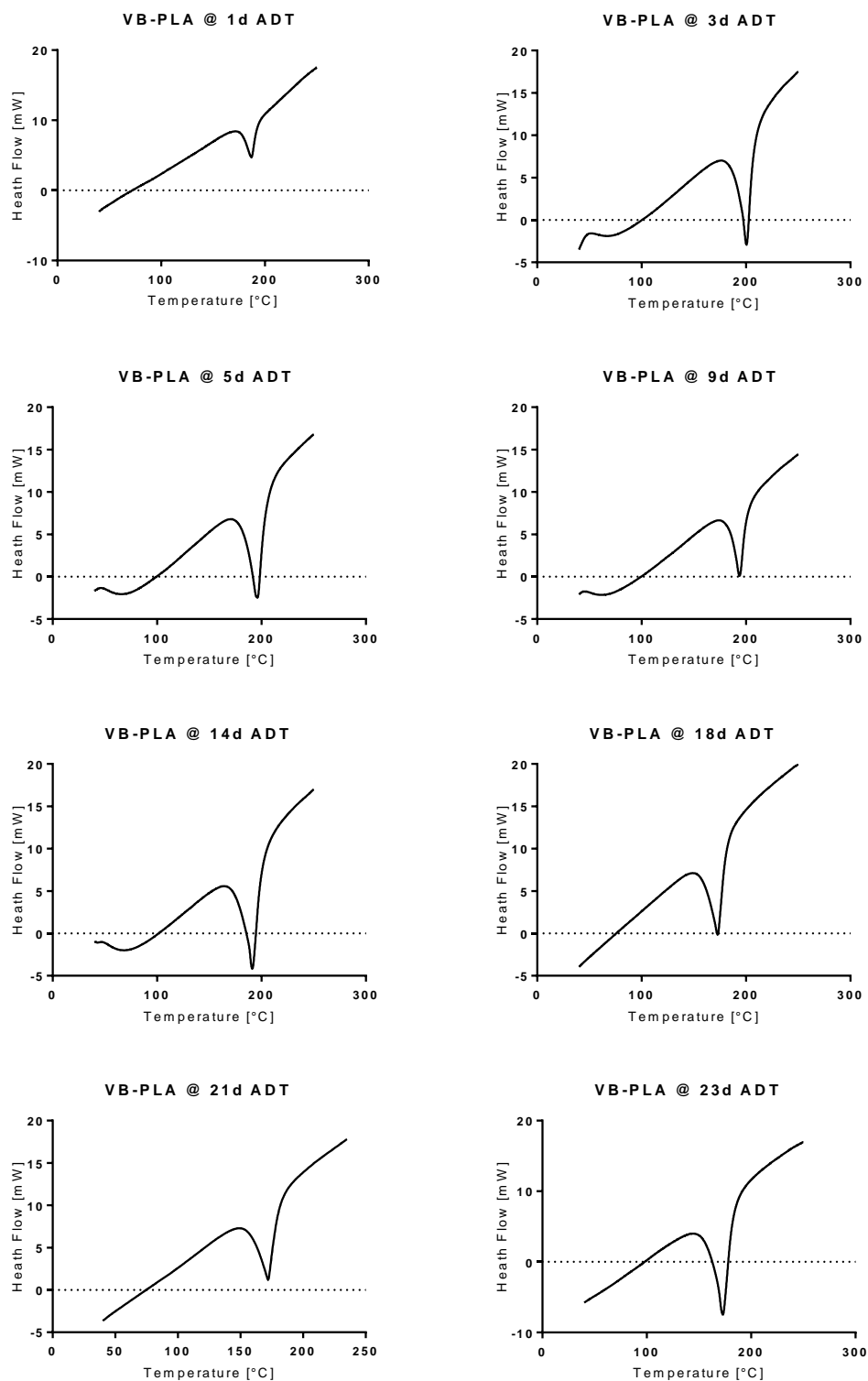


Figure 5.6. Thermograms for VB-PLA after 3DP and after several stages of ADT. The overall shape of the curves is maintained throughout the experiment. The most noticeable changes are in the size of the fusion peak, which is reflective of crystallinity. Endothermic processes are arbitrarily depicted downwards.

ADT Series for VB-3DP - Melting Temperature

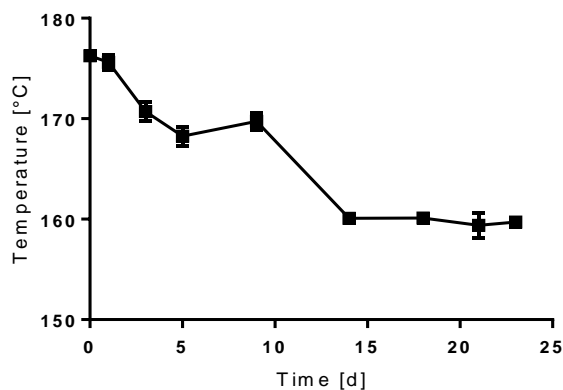


Figure 5.7. Changes in peak melting temperature for VB-PLA throughout ADT. Points correspond to means with standard deviation bars.

5.2.5. MOLECULAR WEIGHT

Number average molecular weight (M_n) during ADT for VB-PLA tensile bars decayed in a well-defined exponential phase ($R^2 = 0.9691$). This is shown in **Figure 5.8**. By 5 days, more than 90% of the samples' M_n had been lost to degradation. By the end of the experiment, M_n had decayed to 1.30% of its starting measurement.

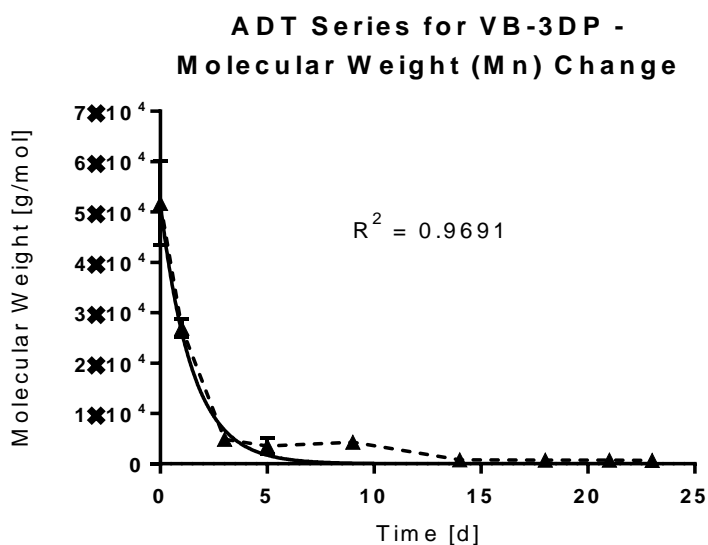


Figure 5.8. Changes in Number Average Molecular Weight (Mn) from VB-PLA throughout ADT. Points correspond to averages with standard deviation error bars, joined by the dashed line. The solid line depicts a one-phase exponential decay model fitted through non-linear regression to the data.

5.2.6. ACCELERATED DISSOLUTION TEST

Mass change results for mADT experiments are collected in **Figure 5.9**, showing an exponential-like decay of bulk degradation, which could potentially be correlated with similar experiments as the shape of the trace appears to follow the expected degradation pattern for PLA [283,290]. BFB-PLA experienced mass loss instantly, with an untraceable infiltration period (which, on this particular setup, would appear as a near-zero mass change as it did for VB-PLA) occurring before the 30-minute reading, and roughly following an exponential trend. This was ultimately followed by a rapid mass loss, and a plateau by the end of the test periods, with a final mass loss of 10.85%. A

faster rate of mass change was consistent with a more amorphous polymer structure, but the contrasting behaviour of VB-PLA, exhibiting a well-defined infiltration period where mass was actually gained, accounting to infiltration onto the internal geometry of the specimen [137,247,294].

This phase is then followed by a plateau where mass loss and further infiltration change the values back and forth. **Figure 5.10** shows a record of the wet weight of VB-PLA mADT samples, measured within three hours after blot-drying (in concordance with *ISO-10993-13-2010*), before their regular oven-drying cycle. An increase of 0.84% in mass was observed on VB-PLA even after oven drying the samples, which suggests medium intake into the geometry of the specimens. Both increments followed closely an exponential trend.

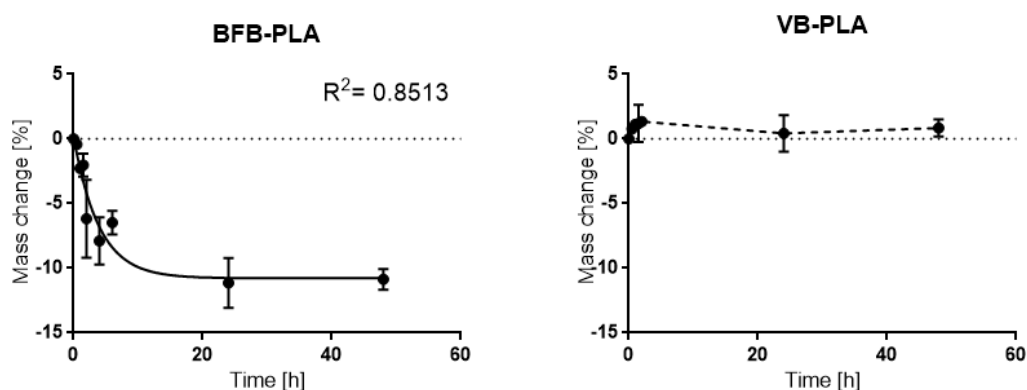


Figure 5.9. Mass change measurements from mADT specimens. Data from degradation on 100.0% pure acetone at 37 °C. Points correspond to means with standard deviation bars. Solid line denotes a non-linear fit to an exponential curve; point-connecting line is shown dashed.

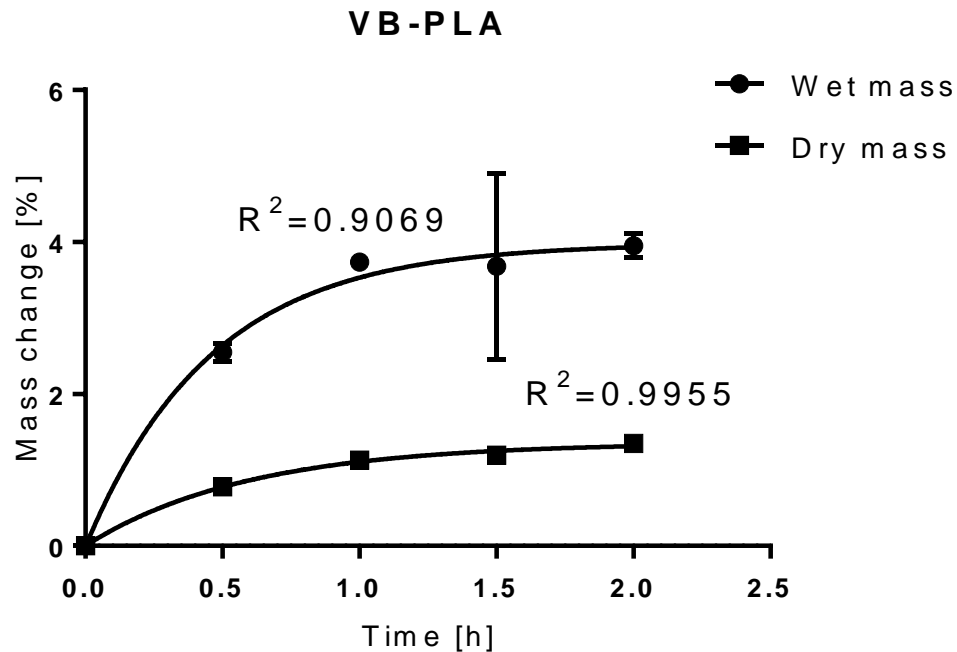


Figure 5.10. Mass change from VB-PLA specimens measured wet and dry after mDTA. Data from degradation on 100.0% pure acetone at 37 °C. Data up to the second hour of degradation is used as it correlates well with the expected infiltration period. Solid line denotes a non-linear fit to an exponential curve. Points correspond to means with standard deviation bars; some error bars are too small to be depicted.

The results for crystallinity change in mADT are shown in **Figure 5.11**, where BFB-PLA experienced an increase from 15.89% to 51.86%, while a similar one happened from 28.15% to 47.19% for VP-PLA. In the subsequent time periods up to 2 hours, crystallinity dropped down to 38.64% for BFB-PLA and to 45.78% for VB-PLA. By the final time period, the value was 44.94% for BFB-PLA, and 29.92% for VB-PLA. The 24 hour time period shows an increase in crystallinity to 48.95% for BFB-PLA and 43.21% for VB-PLA.

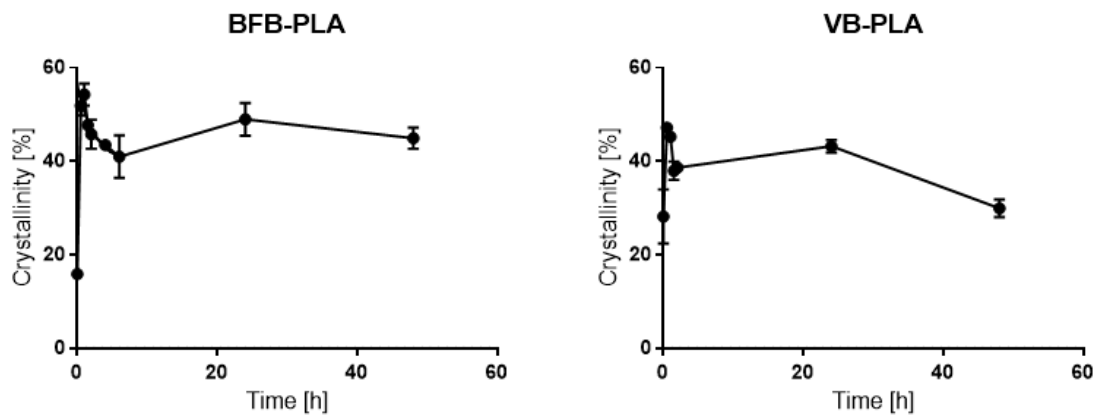


Figure 5.11. Crystallinity loss during mADT. Data from degradation on pure acetone at 37 °C Points correspond to means with standard deviation bars.

Related to this, the point of structural break down of BFB-PLA specimens was determined by these tests to be 1.5 hours under mADT testing, while VB-PLA reached it at some point between 2 hours and 24 hours – relating closely to the surge in crystallinity observed. After this point the geometries and mechanical resistances of these materials suffer changes too drastic to allow them to retain their original features. It is to be noted that after the dismantling point has been reached in one of these specimens, tensile testing becomes impossible. **Figure 5.12** shows the progressive deterioration of FFF specimens subject to mADT. This deformation eventually leads to failure of the central shaft of the specimen after its dismantling period, while the individual layers gradually lose bonding with each other, especially near the perimeter of the model. Notably, layer fragments do not appear to detach completely until the 48 hour mark was reached.

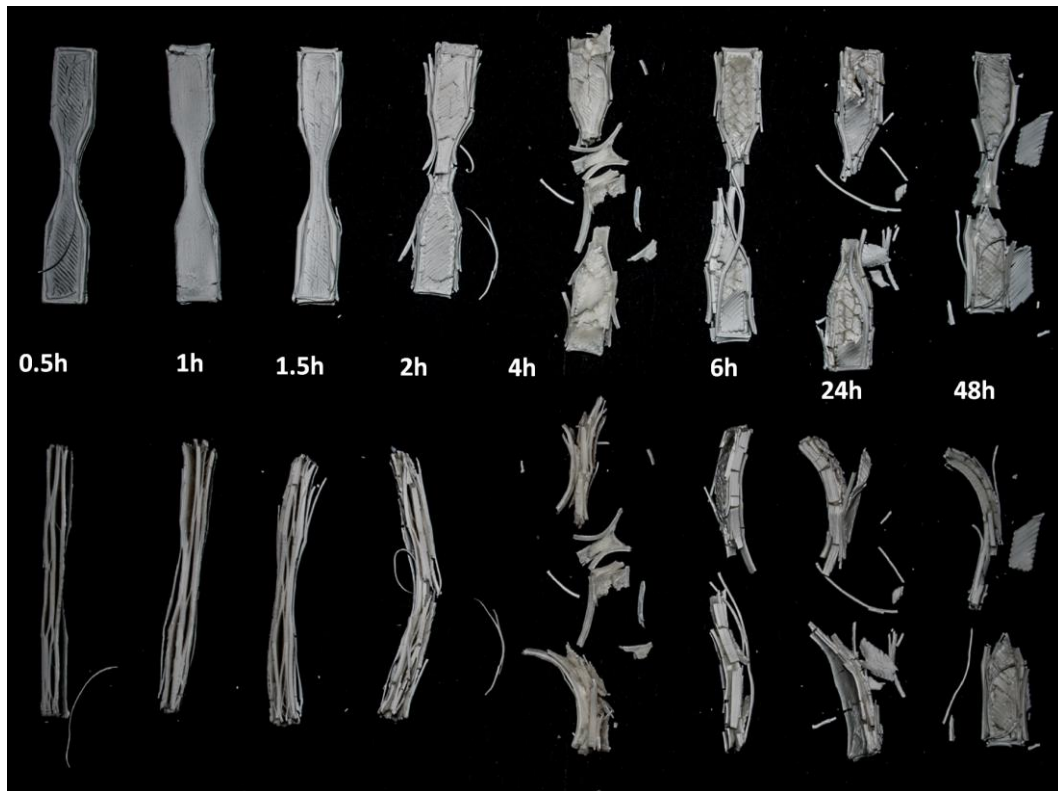


Figure 5.12. Photograph of BFB-PLA tensile specimens at progressive stages of mADT. Depictions of frontal views are above, with their corresponding lateral views below. The dismantling period for this particular material under mADT conditions is considered to be 1.5 hours, since the specimen is far too deformed to conduct mechanical testing. The 4 and 6 hours specimens were added for further detail given the rapid progression of the degradation. Each specimen is 63 mm long.

BFB-PLA specimens shown in **Figure 5.12** display cracks on their surface on the later stages of the mADT experiments (6, 24, and 48 hours). There was also severe bending of the structure before large portions of the FFF layers begin to delaminate as the geometry curls around its transversal axis. Notably, layer fragments do not appear to detach completely until the 48 hours mark was reached. In contrast, as evidenced by **Figure 5.13**, VB-PLA undergoes similar changes, but to different magnitudes. While specimens show no significant changes during the first two hours of mADT, degradation becomes evident by the end of the first day. Their mechanical integrity was still good enough to allow handling without damaging them – unlike BFB-PLA

specimens. The layers that have curled away from the main body of the structure, however, appear to have fused in – much like those on the major fragments of the BFB-PLA samples for 24 and 48 hours. Their deformation was too severe to allow for reliable tensile testing. An exponential decay trend was evident in the results compiled by **Figure 5.14**, although less so for BFB-PLA.



Figure 5.13. Detail photograph of VB-PLA 63 mm-long tensile specimens at 24h (left) and 48h (right) after mADT. Depictions of lateral views. The dismantling period for this material under mADT conditions is considered to be 24 hours, since the specimens become far too distorted for mechanical testing. Lower time periods displayed no significant changes.

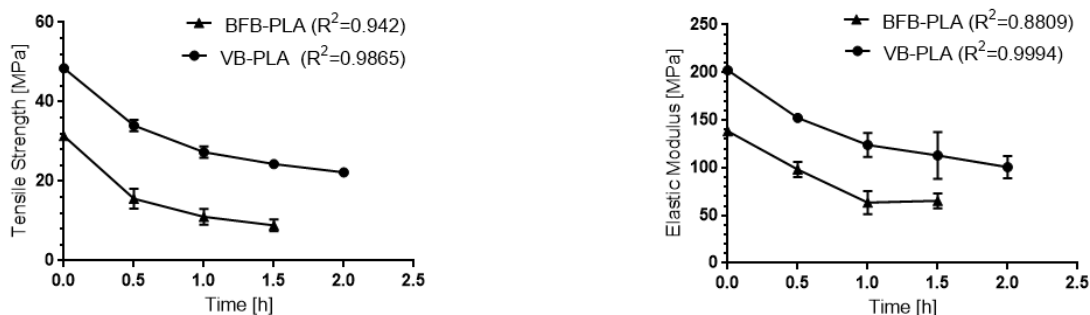


Figure 5.14. Tensile strength and elasticity modulus deterioration during mADT on BFB-PLA and VB-PLA. Points correspond to means with standard deviation bars. Correlation coefficients respectively denote a non-linear fit to an exponential curve (tendency line not plotted for clarity). BFB-PLA specimens lost most mechanical integrity after 1.5 hours. VB-PLA specimens, similarly, became unmeasurable due to heavy distortion of their geometries.

Thermal properties also reflect changes in crystallinity behaviour through mADT, which in turn can be related to these observed changes in mechanical properties. These slight differences can be appreciated in **Figure 5.16** and **Figure 5.5**, corresponding to thermal analyses for the mADT series of BFB-PLA, and a comparison of the properties of filaments before and after FFF.

The first noticeable trend was the almost immediate deviation from the behaviour of the baseline materials (BFB-PLA 3DP and VB-PLA 3DP), followed by an overall similar curve in all subsequent measurements. The crystallisation peak found in the 3DP material was completely lost 30 min into mADT for both types of PLA.

T_f suffered no important variation, remaining stable at average 164 °C for BFB-PLA. For VB-PLA, average T_f was 175 °C, with a drop at the 2 hour mark to 169 °C (**Figure 5.15**). Crystallisation peaks were only present on undegraded

BFB-PLA at 87 °C, and on VB-PLA at 90 °C. For BFB-PLA, T_g (reported as the peak value of the T_g range) was found at 46 °C, but it was not reliably detected in degraded specimens (**Figure 5.16**). For VB-PLA, T_g was found at 69 °C for the undegraded material, but subsequent values were not reliably detected, as can be seen in **Figure 5.17**.

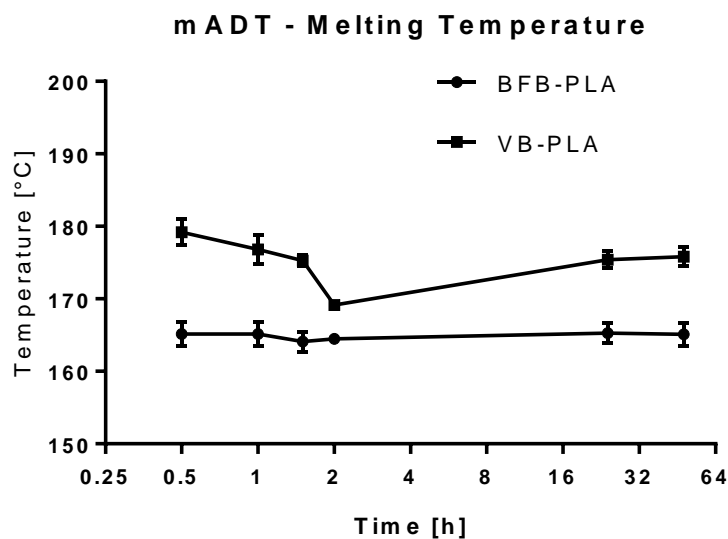


Figure 5.15. Changes in peak melting temperature for BFB-PLA and VB-PLA throughout mADT. Data from degradation in pure acetone at 37 °C. Points correspond to means with standard deviation bars.

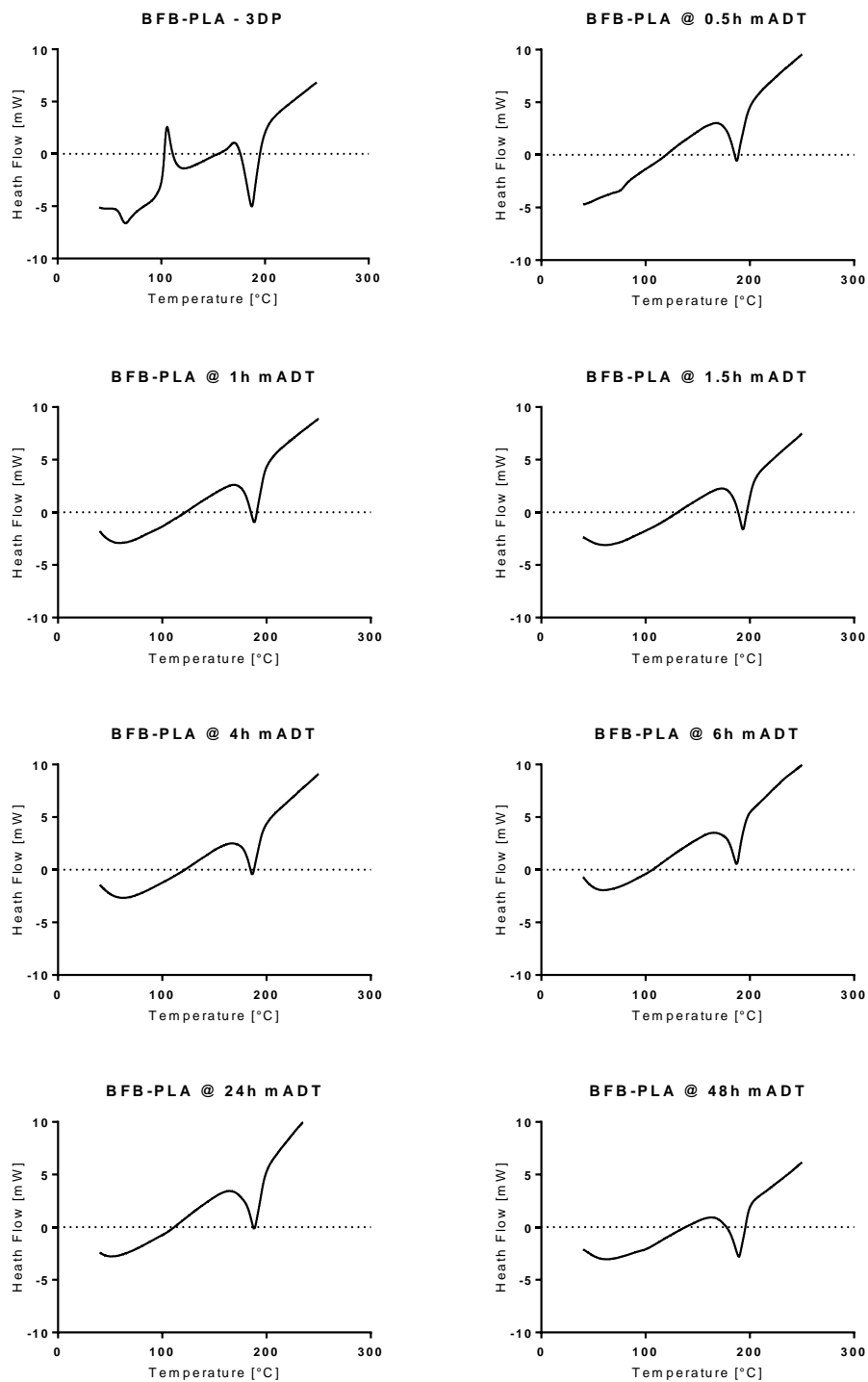


Figure 5.16. DTA curves for BFB-PLA after 3DP and after several stages of mADT. Notice the complete obliteration of the crystallisation peak present at BFB-PLA – 3DP as early as 30 minutes into mADT. The overall shape of the curves after that point is maintained, without important displacement of the melting temperature. Endothermic processes are arbitrarily depicted downwards. The 2 hours time period is intentionally omitted for spatial convenience and similarity to the 1h and 1.5h graphs.

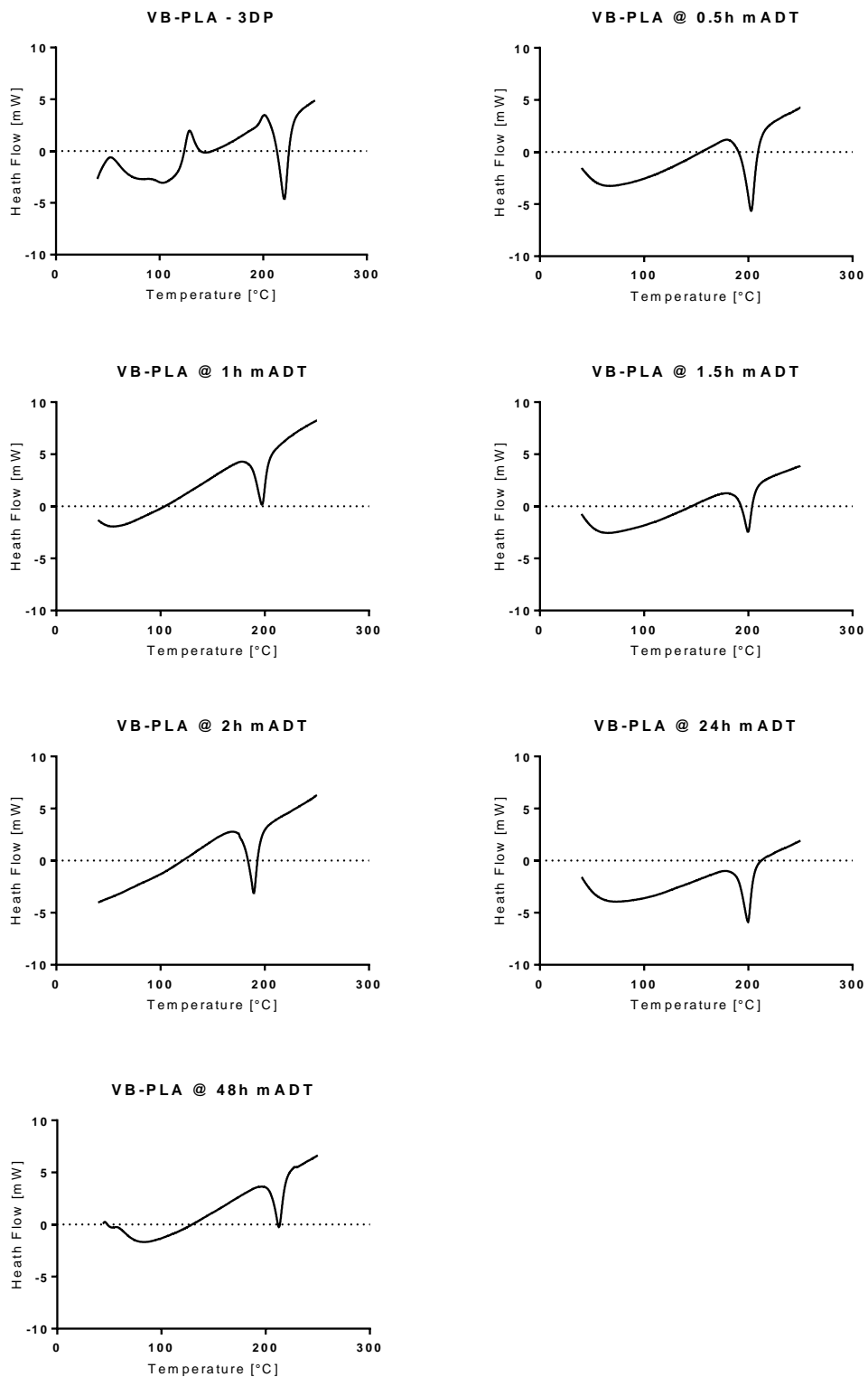


Figure 5.17. DTA curves for VB-PLA after 3DP and after several stages of mADT. The crystallisation peak present at VB-PLA – 3DP is lost 30 minutes into mADT. The overall shape of the curves after that point is maintained, without important displacement of the melting temperature. Endothermic processes are arbitrarily depicted downwards.

5.3. PROCESSING OF 3DP STRUCTURES AND MATERIALS

5.3.1. ANNEALING

The crystallinity values of both materials increased dramatically after annealing, more than doubling their initial values, while having a significant ($p < 0.05$) negative effect on UTS, albeit not so ($p < 0.05$) for E , probably due to the wide standard deviations on these values (**Figure 5.17**). The crystallinity values for BFB-PLA and VB-PLA after annealing rose to 56.92% and 48.58% respectively, with drops in UTS and E . It is also noteworthy that annealing seems to overall improve the reproducibility of the material in regards of crystallinity. Annealing has a negative effect on UTS , which was lowered in

both materials. As evidenced by **Figure 5.19**, for both materials annealing had virtually no effect on mass loss over the sampled period ($p < 0.05$).

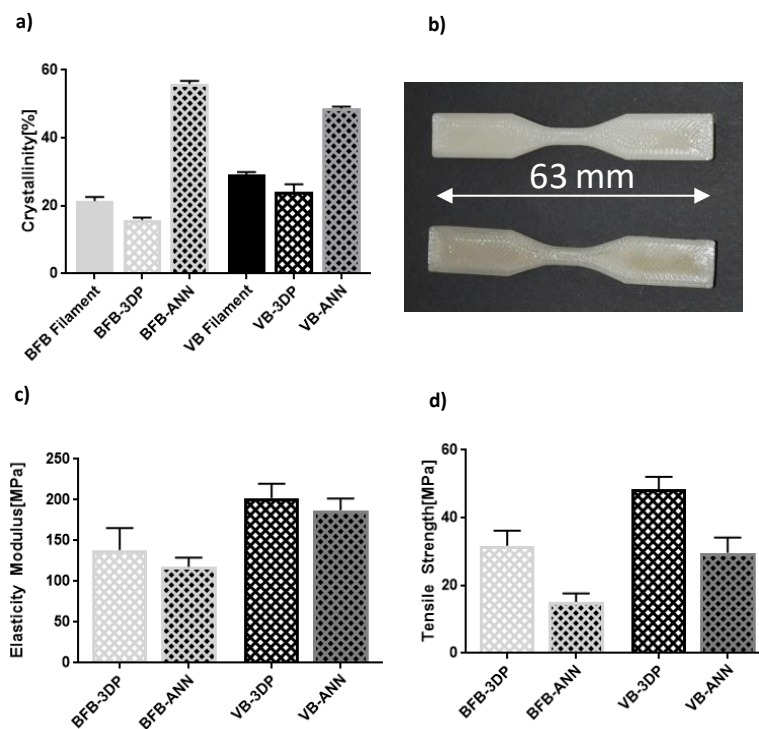


Figure 5.18. Changes in C_r , appearance, E , and UTS on BFB-PLA and VB-PLA at different processing stages. a) Large changes in *crystallinity* ensue after annealing, especially on BFB-PLA, rising to an average of 56.92%. Similarly, VB-PLA exhibited a C_r value of 48.58% after annealing. **b)** The process's effects are also apparent in visual inspection, as expected: the annealed material (shown on top) becomes noticeably more opaque than the 3DP one (on bottom). Elasticity modulus **c)** and tensile strength **d)** are deteriorated by the treatment, which are likely due to the heightened crystallinity. Error bars denote standard deviation. Tests were conducted as described above for each type of measurement. 3DP, 3-D printed specimens; ANN, 3-D printed specimens posteriorly annealed.

Mechanical properties for BFB-PLA were improved in that its dismantling point shifted from 1.5 hours to over 2 hours, remaining over 2 hours for VB-PLA, which suggests that failure of mechanical integrity is very strongly linked with crystalline content, as both annealed materials display around the same proportion by weight (56.92% for BFB-PLA, and 48.58% for VB-PLA). Tensile strength and elastic modulus values were preserved better in both annealed materials, in general maintaining higher values before reaching their dismantling point. Although changes in deterioration of mechanical properties

and mass loss were not significantly different ($p < 0.05$) – except for E on VB-PLA –, the macroscopic behaviour of annealed specimens diverged significantly from that observed for non-annealed samples (**Figure 5.18**), with the materials becoming brittle.

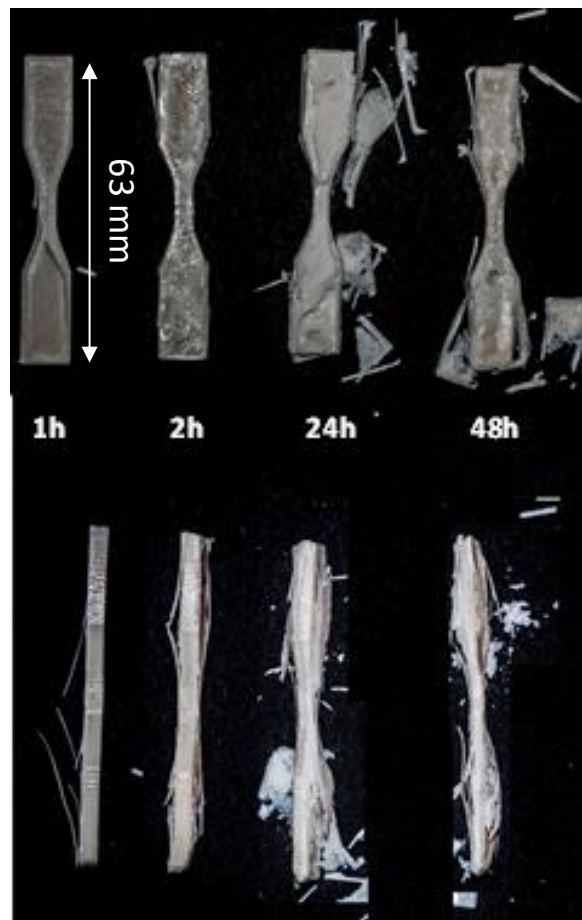


Figure 5.19. Photograph of BFB-PLA tensile specimens at various stages of mADT. Depictions of frontal (top) and lateral (bottom) views. The dismantling period for this material was considered to be 24 hour since the specimens fall apart during handling after this point, as evidenced by the fragmentary remnants visible in the image.

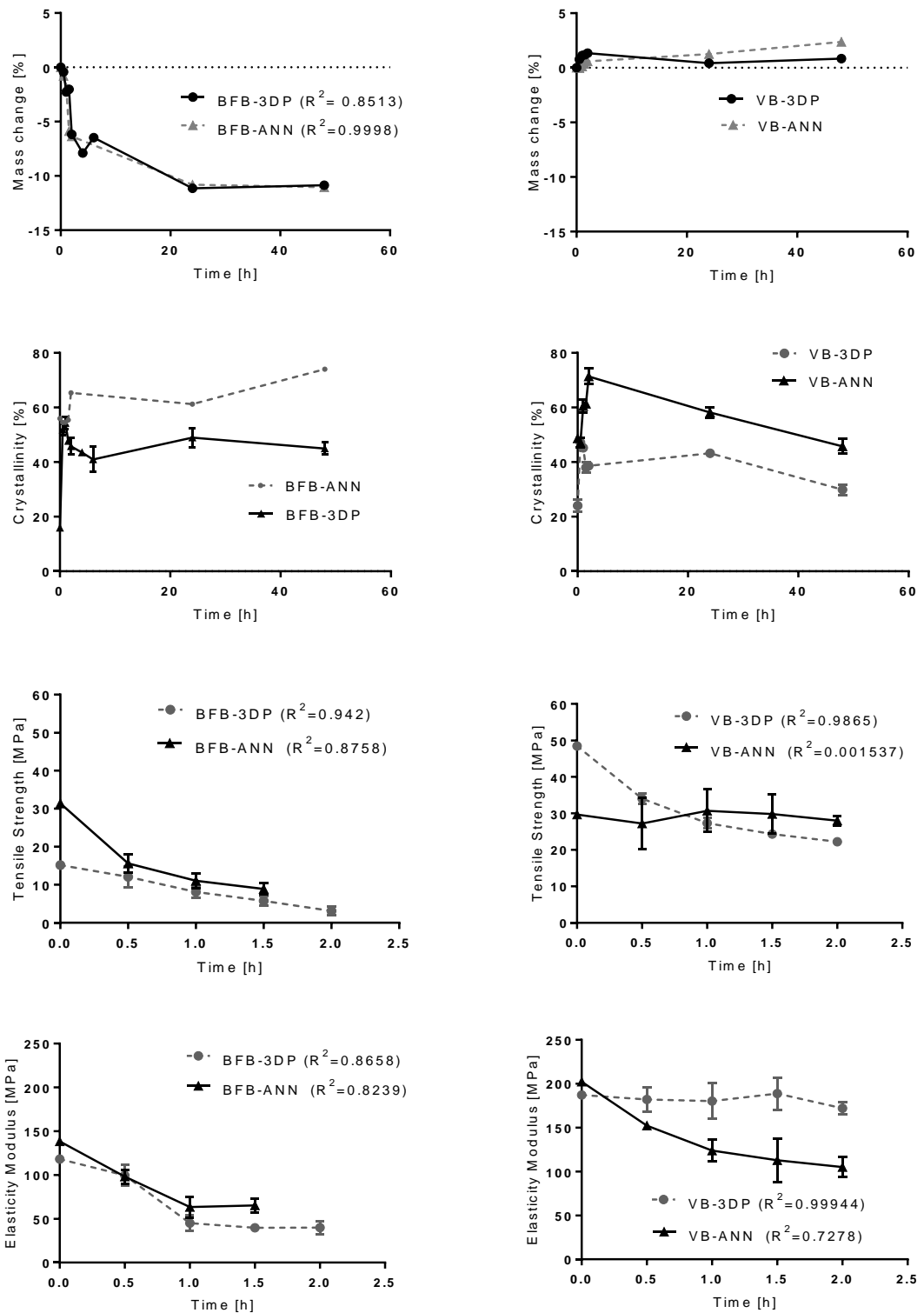


Figure 5.20. From top to bottom: mass change, crystallinity, tensile strength, and elasticity modulus measurements during mADT on BFB-PLA (left) and VB-PLA (right)-when 3D-printed (3DP), and when 3D-printed and annealed (ANN). Points correspond to means with standard deviation bars. Correlation coefficients respectively denote a non-linear fit to an exponential curve (tendency lines and error bars are not plotted for clarity). BFB-ANN and VB-ANN specimens reached their dismantling point after 2h. Measurements for each parameter were gathered with the aforementioned methods. Some connecting-lines and data points depicted in gray and/or dashed for clarity. Crystallinity data for VB-PLA shows only partial results as available at the time of writing.

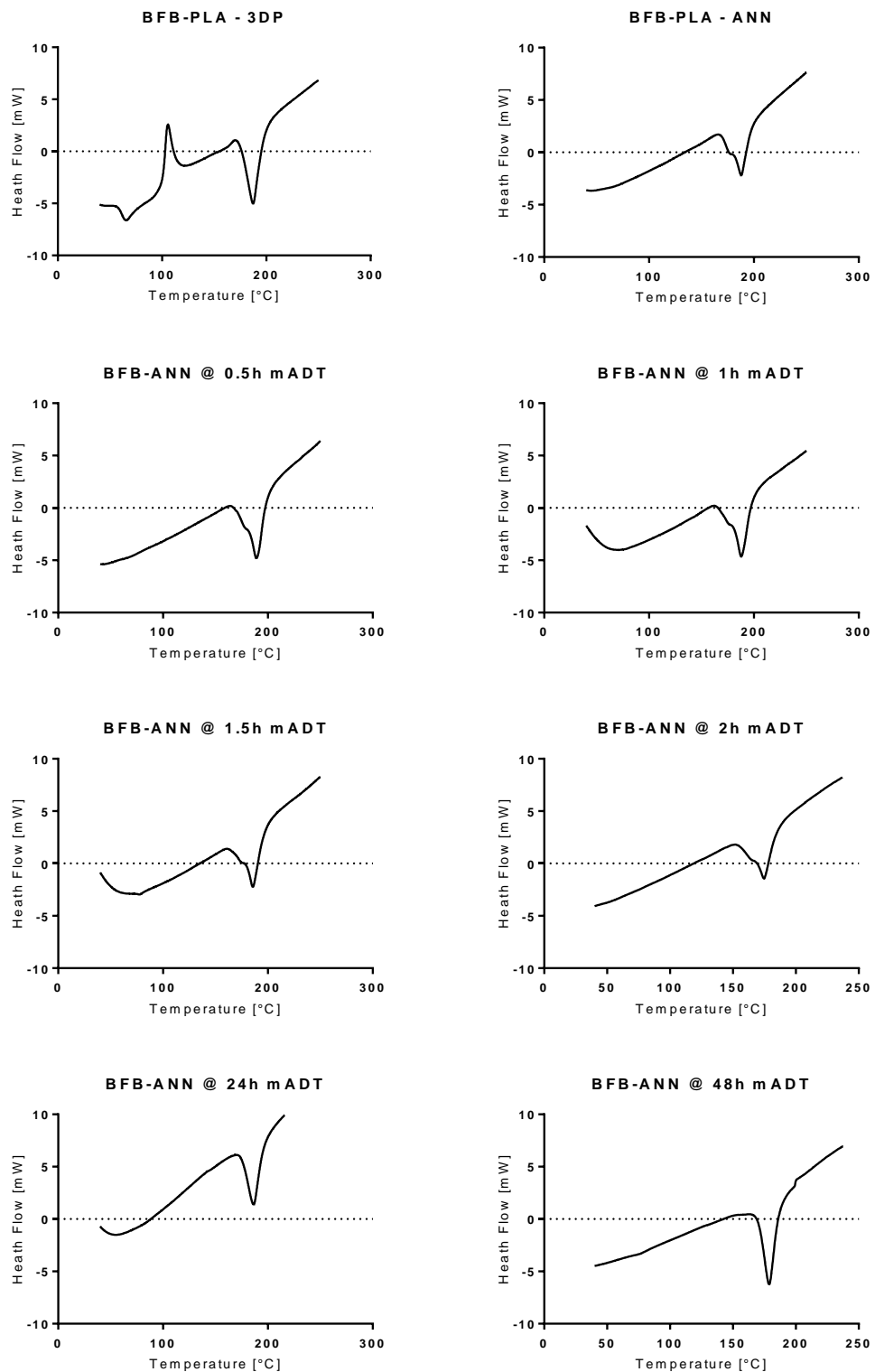


Figure 5.21. DTA curves for BFB-PLA 3DP specimens annealed and at progressive stages of mADT. Annealing (BFB-ANN) completely removes the crystallisation peak present on the 3D-printed samples (BFB-3DP). The overall shape of the curves after that point is maintained after annealing, without important displacement of the melting temperature. After annealing, an endothermic peak appears as a shoulder on the main melting peak. This has been theorised to correspond to a melting peak of crystallised degradation products [290]. Endothermic processes are arbitrarily depicted downwards.

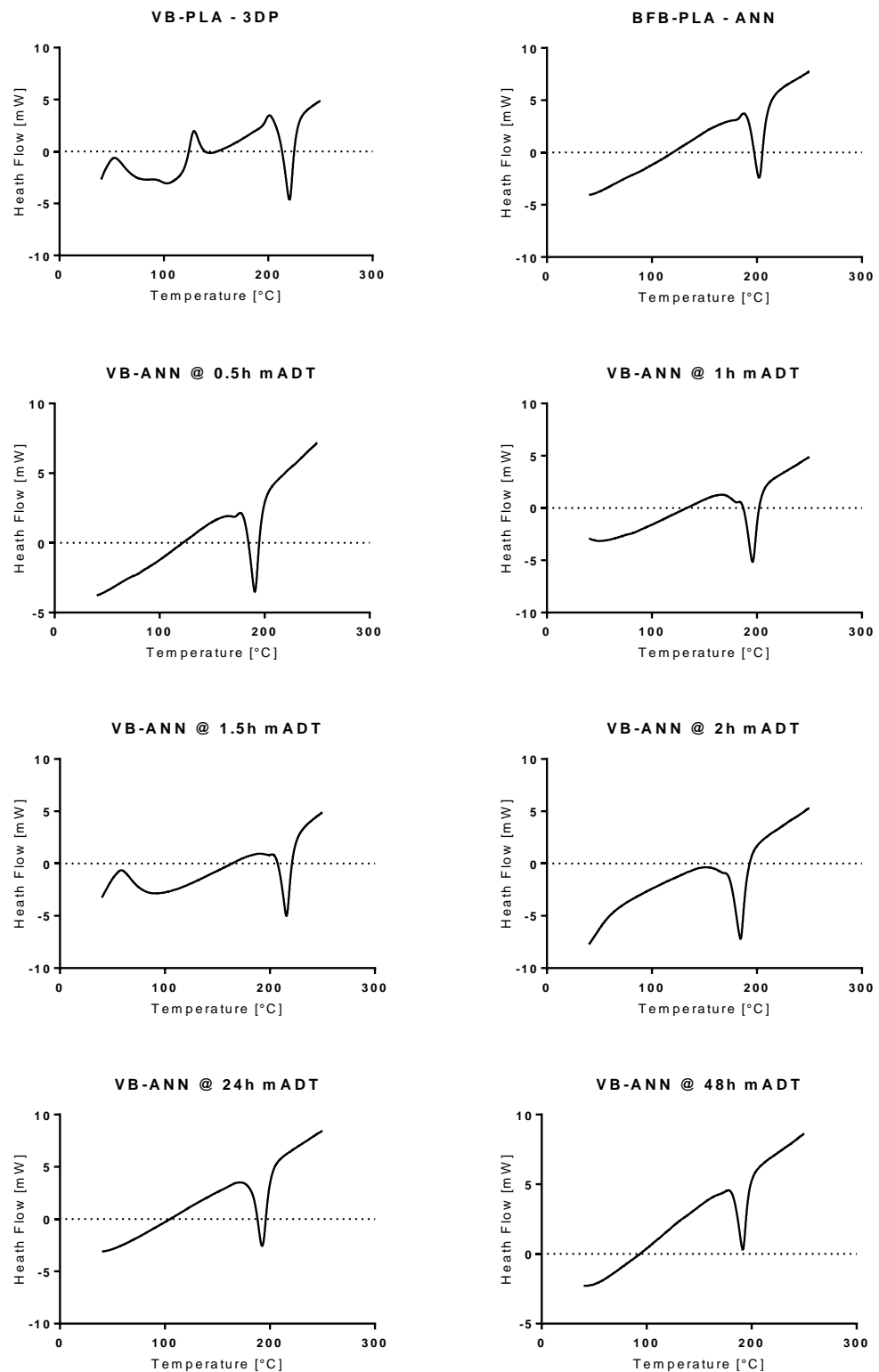


Figure 5.22. DTA curves for VB-PLA 3DP specimens annealed and at progressive stages of mADT. Annealing (VB-ANN) once again removes the crystallisation peak found on the 3D-printed samples (VB-3DP). The overall shape of the curves after that point is maintained, much like for BFB-PLA. Endothermic processes are arbitrarily depicted downwards.

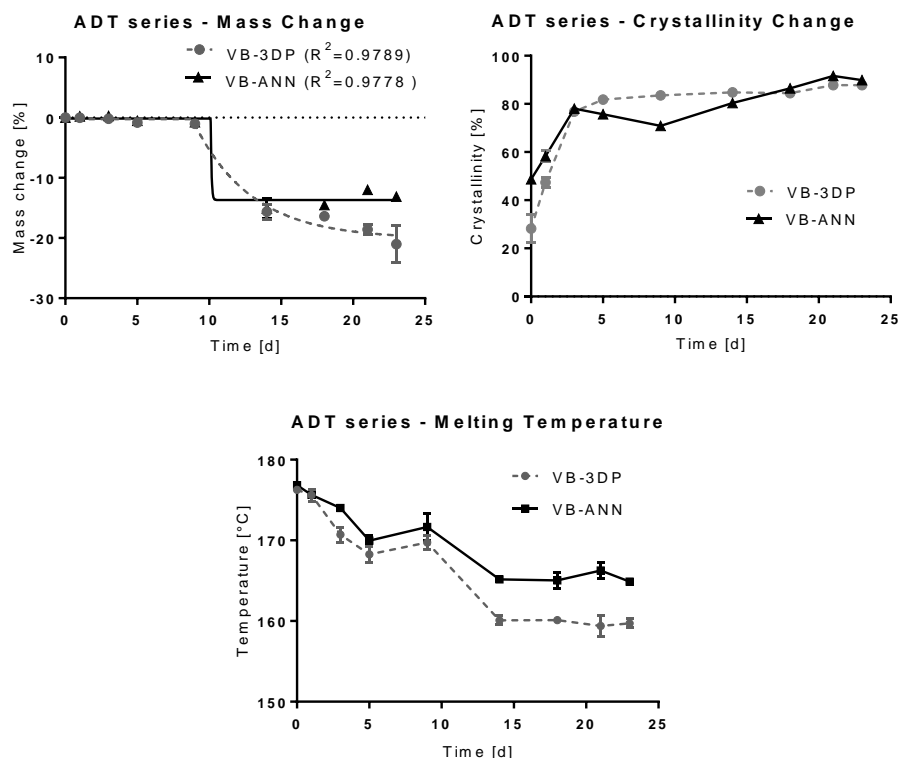


Figure 5.23. Mass change, crystallinity, and fusion temperature measurements during ADT on VB-3DP and VB-ANN. Points correspond to means with standard deviation bars. Correlation coefficients respectively denote a non-linear fit to a plateau-exponential decay curve. BFB-ANN and VB-ANN specimens reached their dismantling point before 24h of the experiment had passed. Measurements for each parameter were gathered with the aforementioned methods. Some connecting-lines and data points depicted in gray and/or dashed for clarity.

Crystallisation peaks are not observable after annealing, as shown in **Figure 5.21** and **Figure 5.22**. As with the thermal analysis presented in section 5.2, a shoulder becomes visible on the main fusion peak of all but the last two sampling periods (24 and 48 hours) during degradation. The other noticeable difference amongst the thermal analysis curves was the change in crystallinity, reflected on the size and area of the fusion peaks.

Results for ADT measurements are found in **Figure 5.22**. The graphs for annealed specimens show no significant deviation ($p < 0.05$) from those of 3DP specimens. It is also noticeable that the plots for both materials were

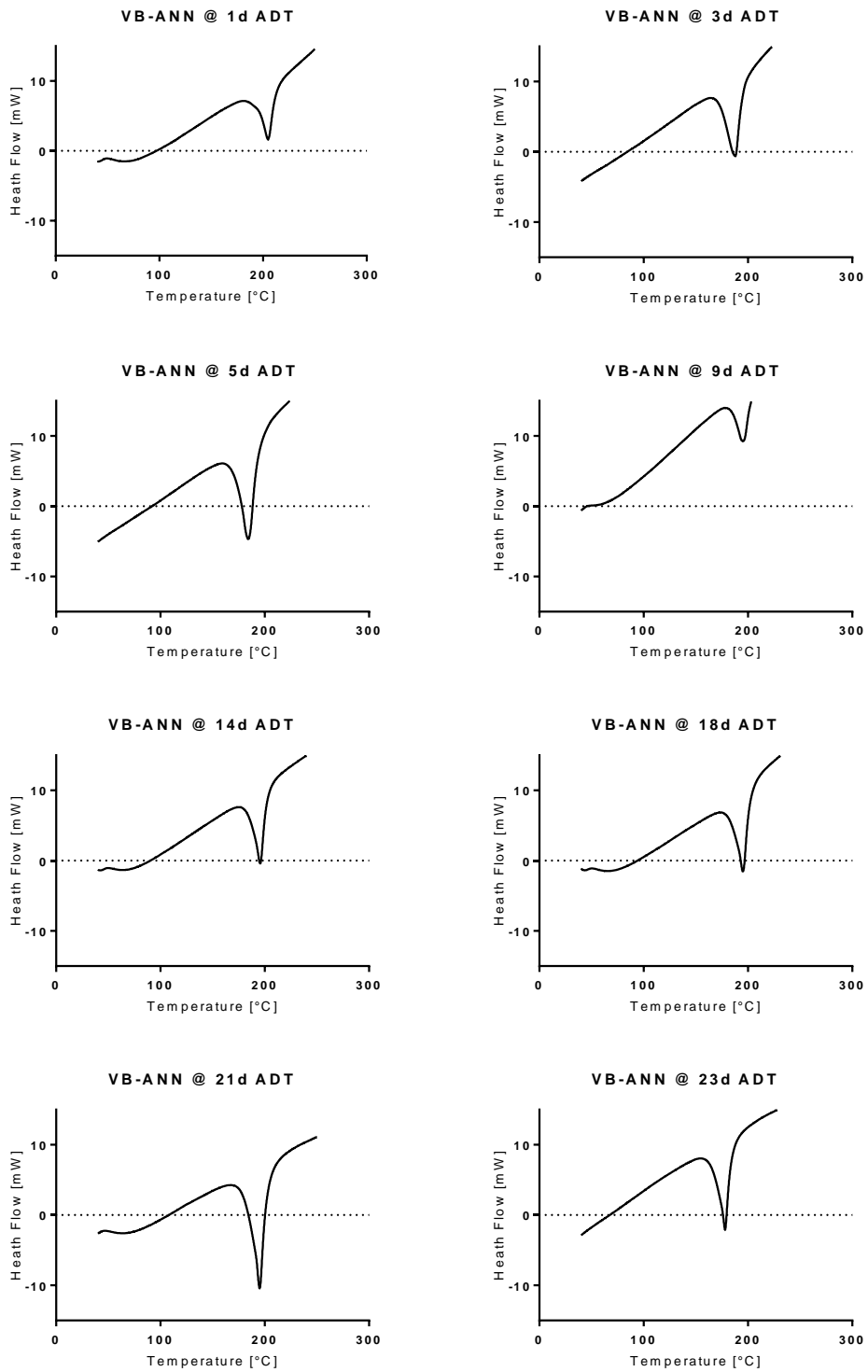


Figure 5.24. DTA curves for VB-PLA annealed specimens annealed and at progressive stages of ADT. The overall shape of the curves after that point is maintained, much like for VB-3DP. Endothermic processes are arbitrarily depicted downwards.

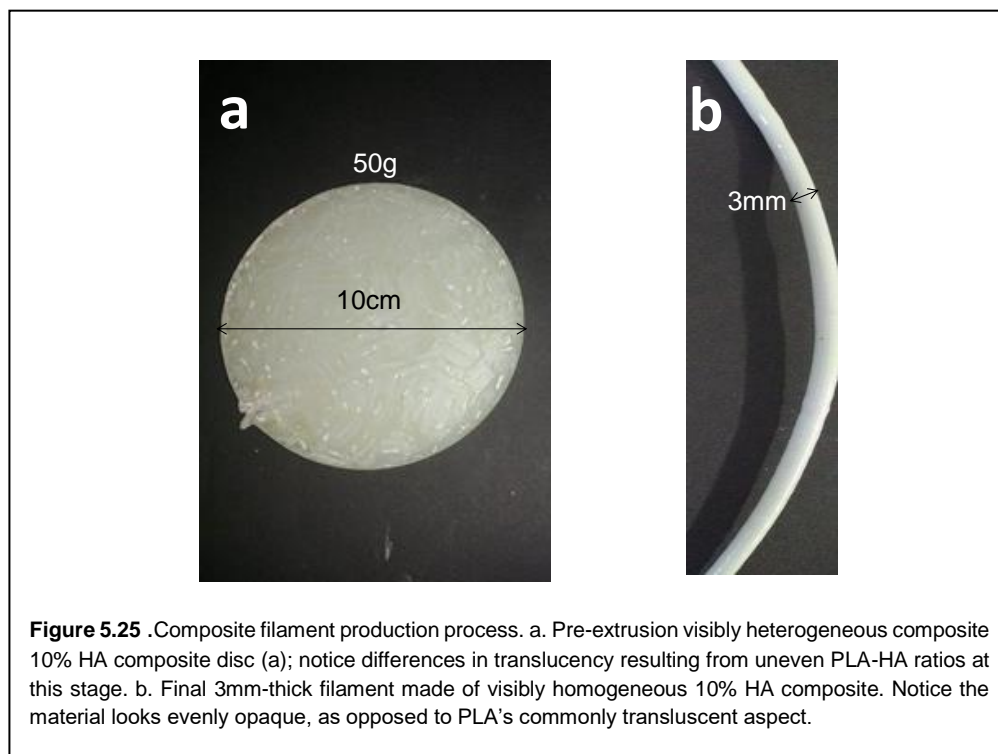
very closely matched at every point. Annealed specimens, however, were found to be more brittle, being impossible to handle and load on the tensile tester without breaking them even after a single degradation time period had passed. The dismantling point for both materials can be safely assumed to be under 1 day for ADT settings.

Plots for DTA through the ADT experiments are shown on **Figure 5.24**. These show a similar pattern to 3DP specimens, where the fusion peak increases in size after the first time period, with the overall behaviour of the curves being similar. Progressive changes in the size of the fusion peak were consistent with changes in crystallinity taking place throughout the experiments. Crystallinity for annealed specimens began at 48.67%, and reached a final value of 89.89% by the 23rd day. Similarly, to 3DP specimens, the initial fusion temperature registered at 176 °C dropped to 164 °C.

5.3.2. PLA-HA COMPOSITE FILAMENT

Consistent production of 3DP composite filament was achieved with an extrusion temperature set at 190 °C. Modifications to the *Filabot Original Filament Extruder* proved necessary to ensure reproducibility of filament in a quality adequate for our 3D printer. Hand-regulated extrusion rates, cooling intensities, and filament-pulling forces were all implemented for successful, reliable extrusion of print-worthy filament. Resulting outputs from the steps of this process are shown in **Figure 5.25**.

In practical terms, the composite filament produced in this study proved to be more brittle than the raw VB-PLA filament, making filament rupture during printing a more common occurrence. The addition of HA also made the extrusion process more difficult to control, especially for the 20% concentration. Additionally, the 10% and 20% composites caused blockage on the printer's nozzle, stopping any material from going through, and therefore stopping or even ruining the printing process at hand. The 10% composite would block the extruder after about 2-4 hours of continuous working, while the 20% would do so after less than 30 minutes. This fact added a further degree of technical difficulty for printing, since larger items – such as tensile bars – require the user to monitor and stop the machine mid-process in order to clean the nozzle. Smaller items – like cell-culture discs and mesh-cubes – would require cleaning after every individual sample is printed.



5.4. IMPLANT GEOMETRIC DESIGN

The characteristics of the designed lattice were compiled in **Table 5.4**. This particular geometry was chosen to roughly resemble a section of maxillary bone. Printing near this limit prevents the STL build from including fill patterns, likely helping to maintain uniformity in the material. With this lattice acting as the inner structure of an implant, its surface area becomes about eight times greater than that of a solid implant of similar dimensions. The openings within the mesh were designed within 2 mm. The final unit is portrayed in **Figure 5.26** and **Figure 5.27**. A series of 20 prints of this unit supports the claim that the structure can be manufactured through FFF in VB-PLA at a resolution of 0.125 mm and the maximum 95% fill setting without supports.



Figure 5.26. Detail photograph of framed 3D-mesh prototype produced on VB-PLA through the procedure described in this section. Lateral view.

Parameter	Magnitude per cm ³	Units	Comments
Material volume	0.35	cm ³	Calculated in <i>Meshmixer V 11.0.554</i>
Material surface	8.55	cm ²	Calculated in <i>Meshmixer V 11.0.554</i>
Mesh void content	64.23	%	Calculated from <i>Meshmixer V 11.0.554 data</i>
Material porosity	8.92	%	Calculated from printer dimensional analysis data for PLA. Average for the 0-0.5cm ³ range
Mesh density	0.453	g/cm ³	Calculated at 1.27g/cm ³ for PLA

Measurements and calculations derived from a 50mm-sided cubic mesh. Mechanical properties for the lattice have not yet been determined.

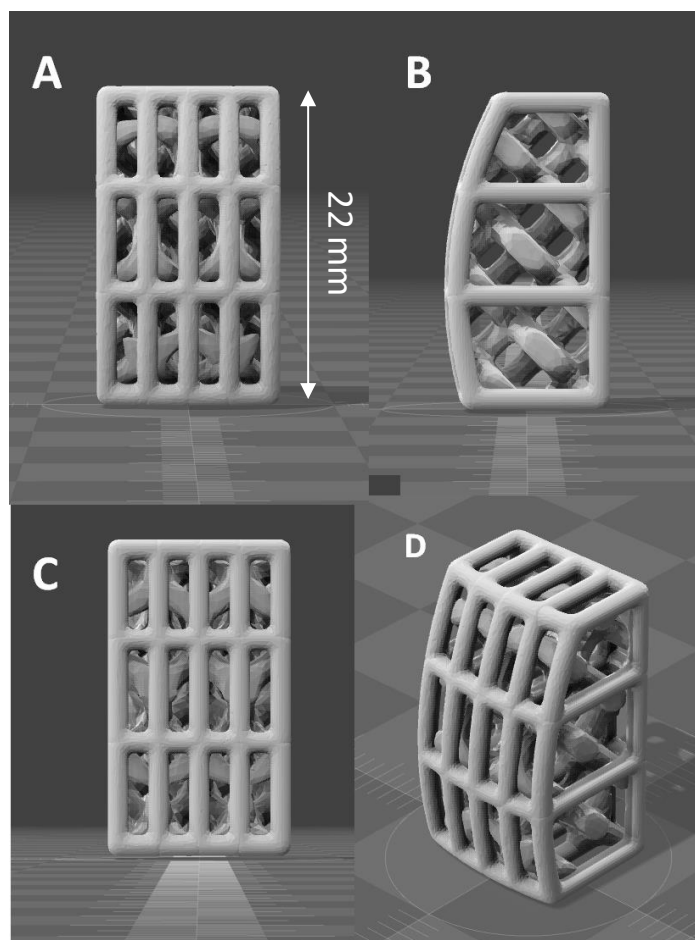


Figure 5.27. Framed 3D-mesh prototype for implant geometric design. The desired shape is once again used as a pattern produce an open frame based on its outline. This frame and the 3D-mesh are then superposed to generate this geometry. Depending on the software used, the precise steps to accomplish this can vary. Models generated in *Autodesk Meshmixer V. 11.0.544*. A, front view; B, lateral view; C, posterior view; D, isometric view.

5.5. COMPOSITE CHARACTERISATION

Characterisation of the composite produced in this study was carried out so as to make the results comparable to those for the base polymer, which are detailed in **Section 5.2**. Where appropriated, the following results were therefore presented in comparison to those covered previously.

5.5.1. COMPOSITE HA CONTENT MEASUREMENT AND DISTRIBUTION

TGA data used to derive the composite's ceramic content showed that ~7% of the HA would remain embedded in the polymer matrix after processing a 10% weight-by-weight formulation of HA (**Figure 5.44**). No significant differences were found between any of the processing steps of the 3DP composite filament production ($p < 0.05$). **Figures 5.45-5.49** show results of SEM-EDS elemental analysis at different production stages of the composite.

Composite Filament Production - HA Content (n=3)

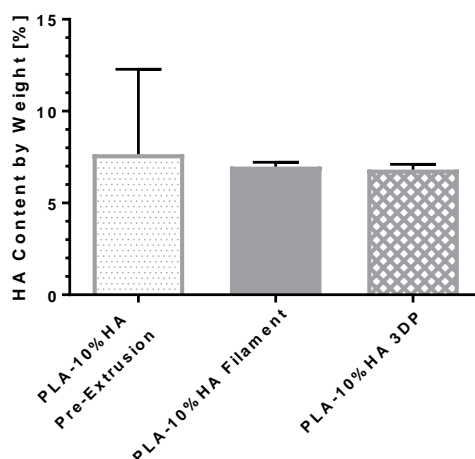


Figure 5.28. Comparison of HA concentration during production phases of 3DP composite filament. TGA was used to determine the ceramic content of composite samples by thermal decomposition of their polymer matrix. No significant differences were found with respect to each of these stages ($p = 0.05$). Error bars denote standard deviation.

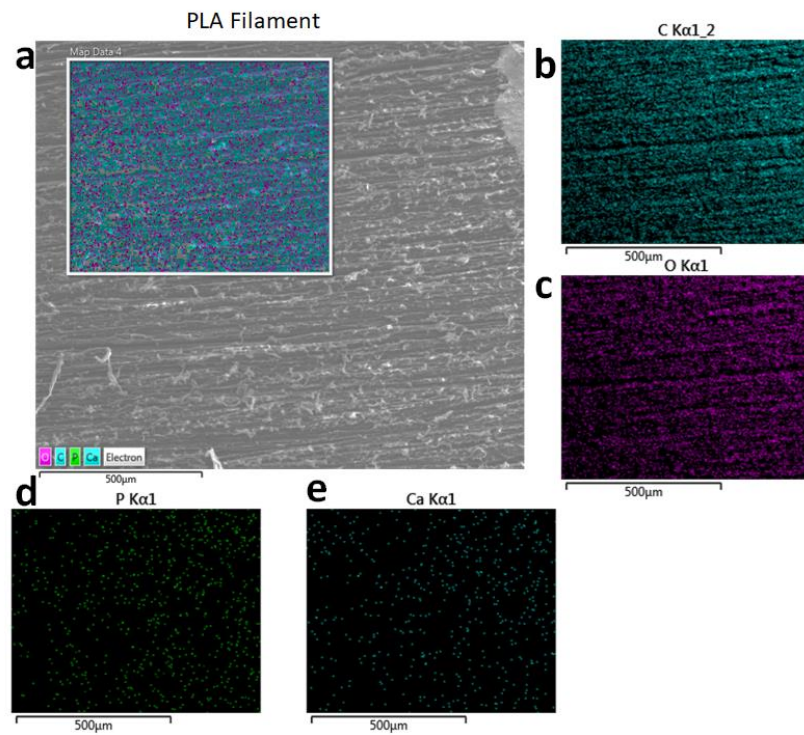


Figure 5.30. SEM-EDS images of VB-PLA filament. SEM image (a) scanned at 20kV to a magnification of 200X. EDS was then performed to look for elemental signals of HA. The polymer matrix's expected distribution of carbon (b) and oxygen (c) was readily apparent in the scan. Only noise-level traces of phosphorus (d) and calcium (e) were detected.

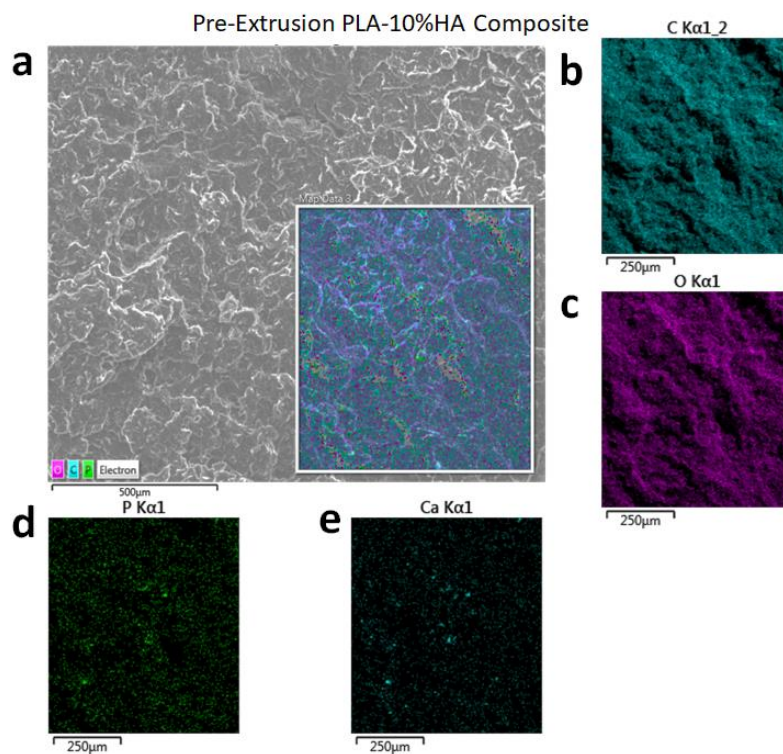


Figure 5.29. SEM-EDS images of pre-extrusion PLA-10%HA composite. SEM image (a) scanned at 20kV. EDS was then performed to look for elemental signals of HA. The polymer matrix's expected distribution of carbon as background reference (b) and oxygen (c) was readily apparent in the scan. Diffuse associated distributions of phosphorus (d) and calcium (e) were detected.

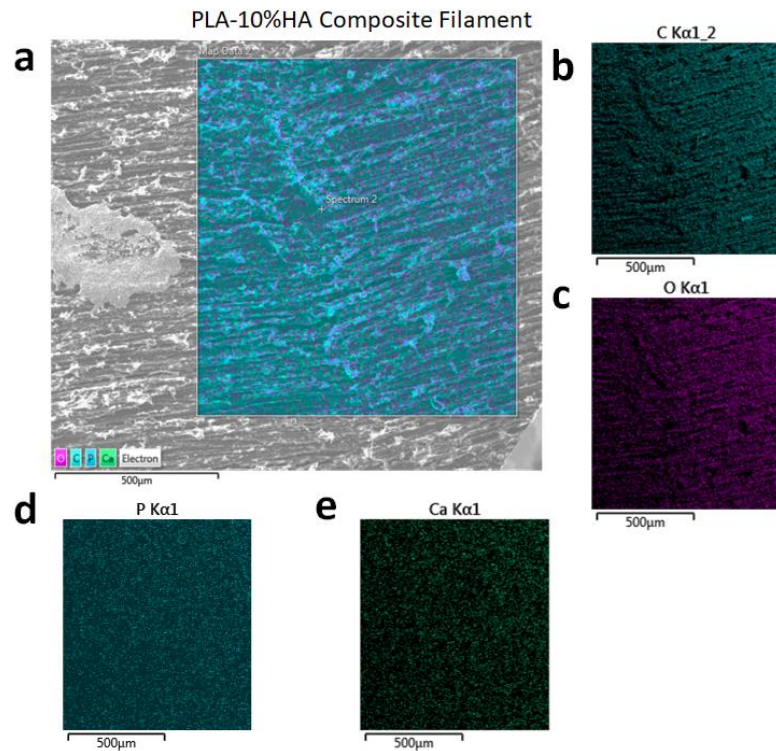


Figure 5.31. SEM-EDS images of PLA-10%HA composite filament. SEM image (a) scanned at 20kV to a magnification of 200X. EDS was then performed to look for elemental signals of HA. The polymer matrix's expected distribution of carbon (b) and oxygen (c) was readily apparent in the scan. Uniform distributions of phosphorus (d) and calcium (e) were detected.

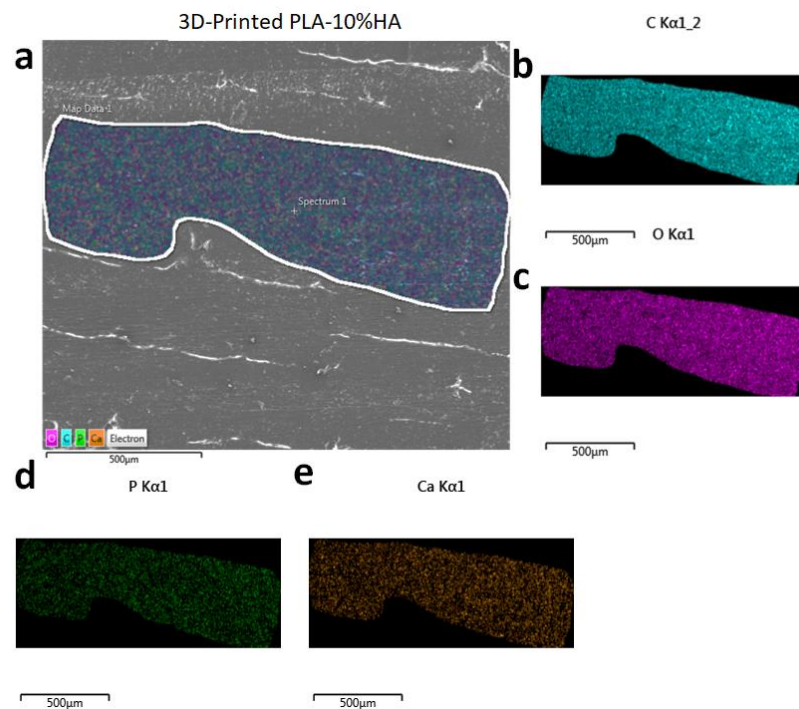


Figure 5.32. SEM-EDS images of 3D-printed PLA-10%HA composite. SEM image (a) scanned at 20kV to a magnification of 200X. EDS was then performed to look for elemental signals of HA. The polymer matrix's expected distribution of carbon (b) and oxygen (c) was readily apparent in the scan. Uniform distributions of phosphorus (d) and calcium (e) were detected.

SEM-EDS analysis showed that PLA filament has no detectable Ca or P content (**Figure 5.45**). Once mixed with HA and molten, the composite shows diffuse and heterogeneous zones where Ca and P were closely distributed, which suggests the presence of HA (**Figure 5.46**). After extrusion into 3DP filament (**Figure 5.47**), and processing through FFF (**Figure 5.48**), the samples were found to have a homogeneous distribution of both elements across the scanned area.

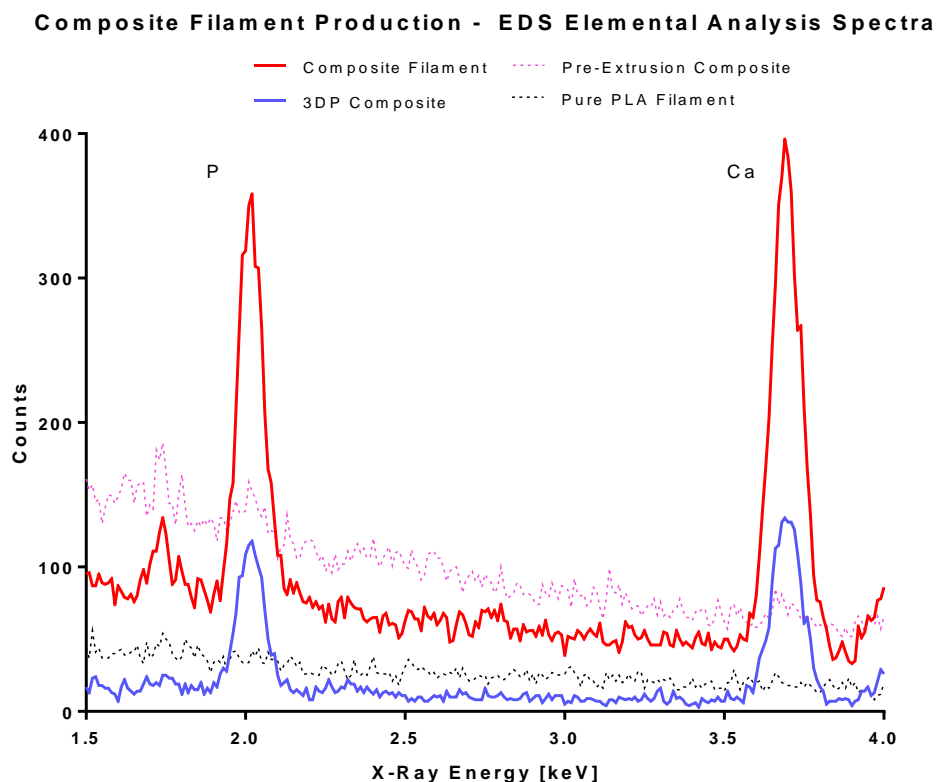


Figure 5.33. Comparison of EDS point-elemental content in SEM images between different stages of PLA-HA composite production. Region in the spectra is zoomed in to the area of interest for energies characteristic of phosphorus (P) and calcium (Ca). These peaks were distinctly detected for the PLA10%-HA composite filament, as well as for the 3D-printed composite. They were less defined but still detectable by the software for the pre-extrusion composite, and overall indistinguishable from background noise for the pure PLA filament.

Figure 5.49 shows EDS data for elemental analysis for each stage of compositing, and **Figure 5.50** summarises a comparison of how the different heat-based processes affect polymer crystallinity and molecular weight. Only controlled annealing as described in **Section 5.5.1** was capable of driving a big enough change in the crystalline content of the PLA matrix to be statistically significant. The rest of the results showed no difference with respect to the values for the base VB-PLA filament, except for the composite's Mn after being subject to 3D-printing ($p < 0.05$).

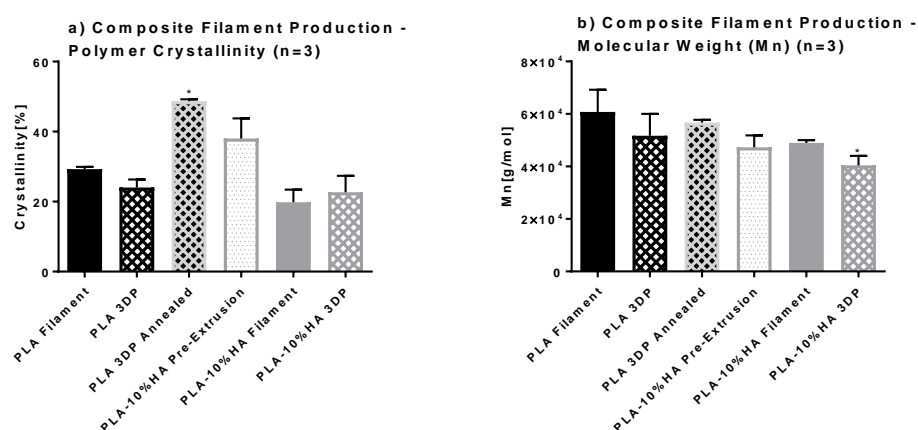


Figure 5.34. Comparison of a) crystalline content and b) number average molecular weight between different stages of PLA-HA composite production. Crystalline content and molecular weight as PLA undergoes the compositing process studied. Annealed 3D-printed PLA was included as a reference for controlled thermal treatment above glass-transition temperature, and was found to be the only process to produce significant differences in crystallinity with respect to the raw VB-PLA filament. Only after 3D-printing of the composite were significant differences in Mn detected. Stars denote significant differences ($p < 0.05$) from the control PLA filament group. Error bars denote standard deviation.

In contrast, calorimetric behaviour of the polymer was found to vary across processing. **Figure 5.53** summarises the TGA-derived thermograms for each material version. Crystallization peaks can be observed at around 90 °C – as expected for PLA. Melting peaks could also be observed in the typical zone:

at 174.8 °C for the 3D-printed composite, 176.0 °C for the pre-extrusion composite, 176.8 °C for the composite filament, and 175.8 °C for the raw PLA filament. Notably, there was an upward shift in the curves as the material experiences successive heat treatments.

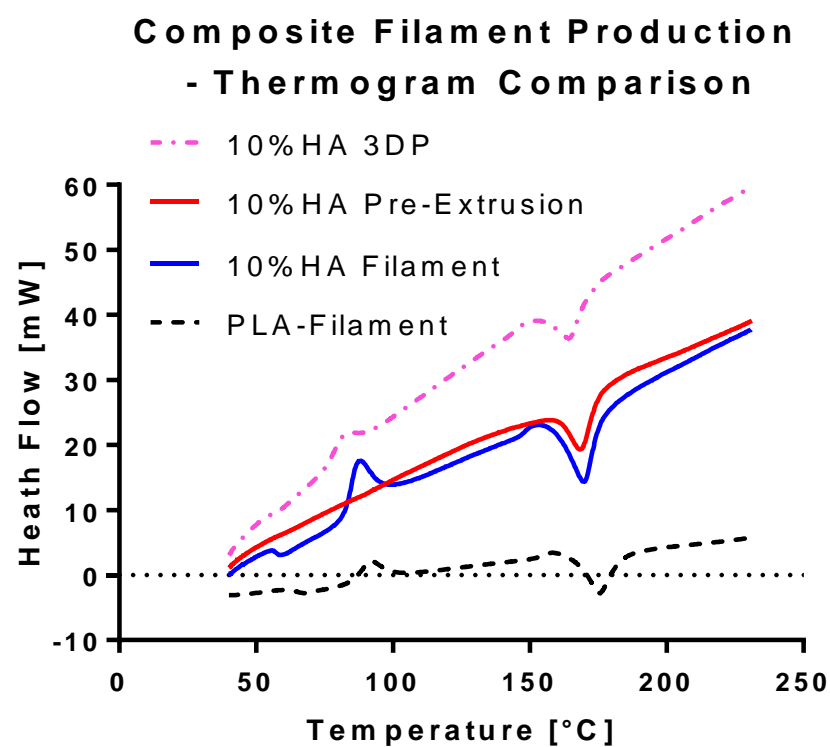


Figure 5.35. Comparison of crystalline content between different stages of PLA-HA composite production. Slight shifts in melting peaks are noticeable as the material undergoes compositing. Endothermic processes are arbitrarily depicted downwards. Notably, extrusion into filament eliminates the crystallisation peak.⁴

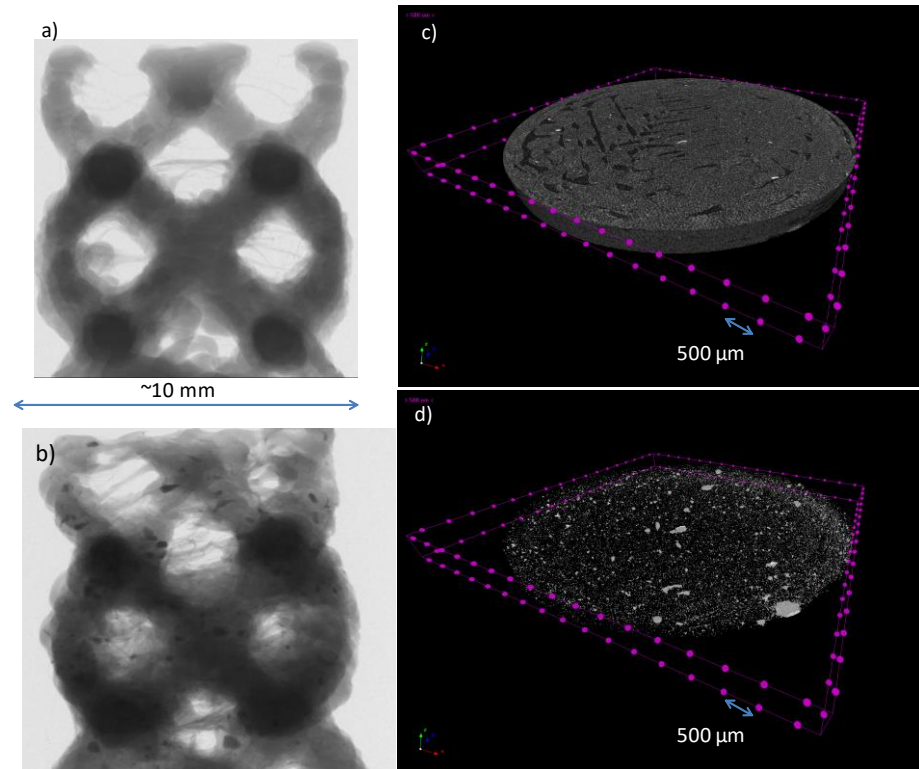


Figure 5.36. Images from μ CT of PLA-10%HA 3D-printed disc and 3D-cell culture samples. a. Axial reconstructions of different disc samples. b. Lateral projection of a 3D cell-culture sample showing embedded HA crystals. c. 3D reconstruction (of sample a) showing the entirety of the sample's mass. d. 3D reconstruction (of sample a) with highly radiolucent mass filtered out of the visualisation.

The μ CT scans of samples made with the 10% HA composite show an uniform distribution of radio-opaque particles all over the visible surfaces of the sample (**Figure 5.52 b, c and d**). These are not present in the reference scan, which was printed with raw VB-PLA (**Figure 5.52a**). Filtering the more radiolucent grayscale values corresponding to the polymer matrix, it was possible to identify a uniform volumetric distribution of radio-opaque micron-sized particles, congruent with calcium atoms from HA (**Figure 5.52d**). Even though variations on polymer density are apparent as more opaque sections within the volume, these transitions are gradual. In contrast, particles with sharply defined edges are evident scattered through the projections (**Figure 5.52d**). Since most of the mass of the sample is polymer, and predominantly carbon

and oxygen, these sharp edges indicate the presence of higher-atomic-number atoms, which attenuate greatly the passing X-ray photons as attenuation is dependent on atomic number and atomic weight [362–364]. As these radio-opaque particles are visible throughout all the volume of the composite samples, they are likely to be hydroxyapatite particles, which contain Ca as the most attenuating element in the material (**Figure 5.52a, b and c**). The abundance of these particles (**Figure 5.52c**) made it impossible to parametrise the images for computation of porosity values, mineral density, mineral volume, and other such calculations. Bigger agglomerations, in the order of hundreds of microns, were also clearly visible even in the unfiltered reconstructions.

5.5.2. 3DP COMPOSITE MECHANICAL PROPERTIES

Mechanical testing (**Figure 5.53a**) revealed that the composite after 3D had lower *UTS* (28.7 MPa) than pure PLA (48.5 MPa). In contrast, results were

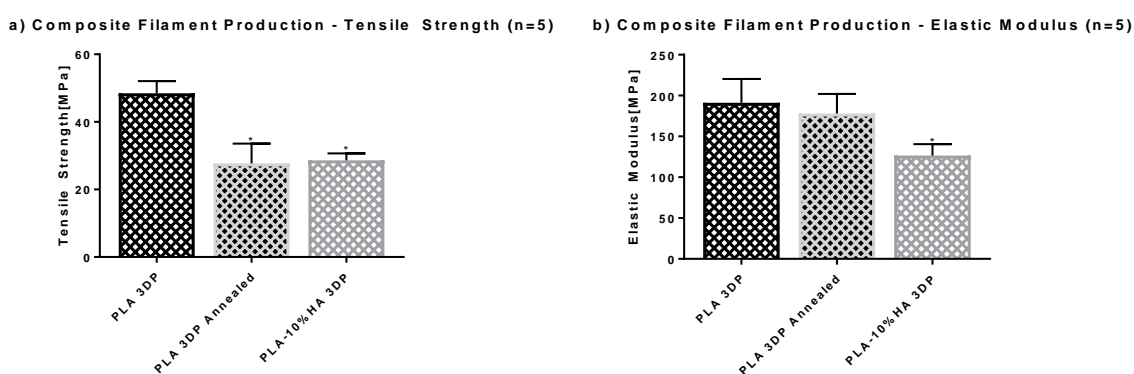


Figure 5.37. Comparison of mechanical properties between 3DP tensile bars on different PLA versions. Tensile strength (a) and elastic modulus (b) measurements for pure PLA (as control group), annealed PLA, and the 10% HA composite used in this study. Pull-to-break testing was conducted on 3D-printed tensile bars (n=5), both with specifications as per ASTM D638-03. Stars denote significant differences (p<0.05) from the control group. Error bars denote standard deviation..

similar for annealed tensile bars (27.7 MPa). In both cases, this meant a significant difference of more than 40% with respect to pure PLA controls ($p < 0.05$). Additionally, there were no significant differences found between the composite and the annealed material ($p < 0.05$). **Figure 5.53b**, in contrast, shows data for E which was similar between pure PLA (191.2 MPa) and the annealed tensile bars (178.0 MPa), with no significant differences ($p < 0.05$). In contrast, the E of the 10% HA composite (126.5 MPa) was significantly lower than that of both of the other materials ($p < 0.05$). This suggests the HA is not interfacing well within the PLA matrix.

5.5.3. COMPOSITE ACCELERATED DEGRADATION

To further illustrate the effects of the compositing process in VB-PLA, the following results are displayed as compared to values and trends explained in **Section 4.2** for the pure version of the material and 3D-printed samples of it.

5.5.4. MASS CHANGE

Data collected for mass loss of composite samples during ADT are shown in **Figure 5.54**. Comparison with this curve against that of pure VB-PLA shows that degradation behaviour starts out similar for both polymers during the first three days of the experiment – corresponding to their water-infiltration periods. The composite reaches its tipping point at some time before the fifth day, where statistical difference in their degradation profile was confirmed through ANOVA analysis ($p < 0.05$). The tipping point was determined to be 2.65 days ($R^2 = 0.9806$) through non-linear regression to a plateau-exponential decay model.

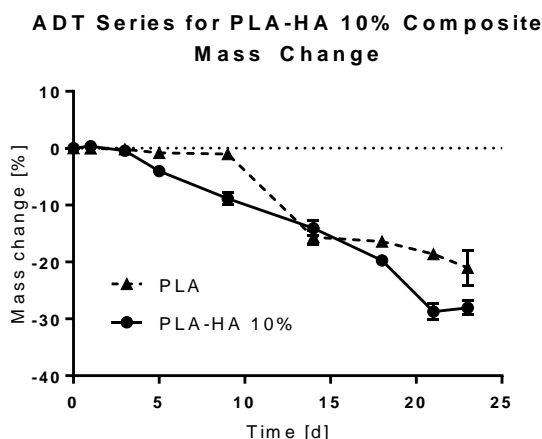


Figure 5.38. Mass change measurements from ADT specimens on PLA-10%HA composite. Data from degradation on PBS at 70 °C. Points correspond to means with standard deviation bars. Solid line denotes values for the composite, with values for pure PLA shown in dashed lines for reference.

5.5.5. CRYSTALLINITY

Throughout degradation, crystallinity for the composite followed a noticeable exponential trend, similar to that found for VB-PLA. However, it experienced pronounced variations in this parameter, which made it difficult to evaluate statistical differences at each individual time-point. Fitting the data to an exponential model through non-linear regression, it became apparent that the composite underwent a more erratic degradation ($R^2= 0.6783$) than the reference PLA ($R^2= 0.9833$). Furthermore, the composite also displayed a larger time constant ($\tau=2.265$) than pure PLA ($\tau=1.951$), suggesting a slower increase in overall crystallinity for it (**Figure 5.55**).

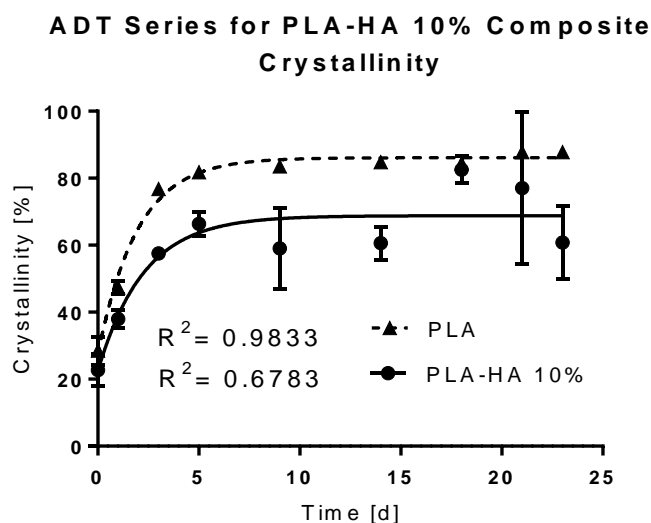


Figure 5.39. Crystallinity change measurements from ADT specimens on PLA-10%HA composite. Data from degradation on PBS at 70 °C. Points correspond to means with standard deviation bars. Solid line denotes an exponential fit for the composite's data, with a fitting line for pure PLA shown dashed for reference.

5.5.6. MECHANICAL PROPERTIES

Similarly to what was observed and described for ADT specimens of VB-PLA, mechanical testing was impossible after the first day of degradation. The specimens became too brittle to be handled, even though their geometry remained preserved.

5.5.7. THERMAL ANALYSIS

In line with what was observed for the other PLA versions trialled in **Section 5.2**, the PLA-10%HA composite displayed no crystallisation peaks after the first day of ADT. A lowering of the melting temperature was another noticeable trend shared with the raw PLA: the composite starts out at a melting temperature of 175.9 °C and ends the experiment with one of 144.5 °C. This is 15.2 °C below that of VB-PLA (which starts at a similar 176.3 °C). **Figure 5.56** compiles the thermograms for the composite's ADT.

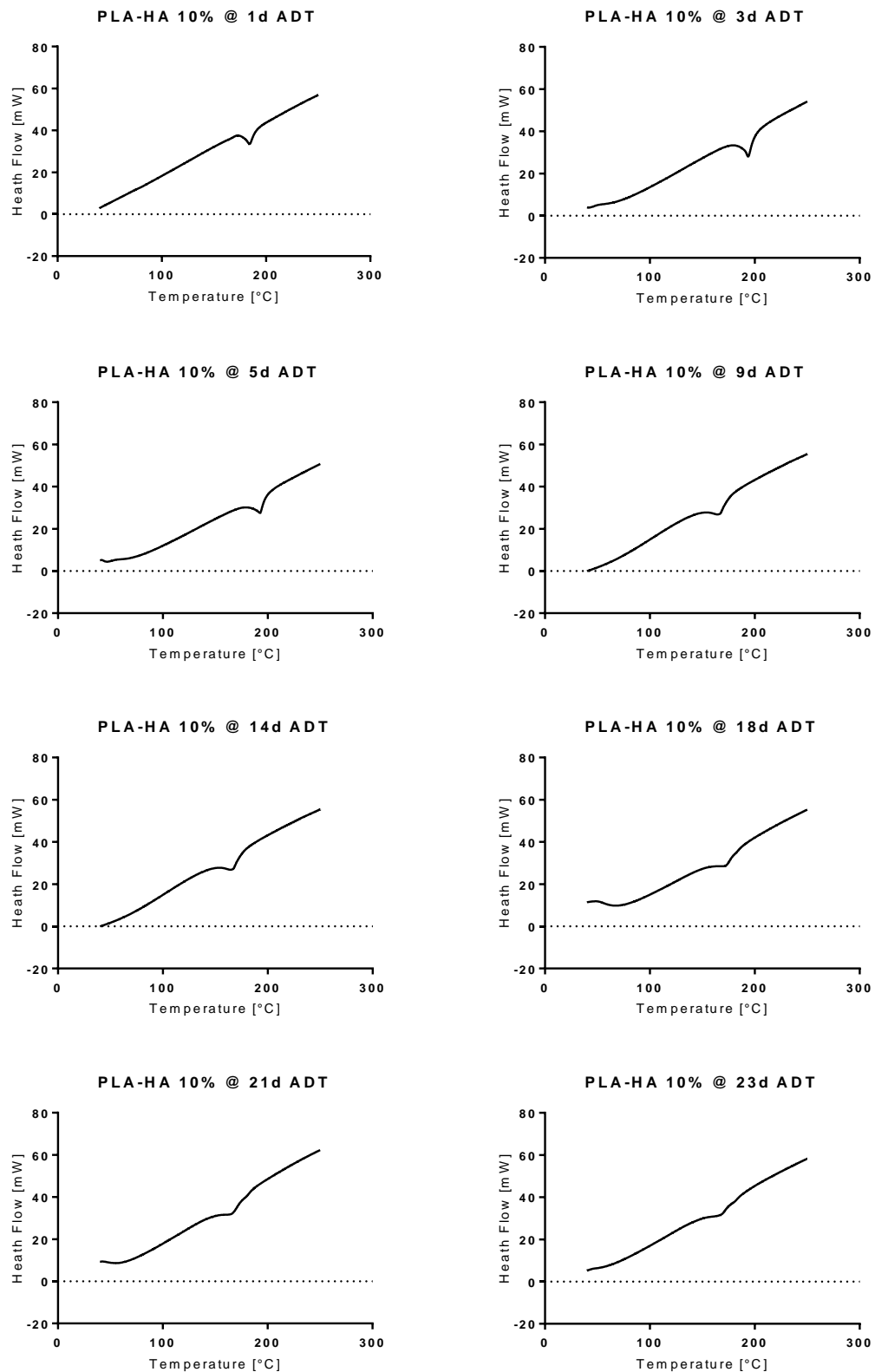


Figure 5.40. Thermograms for the PLA-10%HA composite after several stages of ADT. The overall shape of the curves is maintained throughout the experiment. The most noticeable changes are in the size of the fusion peak, which is reflective of crystallinity. Endothermic processes are arbitrarily depicted downwards. Data from degradation on PBS at 70 °C

As it can be noted in **Figure 5.57**, the melting temperature of the composite drops readily below that of pure PLA. ANOVA analysis of these data sets further confirmed that the processes were significantly different after the first day of degradation ($p < 0.05$).

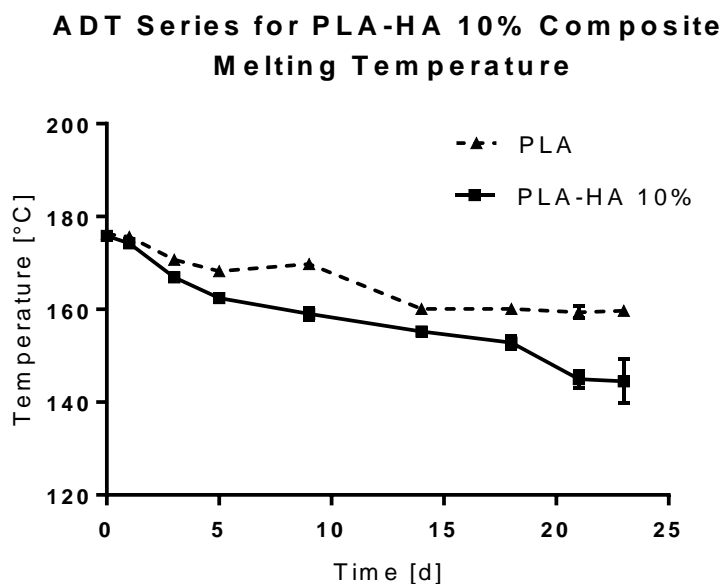


Figure 5.41. Changes in melting temperature for the PLA10%-HA composite throughout ADT. Data from degradation on PBS at 70 °C Points correspond to means with standard deviation bars.

5.5.8. MOLECULAR WEIGHT

Closely to what was expected, number average molecular weight (M_n) during ADT for the PLA-10%HA composite adhered satisfactorily to an exponential non-linear behaviour ($R^2 = 0.9735$). As shown in **Figure 5.58**, the agreement with this model was similar to that found for VB-PLA ($R^2 = 0.9691$). More than 90% of the samples' M_n had decayed by day 3. By the end of the experiment, M_n was measured at 0.99% of its starting value.

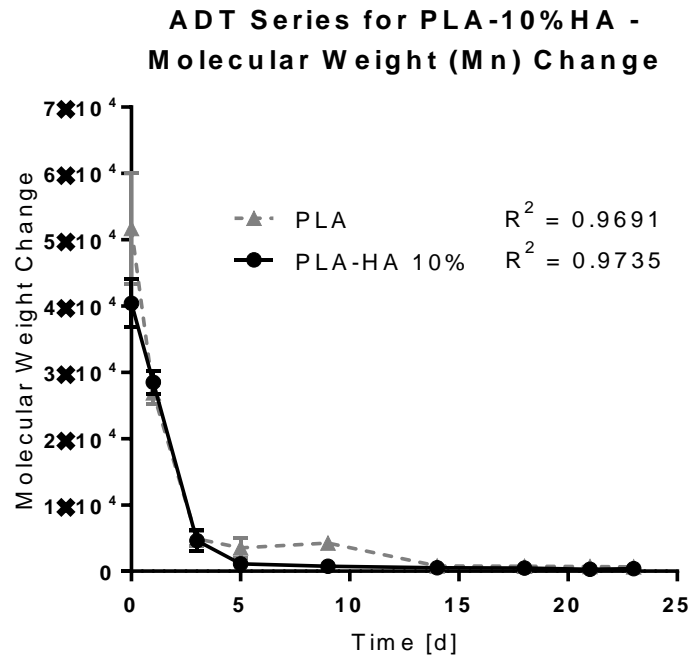


Figure 5.42. Changes in Number Average Molecular Weight (Mn) from the PLA-10%HA composite throughout ADT. Points correspond to averages with standard deviation error bars, joined by the solid line. The dashed line depicts a the Mn ADT data for VB-PLA as reference. Correlation coefficients refer to a non-linear fit to an exponential decay model, different for each of the curves.

5.6. IN VITRO MATERIAL BIOCOMPATIBILITY

5.6.1. 3D-PRINTED PLA STERILISATION

The three sterilisation methods described in **Section 4.5.2** were trialled in regards of suitability for preparation of 3D-printed discs for *in vitro* tissue engineering work. Results from a 24-hour cell attachment test and a 21-day viability study with MG-63 cells are shown in **Figure 5.28** and **Figure 5.29** respectively. The study was performed on pure-PLA 3DP discs of 1cm in diameter.

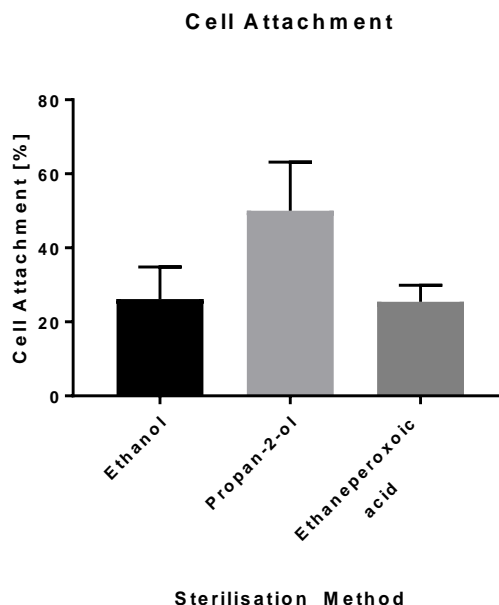


Figure 5.43. MG-63 cell attachment comparison for sterilisation methods for 3DP-PLA items to be used for *in vitro* testing. 3D-Printed PLA discs were chemically sterilised in 2ml of a 70% ethanol solution for 24h, 5% ethaneperoxoic acid for 30 minutes, or a 70% propan-2-ol solution for 15 minutes. Triplicate samples were measured in one biological repeat ($n=3$). ($p < 0.05$) No significant differences were found ($p < 0.05$) through ANOVA. Error bars denote standard deviation.

For cell attachment, no significant differences were found among the three sterilisation methods ($p < 0.05$). Similarly, no significant differences were found between ethanol and propan-2-ol sterilisation ($p < 0.05$) in regards of cell viability. On the other hand, sterilisation with ethaneperoxoic acid performed significantly worse ($p < 0.05$) than both ethanol and isopropanol after day 7 and into the end of the study.

21 Day Viability

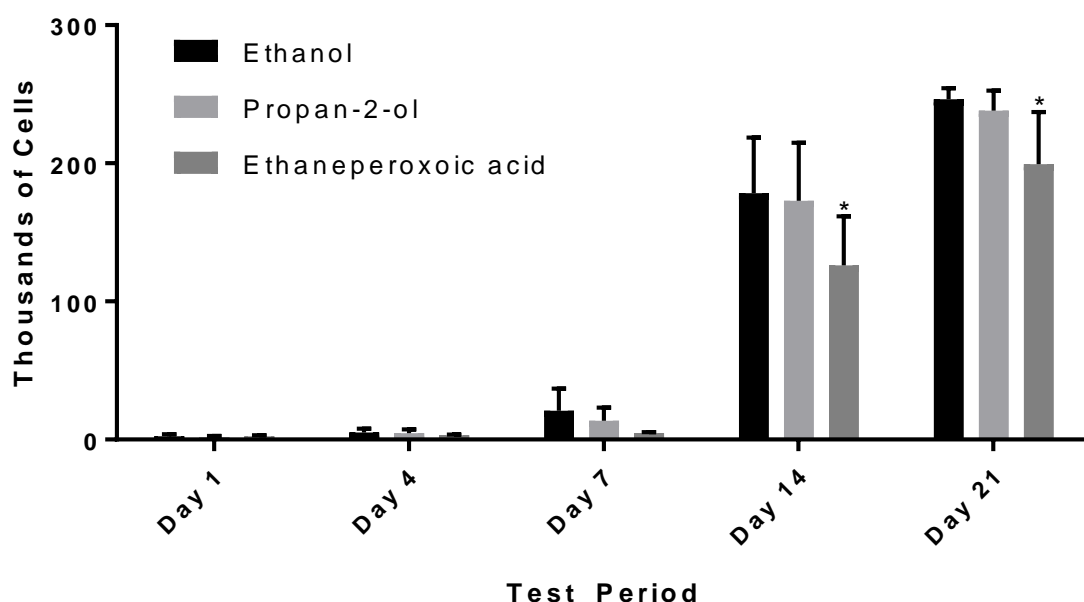


Figure 5.44. MG-63 cell viability comparison for sterilisation methods for 3DP-PLA items to be used for *in vitro* testing. 3D-Printed PLA discs were chemically sterilised in 2ml of a 70% ethanol solution for 24h, 5% ethaneperoxoic acid for 30 minutes, or a 70% propan-2-ol solution for 15 minutes. Triplicate samples were measured in one biological repeat ($n = 3$). Stars denote significant differences with respect to ethanol sterilisation ($p < 0.05$) as found through ANOVA. Error bars denote standard deviation.

Results for measurements of cellular matrix components after 21 days are shown in **Figure 5.30**. Calcium measurement through ARS was not possible

on these samples, as the levels appeared to be below the detection limit for this experimental setup. Conversely, there was no significant difference ($p < 0.05$) between the three sterilisation methods in regards of their potential effect on collagen deposition.

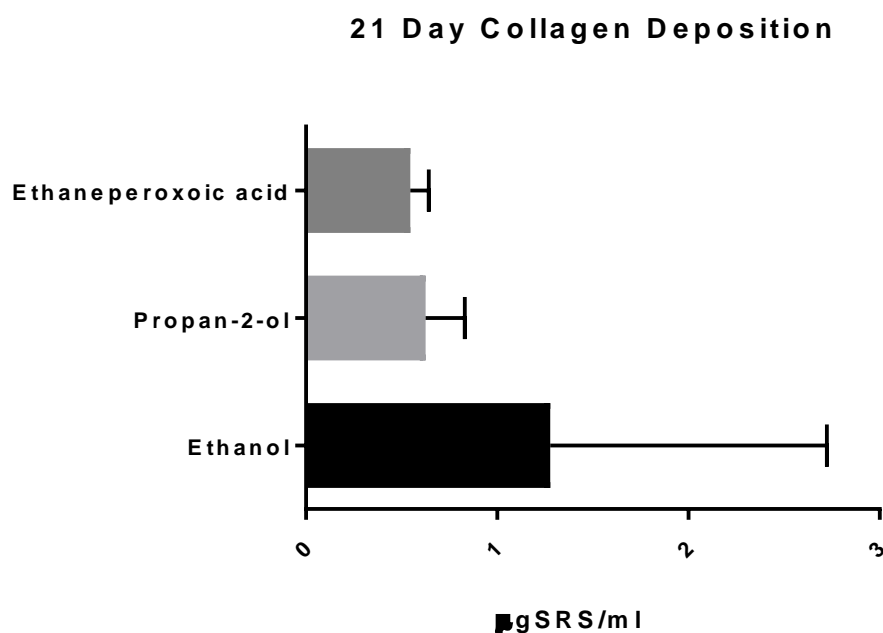


Figure 5.45. MG-63 21-day cellular matrix deposition comparison for sterilisation methods for 3DP items to be used for *in vitro* testing. 3D-Printed PLA discs were chemically sterilised in 2ml of a 70% ethanol solution for 24h, 5% ethaneperoxoic acid for 30 minutes, or a 70% propan-2-ol solution for 15 minutes. Triplicate samples were measured in one biological repeat ($n = 3$). No significant differences were found ($p < 0.05$) through ANOVA. Error bars denote standard deviation.

5.6.2. INITIAL MG-63 CELL VIABILITY STUDY

The different versions of the polymer and its composites were further tested for biocompatibility through the cell-viability experiment described in **Section 4.5.3**. Results for a 24-hour cell-attachment test and subsequent 21-day

viability test for samples incubated in EM are shown in **Figure 5.31** and **Figure 5.32**. The cell attachment data only showed significant differences between the 20%HA and 5%HA composites, with the latter performing better ($p < 0.05$).

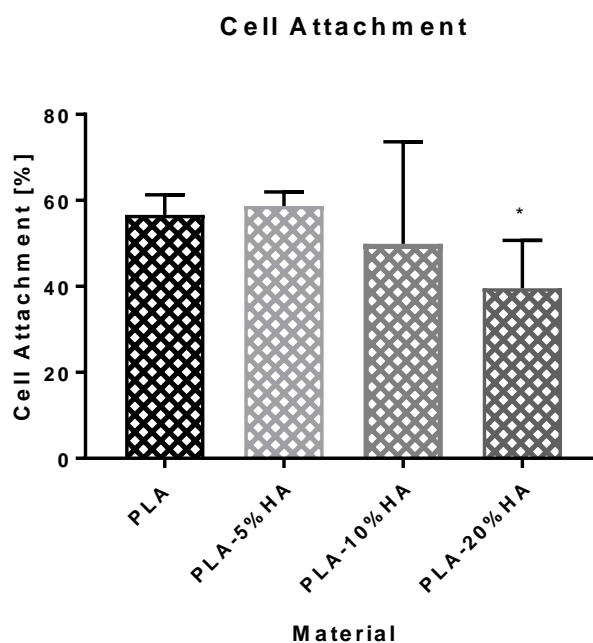


Figure 5.46. MG-63 cell attachment comparison between 3D-Printed composites. 3D-Printed PLA and PLA-HA composite discs seeded with 5000 MG-63 cells, incubated at 37 °C in EM and monitored through 21 days via RRA assays. Normalised fluorescence measurements were compared to standard curve data to generate approximated cell-counts. Triplicate samples were measured in two biological repeats ($n = 6$). Error bars denote standard deviation. Stars denote significant differences with respect to PLA-5%HA ($p < 0.05$) as found through ANOVA.

In contrast, the viability study showed significant differences ($p < 0.05$) at day 7 between the reference PLA and the 10%HA composite versions, with the composite performing better. On this same day, the 5%HA and 10%HA composites were higher than TCP on cell-counts. Similarly, on day 14 PLA showed significantly higher counts better than TCP ($p < 0.05$). By day 21, the only results with significant differences between them were those between TCP and the 5% composite, with the composite performing better ($p < 0.05$).

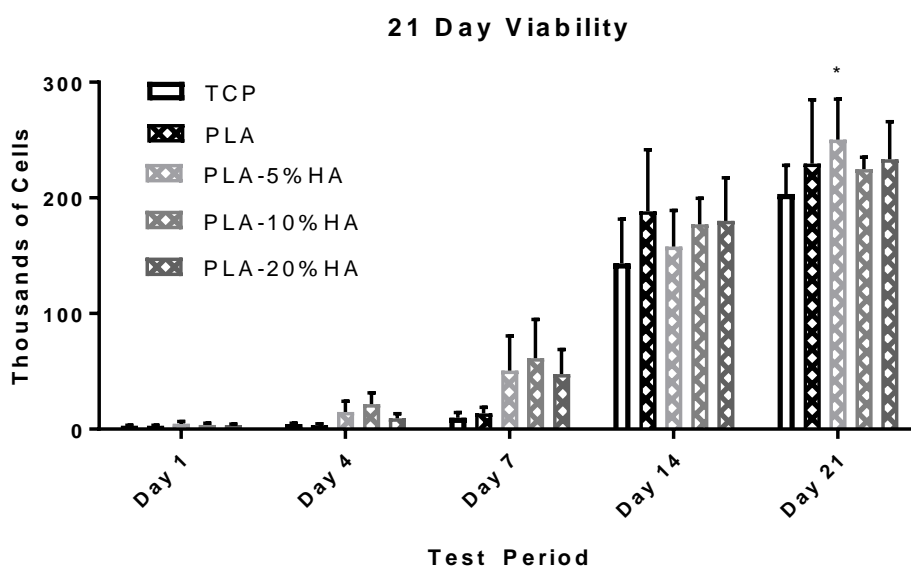


Figure 5.47. MG-63 cell viability comparison between 3D-Printed composites. 3D-Printed PLA and PLA-HA composite discs. Normalised fluorescence measurements were compared to standard curve data to generate approximated cell-counts. Triplicate samples were measured in two biological repeats ($n = 6$). Error bars denote standard deviation. Stars denote significant differences ($p < 0.05$) with respect to TCP.

Results for cellular matrix deposition are shown below in **Figure 5.33**. As with the sterilisation methods comparison described in **Section 5.5.1**, calcium deposition was too low to be measured through ARS assays for these samples. Collagen deposition measured through SRS was only found to

present statistical differences between the 5%HA and the 10%HA composites, favouring the latter ($p < 0.05$).

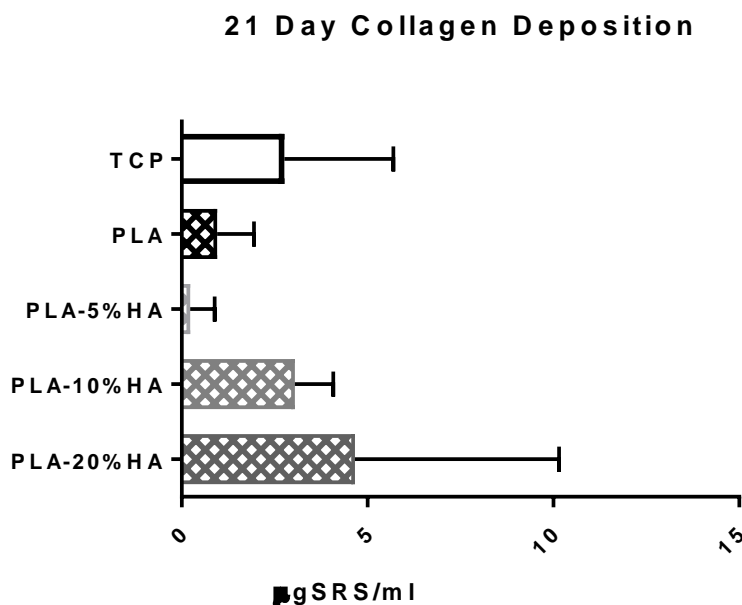


Figure 5.48. MG-63 21-day collagen deposition comparison comparison between 3D-Printed composites. 3D-Printed PLA discs. Normalised fluorescence measurements were compared to standard curve data for SRS to extrapolate collagen-bound stain. Triplicate samples were measured in two biological repeats ($n = 6$). No significant differences were found ($p < 0.05$) through one-way-ANOVA. Error bars denote standard deviation.

5.6.3. MG-63 CELL VIABILITY STUDY IN SM

Given the results observed in the initial viability studies with MG-63 cells, it was deemed necessary to run repeats of these using supplemented medium (SM) in order to stimulate deposition of calcium and collagen as extracellular matrix components. The objective was to establish if the HA in the composites would stimulate mineralisation and osteoblast differentiation given the appropriated environment – which EM alone might not provide. Annealed sample discs were added to this experimental setup to rule out potential effects

of heat treatment and/or crystallinity on the material. Results are shown in **Figure 5.34** for cell attachment, and **Figure 5.35** 21-day cell viability.

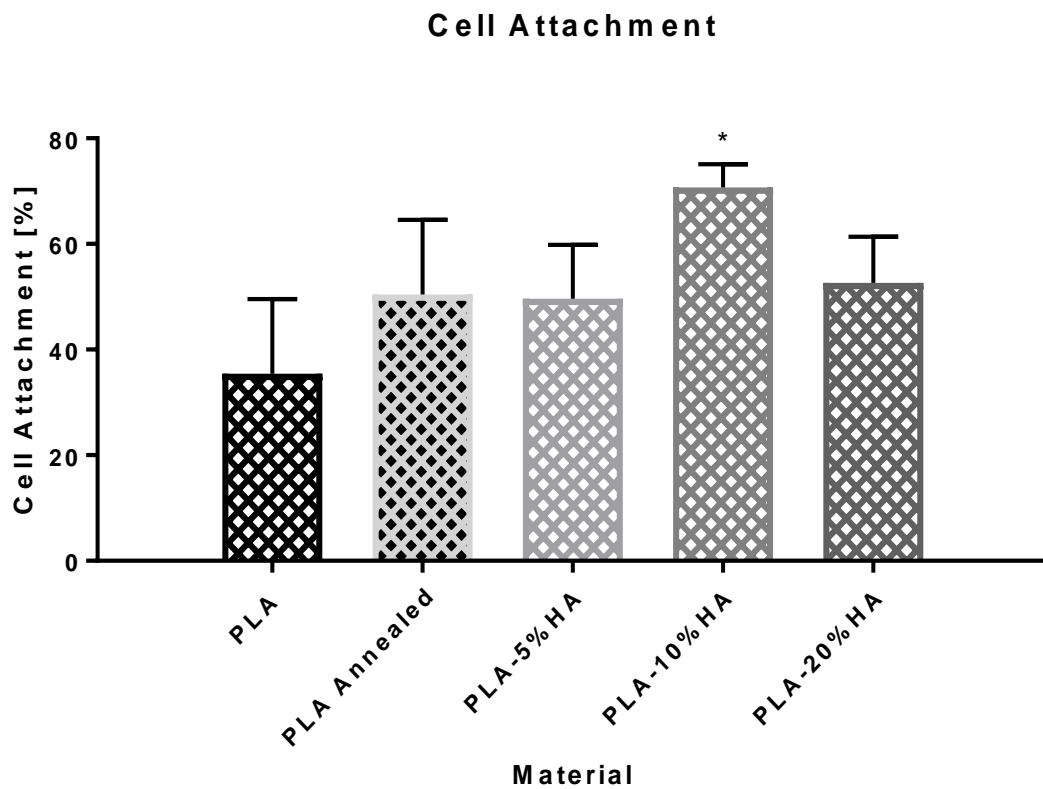


Figure 5.49. MG-63 cell attachment comparison between 3D-Printed composites in SM. D-Printed PLA and PLA-HA composite discs. Cell attachment was then calculated as the percentage between the cells in the sample and the original seeded population. Triplicate samples were measured in two biological repeats ($n = 6$). Error bars denote standard deviation. Stars denote significant differences ($p < 0.05$) with respect to PLA..

Only the 10% composite showed higher cell attachment than the reference PLA, while also displaying better results than the other two composites ($p < 0.05$). Significant differences in viability ($p < 0.05$) were found on day 14 between PLA and the 10% and the 20% composites, with these composites displaying a larger cell population. On day 21 there were significant differences between TCP and every version of the sample discs, with the sample discs supporting higher cell counts. At this final time point, all versions of the material performed with no significant difference from each other.

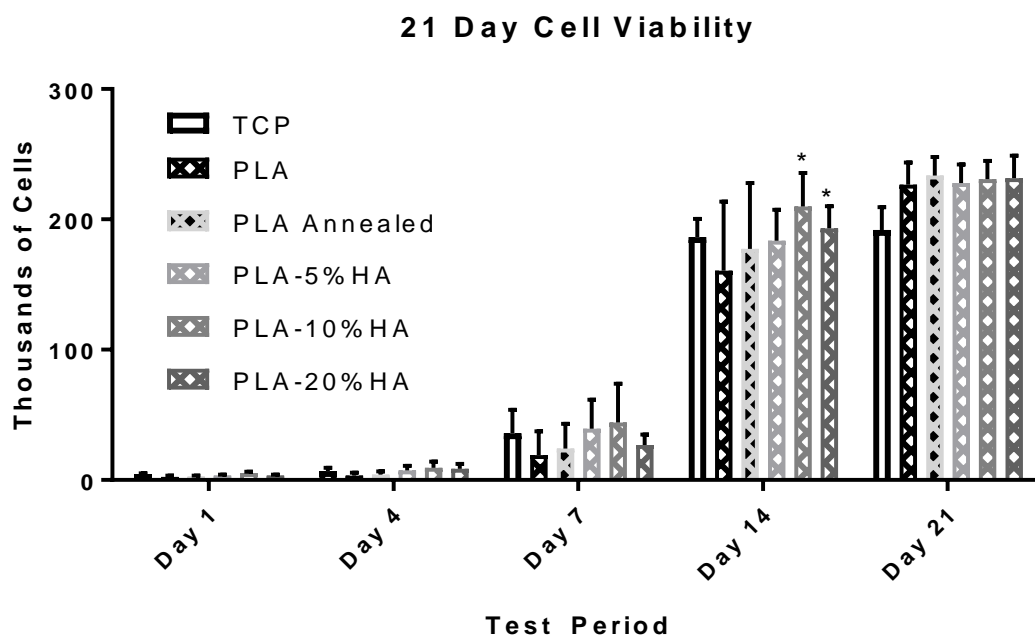


Figure 5.50. MG-63 cell viability comparison between 3D-Printed composites in SM. 3D-Printed PLA, annealed 3D-Printed PLA, and PLA-HA composite discs. Normalised fluorescence measurements were compared to standard curve data to generate approximated cell-counts. Triplicate samples were measured in two biological repeats ($n = 6$). Error bars denote standard deviation. Stars denote significant differences ($p < 0.05$) with respect to PLA.

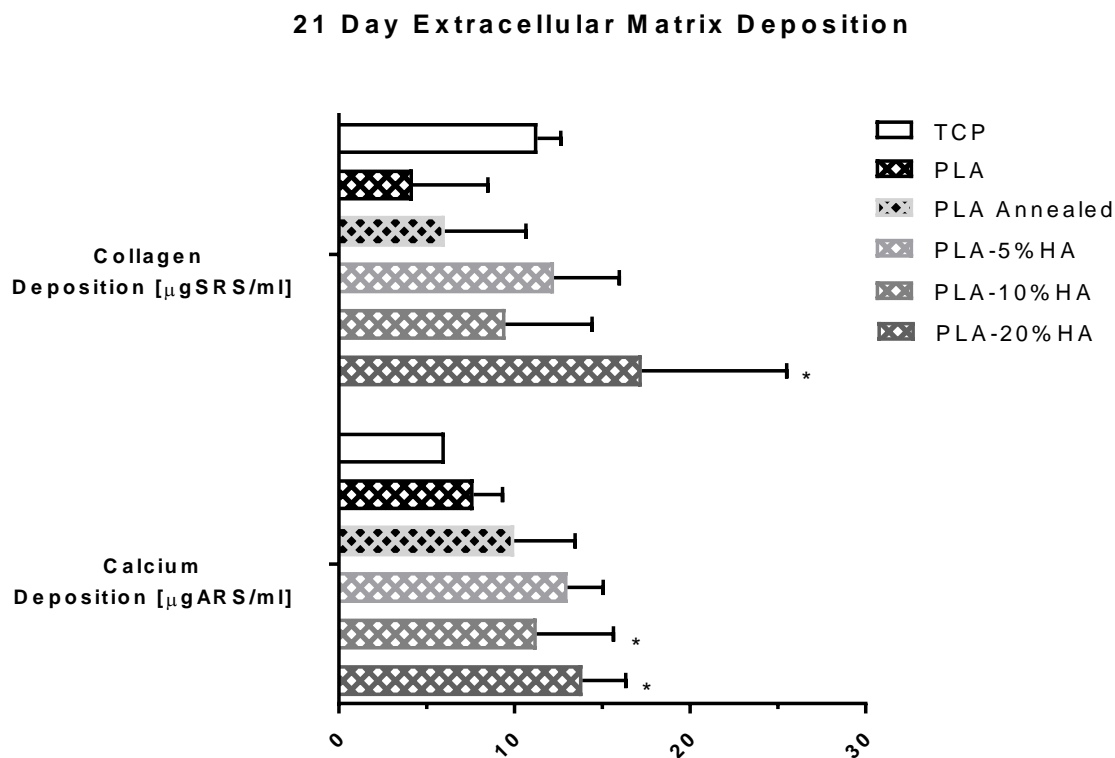


Figure 5.51. MG-63 21-day extracellular matrix deposition comparison between 3D-Printed composites in SM. 3D-Printed PLA and PLA-HA composite discs. Normalised absorbance measurements were compared to standard curve data for SRS to extrapolate calcium and collagen-bound stain concentrations respectively. Triplicate samples were measured in two biological repeats ($n = 6$). Stars denote significant differences with respect to PLA ($p < 0.05$). Error bars denote standard deviation.

The higher concentrations of HA in the composites yielded significantly higher extracellular matrix deposition and mineralisation ($p < 0.05$). Collagen deposition was significantly higher than PLA alone on the 20%HA composite, while calcium was so for both the 10%HA and 20%HA versions – with no statistical difference amongst both composites.

5.6.4. EFFECTS OF OSTEOGENIC SUPPLEMENTS IN MG-63 CULTURE IN PLA AND PLA-HA COMPOSITES

Since the only difference between the EM and SM experiments described in this section was the addition of ascorbic acid and β -glycerophosphate to the culture medium, their results can be compared to determine if the supplements have any effect on cell response. **Figure 5.37** summarises cell attachment data comparison between the two culture-media. PLA showed a significantly less cell attachment ($p < 0.05$) when cultured in SM, while the 10%HA composite experienced higher cell attachment with respect to un-supplemented EM.

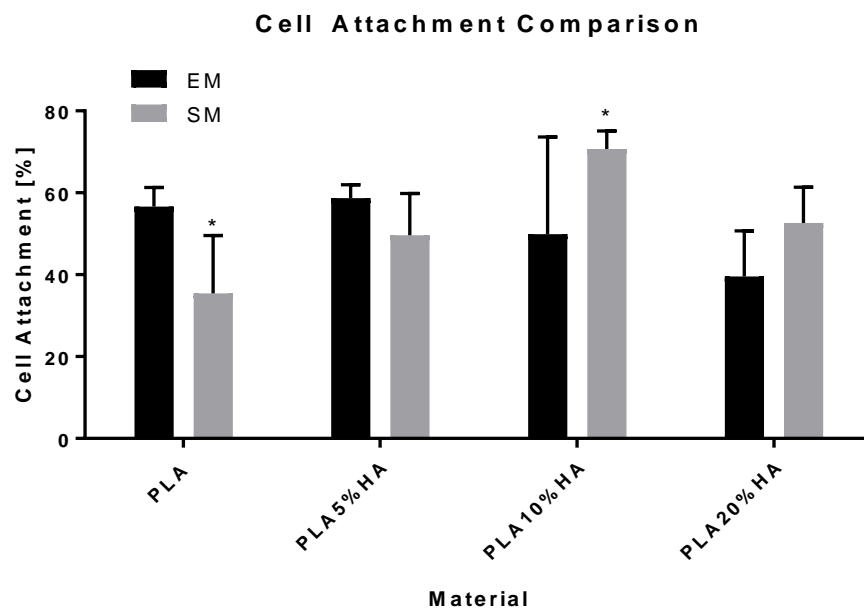


Figure 5.52. MG-63 cell attachment comparison between 3D-Printed composites in EM and SM. 3D-Printed PLA and PLA-HA composite discs. Normalised absorbance measurements were compared to standard curve data to generate approximated cell-counts, which were then compared with counts on each sample's incubation well. Error bars denote standard deviation. Stars denote significant differences ($p < 0.05$) with respect to EM measurements for each material. Triplicate samples were measured in two biological repeats for each dataset depicted ($n = 6$).

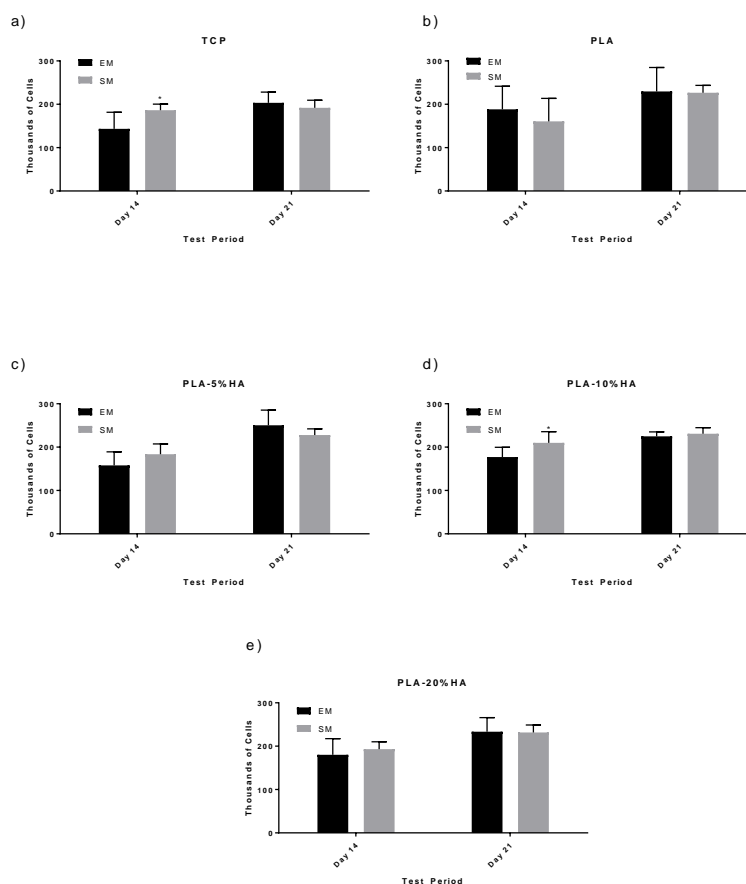


Figure 5.53. MG-63 cell viability comparison between 3D-Printed composites in EM and SM. 3D-Printed PLA, annealed 3D-Printed PLA, and PLA-HA composite. Error bars denote standard deviation. Stars denote significant differences ($p < 0.05$) with respect to EM measurements. Data for days 1, 4 and 7 were omitted for clarity since no relevant variations could be observed. Triplicate samples were measured in two biological repeats for each dataset depicted ($n = 6$).

Cell viability was not affected for the most part (**Figure 5.38**). Significant differences ($p < 0.05$) appeared in day 14 for TCP (**Figure 5.38a**) and for the 10%HA composite (**Figure 5.38d**), with the samples in supplemented medium measuring higher than those of the un-supplemented one. This apparent effect did not affect the final outcome of the experiment, with all 21 day cell counts resulting in statistically equivalent distributions.

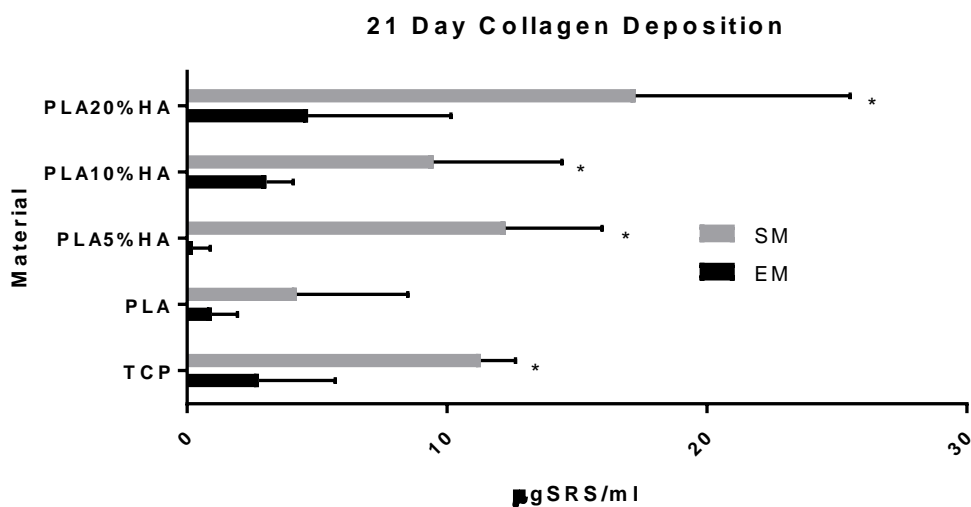


Figure 5.54. MG-63 21-day collagen deposition comparison comparison between 3D-Printed composites in EM and SM. 3D-Printed PLA and PLA-HA composite discs. Normalised absorbance measurements were compared to standard curve data for SRS to extrapolate collagen-bound stain concentrations. Stars denote significant differences with respect to EM ($p < 0.05$). Error bars denote standard deviation. Triplicate samples were measured in two biological repeats for each dataset depicted ($n = 6$).

Collagen deposition was significantly enhanced in all materials, except for PLA (Figure 5.39). The reference pure PLA showed no statistical difference when cultured in SM as compared to EM ($p < 0.05$). Conversely, all materials – including PLA – exhibited measurable levels of SRS-bound calcium when cultured in SM (Figure 5.36), while EM yielded amounts too small to quantify in this experimental setup.

5.6.5. *IN VITRO* CELL CULTURE IN THREE-DIMENSIONAL 3D-PRINTED STRUCTURES

Higher HA concentration did appear to play a role in better cellular responses according to results shown in Section 5.5.3. However, the 20%HA composite proved to be too problematic to both process into filament and to 3D-print.

Results listed below therefore correspond to experiments performed on the 5%HA and 10%HA composites as compared to pure PLA – all on SM. **Figure 5.40** shows results for cell attachment on these 3D models. The 10%HA composite retained significantly fewer cells than pure PLA, although no significant differences were found between the 10%HA and the 5%HA composites ($p < 0.05$).

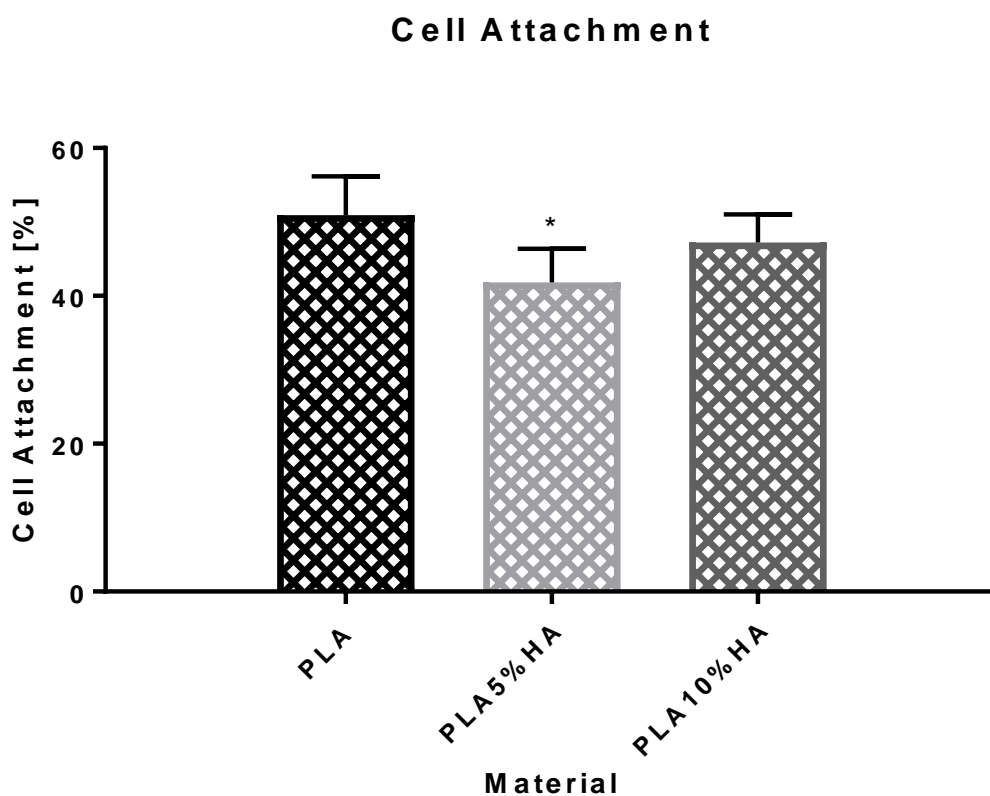


Figure 5.55. MG-63 cell attachment on 3D-Printed Mesh Models on PLA-HA composites in SM. 3D-Printed PLA and PLA-HA composite 3D Mesh Models. Normalised absorbance measurements were compared to standard curve data to generate approximated cell-counts, which were then compared with counts on each sample's incubation wells. Error bars denote standard deviation. Stars denote significant differences ($p < 0.05$) with respect to PLA. Triplicate samples were measured in two biological repeats ($n = 6$).BB1

Results for cell viability are depicted in **Figure 5.41**, showing cell growth on the structure's surface, but no significant differences between any of the materials tested throughout the experiment ($p < 0.05$). Cellular matrix deposition was measurable as both collagen and calcium, with the composites performing significantly better ($p < 0.05$) than PLA alone (**Figure 5.42**). Within these measurements, there were no significant differences between the two versions of the composite.

Though the results between experiments ran on the disc samples cannot be directly compared to those of the 3D mesh models, production of extracellular matrix components can be normalised to the number of cells in each sample. These data can then be directly compared: this analysis is summarised by **Figure 5.43**.

Collagen deposition per amount of cells in a sample did not exhibit significant differences between the disc and the 3D mesh models ($p < 0.05$) for any of the materials tested. In contrast, the 3D mesh models in all materials were measured to have lower deposited calcium per thousand cells than disc samples ($p < 0.05$).

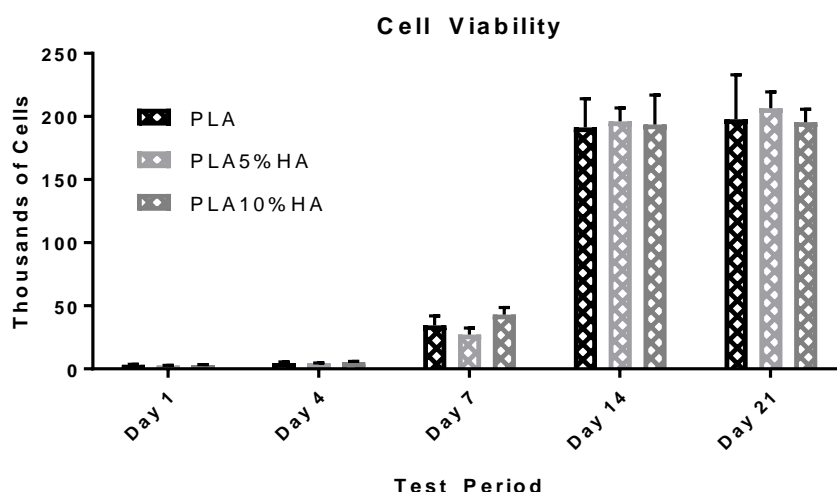


Figure 5.57. MG-63 cell viability on 3D-Printed Mesh Models on PLA-HA composites in SM. 3D-Printed PLA and PLA-HA composite 3D-mesh models. Normalised fluorescence measurements were compared to standard curve data to generate approximated cell-counts. Error bars denote standard deviation. Stars denote significant differences ($p < 0.05$) with respect to PLA. Triplicate samples were measured in two biological repeats ($n = 6$).

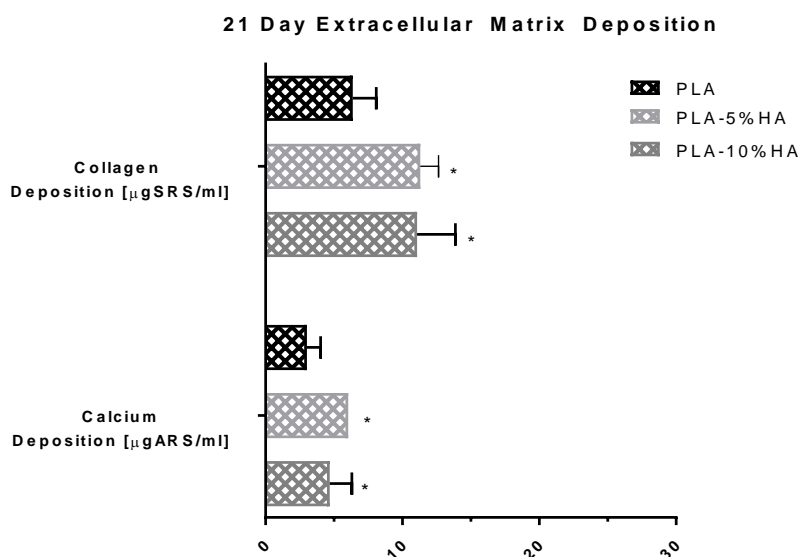
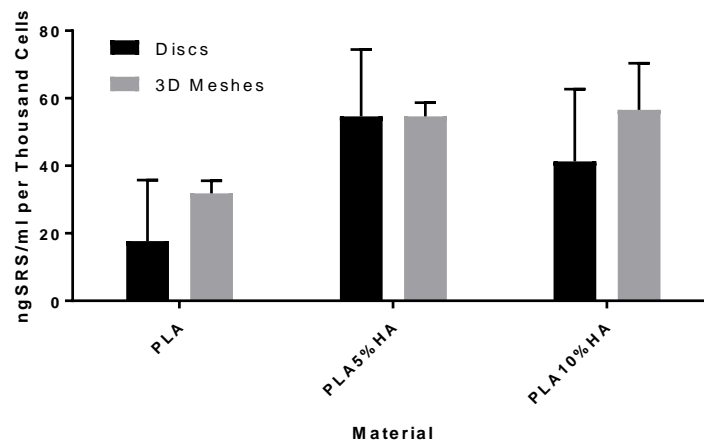


Figure 5.56. MG-63 21-day extracellular matrix deposition comparison between 3D-Printed composites in SM. 3D-Printed PLA and PLA-HA composite discs. Normalised absorbance measurements were compared to standard curve data for SRS to extrapolate calcium and collagen-bound stain concentrations respectively. Stars denote significant differences with respect to PLA ($p < 0.05$). Error bars denote standard deviation. Triplicate samples were measured in two biological repeats ($n = 6$).

a) **MG63 21 Day Normalised Collagen Deposition on PLA-HA Composites (n=6) Discs and 3D Mesh Models in Osteogenic Medium**



b) **MG63 21 Day Normalised Calcium Deposition on PLA-HA Composites (n=6) Discs and 3D Mesh Models in Osteogenic Medium**

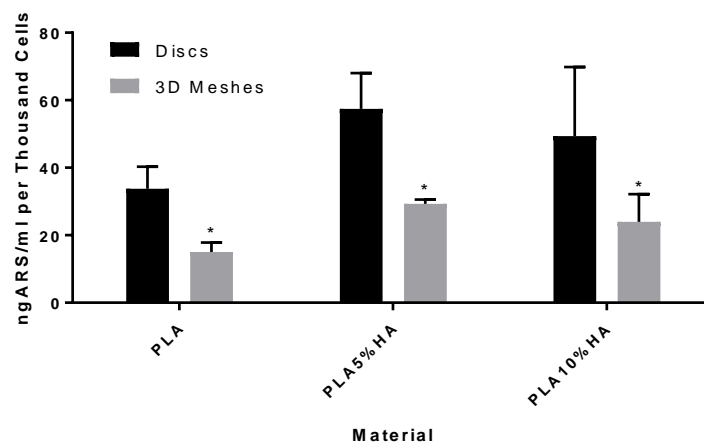


Figure 5.58. MG-63 21-day extracellular matrix deposition normalised to cell number; comparison between discs and 3D-Mesh models in SM. 3D-Printed PLA and PLA-HA composite discs. Normalised absorbance measurements were compared to standard curve data for SRS and ARS to extrapolate calcium and collagen-bound stain concentrations respectively, and were then compared to cell numbers to allow for direct comparison. Stars denote significant differences with respect to disc samples ($p = 0.05$). Error bars denote standard deviation. Triplicate samples were measured in two biological repeats (n = 6).

5.7. MATHEMATICAL MODELLING FOR POLYMER DEGRADATION

Accelerated degradation has been well studied in the literature as a means to extrapolate, through the Arrhenius relation, from short experiments – in the order of months – to the outcomes of degradation setups that can take years to complete [284,290,361,365–367] as per the *ISO-10993-13-2010* standard [328]. In contrast, the present section looks to establish a model to predict degradation data when varying the starting material properties at a set temperature.

5.8.1. MODELLING FOR MOLECULAR WEIGHT BEFORE MASS-LOSS

Taking in account the tendencies found for ADT mass-loss data for pure PLA (VB-PLA) and the PLA-10%HA composite, tipping points were calculated to be somewhere from 8.32 to 10.74 days for PLA, and around 2.65 days for the composite (though the regression proved ambiguous). The data that were clearly before mass loss (up to day 5 for PLA and day 3 for the composite)

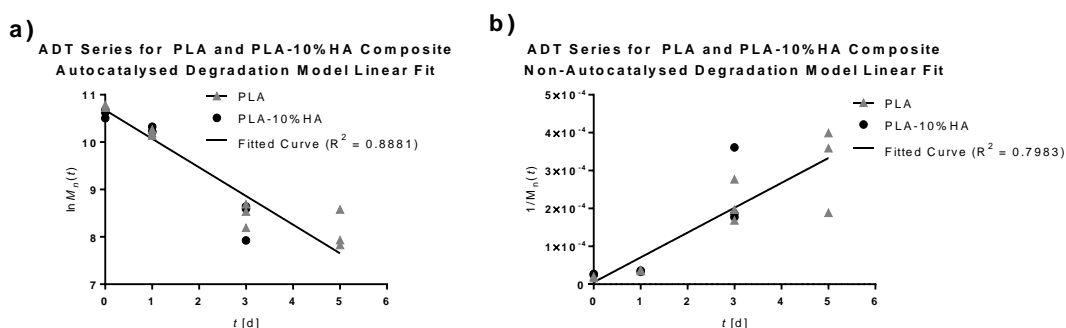


Figure 5.59. Linear fit for a) autocatalysed and b) non-autocatalysed degradation models. Points correspond to means with standard deviation bars. Common linear model for both data sets validated through extra-sum-of-squares F-test method at $p = 0.05$.

were evaluated as per the model in **Equation 4.15** to determine if the degradation process was autocatalysed, or non-autocatalysed as per **Equation 4.17**. The results for this analysis are shown in **Figure 5.59**. Both data sets could be fitted to the same curve in both models through comparison via extra-sum-of-squares F-test ($p < 0.05$). The autocatalysed model provided a better fit for the data ($R^2 = 0.8881$) than that of the non-autocatalysed model ($R^2 = 0.7983$).

Given the autocatalysed model, the parameters that best fit the pre-tipping-point degradation profile for both materials would be:

$$\ln M_n(t) = -0.6045t + 10.68; t \leq t_p \quad \text{Equation 5.1}$$

Such that:

$$M_n(t) = 43,477.55e^{-0.6045t}; t \leq t_p \quad \text{Equation 5.2}$$

If the data are normalised so that the initial M_n for each ADT experiment is 100% (thus constraining the value for M_{n0}), the parameters for the model are still valid through extra-sum-of-squares F-test ($p = 0.05$, $R^2 = 0.9092$), and it can be adjusted to find that:

$$M_{n\%}(t) = 100e^{-0.6320t}; t \leq t_p \quad \text{Equation 5.3}$$

Where $M_{n\%}$ is the remaining percentage of M_n with respect to the pre-degradation measured value. For verification of this model, data from the publication by Weir *et al.* [290] were analysed. The ADT setup of the present research was based upon those of said publication for 70 °C. This makes their

data as comparable as can be reasonably expected from a separate study. The data extracted from the publication are compiled in **Table 5.5**.

Using the parameters from **Equation 5.3** ($k_1 = 0.6320$, $M_{n0} = 100$) non-linear regression was performed on the normalised Mn data of **Table 5.5**. The results of this computation are shown in **Figure 5.60**. This model (**Equation 5.3**) was capable of reasonably fitting the data from the other study ($R^2 = 0.8324$), which had distant starting conditions (namely almost quadruple the Mn of the samples in the present study, reported at 166,000 g/mol, and a higher starting crystallinity of 57.5%). Incidentally, the method used for linear regression in this project calculated the data from Weir *et al.* to yield a k_1 of 0.2091 ($R^2 = 0.9494$), while their study itself reported a rate constant of 0.2155 ($R^2 = 0.95$) for their autocatalysed model [290].

ADT Series for data from Weir et al. - Molecular Weight (Mn%) Change

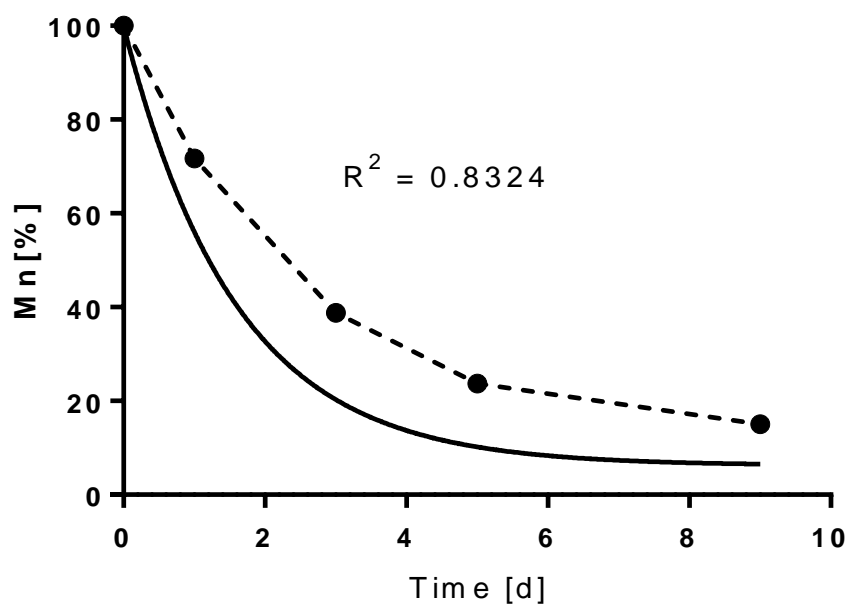


Figure 5.60. Percent Changes in Number Average Molecular Weight (Mn) for data extracted from the work of Weir *et al.* throughout ADT. Points correspond to averages joined by the dashed line. The solid line depicts a fitted curve from the parameters modelled in this section from the present research's data. Correlation coefficient refers to a non-linear fit to such an exponential decay model.

Table 5.5 ADT data from Weir *et al.* [290]

Period	Mn	Mn	Crystallinity
[days]	[g/mol]	[%]	[%]
0	166,000	100.00	57.5
1	119,000	71.69	59.9

3	64,450	39.83	57.5
5	39,300	23.67	77.1
9	24,900	15.00	85.7
14	29,200	17.59	76.2
18	13,750	8.28	88.9
21	11,700	7.04	85.1
23	9,090	5.48	92.2

Data presented as averages as provided by the source

5.8.2. MODELLING FOR MOLECULAR WEIGHT AFTER MASS-LOSS

The overall behaviour of the M_n measurements throughout the all sampling points in this study is plotted in **Figure 5.61**. Both the reference pure PLA and the PLA-10%HA composite displayed an exponential decay profile. This trend was expected and supported by good correlation ($R^2 = 0.9731$ for PLA, $R^2 = 0.9735$ for PLA-10%HA, and $R^2 = 0.9895$ for Weir *et al.* data) found via non-linear regression for each data set. Furthermore, extra-sum-of-squares F-test suggests the data sets' trends cannot be rooted to the same mathematical process ($p = 0.05$).

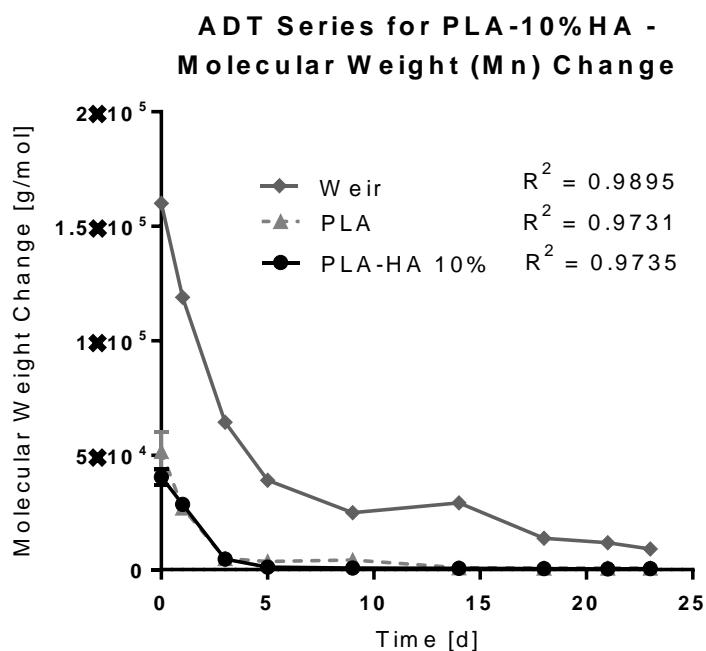


Figure 5.61. Percent Changes in Number Average Molecular Weight (M_n) for pure PLA and the PLA-10%HA composite throughout ADT. Points correspond to averages joined by the indicated lines, with standard deviation error bars. Correlation coefficients refer to a non-linear fit to such an exponential decay model, independent for each data set.

A normalisation of the M_n data to compensate for the disparity in initial values is shown in **Figure 5.62**, including the dataset from Weir *et al.* The individual normalised datasets were found to be best fit to different exponential decay parameters through extra-sum-of-squares F-test ($p < 0.05$), with correlation coefficients of 0.9869 for PLA, 0.9762 for the PLA-10%HA composite, and 0.9900 for the degradation experiments by Weir *et al.* Additionally, a potential shared model that accommodates the three datasets up to day 23 with reasonable fidelity was also found as follows:

$$M_{n\%}(t) = 97.456e^{-0.5696t} + 2.544 \quad \text{Equation 5.4}$$

This model fits the M_n normalised data with correlation coefficients of 0.9754 for PLA, 0.9625 for the PLA-10%HA composite, and 0.8607 for the by Weir *et al* dataset.

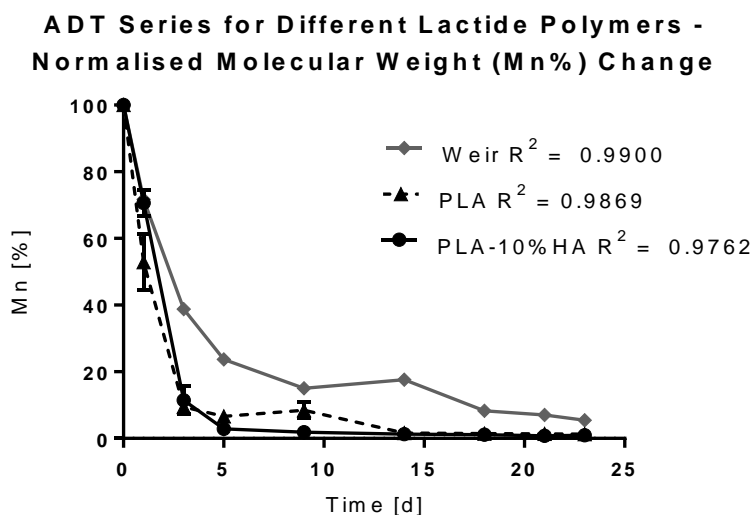


Figure 5.62. Percent Changes in Number Average Molecular Weight (M_n) for pure PLA, the PLA-10%HA composite, and data from Weir *et al.* throughout ADT. Points correspond to averages joined by the indicated lines, with standard deviation error bars. Correlation coefficients refer to a non-linear fit to an exponential decay model, independent for each data set.

Since degradation rate is strongly linked to the amount of polymer present, its surface area, and its contact with the degradation medium, a further attempt was made at generalisation of a degradation model. To account for all these time-dependent factors, normalisation with respect to the half-life of each dataset's Mn_0 was conducted. The half-life (λ) figures were derived from the non-linear regression analysis shown in **Figure 5.61**, and the time-axis data were represented as fractions of their respective dataset's λ (0.9476 days for PLA, 1.258 days for the PLA-10%HA composite, and 1.974 days for the data from Weir *et al.*). Non-linear regression was then performed constrained to a

common rate constant for the PLA and PLA-10%HA data sets. For testing of the model, data for the Weir *et al.* set was then fitted through non-linear regression to a function constrained to this common rate constant. The resulting curves are plotted on **Figure 5.63**.

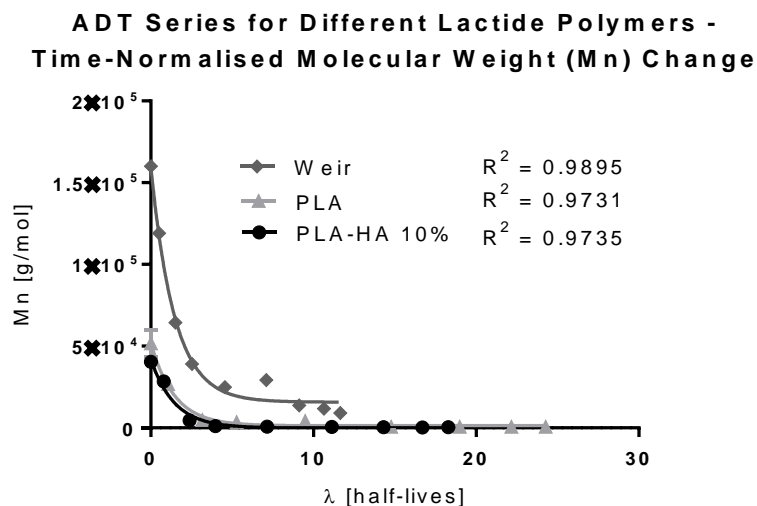


Figure 5.63. Changes in Number Average Molecular Weight (Mn) for pure PLA, the PLA-10%HA composite, and data from Weir *et al.* throughout time-normalised ADT. Points correspond to averages joined by the indicated lines. Correlation coefficients refer to a non-linear fit to an exponential decay model, independent for each data set.

Graphically, this reference frame transformation aligns the half-lives of the datasets over the horizontal axis, scaling the graph appropriately in this same direction. The resulting model is represented as:

$$M_n(\lambda) = (M_{n0} - \Psi)e^{-\kappa_{70}\lambda} + \Psi \quad \text{Equation 5.5}$$

Where λ is the scaled time on the normalised reference frame, Ψ is the vertical offset value to which the function approaches asymptotically at infinite time, and κ_{70} is the proposed common rate constant for ADT at 70 °C (calculated to

be 0.6923 from data in this study). This model implies that for the ADT- $Mn(t)$ values of a PLA sample, the time-normalised $Mn(\lambda)$ curve will be a vertically-offset exponential decay trend, a function of λ , and dependent on Mn_0 , and Ψ . Since the rate constant for this model is dependent on the half-life of the real-time reference frame – which itself is a function of ADT temperature as per the Arrhenius relationship [290,361,365–367] – it follows that the common rate constant proposed for this model should be only valid for PLA undergoing ADT at 70 °C (and that a common rate constant could be determined for each given ADT temperature).

Since Mn_0 is determined experimentally, only the parameter Ψ remains to be defined to be utilised in the proposed model. Since calculation of λ is also necessary for time-normalisation, one of the additional $Mn(t)$ data points can be used to compute Ψ such that:

$$\Psi = \frac{M_{n0}e^{-\kappa_{70}\lambda_a} - M_n(\lambda_a)}{M_{n0} - 1}; \quad M_{n0} \neq 1, M_{n0}(M_n(\lambda_a) - M_{n0})(M_n(\lambda_a) - M_{n0}e^{-\kappa_{70}\lambda_a}) \neq 0$$

Equation 5.6

Where λ_a is a time point with a known value for Mn (different to Mn_0). If a time constant is known for a given data set (taking in account data beyond t_0), the expression can be rewritten as:

$$\Psi = \frac{M_{n0}e^{-\kappa_{70}\frac{t_a}{\lambda}} - M_n\left(\frac{t_a}{\lambda}\right)}{M_{n0} - 1}; \quad M_{n0} \neq 1, M_{n0}\left(M_n\left(\frac{t_a}{\lambda}\right) - M_{n0}\right)\left(M_n\left(\frac{t_a}{\lambda}\right) - M_{n0}e^{-\kappa_{70}\frac{t_a}{\lambda}}\right) \neq 0$$

Equation 5.7

Where t_a is the time at which the known Mn value lies.

Furthermore, this model can be simplified by making some assumptions about the boundary conditions of the experiment. Since the final water-soluble oligomers predominate by the end of ADT, it can be safely assumed that Mn values measured by the final stages of any long enough experiment will be at least several orders of magnitude below that of Mn_0 . Being that the case, their ratio becomes very close to 0. Taking a similar approach to the model in **Equation 5.4**, normalised Mn values as a function of half-life normalised time yield the plots depicted in **Figure 5.64**. In this case, the non-linear regression can be constrained to the following parameters:

$$M_{n\%}(\lambda) = 100e^{-0.6686\lambda} \quad \text{Equation 5.8}$$

Where the time constant was determined to be 0.6686 from the data of PLA and PLA-10%HA. Additionally, Weir *et al.* data was normalised and fitted to

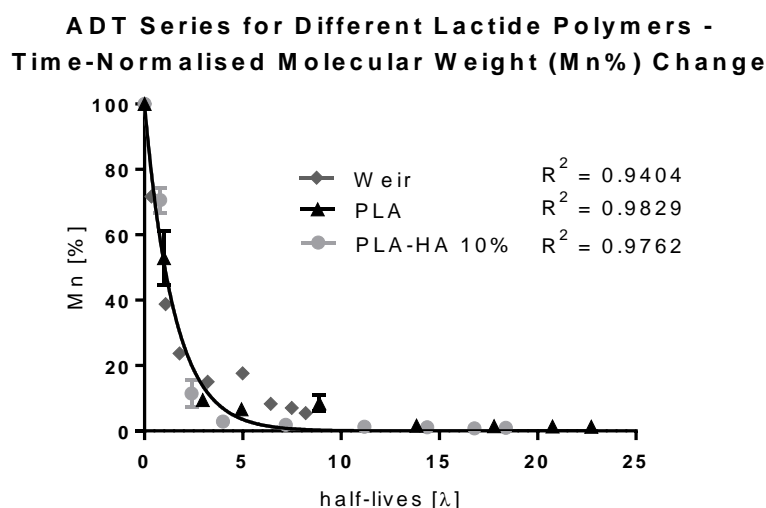


Figure 5.64. Changes in Normalised Number Average Molecular Weight (Mn%) for pure PLA, the PLA-10%HA composite, and data from Weir *et al.* throughout time-normalised ADT. Points correspond to averages joined by the indicated lines. Correlation coefficients refer to a non-linear fit to a common exponential decay model as described in this section.

this model through non-linear regression, with the resulting correlation also shown in **Figure 5.64**. Given a known λ , the model becomes:

$$M_{n\%}(\lambda) = 100e^{-0.6686\frac{t}{\lambda}} \quad \text{Equation 5.9}$$

This model adjusts well for the two datasets from the present study, and accurately represented the independent data from Weir *et al* [290].

Finally, **Figure 5.65**, shows a probable relationship found between initial M_n and the experimental degradation time constant τ of PLA, PLA-10%HA, and the Weir *et al.* dataset.

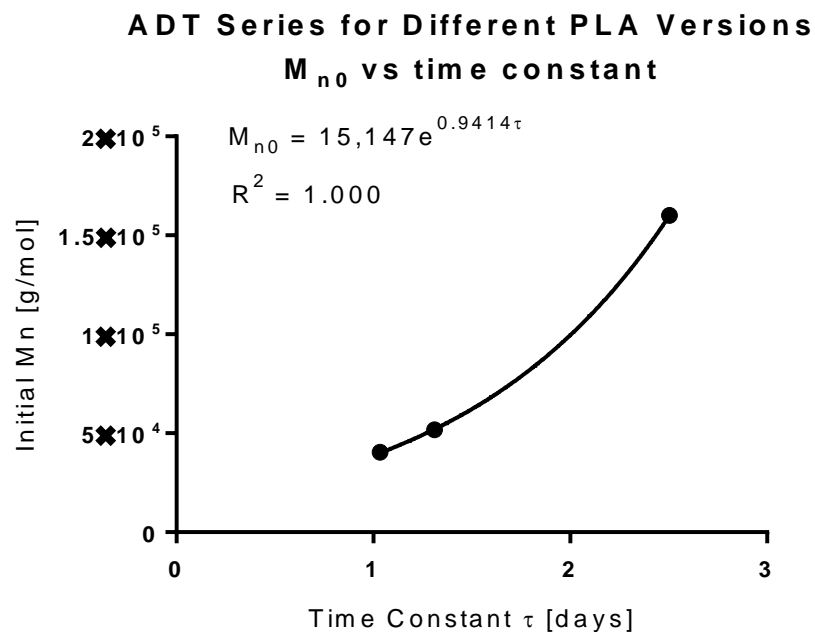


Figure 5.65. Initial Number Average Molecular Weight (M_n) for pure PLA, the PLA-10%HA composite, and the Weir. *et al* data set plotted against their respective non-linear regression time constants. Points correspond to averages. Correlation coefficients refer to a non-linear fit to such an exponential growth curve.

6. DISCUSSION

6.1. DETERMINING THE PRINTER'S RESOLUTION LIMIT AND PRINTING ACCURACY

Using the tolerance model described in **Section 4.1**, a limit on the feature resolution of the printer could be found. On the model, each cylinder (or half-cylinder) is progressively smaller by a fixed amount, proportional to the one at the base. Downscaling of these models helps quantify the consistency on printer performance at various sizes under the same printing settings and conditions. Upscaling, in contrast, makes other phenomena – such as material warping, shrinking, inadequate extrusion, or low bed adhesion – more evident. Measurements on radii were made along the *X* and *Y* printer axes independently, and were denoted as such with a subindex. For the present work, for the design and calculations are listed in **Table 5.2** and **Table 5.3**, and discussed theoretically in **Section 6.1**. Calculations take account the average reported value of 1.27 g/cm³ for PLA density that is widely found in the literature [137,251,293,334] and reported by manufacturers [318,331], who describe a crystallinity-dependent range from 1.25 to 1.29 g/cm³.

Considering that most alveolar defects should fit within a volume of about 11x15x22 mm [343,344] (based on adult average anatomy), variations as reported on section **5.1** become significant as they limit the resolution of details to be accomplished using this equipment. Especially along the *Z* axis, where accuracy varied from 0.56% up to 18.18% from the programmed values, and reproducibility between resulting dimensions varied on average ± 0.23 mm.

This includes modular geometries to control macroscopic porosity and/or void content [108]. Not only cellular attachment is more readily achieved on the surfaces of scaffolds rather than in their inner geometries, but the application of functionalisation coatings and treatments is also mostly confined to the outer surfaces of any given shape [273,368,369].

Semicrystalline PLA density of 1.27 g/cm^3 [137,251,293,318,331,334] should be accounted for as an average when determining the porosity of apparently solid FFF items, as the process is expected to deteriorate the crystallinity and molecular weight of the inputted filament [49] given that it is essentially a high-temperature extrusion technique [297]. Even at the theoretical setting of 95% material fill on the printer's software configuration, the observed density of the prints is scale-dependent and below even amorphous PLA values [318,331], with a range from roughly 1.14 g/cm^3 on the smallest end of the printed range, from where it gradually drops as the scale increases, to up to 0.63 g/cm^3 , as observed in **Figure 5.1**. Parts larger than 7 cm^3 consistently approached a 40% porosity. In terms of the present application, that means that predictable and stable porosity values could only be expected on large implants — such as those found in orthopaedic reconstruction. This could be due to the larger items require larger layers which are allowed to cool for longer, leading to weaker bonding with the subsequent layer and allowing for air pockets to form between them.

Given a small enough geometry (close to the resolution limit of the printer: 2 mm in this case), the fill pattern is not considered necessary by the software since both edges of the outline (normally just below 1 mm in thickness) will be

close enough to fuse, thus producing a surface by themselves. Any additional filling would pile up beyond the intended vertical limit of a given layer. This can account for the near-solid-PLA density on smaller printed geometries where outline material makes up for most of the structure, while the fill pattern contributes to more void pockets being included into the volume as the scale increases. It follows that the apparent density of the finished item is progressively lowered, but plateaus around 40% porosity (0.76 g/cm^3) when the fill material predominates evenly distributed throughout the geometry. This would explain, along with the increase in linear-dimension reproducibility, why errors in expected volume of a FFF structure diminish and stabilise in larger scale measurements (**Section 5.1**)

These sharp differences between material characteristics must play a significant factor on the design of any device on the scales intended by this project. A maxillary implant would be around the dimensions stated in **Section 5.4**, which would, in turn, place it on the plateaued region for both porosity and dimensional values if made completely solid. As well, small details and features, such as internal geometries, are bound to be subject to lower reproducibility – though also reduced porosity, which would impede water, cell and extracellular matrix penetration [8]. The importance of determining these errors and variations becomes evident when considering macroscopic porosity (void content due to internal geometries) has been pointed out as a main concern on scaffold design, listing optimal diameter values from 0.4 to 2 mm for interconnected pores (internal channel systems) to allow vascularisation and bone formation into a scaffold [6,37,369], with a lower limit on 150 μm to accommodate any cellular migration at all [273].

6.2. ACCELERATED DEGRADATION OF FFF PLA

6.2.1. MASS CHANGE

Water degrades long polymer chains by attacking ester bonds in between the monomers [2,294], preferably on the amorphous phase of the network, and first eroding outermost zones of a sample. It must be taken in account that PLA oligomers are inherently hydrophobic, but lactic acid is hydrophilic by itself [137,366]. This is why degradation in aqueous medium proceeds relatively slowly: polymer fragments must reach a critical size before hydrophilic moieties of the molecules overpower their hydrophobic chains, rendering them water-soluble.

ADT test results described in section 5.2 found the onset of mass loss at 70 °C to be between the 9th and 14th day, which is similar to the 10 day value in the study by Weir *et al.*, from which the experimental setup for the present project was derived [290]. Given that crystallinity and molecular weight of VB-PLA differ from that on the base ADT study, it would seem that mass loss was independent of these values, or has a very small effect in its onset. ADT studies in the literature have placed the onset of mass-loss at ~ 60 days at 50 °C, and at about 10 days at 70 °C for PLA with a M_w around 400 kg/mol and a starting crystallinity of 47-57% [290]. Others have reported much faster rates, similar to the one depicted for BFB-PLA, when degrading mostly amorphous

PLA, with an initial crystallinity of around 9% – though with no estimate for M_w reported, with crystallinity reaching about 59% after 6 days in ADT at 75 °C [361]. This further strengthens the hypothesis of acetone's degradation mechanism being comparable to that of water (or PBS), with susceptibility of lactides – and other ester-linked polymers – to degradation being strongly tied to crystallinity.

Apart from changes to the crystalline content proportion of the polymer during FFF, another factor at play affecting mass-loss on the samples could be the aforementioned fill pattern of the printer. This pattern is implemented as part the process's emphasis on recreating the outer surface of the models reproduced. For each layer on the layout of the printing code generated by the software, the material in the outline is laid out first, then joined in by a repeating pattern that turns that outline into an actual surface that can support the layer above it, while fusing it to the previous one (**Figure 6.1**) [370]. This workflow lowers the apparent density of the sample, increasing its surface area available for medium infiltration and degradation.

6.2.2. CRYSTALLINITY

The results showcased in **Figure 5.3** suggested that FFF readily lowers the crystallinity of the inputted filament. Similar results have been reported upon extrusion of PLLA [49]. The ~10% crystallinity difference between both of the starting materials was already big enough to be evident macroscopically: the VB-PLA filament is prone to breaking when being loaded into the printer. Moreover, it will creep and fracture if left loaded with the printer idle overnight.

This could be explained by increased crystallinity, which has been reported to increase brittleness after processes applied to produce functional PLA [371]. Polymer-chain migration is another mechanism of weakening of the polymer matrix could happen during processing into FFF filaments and subsequent FFF. These migration occurrences will happen when the polymer is heated beyond its glass-transition temperature, and will add up and introduce molecular-scale voids all over the geometry. Within these voids, there is no material contributing to the mechanical integrity of the polymer matrix, concentrating stresses on surrounding zones [365], which then can evolve into crazes and cracks. It is thus worth pointing out that both polymers were found to be largely amorphous (~70-80% by weight), since the filament presentation benefits from a less brittle behaviour. These data can prove relevant when investigating in-house fabrication of FFF filaments, since achieving similar crystallinity will likely be desirable.

The agreed-upon explanation in the literature for the sudden rise in crystallinity (as that observed in **Figure 5.3**) considers that amorphous regions are affected first by the degrading medium [372]. Under these experimental conditions it can be assumed that most of the lost mass was lost from those amorphous regions, very likely near the surface of the specimen during the initial stages of degradation. In mass-loss data from **Section 5.2.1**, the first period mass-loss was already nearing 5%. Each sample for DTA included roughly equal amounts of material from all 3DP layers taken from a corner of the geometry (in the shape of a triangular prism). It follows that most of it must have had started degrading by the first time period, as infiltration would have progressed into the sample through four out of its five faces. Thus, since most

of the material was relatively near the surface, the average crystallinity of all the printed layers – including the mostly-unaffected inner ones – would be the value reflected on those elevated DTA measurements (because the outermost layers would have lost amorphous mass). Similar studies have noted a similar final drop in crystallinity, when it is thought that the remaining crystalline matrix would be starting to degrade [290,322,361,372]. The reduction on crystallite size and a wide mixture of polymer chain sizes could then account for the apparent drop in crystallinity.

6.2.3. THERMAL ANALYSIS

Data from Differential Thermal Analysis (DTA) brings forward further evidence for the role of crystallinity on *in vitro* degradation of 3D-printed PLA. Though there were only slight differences between the measurements for the filament and the post-3DP polymer, some of these were illustrative of what crystallinity and degradation data have suggested on the previous sections. These differences show clear deviations from the behaviour of the baseline filament, and then from 3DP material as degradation ensues. These changes and the loss of the crystallisation peak originally observed in the filament and 3DP parts were consistent with other ADT and RSET studies [284,290,361]. The probable explanations involve extended degradation of the amorphous phase of the polymer, as well as the sample's surface-volume ratio increasing after degradation.

In principle, both of those ideas could apply to FFF polymers in general. As mentioned before, samples taken from the edges of a specimen preferably include material that was in direct contact with the degradation medium, as

opposed to material that was mostly infiltrated through the concentration gradient formed with neighbouring polymer – which should happen more slowly. Unfortunately, DTA allows only for a very small mass of sample to be tested at a time, making it extremely hard to devise a sampling policy that doesn't somehow favour internal or superficial portions of the specimen. The sampling criteria used for these experiments – including material from all layers of the model – further limits the options available. Notwithstanding, this sampling policy is strongly supported by the evidence so far put forward by this research regarding the distinct behaviour of FFF structures: taking in account every layer of the model is very likely instrumental to understand their behaviour. Moreover, a similar bias was probably unavoidable when degrading bulk samples, as opposed to thin films or filaments, since it has been pointed out that limited infiltration rates will tend to impede uniform degradation on three-dimensional structures. Even though the size of the samples in this research would make them susceptible to bulk degradation, the time it takes to fully start will depend on the infiltration rate to the whole geometry [322,360].

For ADT specimens, DTA curves displayed moderately pronounced effects, with the most prominent one being the enlargement of the fusion peak. This reflected the gradual increase in crystallinity on the samples as degradation progressed. Notably, no crystallisation peaks or glass transitions were detectable on these specimens at any point during the experiment. This could be partly because all crystallisable amorphous material was beginning to be degraded. The lowering of the melting temperature was probably caused by reduction on crystallite size due to degradation.

6.2.4. MECHANICAL PROPERTIES AND VISUAL INSPECTION

ADT tests did not provide any data for mechanical properties due to excessive brittleness of the material found through all of the degradation time periods. This quick deterioration on mechanical properties is not reported in the literature for non-3D-printed specimens [49,361]. It is likely that this phenomenon is unique to FFF structures, since mechanical integrity of mADT specimens was noticeably compromised from very early stages of degradation. The underlying mechanism of this susceptibility is likely linked to the FFF process in that fusion between layers is non-uniform and heavily dependent on the tessellation algorithm and how each layer is deposited. Layer surface roughness variations, random cooling rates and gradients, and heterogeneity of the deposited polymer have been proposed as causes for this so-called “opening” failure mode of FFF prints, in which the layers become unfused [297]. Layer-layer interface, must then be more weakly bonded, and would be exposed to a higher degradation rate.

All *in vivo* and *in vitro* degradation studies reviewed as part of the present work use a standard manufacturing process different from 3DP – usually casting, extruding, or machining –, and not all of them employ standard tensile specimens. Some used rods, and some finished devices like bone-fixation plates and screws [126,282,285,373]. Direct comparison must be made with caution, as values for *UTS* and *E* are higher in the literature, in the order of several GPa. Those on the present study were in a range of tens of MPa for *UTS*, and under 500 MPa for *E*. It is noteworthy that PLA used in the literature tends to be also of very high molecular weight of around 500,000 to 1,000,000

g/mol, with both of the brands used on the present research averaging around 100,000 g/Mol.

6.2.5. ACCELERATED DISSOLUTION TEST

The results collected from mADT experiments, shown in **Figure 5.9**, display an exponential-like decay, which suggests they can be used to extrapolate these degradation data with those of similar experiments in the literature [283,290]. Water is able to infiltrate polymer networks despite its high polarity and being hindered by hydrogen-bonding with itself [137,366], though that likely accounts for its long degradation periods when compared acetone. Acetone, being a non-protic solvent, acts more aggressively as it is freely available to invade the polymer's structure to interact with its innermost molecules, where a greater surface area due to microporosity further enables the reaction [374]. This is likely why PLA is readily soluble in acetone, and the temperature at 37 °C simply facilitates the process [137].

Acetone acts readily on the intermolecular interactions between polymer chains, which are already weakest at the layer-layer interface. Acetone, non-polar solvent, so it stands to reason that larger polymer chains will be acetone-soluble than those that dissolve in water [2]. The structural failure pattern described **Figure 5.12** and **Figure 5.13** differs from those reported in published experiments on aqueously-degraded PLA to this date [290,329,361,375,376]. It is evident from **Figure 5.9** that VB-PLA dissolves much slower than BFB-PLA, as its mass change oscillates around 1% even

after 48 hours, where BFB-PLA has clearly lost over 10% of its initial mass. The plateau section for VB-PLA was characteristic of the first stages of ADT [290,361], and should persist until the material's tipping point [361], after which net mass loss would be observable. Additional time periods over 48 hours would be necessary for to map its profile after mass-loss ensues. It is worth noting other ADT studies [290,314,322,361] comment on this initial mass increase due to medium uptake by the specimen, but do not report this trend. This is likely due to their sampling times being evenly spaced over long-term studies, therefore masking these initial features. To this author's knowledge, this kind of model for the initial medium uptake of PLA specimens has not been described elsewhere – although it can be inferred from related applications of polymeric adsorption resins and their kinetics [377,378].

The mass increase for VB-PLA as shown in **Figure 5.10** was unexpected after the oven drying cycle, considering the high volatility of acetone. This increase can be partly attributed to some solvent irreversibly adsorbing to the microscopic surface features of the specimen, which, albeit small, would – incidentally – also yield an exponential trend that depends on medium concentration, material, temperature, pH, and the time allowed for the reaction [374,377,378]. An exponential fit was indeed strong for both data-sets. In the case of the wet samples, the additional mass (around 4% at its highest) can be explained by the superposition of both phenomena: the medium's infiltration into the polymer matrix, and its irreversible sorption to its surface. The latter phenomenon, in turn, would be responsible for the dry-mass curve in **Figure 5.10**. Both quantities grow as the infiltrating medium reaches the internal geometries of the specimen, where more volume becomes available for the

liquid to distribute to, and a larger surface is accessible for sorption, as has been described for microporous polymers [374]. The presence of these two mechanisms can be further supported by the fact that the time constants for both curves differ in that the dry-mass one was slower (35.4 minutes) than the wet-mass one (27.6 minutes), which was expected since infiltration must causally precede sorption, and permanent bonding should have a lower chance of occurring [377], with transitorily-adsorbed molecules eluting and volatilising during oven drying.

These comparisons, in summary, describe how typical sorption phenomena could interfere with mADT. The ~1% mass increase found for the dry samples was similar to that reported for water infiltration in ADT [322,361]. This was quickly overpowered by the subsequent mass-loss stage (as the BFB-PLA curve on **Figure 5.9** readily exemplifies) and its effect in measured mass should be minimal.

The results compiled by **Figure 5.14** put the structural failure times for BFB-PLA at 1.5 hours and at over 2 hours for VB-PLA, making them unsuitable for tensile testing after that time period. If not for this fact, *in vitro* degradation could probably be more accurately tracked through mechanical properties given their strong exponential tendency. This would not be unreasonable, given that mechanical properties are somewhat of a superposition of the chemical, crystalline, and intermolecular arrangement of polymers. It must be noted that these specimens were not constrained within their vial during testing, so mechanical loading was limited to the effects of gravity, medium buoyancy, and their contact points with the vial's walls. It can be argued that

being fixed – as when implanted for bone-reconstruction purposes – would include two additional sources of stress: that due to play between fixation sites, and that due to material deformation during the course of degradation. For degradation tests evaluating mechanical properties, tensile specimens are often preferred as mechanical properties are usually severely affected by degradation [126,312]. Mechanical properties are also one of the main concerns in most prosthesis-design applications involving plastics [137,253].

It was evident that BFB-PLA is extremely sensitive to acetone, just as it was noticeable that degradation takes place preferably in the interfaces between layers of the sliced model of the prints, forming longitudinal gaps as seen in **Figure 5.12**. The surface of each layer, in contrast, appears to experience its isolated degradation, with most of the early damage brought on by deformation. This deformation eventually leads to failure of the central shaft of the specimen (after what could be considered its dismantling point), while the individual layers gradually lose bonding with each other, especially near the perimeter of the model. This is similar to the delamination phenomenon described at the surface interface of other composites [108], which suggests intermolecular interactions at these sites are weaker.

The cracks on the traction plates of specimens in the later stages of the experiments (6, 24, and 48 hours) would appear to be the result of the layer weakening beyond the stress induced by its own deformation. This eventually caused severe bending of the structure before degradation could begin to separate the layers, instead bringing them closer together – and fusing them back to some extent –, forming transversal cracks on their lateral surfaces as

the geometry curled around its transversal axis. Notably, layer fragments did not appear to detach completely until the 48 hour mark was reached, after the specimen had lost roughly 10% of its mass, and after its *crystallinity* values were undergoing a second drop, reflecting the degradation of their high-crystalline matrix. This will very likely reduce the dismantling time of implanted FFF devices, since severe deformation is not reported in other degradation studies. The additional mechanical stress will necessarily add up to the implantation-related loads experienced by any device, which themselves have been reported to degrade – both chemically and mechanically – at a much faster rate than what *in vitro* tests suggest [312,373,379].

In contrast, as evidenced by **Figure 5.13**, VB-PLA undergoes similar changes, but to different magnitudes. Structural deterioration becomes obvious by the end of the first day. It is relevant to notice that these specimens had not undergone measurable mass loss up to that point. Though unmeasurable due to deformation, their mechanical integrity was still good enough to allow handling without damaging them – unlike BFB-PLA specimens. The layers that had curled away from the main body of the structure may mean that a tendency to fuse could be characteristic of high-crystallinity PLA, and it becomes more evident with VB-PLA as its starting *crystallinity* value was comparably higher.

Along with this, in the time periods up to 2 hours, crystallinity dropped down to average values of 38% for BFB-PLA and to 45% for VB-PLA. By the final time period, these values were 44% for BFB-PLA, and 29% for VB-PLA. The 24 hour time period showed an increase in crystallinity to 48% for BFB-PLA and

43% for VB-PLA – when much of the amorphous material was likely exhausted. A final decrease was observed at 48 hours.

These differences, found in **Figure 5.16** and **Figure 5.5** for the mADT series of BFB-PLA, show clear deviations from the behaviour of the baseline filament, and then from 3DP material as degradation ensues. These changes and the loss of the crystallisation peak originally observed in the filament and 3DP parts were consistent with other ADT and RSET studies [284,290,361]. The probable explanations involve extended mass-loss from the amorphous phase of the polymer, as well as increased surface-volume ratio, leaving more sample exposed to the solvent.

Changes shown in **Figure 5.5** as a result of thermal treatment were evidently less dramatic for VB-PLA, which was reflected in a drop in *crystallinity* proportionally smaller decrement from 29% to 24%, when compared to BFB-PLA dropping from 21% to 15% (**Figure 5.3**). T_g peaks for both filaments were found higher than for the material after 3DP: 59 °C against 46 °C for BFB-PLA, and 64 °C against 55 °C for VB-PLA. This change can be attributed to the drop in crystallinity itself.

Similarly, the shift in the crystallisation peak on BFB-PLA (from 80 °C to 87 °C) could be due to the higher availability of amorphous material as a result of FFF, but as well due to the more uniform characteristics of such material as it is arranged into tighter filaments with more restricted chains during the process [2]. The former can be argued from the taller and sharper crystallisation peak. The higher crystallisation temperature could also be accounted for by the self-reinforcement phenomenon, with the printer's extruder forcing high-

crystallinity material into more stable aligned arrangements that enhance the thermal and mechanical properties of the matrix by favouring intermolecular interactions between polymer chains, effectively fixing them, therefore increasing the crystallisation temperature. Studies on self-reinforcing of PLA have theorised this [282,292,327,380].

6.3. PROCESSING OF 3DP COMPOSITE MATERIALS AND STRUCTURES

The compositing method developed for this research was designed to require the minimum possible specialised equipment and raw products. It was also expressly designed to avoid the use of any strong organic solvents, which would be relevant for certification of good manufacturing practices of a Class III medical device [381]. All treatments undertaken by the materials in this study were in the form of mechanical and thermal stress.

6.5.1. ANNEALING

The rise in average crystallinity values for BFB and VB after annealing (to 56% and 48% respectively), was concurrent with the drops in *UTS* and *E*, which would explain the more brittle tendencies of the specimens. This reflects the observed differences between BFB-PLA and VB-PLA filaments themselves. Annealing seemed to overall improve the reproducibility of the material in regards of at least the three aforementioned parameters. VB-PLA annealed (VB-ANN) might be the exception to this in terms of *UTS*, which could be due to the reduced flexibility making any deformity more significant during tensile testing, redirecting the intended longitudinal stress into a flexo-compressive load that would fracture the specimen more easily. This could account for the relatively high variability on *UTS* on the more brittle materials, which was on par with the variations experienced by the more plastic failure modes of non-annealed specimens.

Heightened crystallinity proved to also affect some aspects of the specimens' resistance to degradation under mADT conditions, as evidenced by **Figure 5.19**. For both materials, annealing had no significant effect on mass loss, but improved mechanical performance, even pushing the dismantling point of BFB-PLA beyond 2 hours. This suggests that failure of mechanical integrity was very strongly linked with crystalline content, as both annealed materials display around the same proportion by weight (56.92% for BFB-PLA, and 48.58% for VB-PLA). Tensile strength and elastic modulus values were more preserved in both annealed materials as well.

These changes were not only related to crystallinity, but must be intrinsically linked to the initial actual values for *UTS* and *E*, as has been noted [322]. While the way these properties were affected by degradation might be similar when normalised to their initial condition (as retention graphs were plotted), the initial values for *UTS* and *E* for the non-annealed specimens were more than 50% higher than those that undertook the thermal treatment (**Figure 5.18**). Reduced *UTS* and *E* are a reflection of how annealing modifies the polymer's matrix to a higher crystallinity content, where polymer chains undergo extensive fixation due to an increased likelihood of intermolecular interactions between them [2]. They then end up more closely packed into larger crystallites that further restrict deformation, and ultimately resist degradation by slowing down the medium's infiltration rate into the crystalline portions of the matrix [247,322,382].

The initial surges shown in **Figure 5.20** in the early stages of crystallinity plots for mADT (as other studies have pointed out [137,290,294,361,366]) were

likely due to the solvent preferably attacking the more accessible amorphous regions of the structure, but it seems pertinent to point out that this consideration alone would apply to the infiltration stages of dissolution. Since high-crystallinity lactides are inherently very resistant to degradation even *in vivo* [279,283,319,320], it is reasonable to assume that this fact would have the net effect exposing amorphous polymer to a higher *apparent* solvent concentration, since the crystalline portions are unavailable for interaction even as the whole of the geometry is being infiltrated. FFF specimens may have been more susceptible to this process since they were prone to be infiltrated by medium given their porosity (around 35% on the scale of the ASTM specimens), making the amorphous material readily available for degradation. Moreover, this mechanism would account for the exponential mass-loss trend for BFB-PLA. If the reaction is happening fast enough in the amorphous material so that infiltration time is negligible, and slow enough in the crystalline regions so that their contribution to degradation is also small. The result could be a Noyes-Whitney dissolution pattern, which is exponential and depends mostly on the solubility of the material [383]. If the phenomenon can be explained through this model, given equivalently sized and shaped samples, changes in solubility will be the main contributors to changes in dissolution rate. Similarly, given the same material with the same solubility, differences in geometry (reflected in differences in surface area) would be the main drivers on differences in dissolution rate.

This mechanism would also explain the disappearance of crystallisation peaks from DTA curves during mADT (observed as well in other studies [290]), since the amorphous material would be overall exhausted, especially near the

surface of the specimen [322]. The remainder of the amorphous material, in turn, could be prevented from crystallising at the expected temperatures for PLA if it were trapped within the crystallites formed during processing, preventing it from interacting. It would also explain the mismatch between mass-loss and crystallinity, as logic would require the mass-loss to correlate more closely to crystallinity increases as the amorphous regions are exhausted. Finally, differences in molecular weight between BFB-PLA and VB-PLA should account for the marked divergence in mass-loss behaviour between the materials, with the former exhibiting a lower value that favours solubility of early-degraded chains. Coupled with the low crystallinity value of BFB-PLA, these two factors and the mechanisms mentioned in this section would explain the sudden rise in crystallinity at the 0.5 hour period on the non-annealed specimens, as there is less crystalline lattice providing protection for the amorphous polymer.

While changes in failure mechanism were evident in mADT tests after annealing, these were not so in ADT. All samples became slightly distorted and extremely brittle as early as the first time period studied (1 day). The only 2 testable samples allowed for an estimated drop in tensile strength of over 90% within the first 24 hours of the test. Mass loss, fusion temperature, and overall calorimetric values did not show major changes by that point. Crystallinity experienced the surge also found during mADT, so that increase in the crystalline content of the specimens would appear to be the main factor governing structural brittleness in FFF parts. The tendency of layer-layer interfaces to fail first during degradation might account for this phenomenon, as that would facilitate infiltration and a more uniform bulk degradation (as

opposed to simple erosion) of every layer. Crystallinity throughout the whole structure would then be increased, and each individual layer would then be more brittle on its own, diminishing the deformability of the geometry. These phenomena were apparently independent of starting crystallinity, since the higher starting value for annealed specimens yielded a very similar maximum to that of the non-annealed. Should this hypothesis be true, it further supports the idea that some of the amorphous phase is locked within the crystalline matrix, away from the degradation medium but unable to crystallise. The rest of the amorphous material would then be quickly washed away during degradation, which would also explain the disappearance of crystallisation peaks where present on the undegraded specimens.

6.5.2. PLA-HA COMPOSITE FILAMENT PRODUCTION AND CHARACTERISATION

One of the main objectives of this research was to produce a PLA-HA composite filament that could be 3D-printed through FFF. To this author's knowledge, only two publications prior to this work were found to have reported on producing such a material specifically for FFF [264,265]. Notwithstanding, composite 3D-printing filaments are commercially available for general applications – being modified with added pigments, fluorescent compounds, wood particles, metal particles, or plasticisers, in order to modify their appearance and mechanical properties.

The method presented in this work proved to be sufficient to produce 3D-printing filament and 3D-printing parts on a PLA-HA composite using only commercial-grade equipment. As the two studies mentioned also report, a lower concentration of HA is probably desirable [264,265]. The 20% HA composite proved to be problematic to work under the scheme proposed in this research. During extrusion into filament, this mixture of composite softened excessively, making it remarkably difficult to pull into a consistent filament. This causes imperfections on the surface of the resulting filament, along with noticeable inconsistencies in its diameter. In turn, these imprecisions limit the capacity for the 3D-printer to produce consistent prints, and eventually results in either fracture of the filament, or clogging of the printer's extruder within minutes. Accumulation of HA in the nozzle's channel appears to be to blame for this clogging, as residues were found during cleaning. The 5% and 10% composites suffer from these problems less drastically in regards of filament extrusion, though printer blockage did occur within few hours of using these filaments.

The higher concentration of HA in the 20% composite might promote powder agglomeration during the initial melting procedure of compositing. These agglomerates might consolidate further under the pressure of the driving screw during extrusion, which could potentially produce 250 MPa – this pressure has been found to result in cold isostatic pressing of the HA [384]. Grinding the PLA pellets further or using a solvent to homogenize the mixture might be a solution for this issue. However, the Filabot extruder requires the polymer pellets to be big enough for the driving screw; small enough pellet sizes (likely under 5 mm in any direction) will be unsuitable to use on this device. Using

solvents to improve mixing could be a solution, but poses several biological safety issues, as it is difficult to provide evidence that all of it evaporates during extrusion and printing. The composite being meant for resorbable implants, any remaining solvents are guaranteed to leach into extracellular space. The production method proposed in this study was designed to avoid these issues with use of solvents. Moreover, the amount of solvent required to process hundreds of grams of PLA would pose a logistic and economic problem, especially in regards of safe disposal.

Content of HA crystals within the polymer matrix, found through DTA/TGA to be on average 6.97% for the composite filament and 6.82% for 3D-printed parts, was shown to be well distributed by SEM-EDS. All DTA, SEM-EDS, and μ CT testing suggest that the method was reliable, reproducible, and capable of achieving final products with a uniform distribution of HA within a PLA matrix. This is of great interest for bioresorbable devices, since it means that the intended effect of PLA – which is a surface functionalisation in practical terms – will be likely sustained throughout the breakdown of the material. It must be mentioned that sample preparation for SEM-EDS (namely cutting and polishing) could have forced HA crystals off the polymer matrix: this could account for the areas with fainter distribution of Ca and P found in the pre-extrusion composite, as well as for the larger particulates observed in μ CT. Nevertheless, the fact that both the composite filament and the 3D-printed composite parts had a more homogeneous distribution of these elements was evidence that HA crystals were redistributed and mixed during the extrusion and FFF processes.

The traces of calcium and phosphorus atoms detected by EDS on the pure PLA filament sample could likely be accounted for by contamination due to the environment where the samples were processed. This laboratory is home to a number of machining equipment for dental and bone-repair materials, and the printer is not isolated in any way from airborne particulate contaminants – including those released by HA-containing samples which were routinely handled near it for this work. Additionally, it is impossible to guarantee that the extruder-head of the 3D printer is completely free of leftover HA from previous prints using composite, even after purging it with pure PLA. This was further supported by the clear differences on distinct phosphorus and calcium peaks in the EDS spectra of the composites: none could be detected on pure PLA. Similarly, despite sanding and polishing, it is extremely difficult to make the surface of the samples completely flat due to their size and PLA's inherent malleability. Because of this, SEM showed several zones presenting a charge effect that could interfere with EDS measurements. These zones were either at different distances from the detector, or at steep angles from the levelled reference. Visualisation of surface charge artefacts in these zones suggest that their variations go beyond the device's absorption correction [385,386]. To compensate for this, areas scanned for EDS were selected to be as even as the sample provided, though there was still room for errors from this effect.

It was an initial concern that only melting the polymer mixed with HA would not be enough to achieve an even distribution of HA throughout its entire volume. However, the filament extruder seems to provide enough homogenisation through the combination of thermal softening of the initial composite, and of shear due to the action of its driving screw. Though some HA loss was

expected during the whole compositing process, it was not anticipated that most of it appeared to happen at the initial mixing and melting stage. Moreover, this HA loss with respect to the original formulation is likely to be tailorable – either through simple linear relationship or through trial-and-error – so that the desired concentration of HA can be tuned for the output filament and 3D-printed parts. This fact could be also of relevance for the production of long-term drug-delivery devices [45,322] – given sufficiently heat-resistant drugs. Overall, the methods described in this work could be applied to produce and characterise other 3D-printable polymer-ceramic composites.

6.4. IMPLANT GEOMETRIC DESIGN

The test mesh presented on **Section 5.4** takes in account adult average measurements [343,344], so most alveolar clefts will fit within its volume of about 11x15x22 mm. This was very near the edge of dimensions reliably managed by the BFB-3000, especially if fine details are required. An advantage of designing under this printer's limitations would be that any more modern printer would be able to reproduce the results with similar or better accuracy. Building up from stacks of small modules will very likely turn impractical in routine design of geometries based on medical imaging studies, unless software is developed for this purpose using procedural-generation algorithms – such endeavour lies beyond the scope of this research. Rather than that, it is more convenient to work backwards from a base 3D lattice, cutting it down to the desired shape as acquired from imaging files, as this would be achievable in virtually any computer assisted design (CAD) software.

The designed lattice sample was printed near the 2 mm limit of the printer, which prevents the STL build from including fill patterns. This likely helped to maintain uniformity in the material. With this lattice acting as the inner structure of an implant, its surface area became about eight times greater than that of a solid implant of similar dimensions. The 2 mm openings within it, as well, make it suitable both for bone formation, and for revascularisation to take hold, in accordance to current literature [6,37,273,369].

The irregular edges, borders and outer surfaces of the lattice, however, were considered to make it difficult to devise a fixing procedure for implantation, and would leave sharp borders exposed to surrounding tissue. It was therefore considered necessary to enclose the mesh within a more geometric frame. The *desired shape* used represents the maximum limits that can be normally expected to conform an alveolar cleft (11x15x22 mm). This *desired shape* was meant to be replaced by the negative space formed by a cleft – or another facial bone defect – as presented by a CT scan. This lattice also corresponded to the 3D-cell culture samples tested (**sections 4.5 and 5.5**).

6.5. IN VITRO MATERIAL BIOCOMPATIBILITY

6.5.1. 3D-PRINTED PLA STERILISATION

These sterilisation comparison experiments were planned as a preventive measure due to repeated infections – suspecting the culprit was the unsterile state of the 3D-printed cellwork discs. Although the source of the infection turned out to be external to the samples used in this research, the evaluation

of these methods provided some valuable information for future cell-culture work on 3D-printed polymers.

Under the conditions tested in these trials, ethaneperoxoic acid (commonly known as peracetic acid) hampered cell growth following its use for surface sterilisation. Though further testing would be necessary, it is likely that more washing cycles with PBS are necessary for it to elute completely from the micro-scale porosity of the 3D-printed disc samples. The mechanism might be similar to that of adsorption of acetone to PLA, given the similarities of their molecular structure and size [137,247,294]. Additionally, under these experimental conditions, both ethanol and propan-2-ol (isopropanol) functioned statistically equivalent in regards of cellular proliferation and calcium and collagen deposition ($p < 0.05$).

6.6. COMPOSITE ACCELERATED DEGRADATION

6.6.1. MASS CHANGE

The PLA-10%HA composite followed relatively closely the expected degradation pattern found for VB-PLA in the ADT experiments presented here. These were consistent with the literature [283,290]. The very early onset of mass loss for the composite (around day 3) when compared to VB-PLA results (around day 9) was indicative of the detrimental effects the compositing procedure has in the macromolecular integrity of the polymer matrix. These were likely to further accentuate weakening caused by FFF after compositing, as discussed in **Section 6.2.1**. Moreover, by the end of the experiment – in day 23 –, the composite was further along its mass-loss process, having

degraded 28.07% of its starting mass: significantly more than the 21.02% found for VB-PLA.

This discrepancy very likely reflected the weakening of intermolecular interactions caused by HA crystals lodged between main polymer chains. If this was the case, these voids could expose bonds in monomer-linking ester sites to be broken down by degradation medium. These sites would leave behind either hydroxyl or carboxylic-acid end groups, which would interact through weaker hydrogen bonds or Van der Waals forces. Weakened bonding between shorter polymer chains would eventually allow for increased chain mobility, and even faster water infiltration of the samples' inner geometry [2,294,374]. This sequence of conditions could be attributed to the differences observed in number average molecular weight for pure VB-PLA (51,715 g/mol) and the 10%HA composite (40,420 g/mol) at the start of their respective ADT runs.

6.6.2. CRYSTALLINITY, MECHANICAL, AND THERMAL PROPERTIES

ADT experiments on the PLA-10%HA composite found a tipping point for mass-loss of the samples before day 3 of degradation, well below the 9 days recorded for VB-PLA. At their respective tipping points, average crystallinity had increased by 55% for VB-PLA, and 34% for the composite. In both cases, this increase corresponds to ~0.95 times their final plateau values for crystallinity in the experiment – 87% for VB-PLA and 60% for the composite at day 23. Though further testing would be required, if this tendency holds for differently-sourced PLA, it could reflect a potential critical point for degradation

tests to indirectly determine their tipping points through calorimetric crystallinity measurements.

There was an apparent discrepancy in the results shown in **Sections 5.2** and **5.7**. Crystallinity surges to maximum levels before the tipping point in all degradation experiments conducted in this research. Though a rise in crystallinity was to be expected, the accepted theory is that this is due to loss of amorphous mass [187,220,263,272]. This inconsistency can be observed in data of at least one other similar degradation study in lactide polymers [290]. It is suggested that this could be due to the effect of the degradation medium acting as a solvent, which could lower glass transition temperatures of polymers, as the literature reports [387,388]. Along with the temperature of 70 °C of the experiment, this could potentially imply overall increased mean chain motility, and a lowering of the crystallisation energy barrier, prompting the amorphous mass to crystallise during the initial phases of degradation – this conjecture would require further experimentation.

The results, shown in **Figure 5.51**, provided additional evidence that thermal stress due to the compositing process, filament extrusion, and FFF may lower the crystallinity of the raw PLA filament used. Other studies report similar effects on crystallinity from thermally-intensive treatments [49,371]. VB-PLA reached an average of 28.55% crystallinity after 3D-printing, while the 10%HA composite drops to 22.67%. at that same stage. Results from mADT showed that BFB-PLA and VB-PLA respond similarly to acetone degradation in terms of crystallinity change at all but the last stages of those experiments (**Figure 5.6**). Though further testing would be required to confirm it, this may hint that

BFB-PLA crystallinity behaviour might be similar during ADT. Should that be the case, it would be reasonable to expect a similar general behaviour from other 3D-printed PLA – in terms of reaching peak crystallinity values around 80% early during degradation tests (and prior to significant deterioration of these). Semi-crystalline polymers are not expected to achieve values much higher than 80% crystallinity [291] [389], so it would follow that PLA samples would reach values on that range as their amorphous phase degrades.

Since this was not the case for the PLA-10%HA composite (maxing out at 60.78% crystallinity), it is feasible that the strong capacity for hydrogen bonding of HA is to blame for negatively impacting crystallisation. The mechanism would be by interfering with chain alignment and fixation [390]. This disruption could potentially be through increasing inter-lamellar distance in the crystals through HA particles getting lodged between them. The fact that crystallinity drops on the composite – and that measurements never go up to 80% as expected – suggests this role for HA, rather than it acting as a nucleation agent (since most such agents would be expected to be nano-scale and this HA was over 3 μm in particle size). Further testing would be required to determine if thermal stress during compositing process, the addition of HA, or both were responsible for crystallinity deterioration on the composite.

This constellation of factors could also explain the composite's significant drop in tensile strength reported in **Figure 5.49** and **Section 5.6.3**. Since annealing showed a similar tendency to weaken 3D-printed tensile bars, similar mechanisms should account for the polymer's drop of over 40% in tensile

strength – in line with what has been previously suggested in the literature [371].

Composite tensile bars showed a significant drop in elasticity (**Figure 5.51**) not found in annealed specimens, thus crystallinity could not be the only factor affecting the composite's mechanical behaviour. Since molecular weight was found to remain largely unaffected, the presence of HA must play an important role in regards to elasticity. It is proposed, thus, that HA particles disrupt intermolecular interactions between PLA polymer chains, and since the compositing and 3DP processes do not provide suitable temperatures for these particles to consolidate, weaker HA-HA interactions embedded in the amorphous polymer matrix may have caused this observed drop in elastic modulus. In summary, thermally-induced chain migration, coupled with the presence of embedded HA particles (which were likely far beyond nano-scale), could facilitate micro-fracture formation and stress-concentration around these particles and voids due to their presence, and could account for mechanical deterioration on polymers [365].

6.6.3. THERMAL PROPERTIES

Thermal degradation behaviour under TGA measurements was markedly different for the PLA-10%HA composite when compared to VB-PLA. Although their melting points started ADT without significant differences, by the third day both curves drifted significantly from each other. The 10%HA composite showed a faster decrease in melting temperature, ending the experiment at an average of 144.5 °C, while VB-PLA did so at 159.7 °C. This signified a drop of

9.4% for the VB-PLA, and 17.2% for the composite by the end of the experiment (**Figure 5.55**).

The lowering of melting peaks for the composite after 3D-printing was likely due to repeated thermal treatments during processing lowering the molecular weight of the polymer matrix (**Figure 5.49**). The resulting upward shift in the DTA curves (**Figure 5.54**) could be the result of intermolecular interactions with hydroxyl moieties provided by the presence of HA [390], which could potentially facilitate hydrogen bonding to account for the heightened heat capacity at the compositing stages before 3D-printing. Notably, for the sample masses used in DTA/TGA measurements done here, sample mass did not influence heat-flow offset, as would be expected – at this scale, the dominant property is likely surface area. Furthermore, the self-reinforcing phenomenon [292] could also be a potential explanation for the second shift happening after 3D-printing, since polymer-chain alignment could further favour intermolecular interactions with HA particles, and likely strengthen them through reorientation into more favourable bonding angles on a more tightly packed matrix, dampening thermal motion.

If this is the case, addition of HA would require extensive fine-tuning of printer settings in order to fully optimise a lower-temperature FFF procedure. This effect would be naturally limited by the concentration of HA in the composite, which this study found to be difficult to get over 20% due to manufacturing problems encountered while doing so (**Section 5.6.1**). By modifying the 3D-printing process' settings and further fine-tuning the equipment, it might even be possible to utilise concentrations of HA – or ceramics in general – beyond what was found applicable under the methods used for this research. Contrary

to what the present results suggest, it has been shown that PLA composite concentrations of up to 70% HA by weight are achievable through hot-pressing, reporting even improvements in mechanical properties [136].

6.5.2. MG-63 CELL VIABILITY STUDY

The first cell viability experiments for this project – done in expansion medium – provided evidence that the MG-63 cell line was not able to synthesise mineral on pure PLA without the addition of ascorbic acid and β -glycerolphosphate. This was expected, since the supplements provide a phosphate source for such mineral formation in both traditional and 3D cell culture [345,391–393]. In the second batch of experiments, osteogenic medium did promote deposition of detectable levels of calcium and collagen. With those results as a baseline, it was expected that the addition of HA to the polymer would further promote the production of mineralised extracellular matrix as an osteoinductor, as variations of HA and other calcium phosphates have been found to do [250,302–307]. Nevertheless, viability and matrix-deposition experiments for the composites generated for this study showed only a marginal increase in collagen production, which was apparently linked to concentration of HA in the composite. Despite this, the PLA-20%HA composite was found to be harder to process for filament production and subsequent 3D-printing. The remaining two composite concentrations (PLA-5%HA and PLA-10%HA) displayed no further differences in cellular response. The PLA-10%HA composite, thus, was favoured for the rest of the study, since it comprises the maximum concentration of HA – likely favouring

osteoinductive action – with minimal decline in the processability of the material.

Since the cellular response was otherwise equivalent between EM and SM experiments, and between PLA and the PLA-HA composites, it is safe to assume that this PLA itself is biologically inert for the most part, and that compositing and 3D-printing are probably safe for implantable device manufacture. Biological and chemical degradation of PLA produce no by-products other than lactic acid. This compound is anaerobically metabolized *in vivo* – via the Cori cycle –, and is only known to cause inflammatory responses when given the chance to accumulate [394,395]. *In vitro*, additional mechanisms to cope with lactic acid leachate from the samples are likely similar to vascular drainage. As well, osteosarcoma cells, such as the MG-63 cell-line, are known to express MCT-1 membrane receptors, which facilitate lactic acid uptake [396]. This suggests that cells in tissue culture wells on these experiments might have played a role in disposal of excess lactic acid through their own metabolism. Additionally, EM changes and well washes during RRA limited the possibility for an unmanageable build-up of this by-product.

Moreover, one of the main findings derived from these experiments was the evidence that MG-63 cells respond similarly to 3D-printed commercial-grade PLA as they do to tissue culture plastic in terms of cell viability; the same was true for the PLA-10%HA composite. Though the biocompatibility of PLA has been widely tested – to this author's knowledge – the data provided by this study is the first evidence produced specifically for 3D-printed specimens made of PLA and PLA-HA composites. It must be noted that there are studies in 3D-printed scaffolds made from other polymers, and of PLA blends 3D-

printed through methods different to FFF [45,397–400]. One study provides similar data for *in vitro* biocompatibility using bovine primary articular chondrocytes and nucleus pulposus cells in PLA FFF scaffolds [138]. Their findings are like those of the present study in that cell proliferation did not seem to be limited by the material. Complementing these results with replicate experiments, *ex vivo* setups, and trials on different cell-lines would enhance our understanding of the *in vitro* behaviour of 3D-printed PLA. Trials on non-cancerous cells (such as primary bone cells or stem cells) could potentially evidence factors unfavourable for cell survival that are not evident on MG-63 cells, since the latter are known to be more resilient given their cancerous phenotype. Notwithstanding, given how well-studied are lactide polymers, this author considers unlikely that the outcome of further biocompatibility tests will be any different. Further testing on different HA concentrations for the composite, however, would provide a clearer notion of its effects on osteoinduction in 3D-printed parts, and would help narrow down an ideal concentration for compositing. Similarly, mineral-substituted versions of HA – such as those with strontium, silicate, magnesium oxide, carbonate or bismuth [401–405] – could be relevant to the manufacturing process described in this project. A caveat in this respect stems from the unsuccessful attempt at compositing nano-scale HA in the present project: it could be the case that some of such forms of HA prove impractical or impossible to extrude or print through FFF.

6.5.3. *IN-VITRO* CELL CULTURE IN THREE-DIMENSIONAL 3D-PRINTED STRUCTURES

Since applying a functionalised 3D-printing composite filament in a bone-regeneration setting will necessarily require the production of 3D-geometries, it was of the outmost importance to explore cell behaviour when confronted with that specific scenario. Since the meshing procedure detailed in **Section 4.4.1** proved to be adequate to process 3D shapes into stacks of mesh units, one of these units was chosen to be tested in this part of the study.

The 3D-mesh model provided a surface area roughly 10 times higher than one face of the disc samples used for cell culture in this study (**Section 4.5**) – 8.55 cm² against 0.78 cm². By design, this increment was meant to compensate for the intrinsic difficulty of cell-seeding against gravity in the thin columns of the mesh. The significantly lower cell attachment observed for the PLA-5%HA composite with respect to pure PLA might be due to inconsistent results in seeding rather than some effect of the material itself. This notion was further supported by the fact that there were no significant differences between the PLA-10%HA composite and either of the other materials.

Overall, all three materials elicited an equivalent response from the MG-63 cell-line throughout the 21-day cell viability experiments. In contrast, SRS and ARS testing showed that both composites perform significantly better than pure PLA in the induction of extracellular matrix excretion and mineralisation – as suggested from detectable levels of collagen and calcium. These results were further evidence that functionalisation of 3D-printed parts with ceramics can be achieved by the compositing method developed during this project.

From these results, it is suggested that HA crystals in the polymer matrix's surface were inducing a strong enough cellular signalling for mineralisation, even with the HA used in this research being micro-scale rather than the preferred nano-scale, which is thought to be more biomimetic [306,307]. In turn, this would also be favoured by the presence of ascorbic acid and β -glycerophosphate in the medium, which provide co-factors and a phosphate source for the cells [348,349].

When comparing between the results obtained with the disc samples and the 3D-meshes, it is noteworthy that the change in distribution of cells from one to the other has a noticeable effect in calcium deposition per number of cells. This was not true for collagen deposition per number of cells, which maintained a similar level in both experimental setups. This could be due to the cells being spread over a larger area, with paracrine signalling weakening as a result. It is to be noted that, for higher cell densities, a positive effect of cell-density on OM-assisted-bone-regeneration parameters has been reported for polymeric tissue-engineering scaffolds [350].

6.7.1. MODELLING FOR MOLECULAR WEIGHT BEFORE MASS-LOSS

6.7. MATHEMATICAL MODELLING FOR POLYMER

DEGRADATION

Though at first instance the data for PLA and the PLA-10%HA composite did not appear to originate from the same physico-chemical processes, given fixed

experimental conditions and temperature, it is possible to use the model in **Equation 5.4** to approximately estimate the behaviour of even a distantly related material such as that of the Weir *et al.* data used for comparison in this study. The extrinsic differences between the three materials (molecular weight, crystallinity, geometry, mass, and all such experiment-specific variations) are likely accountable for the relatively low correlation coefficient ($R^2 = 0.8324$) obtained analysing the Weir *et al.* dataset. Additionally, the published data by Weir *et al.* provides only averages and not individual data-points for M_n : the dispersion could drive correlation via non-linear regression either way. However, using the parameters calculated by that study, it was impossible to account for the behaviour of the PLA and PLA-10%HA composites used for the present research, unless the results are normalised to M_{n0} (**Figure 5.60**).

In the region before t_p , it is very likely that the lack of additional data points for the materials studied in this research affected the outcome of any regression analysis. The experimental design used in this project was based on the Weir *et al.* study, which used PLA of much higher molecular weight (and therefore a slower degradation process). As such, time points were not ideal for the degradation rates of materials studied here. From what is observed in the literature and the present research, for ADT at 70 °C, additional measurement points before day 15 can be safely assumed to cover the pre-mass-loss profile of degradation for initial M_n of up to 166,000 g/mol. This would, in turn, provide a clearer distinction between autocatalysed and non-autocatalysed processes.

6.7.2. MODELLING FOR MOLECULAR WEIGHT AFTER MASS-LOSS

The main objective of the analysis of this region of the datasets was to look for an experimentally-based model of the degradation profile of PLA encompassing the whole dataset – before and after t_p . Unfortunately, no relation could be found between any of the parameters studied (mass-loss, crystallinity, M_n , M_w , or thermal properties) and the onset of mass-loss in the samples (t_p). It is proposed that the fundamental behaviour behind this process is more accurately described through the Noyes-Whitney dissolution model, and is therefore most sensitive to surface-area availability, such that:

$$\frac{dC(t)}{dt} = \frac{KS_a(t)}{Vl_d} C_S e^{-\frac{KS_a(t)}{Vl_d}} \quad \text{Equation 6.1 [383,406]}$$

With $C(t)$ being the instantaneous concentration of a solute as a function of time, K is a dissolution rate constant, $S_a(t)$ is the surface area of the solute exposed to solvent as a function of time, V is the volume of solvent, l_d is the depth of the solute diffusion layer from its surface into the solvent, and C_S is the solubility concentration of solute.

Given that PLA is a semicrystalline polymer, its dissolution rate is unavoidably uneven throughout its geometry – since amorphous zones would be naturally more prone to degradation and eventual dissolution. If viewed as a dissolution process, it would imply time-dependent dissolution rate constants. This fact complicates the above model, since it means both phases must then be considered separately, as rate constants must be weighed independently for

their exposed surface area. Such a superposition, in the best-case-scenario, would amount to:

$$\frac{dC(t)}{dt} = \frac{C_S}{V} \left(\frac{K_C S_{aC}(t)}{l_{dC}} e^{-\frac{K_C S_{aC}(t)}{V l_{dC}}} + \frac{K_A S_{aA}(t)}{l_{dA}} e^{-\frac{K_A S_{aA}(t)}{V l_{dA}}} \right) \quad \text{Equation 6.2}$$

Where the added subindexes C and A indicate parameters for the crystalline and amorphous phases respectively. However, the unevenness of the polymer's mass loss process likely implies that the functions $S_{aC}(t)$ and $S_{aA}(t)$ are highly non-linear – probably near random. Microscopic differences on chain alignment, crystallite formation, and microporosity could make these functions unpredictable for all practical purposes. Moreover, molecular weight itself – reflected in the availability of ester moieties available for hydrolysis – might even render dissolution rate constants time-dependent, and perhaps even layer diffusion depths as well. On top of this, ADT experiments show that PLA crystallinity tends to increase during early degradation, and to decrease on later stages, thus linking $S_{aC}(t)$ and $S_{aA}(t)$ through higher-order functions of time. A more comprehensive approach would have a similar arrangement to:

$$\frac{dC(t)}{dt} = \frac{C_S}{V} \sum_{i=1}^j \left(\frac{K_{Ci} S_{aCi}}{l_{dCi}} e^{-\frac{K_{Ci} S_{aCi}}{V l_{dCi}}} + \frac{K_{Ai} S_{aAi}}{l_{dAi}} e^{-\frac{K_{Ai} S_{aAi}}{V l_{dAi}}} \right) \quad \text{Equation 6.3}$$

Where the set of integer values from i to j each represents an individual molecular weight value found in the mixture of the polymer's available surface, considered in the equation in both crystalline and amorphous phases. Additionally, every parameter in this model would likely be a time-dependent function by itself – except, perhaps, for C_S and V . The number of sum factors would be dependent on the polydispersity of the polymer, though any time-

variation would be accounted for in the S_a function. Note that **Equation 6.9** must still be integrated to determine – or model – the concentration of polymer degraded into the degradation medium: the specimen's mass loss divided by V .

Complex geometries, porosities, and micro-porosities produced on specimens manufactured through 3D-printing are definitively detrimental on the simplicity of mathematically describing the dissolution rate of lactides. In summary, given results from this research's experiments and review of the literature – and least further experimental evidence suggests otherwise –, it is postulated that t_p values for PLA are inherently unpredictable through analytical chemistry, and must be determined experimentally through ADT. The former likely applies to lactides in general, and similar ester-polymers.

In terms of overall behaviour of their degradation profiles, **Equation 5.5** could be used to approximate the real-time plot of a given sample of PLA (or other similar polymers) using a reduced number of experimental Mn measurements for boundary conditions. Parameters for a given material can potentially be derived from measuring similar materials which differ in starting molecular weight, crystallinity, and even shape (which translates to area-volume ratio).

Naturally, this is not an entirely predictive model, since it requires of several calculations and experimental data points, but its value lies in abridging otherwise time-consuming and costly *in vitro* degradation testing. Additionally, it can be of potential value as a shorthand method to compare different formulations of a given material before committing to full characterisation of a given version.

Models represented by **Equation 5.7** and **Equation 5.9** were those found to best adjust to the trend of the datasets obtained through this research, and were also able to describe the independent data from the cited study by Weir *et al* [290]. Since both temperature and initial Mn are major factors dictating degradation rate, it is reasonable to expect that normalisation with respect to Mn_0 could allow different PLA instances to correlate in terms of ADT (**Equation 5.7**). Furthermore, normalisation of degradation time (**Equation 5.9**) with respect to Mn half-life yielded promising results in predicting the behaviour of the independent Weir dataset. Taking in account enough data to work out the polymer's half-life (which could be as little as an initial Mn measurement and a single other point to get a reasonable estimate) has the advantage of intrinsically encompass into that half-life a lot of the unmeasurable chemical and microscopic characteristics of a sample. This, in effect, has more practical value than theoretical merit.

Once again, this model is not meant to be completely predictive from an initial Mn , but it can shorten the experimental work needed to produce a reliable *in vitro* degradation dataset. Working out similar parameters for two or three additional degradation temperatures could in turn allow for enough data to apply the Arrhenius relationship to extrapolate non-accelerated degradation results. Using a model like those presented here would cut the number of samples to analyse for an Arrhenius plot from nearly one hundred to around a dozen.

An ideal model would allow for modelling from an initial molecular weight measurement, producing a complete degradation profile. A potential point of

further investigation towards such a model is depicted in **Figure 6.2**, where the possibility of a trend is hinted between the initial value of Mn and the time constants calculated for each of the datasets studied for modelling in this work. By necessity, more data points on the Mn_0 range around 100,000 g/mol and up to 3,000,000 g/mol (typical for medical-grade PLA) would be part of the work required to confirm this possibility. If so, it would allow for use of **Equation 5.7** and **Equation 6.6** with a very small number of experimental measurements – essentially to accurately define Mn_0 . From **Figure 6.2**:

$$M_{n0} = 15147e^{0.9491\tau_{70}} \quad \text{Equation 6.6}$$

Where τ_{70} would be the time constant for degradation at the given temperature (70 °C in this case), so that:

$$\tau_{70} = \frac{\ln[M_{n0}] - 9.6256}{0.9414} \quad \text{Equation 6.7}$$

Care must be taken with these observations and conclusions, since the number of experiments used to produce all these models is limited to the two ADT setups explored in this research. Though testing on the dataset by Weir *et al.* was modestly successful, correlation was less than perfect, and further testing with other datasets and the non-average data points by Weir *et al.* could reveal inadequacies in the modelled parameters. Notwithstanding, this work provides a starting point from which to pursue further development on the science of 3D-printable resorbable medical polymers.

7. GENERAL CONCLUSIONS

Additive manufacturing and 3D-printing (3DP) comprehend technological fields that will be formally incorporated into the development of medical devices in the years to come. The possibility of cost-effective Free Form Fabrication (FFF) 3DP brought forward by the advent of commercial 3D-printers is making rapid-medical-prototyping a field of investment in hospital-based medical engineering. The conclusions drawn from the present work stand promisingly for its implementation in the development of facial reconstruction techniques in particular, and regenerative medicine in general. Moreover, these findings and reflections can help develop guidelines and standardisation for the application of these emerging advances in a scientific manner. In brief, such conclusions can be presented as follows:

- The BFB-3000 FFF 3D-printer displays a scale-dependent accuracy and precision in terms of delivered linear dimensions, volume, and material microporosity. It is reasonable to assume FFF systems in general will be subject to such variations, especially on the smaller end of scales (from 0 to 5 cm³), and thus the evaluation procedure here presented is recommended as a baseline to quantify such error.
- FFF 3DP has immediate and measurable effects in polylactic acid (PLA), readily reducing the material's measured crystallinity content and mechanical properties. This probably depends on the material's starting crystallinity and molecular weight, and could be influenced by

additives incorporated by the manufacturer. It is suspected from the gathered data that long-term *in vivo* degradation properties of parts produced by 3DP will be as well affected. This will likely lead to faster mechanical deterioration due to the layer-layer interface on the perimeter of prints being consistently susceptible to quicker degradation, and due to the tendency of the tested specimens to deform. Additionally, both FFF 3DP and compositing – with the thermal stress they impose on the material – are not prolonged or controlled enough to produce dramatic changes in crystallinity. Crystallinity values are only greatly affected by formal annealing procedures. Similarly, FFF by itself does not affect significantly the molecular weight of the processed polymer. Contrary to what was initially expected (based on other manufacturing processes), the whole compositing procedure and eventual FFF 3DP do not deteriorate the molecular weight of the polymer significantly either.

- The experiments undertaken to produce a PLA and hydroxyapatite (HA) composite by this project have returned promising results in the extrusion of an FFF filament of such a composite. Test prints and reproducibility of the method were successful. The production method outlined here also showed that HA can be thoroughly dispersed within a polymer matrix without using solvents – this is relevant to the implementation of similar composites with other polymers and ceramics.

- Overall results for characterisation of 3D-printed structures made from the composite were comparable to those obtained for pure PLA. The compositing process did not affect polymer crystallinity beyond what FFF does by itself, although mechanical properties did decrease significantly with respect to pure PLA. This is in contrast to other studies on PLA-HA composites (manufactured through other methods), where addition of HA and similar ceramics was reported to increase mechanical performance [298,407] – this appears to be unique to 3D-printed parts. Only a slight but significant decrease in molecular weight was measured after 3DP of the composite.
- The initial in vitro biocompatibility testing carried out in this project suggests that the processes of compositing and FFF are biologically safe. Cell response to the three HA concentrations studied (5%, 10%, and 20% by weight) was equivalent to tissue-culture plastic. Osteogenicity indicators suggested that a higher concentration of HA would yield higher extracellular matrix deposition and mineralisation. However, the 20% by weight concentration was found to hinder composite processability for this application. The 10% by weight concentration was found to be a good compromise between cell-response benefits and material machinability properties. These observations are relevant for the production of this and other FFF polymer-ceramic composites.

- *In vitro* testing with the MG-63 cell-line was overall favourable, with 3D-printed materials performing equivalent or better than tissue culture plastic in cell survivability and collagen and calcium deposition. These results suggest that the manufacturing methods reported in this work would only require reasonable adjustments (like sterilizing the filament extruder and 3D-printer, and using medical-grade raw materials) to move forward to *ex vivo* and *in vivo* testing for biocompatibility, bone-regeneration capabilities, and implant *in vivo* degradation. The tests conducted on 3D structures were also promising in regards to the material's geometry being hospitable to cells, as well as providing a reliable attachment surface. Similar to what was expected, the addition of hydroxyapatite to the polymer matrix modestly influenced the response of osteogenic cells, as the literature suggests [136,298]. Although far from conclusive, these results are at least promising for other projects pursuing the development of this technology, especially looking towards *ex vivo* and *in vivo* testing. As far as biocompatibility of 3D-printed parts is concerned, this work provides evidence that FFF is safe for use in *in vitro* tissue engineering, though testing with less resilient cell-lines should not be disregarded.
- The design procedure proposed in this work is meant to address not only the eventualities of implementing FFF in the fabrication of implantable devices and tissue engineering scaffolds, but is intended as well to tackle some of the common concerns of bone regeneration materials. Such concerns include void content of the geometries, open

porosity, maximised surface area for cell attachment, and patient-specific anatomical design. It also bears consideration to practical computer-assisted engineering/design issues like implementation of the design procedure, and standard software capabilities, such that it can be followed easily and using virtually any design software. All of the above are tailored to fit FFF technologies, within the scope of their virtues and limitations.

- Accelerated degradation tests (ADT) carried out in this work were relatively consistent with the behaviours reported in the literature. As expected, degradation of PLA 3D-printed parts proceeded faster than it has been documented for similar solid structures of PLA. Thermal treatment of the printed material in the form of an annealing procedure showed little effect on its degradation behaviour in both types of PLA investigated in this research, except in the case of elasticity modulus for VB-PLA, which is more crystalline, and of higher molecular weight than BFB-PLA. Annealing, however, drastically modified the macroscopic mode of degradation of the materials, allowing them to retain their integrity longer, at the expense of reduced elasticity and increased deformation during degradation. These characteristics can factor in when producing implants, since both will very likely contribute to a faster structural failure, which might be desirable for absorbable devices.
- Results for the modified accelerated dissolution test using acetone indicate that it could potentially be used as a shorthand method for

estimating the mode of mechanical failure of structures or devices made of lactide polymers. Thermal analysis of samples subjected to this procedure showed similar trends to those reported in the literature for these materials for accelerated degradation methods, and the solvent's attack seems to focus as expected on the weaker layer-layer interfaces of the 3DP parts. This could in principle be indicative of how a given device would fail due to degradation, but more work would be required to validate this idea.

- The data derived from Accelerated Degradation Tests (ADT) experiments performed on this research yielded some potential mathematical models for prediction of molecular weight behaviour during polymer degradation. Although not entirely predictive, the relationships found during this work can be applied to abridge the laboratory work required to fully characterise degradation of PLA – the ideas presented here could also be applied to different polymers. These potential models are meant to complement the existing Arrhenius relation – which allows for extrapolation of experimental setups –, with the possibility of extrapolating results for different starting conditions of the material being analysed – namely from a variety of molecular weights. Further research into this topic will gradually become more important, as faster methods for characterising medical polymers produced on-site through different 3D-printing methods become widespread-available – especially with respect to surgical implants.

This project produced evidence on the basic science of FFF as a safe manufacturing method for 3D-printing bone-regeneration materials. It also showed that the mixing and melting compositing method used to produce the PLA-HA composites was effective at achieving an uniform FFF filament and 3D-printing parts. Additionally, considering the positive results from the *in vitro* testing done for this project, it is reasonable to state that these and similar materials and techniques could be eventually validated for clinical use. Naturally, these could benefit from further reproduction, as well as measurement of more or different variables which were beyond the scope of this project. A considerable amount of additional work would be required to follow up on this line of research, almost certainly requiring a multi-disciplinary collaboration. The most immediate of these details are discussed in the following section.

8. FURTHER WORK

The work and results presented so far in this research point towards complementary and deeper questions to be answered. One of first areas this author would like to be tackled is the completion of the degradation data compilation. The mADT and ADT profiles and the mathematical models proposed to this point will benefit from further experimental data. This data gathering should be relatively straight-forward, since further time periods can be determined from the data gathered on this work.

Furthermore, given the positive biocompatibility and osteogenic tests carried out, it would seem reasonable to commence pursuit of *ex vivo* and *in vivo* testing to determine if FFF and compositing have any effect at all on the well-studied advantages of PLA. Posteriorly – and potentially in critical-size defects or calvarial defects –, this testing would be required on 3D models patterned and designed under the procedure described in this research, in order to study their viability as an artificial graft, their osteoconduction and osteointegration, as well as other potential methods for surface functionalisation of this material. As of this point, it is considered that, should these materials and models be prone to osteointegration, it will be a reliable indicator that the techniques described on this project can be successfully implemented in implant production.

Finally, it is of the utmost importance to ground the base science developed in this research in the clinical reality in which it is meant to be implemented. A relevant step in this direction would be the design and production of prototype

implants based on actual CT scans of cleft palate and other facial reconstruction patients. Considerable knowledge can be drawn from such an exercise, including considerations regarding fixation methods for implants produced as intended in this work. As well, it would be illustrative in regards to at least some part of the perioperative, intraoperative, and postoperative considerations that would go into implementing this technology.

9. PUBLICATIONS ARISING FROM THE THESIS

9.1. PEER-REVIEWED PUBLICATIONS IN PREPARATION

C. A. Orozco-Díaz, R. Moorehead, G. Reilly, F. Gilchrist, C. Miller. (2019) Characterization of a composite polylactic acid-hydroxyapatite 3D-printing filament for bone-regeneration. The University of Sheffield, United Kingdom. Unpublished.

C. A. Orozco-Díaz, R. Moorehead, G. Reilly, F. Gilchrist, C. Miller. (2019) In-vitro degradation and 3D-biocompatibility of polylactic acid/hydroxyapatite-composite 3D-printed structures. The University of Sheffield, United Kingdom. Unpublished.

9.2. CONFERENCES

C. A. Orozco-Díaz, R. Moorehead, G. Reilly, F. Gilchrist, C. Miller. (2018) “In-Vitro Degradation and Biocompatibility of a Polylactic-Acid/Hydroxyapatite 3D-Printable Composite for Maxillofacial Bone Regeneration”. Presentation at the United Kingdom Society of Biomaterials Conference 2018, United Kingdom, Bath, 18th of May 2018.

C. A. Orozco-Díaz, R. Moorehead, G. Reilly, F. Gilchrist, C. Miller. (2018) “Development of a 3D-printable composite for paediatric maxillofacial bone regeneration implants”. Presentation at the International Conference on Bioengineering 2018, Czech Republic, Prague, 3rd of September 2018.

C. A. Orozco-Díaz, R. Moorehead, G. Reilly, F. Gilchrist, C. Miller. (2017) “Production and Characterisation of a PLA-HA composite 3D-Printing Filament for Bone Regeneration Applications in Maxillofacial Reconstruction.” Presentation at Medical Engineering Initiative Bioeng/Medical Physics and Engineering Conference, MEDIBioeng/MPEC 2017, United Kingdom, Esher, 13th of September 2017.

10. REFERENCES

- [1] F.A. Probst, D.W. Hutmacher, D.F. Müller, H.-G. Machens, J.-T. Schantz, Calvarial reconstruction by customized bioactive implant., *Handchirurgie, Mikrochirurgie, Plast. Chir. Organ Der Deutschsprachigen Arbeitsgemeinschaft Für Handchirurgie Organ Der Deutschsprachigen Arbeitsgemeinschaft Für Mikrochirurgie Der Peripher. Nerven Und Gefäße Organ Der Vereinigung Der D.* 42 (2010) 369–73. doi:10.1055/s-0030-1248310.
- [2] Xichen Zhang, U.P. Wyss, D. Pichora, M.F.A. Goosen, An Investigation of Poly(lactic acid) Degradation, *J. Bioact. Compat. Polym.* 9 (1994) 80–100. doi:10.1177/088391159400900105.
- [3] Q. Chen, C. Zhu, G.A. Thouas, Progress and challenges in biomaterials used for bone tissue engineering: bioactive glasses and elastomeric composites, *Prog. Biomater.* 1 (2012) 2. doi:10.1186/2194-0517-1-2.
- [4] R.A. Sousa, R.L. Reis, A.M. Cunha, M.J. Bevis, Processing and properties of bone-analogue biodegradable and bioinert polymeric composites, *Compos. Sci. Technol.* 63 (2003) 389–402. doi:10.1016/S0266-3538(02)00213-0.
- [5] G.M. Cunniffe, F.J. O'Brien, S. Partap, T.J. Levingstone, K.T. Stanton, G.R. Dickson, The synthesis and characterization of nanophase hydroxyapatite using a novel dispersant-aided precipitation method, *J. Biomed. Mater. Res. - Part A.* 95 (2010) 1142–1149. doi:10.1002/jbm.a.32931.
- [6] A. Rainer, P. Mozetic, S.M. Giannitelli, D. Accoto, S. De Porcellinis, E. Guglielmelli, M. Trombetta, Computer-aided tissue engineering for bone regeneration, *Proc. IEEE RAS EMBS Int. Conf. Biomed. Robot. Biomechatronics.* (2012) 473–476. doi:10.1109/BioRob.2012.6290894.
- [7] J. Korpela, A. Kokkari, H. Korhonen, M. Malin, T. Narhi, J. Seppälä, Biodegradable and bioactive porous scaffold structures prepared using fused deposition modeling, *J. Biomed. Mater. Res. - Part B Appl. Biomater.* 101 (2013) 610–619. doi:10.1002/jbm.b.32863.
- [8] M.A. Woodruff, C. Lange, J. Reichert, A. Berner, F. Chen, P. Fratzl,

- J.T. Schantz, D.W. Hutmacher, Bone tissue engineering: From bench to bedside, *Mater. Today*. 15 (2012) 430–435. doi:10.1016/S1369-7021(12)70194-3.
- [9] D. Joy, R. Probert, J.I. Bisson, J.P. Shepherd, Posttraumatic Stress Reactions after Injury, *J. Trauma-Injury Infect. Crit. Care*. 48 (2000) 490–494.
- [10] I. Bugge, G. Dyb, S.Ø. Stensland, Ø. Ekeberg, T. Wentzel-Larsen, T.H. Diseth, Physical injury and posttraumatic stress reactions. A study of the survivors of the 2011 shooting massacre on Utøya Island, Norway, *J. Psychosom. Res.* 79 (2015) 384–390. doi:10.1016/j.jpsychores.2015.09.005.
- [11] K.A. Athanasiou, G.G. Niederauer, C.M. Agrawal, Sterilization, toxicity, biocompatibility and clinical applications of polylactic acid/polyglycolic acid copolymers, *Biomaterials*. 17 (1996).
- [12] P. Törmälä, T. Pohjonen, P. Rokkanen, Bioabsorbable polymers: materials technology and surgical applications., *Proc. Inst. Mech. Eng. H*. 212 (1998) 101–111. doi:10.1243/0954411981533872.
- [13] A.L. Jardini, M.A. Larosa, R.M. Filho, C.A.D.C. Zavaglia, L.F. Bernardes, C.S. Lambert, D.R. Calderoni, P. Kharmandayan, Cranial reconstruction: 3D biomodel and custom-built implant created using additive manufacturing, *J. Cranio-Maxillofacial Surg.* 42 (2014) 1877–1884. doi:10.1016/j.jcms.2014.07.006.
- [14] S.A. Seifeldin, Is alveolar cleft reconstruction still controversial? (Review of literature), *Saudi Dent. J.* 28 (2016) 3–11. doi:10.1016/j.sdentj.2015.01.006.
- [15] W.B. Zhang, T. Liang, X. Peng, Mandibular growth after paediatric mandibular reconstruction with the vascularized free fibula flap: A systematic review, *Int. J. Oral Maxillofac. Surg.* 45 (2016) 440–447. doi:10.1016/j.ijom.2015.12.014.
- [16] M. Rashid, M.S. Tamimy, Ehtesham-UI-Haq, S.U.R. Sarwar, S.T.A. Rizvi, Benign paediatric mandibular tumours: Experience in reconstruction using vascularised fibula, *J. Plast. Reconstr. Aesthetic Surg.* 65 (2012) e325–e331. doi:10.1016/j.bjps.2012.07.006.
- [17] R.B. Ross, C. Treatment variables affecting facial growth in complete

- unilateral cleft lip and palate. Part 3, *Cleft Palate J.* 24 (1987) 5–77.
<http://www.ncbi.nlm.nih.gov/pubmed/3542303>.
- [18] R.B. Ross, F. Treatment variables affecting facial growth in complete unilateral cleft lip and palate. Part 6, *Cleft Palate J.* 24 (1987) 5–77.
<http://www.ncbi.nlm.nih.gov/pubmed/3542303>.
- [19] W. Schweckendiek, P.- Doz, Primary veloplasty: long-term results without maxillary deformity. A twenty-five year report, *Cleft Palate J.* 15 (1978) 268–74.
<http://digital.library.pitt.edu/c/cleftpalate/pdf/e20986v15n3.13.pdf>.
- [20] R.B. Ross, A. Treatment variables affecting facial growth in complete unilateral cleft lip and palate. Part 1: Treatment Affecting Growth, *Cleft Palate J.* 24 (1987) 5–77.
<http://www.ncbi.nlm.nih.gov/pubmed/3542303>.
- [21] M.T. Corbo Rodríguez, M.E. Marimón Torres, Labio Y Paladar Fisurados. Aspectos Generales Que Se Deben Conocer En La Atencion Primaria De Salud, *Rev Cuba. Med Gen Integr.* 17 (2001) 379–385.
- [22] L.N.R. Gómez García R., Incidencia de laio y paladar hendido en México: 2003-2006, *Rev. ADM.* LXVI (2008) 309–313.
- [23] a P. Vanderas, Incidence of cleft lip, cleft palate, and cleft lip and palate among races: a review., *Cleft Palate J.* 24 (1987) 216–225.
 doi:10.1002/(SICI)1096-8628(19980113)75:2<126::AID-AJMG2>3.0.CO;2-R.
- [24] M. Tolarova, J. Harris, Reduced recurrence of orofacial clefts after periconceptional supplementation with high-dose folic acid and multivitamins., *Teratology.* 51 (1995) 71–8.
 doi:10.1002/tera.1420510205.
- [25] S. Tavakolinejad, A. Ebrahimzadeh Bidskan, H. Ashraf, D. Hamidi Alamdari, A glance at methods for cleft palate repair., *Iran. Red Crescent Med. J.* 16 (2014) e15393. doi:10.5812/ircmj.15393.
- [26] R. Blanco, A. Colombo, J. Suazo, Maternal obesity is a risk factor for orofacial clefts: a meta-analysis, *Br. J. Oral Maxillofac. Surg.* 53 (2015) 699–704. doi:10.1016/j.bjoms.2015.05.017.
- [27] X. Fu, Y. Cheng, J. Yuan, C. Huang, H. Cheng, R. Zhou, Loss-of-

- function mutation in the X-linked TBX22 promoter disrupts an ETS-1 binding site and leads to cleft palate, *Hum. Genet.* 134 (2015) 147–158. doi:10.1007/s00439-014-1503-8.
- [28] J. Okano, S. Suzuki, K. Shiota, Involvement of apoptotic cell death and cell cycle perturbation in retinoic acid-induced cleft palate in mice., *Toxicol. Appl. Pharmacol.* 221 (2007) 42–56. doi:10.1016/j.taap.2007.02.019.
- [29] S. Simona, E. Dm, Considerations Regarding Age at Surgery and Fistula Incidence Using One- and Two-stage Closure for Cleft Palate, *Acta Medica Marisiensis.* 59 (2013) 302–305. doi:10.2478/amma-2013-0069.
- [30] T. Yamanishi, C. Kobayashi, I. Tsujimoto, H. Koizumi, S. Miya, Y. Yokota, R. Okamoto, S. Iida, T. Aikawa, H. Kohara, J. Nishio, M. Kogo, An uncommon cleft subtype of unilateral cleft lip and palate., *J. Dent. Res.* 87 (2008) 164–168. doi:10.1177/154405910808700212.
- [31] H.G. Programme, *World Atlas of Birth Defects*, (2003).
- [32] S.D. Colbert, B. Green, P.A. Brennan, N. Mercer, Contemporary management of cleft lip and palate in the United Kingdom. Have we reached the turning point?, *Br. J. Oral Maxillofac. Surg.* 53 (2015) 594–8. doi:10.1016/j.bjoms.2015.06.010.
- [33] Organización Mundial de la Salud, W.H. Federation, W. Organization Stroke, *Global Atlas on cardiovascular disease prevention and control*, (2011).
[http://www.ncdalliance.org/sites/default/files/rfiles/Global_Atlas_on_CV_D_Prevention_and_Control_smaller\[1\]_0.pdf](http://www.ncdalliance.org/sites/default/files/rfiles/Global_Atlas_on_CV_D_Prevention_and_Control_smaller[1]_0.pdf).
- [34] C.A. González-Osorio, C.E. Medina-Solís, A.P. Pontigo-Loyola, J.F. Casanova-Rosado, M. Escoffié-Ramírez, M.G. Corona-Tabares, G. Maupomé, Estudio ecológico en México (2003-2009) sobre labio y/o paladar hendido y factores sociodemográficos, socioeconómicos y de contaminación asociados, *An. Pediatria.* 74 (2011) 377–387. doi:10.1016/j.anpedi.2011.01.011.
- [35] I. Silva-Zolezzi, A. Hidalgo-Miranda, J. Estrada-Gil, J.C. Fernandez-Lopez, L. Uribe-Figueroa, A. Contreras, E. Balam-Ortiz, L. del Bosque-Plata, D. Velazquez-Fernandez, C. Lara, R. Goya, E. Hernandez-

- Lemus, C. Davila, E. Barrientos, S. March, G. Jimenez-Sanchez, Analysis of genomic diversity in Mexican Mestizo populations to develop genomic medicine in Mexico., *Proc. Natl. Acad. Sci. U. S. A.* 106 (2009) 8611–6. doi:10.1073/pnas.0903045106.
- [36] E.B. Katzel, P. Basile, P.F. Koltz, J.R. Marcus, J.A. Giroto, Current Surgical Practices in Cleft Care: Cleft Palate Repair Techniques and Postoperative Care, *Plast. Reconstr. Surg.* 124 (2009) 899–906. doi:10.1097/PRS.0b013e3181b03824.
- [37] S. Puwanun, Developing a tissue engineering strategy for cleft palate repair., University of Sheffield, 2014.
- [38] J. Lilja, Alveolar bone grafting, *Indian J. Plast. Surg.* 42 (2009) 110. doi:10.4103/0970-0358.57200.
- [39] P.H. de Moraes, S. Olate, M. Cantín, A.F. Assis, E. Santos, F. de O. Silva, L. de O. Silva, Anatomical Reproducibility through 3D Printing in Cranio-Maxillo-Facial Defects, *Int. J. Morphol.* 33 (2015) 826–830. doi:10.4067/S0717-95022015000300003.
- [40] P. Stoor, A. Suomalainen, C. Lindqvist, K. Mesimäki, D. Danielsson, A. Westermarck, R.K. Kontio, Rapid prototyped patient specific implants for reconstruction of orbital wall defects, *J. Cranio-Maxillofacial Surg.* 42 (2014) 1644–1649. doi:10.1016/j.jcms.2014.05.006.
- [41] A. Davis, Layer-by-Layer: The Evolution of 3-D Printing, *Inst. Electr. Electron. Eng. News Source Tech Focus. Tech Hist.* (2014). <http://theinstitute.ieee.org/technology-focus/technology-history/layerbylayer-the-evolution-of-3d-printing> (accessed April 1, 2014).
- [42] P. Olla, Opening Pandora's 3D Printed Box, (2015) 74–80.
- [43] A.F. Antas, F.J. Lino, Utilização das tecnologias de prototipagem rápida na área médica, *Design.* (2008) 2–4.
- [44] D. Espalin, K. Arcaute, D. Rodriguez, F. Medina, M. Posner, R. Wicker, Fused deposition modeling of patient-specific polymethylmethacrylate implants, *Rapid Prototyp. J.* 16 (2010) 164–173. doi:10.1108/13552541011034825.
- [45] H.N. Chia, B.M. Wu, Recent advances in 3D printing of biomaterials, *J. Biol. Eng.* 9 (2015) 4. doi:10.1186/s13036-015-0001-4.

- [46] A. Lazarides, D. Erdmann, D. Powers, W. Eward, Custom facial reconstruction for osteosarcoma of the jaw, *J. Oral Maxillofac. Surg.* 72 (2014) 2375.e1-2375.e10. doi:10.1016/j.joms.2014.07.018.
- [47] C.W. Hughes, K. Page, R. Bibb, J. Taylor, P. Revington, The custom-made titanium orbital floor prosthesis in reconstruction for orbital floor fractures., *Br. J. Oral Maxillofac. Surg.* 41 (2003) 50–53. doi:10.1016/S0266-4356(02)00249-8.
- [48] S. Mazzoni, A. Bianchi, G. Schiariti, G. Badiali, C. Marchetti, Computer-aided design and computer-aided manufacturing cutting guides and customized titanium plates are useful in upper maxilla waferless repositioning, *J. Oral Maxillofac. Surg.* 73 (2015) 701–707. doi:10.1016/j.joms.2014.10.028.
- [49] N.A.A. Weir, F.J.J. Buchanan, J.F.F. Orr, D.F.F. Farrar, A. Boyd, Processing, annealing and sterilisation of poly-L-lactide, *Biomaterials.* 25 (2004) 3939–3949. doi:10.1016/j.biomaterials.2003.10.076.
- [50] R. Porter, *Breve Historia de la Medicina: De la Antigüedad hasta Nuestros Días*, Taurus, Madrid, 2004.
- [51] G.E. Marks, *A Treatise on Artificial Limbs*, A. A. Marks, New York, 1888.
- [52] H.F. Hildebrand, Biomaterials - a history of 7000 years, *BioNanoMaterials.* 14 (2013) 119–133. doi:10.1515/bnm-2013-0014.
- [53] D.A. Harris, A.J. Fong, E.P. Buchanan, L. Monson, D. Khechoyan, S. Lam, History of synthetic materials in alloplastic cranioplasty, *Neurosurg. Focus.* 36 (2014) E20. doi:10.3171/2014.2.FOCUS13560.
- [54] V. Warne, Artificial Leg, *Vic. Rev.* 34 (2008) 29–33. <http://www.jstor.org/stable/41039105>.
- [55] D.S. Childress, D. Ph, Historical Aspects of Powered Limb Prostheses, *Clin. Prosthetics Orthot.* 9 (1985) 2–13.
- [56] G.B. Risse, Development of Anesthesia and Antisepsis, in: *Mending Bodies, Sav. Souls A Hist. Hosp.*, Oxford University Press, San Francisco, 1999.
- [57] F. Mary, The Disappearance of the Patient's Narrative and the Invention of Hospital Medicine, in: *Br. Med. an Age Reform*, Routledge, London, 1991: pp. 92–109.

- [58] R.H. Baughman, Playing Nature's Game with Artificial Muscles, *Sci. New Ser.* 308 (2005) 63–65.
- [59] K. Atsumi, History of artificial organs in Japan, *J. Artif. Organs.* 8 (2005) 1–12. doi:10.1007/s10047-004-0283-7.
- [60] Y. Nosé, Is It True That “Artificial Organ Development” Is Over?, *Artif. Organs.* 35 (2011) 679–681. doi:10.1111/j.1525-1594.2011.01299.x.
- [61] T. Agishi, Beyond a Boundary Between the Scientific Artificial Organ World and the Nonscientific Spiritual World, *Artif. Organs.* 36 (2012) 1012–1014. doi:10.1111/aor.12008.
- [62] M.C.Y. Heng, Wound healing in adult skin: Aiming for perfect regeneration, *Int. J. Dermatol.* 50 (2011) 1058–1066. doi:10.1111/j.1365-4632.2011.04940.x.
- [63] C.E. Gargett, H.P.T. Nguyen, L. Ye, Endometrial regeneration and endometrial stem/progenitor cells, *Rev. Endocr. Metab. Disord.* 13 (2012) 235–251. doi:10.1007/s11154-012-9221-9.
- [64] R. Ciecierski, M. Wisniewski, L. Paczek, [Liver regeneration], *Pol Merkur Lek.* 18 (2005) 473–477. doi:10.1016/B978-0-12-420128-6.00001-4.
- [65] C. Power, J.E.J. Rasko, Whither Prometheus' liver? Greek myth and the science of regeneration, *Ann. Intern. Med.* 149 (2008) 421–426. doi:10.7326/0003-4819-149-6-200809160-00009.
- [66] J. Wicker, K. Kamler, Current concepts in limb regeneration: A hand surgeon's perspective, *Ann. N. Y. Acad. Sci.* 1172 (2009) 95–109. doi:10.1111/j.1749-6632.2009.04413.x.
- [67] P. Vidal, M.G. Dickson, Regeneration of the distal phalanx: A case report, *J. Hand Surg.* 18 (1993) 230–233.
- [68] L.H. McKim, Regeneration of the Distal Phalanx., *Can. Med. Assoc. J.* 26 (1932) 549–50. doi:10.1136/bmj.1.5119.440.
- [69] L.E. Lindley, O. Stojadinovic, I. Pastar, M. Tomic-Canic, Biology and biomarkers for wound healing, *Plast. Reconstr. Surg.* 138 (2016) 18S–28S. doi:10.1097/PRS.0000000000002682.
- [70] C. Ventura, F. Bianchi, C. Cavallini, E. Olivi, R. Tassinari, The use of physical energy for tissue healing, *Eur. Hear. Journal, Suppl.* 17 (2015) A69–A73. doi:10.1093/eurheartj/suv010.

- [71] J.M. Saucedo, M.A. Yaffe, J.C. Berschback, W.K. Hsu, D.M. Kalainov, Platelet-rich plasma, *J. Hand Surg. Am.* 37 (2012) 587–589. doi:10.1016/j.jhsa.2011.12.026.
- [72] S.P. Franklin, E.E. Burke, S.P. Holmes, The effect of platelet-rich plasma on osseous healing in dogs undergoing high tibial osteotomy, *PLoS One.* 12 (2017). doi:10.1371/journal.pone.0177597.
- [73] A.M. Tambella, A.R. Attili, G. Dupré, A. Cantalamessa, S. Martin, V. Cuteri, S. Marcazzan, M. Del Fabbro, M. Del Fabbro, Platelet-rich plasma to treat experimentally- induced skin wounds in animals: A systematic review and meta-analysis, *PLoS One.* 13 (2018) e0191093. doi:10.1371/journal.pone.0191093.
- [74] B.J. Cole, V. Karas, K. Hussey, D.B. Merkow, K. Pilz, L.A. Fortier, Hyaluronic Acid Versus Platelet-Rich Plasma: A Prospective, Double-Blind Randomized Controlled Trial Comparing Clinical Outcomes and Effects on Intra-articular Biology for the Treatment of Knee Osteoarthritis, *Am. J. Sports Med.* 45 (2017) 339–346. doi:10.1177/0363546516665809.
- [75] J. Fitzpatrick, M. Bulsara, M.H. Zheng, The Effectiveness of Platelet-Rich Plasma in the Treatment of Tendinopathy, *Am. J. Sports Med.* 45 (2017) 226–233. doi:10.1177/0363546516643716.
- [76] M. Kieb, F. Sander, C. Prinz, S. Adam, A. Mau-Möller, R. Bader, K. Peters, T. Tischer, Platelet-Rich Plasma Powder: A New Preparation Method for the Standardization of Growth Factor Concentrations, *Am. J. Sports Med.* 45 (2017) 954–960. doi:10.1177/0363546516674475.
- [77] E. Marukawa, H. Oshina, G. Iino, K. Morita, K. Omura, Reduction of bone resorption by the application of platelet-rich plasma (PRP) in bone grafting of the alveolar cleft, *J. Cranio-Maxillofacial Surg.* 39 (2011) 278–283. doi:10.1016/j.jcms.2010.04.017.
- [78] C. Wu, W. Pan, C. Feng, Z. Su, Z. Duan, Q. Zheng, C. Hua, C. Li, Grafting materials for alveolar cleft reconstruction: a systematic review and best-evidence synthesis, *Int. J. Oral Maxillofac. Surg.* 47 (2018) 345–356. doi:10.1016/j.ijom.2017.08.003.
- [79] R. Kumar, G. Clermont, Y. Vodovotz, C.C. Chow, The dynamics of acute inflammation, *J. Theor. Biol.* 230 (2004) 145–155.

- doi:10.1016/j.jtbi.2004.04.044.
- [80] S.Y. Seong, P. Matzinger, Hydrophobicity: An ancient damage-associated molecular pattern that initiates innate immune responses, *Nat. Rev. Immunol.* 4 (2004) 469–478. doi:10.1038/nri1372.
- [81] E. Maverakis, K. Kim, M. Shimoda, M.E. Gershwin, F. Patel, R. Wilken, S. Raychaudhuri, L.R. Ruhaak, C.B. Lebrilla, Glycans in the immune system and The Altered Glycan Theory of Autoimmunity: A critical review, *J. Autoimmun.* 57 (2015) 1–13. doi:10.1016/j.jaut.2014.12.002.
- [82] N.K. Banda, M. Takahashi, K. Takahashi, G.L. Stahl, S. Hyatt, M. Glogowska, T.A. Wiles, Y. Endo, T. Fujita, V. Michael Holers, W.P. Arend, Mechanisms of mannose-binding lectin-associated serine proteases-1/3 activation of the alternative pathway of complement, *Mol. Immunol.* 49 (2011) 281–289. doi:10.1016/j.molimm.2011.08.021.
- [83] R.S. Mahla, M.C. Reddy, D. Vijaya Raghava Prasad, H. Kumar, Sweeten PAMPs: Role of sugar complexed PAMPs in innate immunity and vaccine biology, *Front. Immunol.* 4 (2013) 1–17. doi:10.3389/fimmu.2013.00248.
- [84] P. Nesargikar, B. Spiller, R. Chavez, The complement system: History, pathways, cascade and inhibitors, *Eur. J. Microbiol. Immunol.* 2 (2012) 103–111. doi:10.1556/EuJMI.2.2012.2.2.
- [85] A.T. Long, E. Kenne, R. Jung, T.A. Fuchs, T. Renné, Contact system revisited: An interface between inflammation, coagulation, and innate immunity, *J. Thromb. Haemost.* 14 (2016) 427–437. doi:10.1111/jth.13235.
- [86] B.B.C. Furie, B.B.C. Furie, Review series Thrombus formation in vivo, *J. Clin. Invest.* 115 (2005) 3355–3362. doi:10.1172/JCI26987.trical.
- [87] N.G. Frangogiannis, The extracellular matrix in myocardial injury, repair, and remodeling., *J. Clin. Invest.* 127 (2017) 1600–1612. doi:10.1172/JCI87491.
- [88] J.M. Estes, J.S.V. Berg, N.S. Adzick, T.E. MacGillivray, A. Desmoulière, G. Gabbiani, Phenotypic and functional features of myofibroblasts in sheep fetal wounds, *Differentiation.* 56 (1994) 173–181. doi:10.1046/j.1432-0436.1994.5630173.x.

- [89] M.W.J. Ferguson, S. O’Kane, Scar-free healing: from embryonic mechanisms to adult therapeutic intervention, *Philos. Trans. R. Soc. B Biol. Sci.* 359 (2004) 839–850. doi:10.1098/rstb.2004.1475.
- [90] J.R. Lieberman, G.E. Friedlaender, *Bone Regeneration and Repair: Biology and Clinical Applications*, Humana Press, Totowa, NJ, 2005. doi:10.1385/1592598633.
- [91] E.M. Bueno, J. Glowacki, *Biologic Foundations for Skeletal Tissue Engineering*, 2011. doi:10.2200/S00329ED1V01Y201101TIS007.
- [92] E.D. Pellegrino, R.M. Blitz, Mineralization in the chick embryo, *Calcif. Tissue Int.* 10 (1972) 128–135. doi:10.1007/BF02012542.
- [93] Y. Suetsugu, I. Shimoya, J. Tanaka, Configuration of Carbonate Ions in Apatite Structure Determined by Polarized Infrared Spectroscopy, *J. Am. Ceram. Soc.* 81 (1998) 746–748. doi:10.1111/j.1151-2916.1998.tb02403.x.
- [94] F.J. Cruz, J.N. Lopes, J.C. Calado, M.E. Minas da Piedade, A molecular dynamics study of the thermodynamic properties of calcium apatites. 1. Hexagonal phases, *J Phys Chem B.* 109 (2005) 24473–24479. doi:10.1021/jp054304p.
- [95] D.L. Worthley, M. Churchill, J.T. Compton, Y. Tailor, M. Rao, Y. Si, D. Levin, M.G. Schwartz, A. Uygur, Y. Hayakawa, S. Gross, B.W. Renz, W. Setlik, A.N. Martinez, X. Chen, S. Nizami, H.G. Lee, H.P. Kang, J.M. Caldwell, S. Asfaha, C.B. Westphalen, T. Graham, G. Jin, K. Nagar, H. Wang, M.A. Kheirbek, A. Kolhe, J. Carpenter, M. Glaire, A. Nair, S. Renders, N. Manieri, S. Muthupalani, J.G. Fox, M. Reichert, A.S. Giraud, R.F. Schwabe, J.P. Pradere, K. Walton, A. Prakash, D. Gumucio, A.K. Rustgi, T.S. Stappenbeck, R.A. Friedman, M.D. Gershon, P. Sims, T. Grikscheit, F.Y. Lee, G. Karsenty, S. Mukherjee, T.C. Wang, Gremlin 1 identifies a skeletal stem cell with bone, cartilage, and reticular stromal potential, *Cell.* 160 (2015) 269–284. doi:10.1016/j.cell.2014.11.042.
- [96] M. Pavelka, J. Roth, Osteoclast, in: *Funct. Ultrastruct.*, Springer Vienna, Vienna, 2010. doi:10.1007/978-3-211-99390-3_153.
- [97] M.E. HOLTROP, G.J. KING, The Ultrastructure of the Osteoclast and its Functional Implications, *Clin. Orthop. Relat. Res. NA*; (1977)

- 177???196. doi:10.1097/00003086-197703000-00062.
- [98] D. Duraccio, F. Mussano, M.G. Faga, Biomaterials for dental implants: current and future trends, *J. Mater. Sci.* 50 (2015) 4779–4812. doi:10.1007/s10853-015-9056-3.
- [99] C.M. Xiao, Rationalizing the development of biomaterials with a new way of thinking, *Chin. J. Integr. Med.* 17 (2011) 864–866. doi:10.1007/s11655-011-0801-4.
- [100] A.M. Shah, H. Jung, S. Skirboll, Materials used in cranioplasty: a history and analysis, *Neurosurg. Focus.* 36 (2014) E19. doi:10.3171/2014.2.FOCUS13561.
- [101] B.D. Ratner, A History of Biomaterials, *Biomater. Sci. An Introd. to Mater.* Third Ed. (2013) xli–liii. doi:10.1016/B978-0-08-087780-8.00154-6.
- [102] Repairing holes in the head - a history of cranioplasty.pdf, (n.d.).
- [103] A. Ducati, From Incan time to today, the unresolved problem of cranioplasty, *World Neurosurg.* 82 (2014) E439–E441. doi:10.1016/j.wneu.2013.07.089.
- [104] R. Assina, C.E. Sarris, A. Mammis, The history of craniotomy for headache treatment, *Neurosurg. Focus.* 36 (2014) E9. doi:10.3171/2014.1.FOCUS13549.
- [105] A. Sanan, S.J. Haines, Repairing holes in the head: A history of cranioplasty, *Neurosurgery.* 40 (1997) 588–603. doi:10.1097/00006123-199710000-00067.
- [106] M. Gosau, M. Schöneich, F.G. Draenert, T. Ettl, O. Driemel, T.E. Reichert, Retrospective analysis of orbital floor fractures-complications, outcome, and review of literature, *Clin. Oral Investig.* 15 (2011) 305–313. doi:10.1007/s00784-010-0385-y.
- [107] L. Zhou, P. Wang, H. Han, B. Li, H. Wang, G. Wang, J. Zhao, Y. Liu, W. Wu, Prototyped grafting plate for reconstruction of mandibular defects, *J. Cranio-Maxillofacial Surg.* 42 (2014) 1723–1729. doi:10.1016/j.jcms.2014.06.006.
- [108] A. Kantaros, N. Chatzidai, D. Karalekas, 3D printing-assisted design of scaffold structures, *Int. J. Adv. Manuf. Technol.* 82 (2016) 559–571. doi:10.1007/s00170-015-7386-6.

- [109] BKH, Searched Seas of Gold, (2011).
<http://wheretheairisrarified.blogspot.com/2011/06/searched-seas-of-gold.html> (accessed July 7, 2018).
- [110] M. Artico, L. Ferrante, F.S. Pastore, E.O. Ramundo, D. Cantarelli, D. Scopelliti, G. Iannetti, Bone autografting of the calvaria and craniofacial skeleton: Historical background, surgical results in a series of 15 patients, and review of the literature, *Surg. Neurol.* 60 (2003) 71–79. doi:10.1016/S0090-3019(03)00031-4.
- [111] J.J. van Meek 'ren, *Observationes Medico-Chirurgicae, Ex Officina Henrici el viduae Theodori Boom*, Italy, 1682.
- [112] M. Olaus, *Historiae de gentibus septentrionalibus*, Antverpiae: Apud Ioannem Bellerum, 1557.
- [113] S. Bhattacharya, V. Khanna, R. Kohli, Cleft lip: The historical perspective, *Indian J. Plast. Surg.* 42 (2009) 4. doi:10.4103/0970-0358.57180.
- [114] K. Reemtsma, *Xenotransplantation : A Historical Perspective*, 37 (2018) 26–28.
- [115] D. Hosler, S.L. Burkett, M.J. Tarkanian, Prehistoric polymers: Rubber processing in ancient Mesoamerica, *Science* (80-.). 284 (1999) 1988–1991. doi:10.1126/science.284.5422.1988.
- [116] A. Parkes, *Improvements in the Manufacture of Parkesine or Compound of Pyroxyline, and also Solutions of Pyroxyline known as collodion.*, No. 1313, 1865.
- [117] J.W. Hyatt, I.S. Hyatt, *Improvement in Treating and Molding Pyroxyline*, US105338A, 1870.
- [118] M. Vert, *Polymeric biomaterials: Strategies of the past vs. strategies of the future*, *Prog. Polym. Sci.* 32 (2007) 755–761. doi:10.1016/j.progpolymsci.2007.05.006.
- [119] D. Cam, S.H. Hyon, Y. Ikada, *Degradation of high molecular weight poly(L-lactide) in alkaline medium.*, *Biomaterials.* 16 (1995) 833–843. doi:10.1016/0142-9612(95)94144-A.
- [120] H.S. Azevedo, R.R.L. Reis, *Understanding the enzymatic degradation of biodegradable polymers and strategies to control their degradation rate*, *Biodegrad. Syst. Tissue* (2005) 177–202.

- doi:10.1201/9780203491232.ch12.
- [121] D.K. Gilding, A.M. Reed, Biodegradable polymers for use in surgery-polyglycolic/poly(lactic acid) homo- and copolymers: 1, *Polymer (Guildf)*. 20 (1979) 1459–1464. doi:10.1016/0032-3861(79)90009-0.
- [122] J.P. Levine, J.S. Bae, M. Soares, L.E. Brecht, P.B. Saadeh, D.J. Ceradini, D.L. Hirsch, Jaw in a day: Total maxillofacial reconstruction using digital technology, *Plast. Reconstr. Surg.* 131 (2013) 1386–1391. doi:10.1097/PRS.0b013e31828bd8d0.
- [123] L.L. Dincă, A. Banu, A. Vișan, Additive manufacturing in maxillofacial reconstruction, *MATEC Web Conf.* 137 (2017) 02001. doi:10.1051/mateconf/201713702001.
- [124] D. Rohner, R. Guijarro-Martínez, P. Bucher, B. Hammer, Importance of patient-specific intraoperative guides in complex maxillofacial reconstruction, *J. Cranio-Maxillofacial Surg.* 41 (2013) 382–390. doi:10.1016/j.jcms.2012.10.021.
- [125] J. Winder, R. Bibb, Medical Rapid Prototyping Technologies: State of the Art and Current Limitations for Application in Oral and Maxillofacial Surgery, *J. Oral Maxillofac. Surg.* 63 (2005) 1006–1015. doi:10.1016/j.joms.2005.03.016.
- [126] R.R.M. Bos, F.R. Rozema, G. Boering, A.J. Nijenhuis, A.J. Pennings, H.W.B. Jansen, Bone-plates and screws of bioabsorbable poly (L-lactide) An animal pilot study, *Br. J. Oral Maxillofac. Surg.* 27 (1989) 467–476. doi:10.1016/S0266-4356(89)80004-X.
- [127] E.J. Bergsma, F.R. Rozema, R.R. Bos, W.C. de Bruijn, Foreign body reactions to resorbable poly(L-lactide) bone plates and screws used for the fixation of unstable zygomatic fractures., *J. Oral Maxillofac. Surg.* 51 (1993) 666–670. doi:10.1016/S0278-2391(10)80267-8.
- [128] F.W. Cordewener, R.R. Bos, F.R. Rozema, W. a Houtman, Poly(L-lactide) implants for repair of human orbital floor defects: clinical and magnetic resonance imaging evaluation of long-term results., *J. Oral Maxillofac. Surg.* 54 (1996) 9-13; discussion 13–4.
- [129] S. Macneil, Biomaterials for Tissue Engineering, in: *Introd. to Tissue Eng. Appl. Challenges*, 2008: pp. 26–35.
- [130] L.C. Becker, W.F. Bergfeld, D. V. Belsito, R.A. Hill, C.D. Klaassen,

- D.C. Liebler, J.G. Marks, R.C. Shank, T.J. Slaga, P.W. Snyder, F.A. Andersen, Final Report of the cosmetic ingredient review expert panel safety assessment of polymethyl methacrylate (PMMA), methyl methacrylate crosspolymer, and methyl methacrylate/glycol dimethacrylate crosspolymer, *Int. J. Toxicol.* 30 (2011). doi:10.1177/1091581811407352.
- [131] M. Horwich, Hernia repair using nylon tricot implant, *Br. J. Surg.* 45 (1958) 320–322. doi:10.1002/bjs.18004519204.
- [132] H.J. Brody, Complications of expanded polytetrafluoroethylene (e-PTFE) facial implant, *Dermatologic Surg.* 27 (2001) 792–794. doi:10.1046/j.1524-4725.2001.01014.x.
- [133] A. Cucchi, E. Vignudelli, A. Napolitano, C. Marchetti, G. Corinaldesi, Evaluation of complication rates and vertical bone gain after guided bone regeneration with non-resorbable membranes versus titanium meshes and resorbable membranes. A randomized clinical trial, *Clin. Implant Dent. Relat. Res.* 19 (2017) 821–832. doi:10.1111/cid.12520.
- [134] J.S.T. Yao, M.K. Eskandari, Accidental discovery: The polytetrafluoroethylene graft, *Surgery.* 151 (2012) 126–128. doi:10.1016/j.surg.2011.09.036.
- [135] A. Kantaros, N. Chatzidai, D. Karalekas, 3D printing-assisted design of scaffold structures, *Biomaterials.* 16 (2015) 1–4. doi:10.1007/s00170-015-7386-6.
- [136] T. Kasuga, Y. Ota, M. Nogami, Y. Abe, Preparation and mechanical properties of polylactic acid composites containing hydroxyapatite "bers, *Powder Metall.* 22 (2001) 19–23.
- [137] D.E. Henton, P. Gruber, J. Lunt, J. Randall, Polylactic Acid Technology, *Nat. Fibers, Biopolym. Biocomposites.* (2005) 527–578. doi:10.1201/9780203508206.ch16.
- [138] D. Rosenzweig, E. Carelli, T. Steffen, P. Jarzem, L. Haglund, 3D-Printed ABS and PLA Scaffolds for Cartilage and Nucleus Pulposus Tissue Regeneration, *Int. J. Mol. Sci.* 16 (2015) 15118–15135. doi:10.3390/ijms160715118.
- [139] M. Oztel, B. Rahmel, F. Oms, M. Van Genechten, F. Oms, A Tip for the Reconstruction of Larger Maxillary Defects in Complicated Cleft

- Patients, 55 (2018) 132–135. doi:10.1177/1055665617723917.
- [140] D. Deluiz, L. Santos Oliveira, F. Ramı̃ez Pires, T. Reiner, L. Armada, M.A. Nunes, E. Muniz Barretto Tinoco, Incorporation and Remodeling of Bone Block Allografts in the Maxillary Reconstruction: A Randomized Clinical Trial, *Clin. Implant Dent. Relat. Res.* 19 (2017) 180–194. doi:10.1111/cid.12441.
- [141] M. Fukuda, T. Takahashi, M. Iino, Dentoalveolar reconstruction of a missing premaxilla using bone graft and endosteal implants, *J. Oral Rehabil.* 30 (2003) 87–90. doi:10.1046/j.1365-2842.2003.00999.x.
- [142] M. Dudas, W.Y. Li, J. Kim, A. Yang, V. Kaartinen, Palatal fusion - Where do the midline cells go?. A review on cleft palate, a major human birth defect, *Acta Histochem.* 109 (2007) 1–14. doi:10.1016/j.acthis.2006.05.009.
- [143] A.J.. Luijsterburg, C. Vermeij-Keers, Ten Years Recording Common Oral Clefts With a New Descriptive System, *Cleft Palate-Craniofacial J.* 48 (2011) 173–182. doi:10.1597/08-150.
- [144] A.W. Smith, A.K. Khoo, I.T. Jackson, A modification of the Kernahan “Y” classification in cleft lip and palate deformities., *Plast. Reconstr. Surg.* 102 (1998) 1842–1847. doi:10.1097/00006534-199911000-00058.
- [145] M. Khan, H. Ullah, S. Naz, T. Iqbal, T. Ullah, M. Tahir, O. Ullah, A revised classification of the cleft lip and palate., *Can. J. Plast. Surg.* 21 (2013) 48–50.
<http://www.pubmedcentral.nih.gov/articlerender.fcgi?artid=3891101&tool=pmcentrez&rendertype=abstract>.
- [146] A.R. Burdi, State-of-Art: Epidemiology. Section I: Epidemiology, Etiology and Pathogenesis of Cleft Lip and Palate, *Cleft Palate J.* 14 (1977) 262–269.
- [147] A. Burdi, M. Feingold, K.S. Larsson, L.I. Leck, E.F. Zimmerman, F.C. Fraser, Etiology and pathogenesis of congenital cleft lip and cleft palate, an NIDR state of the art report, *Teratology.* 6 (1972) 255–268. doi:10.1002/tera.1420060302.
- [148] I.P. Krapels, C. Vermeij-Keers, M. Müller, A. de Klein, R.P. Steegers-Theunissen, Nutrition and genes in the development of orofacial

- clefting., *Nutr. Rev.* 64 (2006) 280–288. doi:10.1301/nr.2006.jun.280.
- [149] C. Braybrook, K. Doudney, a C. Marçano, a Arnason, a Bjornsson, M. a Patton, P.J. Goodfellow, G.E. Moore, P. Stanier, The T-box transcription factor gene TBX22 is mutated in X-linked cleft palate and ankyloglossia., *Nat. Genet.* 29 (2001) 179–183. doi:10.1038/ng730.
- [150] S. Kondo, B.C. Schutte, R.J. Richardson, B.C. Bjork, S. Daack-hirsch, A. Sander, D.M. Mcdonald-mcginn, E.H. Zackai, Mutations in IRF6 cause Van der Woude and popliteal pterygium syndromes, 32 (2011) 285–289. doi:10.1038/ng985.Mutations.
- [151] S.S. Kohli, V.S. Kohli, A comprehensive review of the genetic basis of cleft lip and palate, *J Oral Maxillofac Pathol.* 16 (2012) 64–72. doi:10.4103/0973-029X.92976rJOMFP-16-64 [pii].
- [152] B.L. Eppley, J. a van Aalst, A. Robey, R.J. Havlik, a M. Sadove, The spectrum of orofacial clefting., *Plast. Reconstr. Surg.* 115 (2005) 101e–114e. doi:10.1097/01.PRS.0000164494.45986.91.
- [153] M.M.G. Ackermans, H. Zhou, C.E.L. Carels, F. a D.T.G. Wagener, J.W. Von den Hoff, Vitamin A and clefting: putative biological mechanisms., *Nutr. Rev.* 69 (2011) 613–24. doi:10.1111/j.1753-4887.2011.00425.x.
- [154] I.P.C. Krapels, I.A.L.M. Rooij, R.A. Wevers, G.A. Zielhuis, P.H.M. Spauwen, W. Brussel, R.P.M. Steegers-Theunissen, *Myo*-inositol, glucose and zinc status as risk factors for non-syndromic cleft lip with or without cleft palate in offspring: a case-control study, *BJOG An Int. J. Obstet. Gynaecol.* 111 (2004) 661–668. <http://www.blackwell-synergy.com/links/doi/10.1111/j.1471-0528.2004.00171.x/abs>.
- [155] M. Vinceti, C. Malagoli, K.J. Rothman, R. Rodolfi, G. Astolfi, E. Calzolari, A. Puccini, M. Bertolotti, M. Lunt, L. Paterlini, M. Martini, F. Nicolini, Risk of birth defects associated with maternal pregestational diabetes., *Eur. J. Epidemiol.* 29 (2014) 411–8. doi:10.1007/s10654-014-9913-4.
- [156] P. Stanier, S.. Forbes, A. Arnason, A. Bjornsson, E. Sveinbjornsdottir, R. Williamson, G. Moore, The Localization of a gene causing X-linked cleft palate and ankyloglossia (CPX) in an Icelandic kindred is between DXS326 and DXYS1X., *Genomics.* 17 (1993) 549–555.

- doi:10.1006/geno.1993.1370.
- [157] K. Suzuki, D. Hu, T. Bustos, J. Zlotogora, a Richieri-Costa, J. a Helms, R. a Spritz, Mutations of PVRL1, encoding a cell-cell adhesion molecule/herpesvirus receptor, in cleft lip/palate-ectodermal dysplasia., *Nat. Genet.* 25 (2000) 427–430. doi:10.1038/78119.
- [158] R.A.S. Mehmet A. Sözen, Koji Suzuki, Marie M. Tolarova, Tania Bustos, Jesús E. Fernández Iglesias, Mutation of PVRL1 is associated with sporadic, non-syndromic cleft lip/palate in northern Venezuela, *Nat. Genet.* 29 (2001) 141–142.
<http://www.nature.com/ng/journal/v29/n2/full/ng740.html>.
- [159] L. Eppley, Alveolar Cleft Bone Grafting Primary (Part I): Bone Grafting, (1996) 74–82.
- [160] R. Gorlin, M. Cohen, S. Levin, *Syndromes of the Head and Neck*, Oxford University Press, Oxford, 1990.
- [161] D.F. Wyszynski, T. Wu, Use of U.S. birth certificate data to estimate the risk of maternal cigarette smoking for oral clefting, *Cleft Palate-Craniofacial J.* 39 (2002) 188–192. doi:10.1597/1545-1569(2002)039<0188:UOUSBC>2.0.CO;2.
- [162] I.A.L.M. Van Rooij, M.J.M. Wegerif, H.M.J. Roelofs, H.M. Wilbert, G.A. Zielhuis, H.M.W.M. Merkus, P. Régine, S. Epidemiology, N. Sep, A. Iris, Smoking , Genetic Polymorphisms in Biotransformation Enzymes , and Nonsyndromic Oral Clefting : A Gene-Environment Interaction
Linked references are available on JSTOR for this article :, (2015).
- [163] M. Durner, D.A. Greenberg, A. V Delgado-Escueta, Is there a genetic relationship between epilepsy and birth defects?, *Neurology.* 42 (1992) 63–7. <http://www.ncbi.nlm.nih.gov/pubmed/1574178>.
- [164] B. Zhang, X. Jiao, L. Mao, J. Xue, Maternal cigarette smoking and the associated risk of having a child with orofacial clefts in China: A case-control study, *J. Cranio-Maxillofacial Surg.* 39 (2011) 313–318. doi:10.1016/j.jcms.2010.07.005.
- [165] G.M. Shaw, E.J. Lammer, Maternal periconceptional alcohol consumption and risk for orofacial clefts., *J. Pediatr.* 134 (1999) 298–303. doi:10.1093/aje/kwm146.
- [166] N. Natsume, T. Kawai, N. Ogi, W. Yoshida, Maternal risk factors in

- cleft lip and palate : case control study, (2000) 23–25.
doi:10.1054/bjom.1998.0133.
- [167] J. Hall, F. Solehdin, Folic acid for the prevention of congenital anomalies., *Eur. J. Pediatr.* 157 (1998) 445–50.
doi:10.1007/s004310050850.
- [168] a. Ejdesjo, P. Wentzel, U.J. Eriksson, Influence of maternal metabolism and parental genetics on fetal maldevelopment in diabetic rat pregnancy, *AJP Endocrinol. Metab.* 302 (2012) E1198–E1209.
doi:10.1152/ajpendo.00661.2011.
- [169] F. Özgür, T. Doğan, Acquired Clefting as a Consequence of Palate Infection, *Plast. Reconstr. Surg.* 104 (1999) 1934.
- [170] N. Tetsuya, N. Natsume, T. Kawai, STAPHYLOCOCCUS-AUREUS INFLAMMATION AND CLEFT-PALATE IN MICE, *Plast. Reconstr. Surg.* 85 (1990) 637.
- [171] E. Teng, D.M. Steinbacher, Repair of the Cocaine-Induced Cleft Palate Using the Modified Double-Opposing Z-Plasty, *Cleft Palate-Craniofacial J.* 50 (2013) 494–497. doi:10.1597/11-178.
- [172] A. Baylis, *Head and Neck Embryology : An Overview of Development , Growth and Defect in the Human Fetus*, (2009).
- [173] J.O. Bush, R. Jiang, Palatogenesis: morphogenetic and molecular mechanisms of secondary palate development, *Development.* 139 (2012) 828–828. doi:10.1242/dev.079152.
- [174] T. Tamura, R.L. Goldenberg, Zinc nutriture and pregnancy outcome, *Nutr. Res.* 16 (1996) 139–181. doi:10.1016/0271-5317(95)02068-3.
- [175] H. Gray, *Anatomy of the Human Body*, 1st ed., LEA & FEBIGER, Philadelphia, 1918.
- [176] P.M. Som, T.P. Naidich, *Illustrated Review of the Embryology and Development of the Facial Region , Part 2 : Late Development of the Fetal Face and Changes in the Face from the Newborn to Adulthood*, (2014) 1–9. doi:10.3174/ajnr.A3414.
- [177] L. Meng, Z. Bian, R. Torensma, J.W. Von den Hoff, Biological mechanisms in palatogenesis and cleft palate., *J. Dent. Res.* 88 (2009) 22–33. doi:10.1177/0022034508327868.
- [178] C. Lorente, S. Cordier, A. Bergeret, H.E.K. De Walle, J. Goujard, S.

- Aymé, R. Knill-Jones, E. Calzolari, F. Bianchi, Maternal occupational risk factors for oral clefts, *Scand. J. Work. Environ. Heal.* 26 (2000) 137–145.
- [179] D.-Z. Wang, G. Chen, Y.-M. Liao, S.-G. Liu, Z.-W. Gao, J. Hu, J.-H. Li, C.-H. Liao, A new approach to repairing cleft palate and acquired palatal defects with distraction osteogenesis., *Int. J. Oral Maxillofac. Surg.* 35 (2006) 718–26. doi:10.1016/j.ijom.2006.03.010.
- [180] B. Levi, S. Brugman, V.W. Wong, M. Grova, M.T. Longaker, D.C. Wan, Palatogenesis: Engineering, pathways and pathologies, *Organogenesis.* 7 (2011) 242–254. doi:10.4161/org.7.4.17926.
- [181] P. Blijdorp, P. Egyedi, The influence of age at operation for clefts on the development of the jaws., *J. Maxillofac. Surg.* 12 (1984) 193–200. doi:10.1097/00006534-198610000-00056.
- [182] P. Blijdorp, H. Miiller, The Influence of the Age at which the Palate is Closed on Speech in the Adult Cleft Patient, *J. Maxillofac. Surger.* 12 (1984) 239–246.
- [183] K. Agrawal, Cleft palate repair and variations, *Indian J. Plast. Surg.* 42 (2009) 102. doi:10.4103/0970-0358.57197.
- [184] J. Lilja, A. Kalaaji, H. Friede, A. Elander, Combined bone grafting and delayed closure of the hard palate in patients with unilateral cleft lip and palate: facilitation of lateral incisor eruption and evaluation of indicators for timing of the procedure, *Cleft Palate. Craniofac. J.* 37 (2000) 98–105. doi:10.1597/1545-1569(2000)037<0098:CBGADC>2.3.CO;2.
- [185] M. Ohishi, Y. Miyanoshita, A. Suzuki, K. Goto, A Revised Method of Conservative Palatoplasty, *J. Cranio-Maxillofacial Surg.* 20 (1992) 198–202.
- [186] W. Schweckendiek, *Nasal Abnormalities in Facial Clefts*, (1976).
- [187] B. Hartung, W. Schweckendiek, S. Clinic, D.-M. L, H.W. Schwe, *Malformations of the Ear in Cleft Palate Patients*, (1973) 253–258.
- [188] V.P. Blair, J.B. Brown, The dieffenbach-warren operation for closure of the congenitally cleft palate, *Int. J. Orthod. Oral Surg.* 22 (1936) 853–868. doi:10.1016/S1072-3498(36)80108-3.
- [189] J.C. WARREN, *On an Operation for the Cure of Natural Fissure of the*

- Soft Palate, *Am. J. Med. Sci.* 5 (1828).
- [190] Robert, *Memoires sur different objet de medicin*, Masson & Cie, Paris, 1764.
- [191] Robert, *Traite de principaux objets de médecine, avec un sommaire de la plûpär des these soutenues aux Ecoles de Paris, depuis 1762 jusqu'en 1746*. Vol I, Chez Lacombe, Paris, 1766.
- [192] B.R.C. v Langenbeck, *Operation der angeborenen totalen Spaltung des harten Gaumens nach einer neuen Method*, Deutsche Klinik, 1861.
- [193] A. Rajendran, S. Sundaram, *Shafer's Textbook of Oral Pathology*, 7th ed., Elsevier India, 2014.
- [194] B. Johanson, Å. Ohlsson, H. Friede, J. Ahlgren, *A Follow-Up Study of Cleft Lip and Palate Patients Treated with Orthodontics, Secondary Bone Grafting, and Prosthetic Rehabilitation*, *Scand. J. Plast. Reconstr. Surg. Hand Surg.* 8 (1974) 121–135.
doi:10.3109/02844317409084381.
- [195] F.O.R. The, *O. On, Bone-Graft Substitutes : Facts , Fictions , and Applications*, (2001).
- [196] K.K.H. Gundlach, J. Bardach, D. Filippow, F. Stahl-De Castrillon, J.H. Lenz, *Two-stage palatoplasty, is it still a valuable treatment protocol for patients with a cleft of lip, alveolus, and palate?*, *J. Cranio-Maxillofacial Surg.* 41 (2013) 62–70. doi:10.1016/j.jcms.2012.05.013.
- [197] L.T. Furlow, *Cleft palate repair by double opposing Z-plasty.*, *Plast. Reconstr. Surg.* 78 (1986) 724–738. doi:10.1097/00006534-198678060-00002.
- [198] R.E. Krischner, P. Wang, A.F. Jawad, M. Duran, M. Cohen, C. Solot, P. Randal, D. LaRossa, *Cleft-Palate Repair by Modified Furlow Double-Opposing Z-Plasty: The Children's Hospital of Philadelphia Experience*, *Plast. Reconstr. Surg.* 104 (1999) 1998–2001.
- [199] W.E.M. Wardill, *The technique of operation for cleft palate*, *Br. J. Surg.* 25 (1937) 117–130. doi:10.1002/bjs.1800259715.
- [200] R.B. Ross, *Treatment variables affecting facial growth in complete unilateral cleft lip and palate*. Part 7: An Overview of Treatment and Facial Growth, *Cleft Palate J.* 24 (1987) 71–77.
- [201] T.P. Kilner, *The management of the patient with cleft lip and/or palate*,

- Am. J. Surg. 95 (1958) 204–210. doi:10.1016/0002-9610(58)90503-8.
- [202] J. Bardach, Two-Flap palatoplasty: Bardach's technique, Oper. Tech. Plast. Reconstr. Surg. 2 (1995) 211–214. doi:10.1016/S1071-0949(06)80034-X.
- [203] K.Y. Lin, D. Goldberg, C. Williams, K. Borowitz, J. Persing, M. Edgerton, Long-Term Outcome Analysis of Two Treatment Methods for Cleft Palate: Combined Levator Retropositioning and Pharyngeal Flap Versus Double-Opposing Z-Plasty, Cleft Palate-Craniofacial J. 36 (1999) 73–78. doi:10.1597/1545-1569(1999)036<0073:LTOAOT>2.3.CO;2.
- [204] R.B. Ross, B. Treatment variables affecting facial growth in complete unilateral cleft lip and palate. Part 2, Cleft Palate J. 24 (1987) 5–77. <http://www.ncbi.nlm.nih.gov/pubmed/3542303>.
- [205] O. Herfert, Fundamental investigations into problems related to cleft palate surgery, Br. J. Plast. Surg. 11 (1958) 97–105. doi:10.1016/S0007-1226(58)80014-4.
- [206] C.R. Kremenak, W.C. Huffman, W.H. Olin, Growth of maxillae in dogs after palatal surgery. II., Cleft Palate J. 7 (1970) 719–736. doi:10.1097/00006534-196710000-00020.
- [207] C.R. Kremenak, W.C. Huffman, W.H. Olin, Growth of maxillae in dogs after palatal surgery. I., Cleft Palate J. 4 (1967) 6–17. <http://www.ncbi.nlm.nih.gov/pubmed/5225592>.
- [208] M.W. Ochs, P. li, Alveolar Cleft Bone Grafting Part II: Secondary Bone Grafting, Cleft Palate J. (1996) 83–88.
- [209] J. Nishio, T. Yamanishi, H. Kohara, Y. Hirano, M. Sako, T. Adachi, T. Mukai, S. Miya, Early two-stage palatoplasty using modified Furlow's veloplasty, Cleft Palate-Craniofacial J. 47 (2010) 73–81. doi:10.1597/08-067.1.
- [210] L. Eppley, Alveolar Cleft Bone Grafting Part I: Primary Bone Grafting, (1996) 74–82.
- [211] P.D. Hodgkinson, S. Brown, D. Duncan, C. Grant, A. Mcnaughton, P. Thomas, C.R. Mattick, Management Of Children With Cleft Lip And Palate: A Review Describing The Application Of Multidisciplinary Team Working In This CONDITION BASED UPON THE EXPERIENCES OF

- A REGIONAL CLEFT LIP AND PALATE CENTRE IN THE UNITED KINGDOM, *Fetal Matern. Med. Rev.* 16 (2005) 1–27.
doi:10.1017/S0965539505001452.
- [212] W. Schweckendiek, 30 Jahre Erfahrungen mit der primären Veloplastik, *Arch. Otorhinolaryngol.* 216 (1977) 501–502.
doi:10.1007/BF00458926.
- [213] R.B. Ross, Treatment variables affecting facial growth in complete unilateral cleft lip and palate. Part 5, *Cleft Palate J.* 24 (1987) 5–77.
<http://www.ncbi.nlm.nih.gov>.
- [214] A.H. Rehrmann, W.R. Koberg, H. Koch, Long-term postoperative results of primary and secondary bone grafting in complete clefts of lip and palate., *Cleft Palate J.* 7 (1970) 206–21.
- [215] M.D. Moore, W.T. Lawrence, J.J. Ptak, W.C. Trier, Complications of primary palatoplasty: a twenty-one-year review., *Cleft Palate J.* 25 (1988) 156–62. <http://www.ncbi.nlm.nih.gov/pubmed/3163291>.
- [216] K.M. Paine, J.T. Paliga, J. Fischer, Y. Tahiri, J.A. Taylor, K.M. Paine, Y. Tahiri, J. Fischer, A. Wes, B. The, A. College, N. Wink, J.A. Taylor, An Assessment of 30-Day Complications in Primary Cleft Palate Repair - A Review of the 2012 ACS NSQIP Pediatric The Status of Cleft Lip Repair - An Assessment Using the 2012 ACS NSQIP Pediatric A Preoperative Risk-Stratification Model for Medical and Surg, *Plast. Reconstr. Surg.* 134 (2012) 0–1. doi:10.1597/14-251.
- [217] M. Brown, C. Verheyden, Posterior fossa infarction following cleft palate repair and the arcuate foramen., *Plast. Reconstr. Surg.* 124 (2009) 237e–9e. doi:10.1097/PRS.0b013e3181b98bcb.
- [218] J.T. Hardwicke, G. Landini, B.M. Richard, Fistula Incidence after Primary Cleft Palate Repair, *Plast. Reconstr. Surg.* 134 (2014) 618e–627e. doi:10.1097/PRS.0000000000000548.
- [219] K. Agrawal, K.N. Panda, An Innovative Management of Detached Palatal Mucoperiosteal Flap from the Hard Palate (Hanging Palate), *Plast. Reconstr. Surg.* 115 (2005) 875–879.
doi:10.1097/01.PRS.0000153234.58643.44.
- [220] H. Maple, J. Chilcot, V. Lee, S. Simmonds, J. Weinman, N. Mamode, Brain , Behavior , and Immunity Stress predicts the trajectory of wound

- healing in living kidney donors as measured by high-resolution ultrasound, *Brain Behav. Immun.* 43 (2015) 19–26.
doi:10.1016/j.bbi.2014.06.012.
- [221] E. Broadbent, *Brain , Behavior , and Immunity Operating principles in surgical wound healing*, *Brain Behav. Immun.* 43 (2015) 17–18.
doi:10.1016/j.bbi.2014.09.010.
- [222] R.A. Hopper, R. Tse, J. Smartt, J. Swanson, S. Kinter, *Cleft Palate Repair and Velopharyngeal Dysfunction*, *Plast. Reconstr. Surg.* 133 (2014) 852e–864e. doi:10.1097/PRS.0000000000000184.
- [223] R.B. Ross, *Treatment variables affecting facial growth in complete unilateral cleft lip and palate. Part 5*, *Cleft Palate J.* 24 (1987) 5–77.
<http://www.ncbi.nlm.nih.gov/pubmed/3542303>.
- [224] E. Schmid, *Annäherung der Kieferstümpfe bei Lippen-Kiefer-Gaumenspalten: Ihre schädlichen Folgen und Vermeidung.*, *Fortschr Kiefer u Gesichtschir.* 1 (1955).
- [225] B. Loeffler, J. Kellam, S. Sims, M. Bosse, *Prospective Observational Study of Donor-Site Morbidity Following Anterior Iliac Crest Bone-Grafting in Orthopaedic Trauma Reconstruction Patients*, *J. Bone Jt. Surg.* 94 (2012) 1649–1654. doi:10.1016/S0021-9355(12)70453-8.
- [226] S.A. Lazarou, G.B. Contodimos, I.D. Gkegkes, *Correction of alveolar cleft with calcium-based bone substitutes.*, *J. Craniofac. Surg.* 22 (2011) 854–7. doi:10.1097/SCS.0b013e31820f7f19.
- [227] B.N. Summers, S.M. Eisenstein, *Donor site pain from the ilium. A complication of lumbar spine fusion*, *J. Bone Jt. Surgery, Br. Vol.* 71–B (1989) 677–680. <http://www.bjj.boneandjoint.org.uk/content/71-B/4/677.abstract>.
- [228] G. Kumar, B. Narayan, *Morbidity at bone graft donor sites*, *Class. Pap. Orthop.* (2014) 503–505. doi:10.1007/978-1-4471-5451-8_132.
- [229] J.S. Silber, D.G. Anderson, S.D. Daffner, B.T. Brislin, J.M. Leland, A.S. Hilibrand, A.R. Vaccaro, T.J. Albert, *Donor site morbidity after anterior iliac crest bone harvest for single-level anterior cervical discectomy and fusion.*, *Spine (Phila. Pa. 1976).* 28 (2003) 134–9.
doi:10.1097/01.BRS.0000041587.55176.67.
- [230] J.D. Martin-Smith, J.B. O’Sullivan, L. Duggan, A. O’Mahony, D.J.A.

- Orr, Repair of Anterior Cleft Palate Fistulae with Cancellous Bone Graft, *Plast. Reconstr. Surg.* 131 (2013) 380e–387e.
doi:10.1097/PRS.0b013e31827c7027.
- [231] Y.A.N. Yongnian, L.I. Shengjie, Z. Renji, L.I.N. Feng, Rapid Prototyping and Manufacturing Technology : Principle , Representative Technics , Applications , and Development Trends *, 14 (2009) 1–12.
- [232] F. Liu, H. Zhou, D. Li, Repair of STL errors, *Int. J. Prod. Res.* 47 (2008) 105–118. doi:10.1080/00207540701424539.
- [233] K. V. Wong, A. Hernandez, A Review of Additive Manufacturing, *ISRN Mech. Eng.* 2012 (2012) 1–10. doi:10.5402/2012/208760.
- [234] M. Szilvsi-Nagy, G. Mátyási, Analysis of STL files, *Math. Comput. Model.* 38 (2003) 945–960. doi:10.1016/S0895-7177(03)90079-3.
- [235] E. Huutilainen, R. Jaanimets, J. Tuomi, A. Mäkitie, J. Wolff, J. Valkeak, P. Marcin, M. Salmi, J. Tuomi, A. Mäkitie, J. Wolff, Inaccuracies in additive manufactured medical skull models caused by the DICOM to STL conversion process, *J. Cranio-Maxillofacial Surg.* 42 (2014) 259–265. doi:10.1016/j.jcms.2013.10.001.
- [236] T. Cai, F.J. Rybicki, A.A. Giannopoulos, K. Schultz, K.K. Kumamaru, P. Liacouras, S. Demehri, K.M. Shu Small, D. Mitsouras, The residual STL volume as a metric to evaluate accuracy and reproducibility of anatomic models for 3D printing: application in the validation of 3D-printable models of maxillofacial bone from reduced radiation dose CT images, *3D Print. Med.* 1 (2015) 2. doi:10.1186/s41205-015-0003-3.
- [237] N. Guo, M.C. Leu, Additive manufacturing: Technology, applications and research needs, *Front. Mech. Eng.* 8 (2013) 215–243. doi:10.1007/s11465-013-0248-8.
- [238] D.L. Bourell, Selective laser sintering of metals and ceramics, *Met. Powder Rep.* 48 (1993) 47. doi:10.1016/0026-0657(93)90473-6.
- [239] R. Landers, U. Hübner, R. Schmelzeisen, R. Mülhaupt, Rapid prototyping of scaffolds derived from thermoreversible hydrogels and tailored for applications in tissue engineering, *Biomaterials.* 23 (2002) 4437–4447. doi:10.1016/S0142-9612(02)00139-4.
- [240] S.S. Crump, Apparatus and Method for Creating Three-Dimensional Objects, (1992) 15.

- [241] J. Gardan, Additive manufacturing technologies: state of the art and trends, *Int. J. Prod. Res.* 7543 (2015) 1–15.
doi:10.1080/00207543.2015.1115909.
- [242] S.-H. Ahn, M. Montero, D. Odell, S. Roundy, P.K. Wright, Anisotropic material properties of fused deposition modeling ABS, *Rapid Prototyp. J.* 8 (2002) 248–257. doi:10.1108/13552540210441166.
- [243] W.K. Langford, T. Paper, Achieving Precise Flow in Fused Deposition Modeling Extruders, (2012).
- [244] R. van Noort, The future of dental devices is digital, *Dent. Mater.* 28 (2012) 3–12. doi:10.1016/j.dental.2011.10.014.
- [245] R. Bibb, D. Eggbeer, P. Evans, A. Bocca, A. Sugar, Rapid manufacture of custom-fitting surgical guides, *Rapid Prototyp. J.* 15 (2009) 346–354. doi:10.1108/13552540910993879.
- [246] S. Mihai, V. Filip, 3D Modeling and Performing of Orthopedic Implants by Material Deposition Rapid Prototyping, *Rom. Rev. Precis. Mech. Opt. Mechatronics.* (2012) 1–4.
- [247] R. Birla, Introduction to Tissue Engineering: Applications and Challenges, 11 (2014) 84–129. doi:10.1002/9781118886410.
- [248] M. Klein, C. Glatzer, Individual CAD/CAM fabricated glass-bioceramic implants in reconstructive surgery of the bony orbital floor., *Plast. Reconstr. Surg.* 117 (2006) 565–70.
doi:10.1097/01.prs.0000200770.83864.bc.
- [249] B.C. Kim, C.E. Lee, W. Park, M.K. Kim, P. Zhengguo, H.S. Yu, C.K. Yi, S.H. Lee, Clinical experiences of digital model surgery and the rapid-prototyped wafer for maxillary orthognathic surgery, *Oral Surgery, Oral Med. Oral Pathol. Oral Radiol. Endodontology.* 111 (2011) 278–285.
doi:10.1016/j.tripleo.2010.04.038.
- [250] M.A. Lopez-Heredia, J. Sohier, C. Gaillard, S. Quillard, M. Dorget, P. Layrolle, Rapid prototyped porous titanium coated with calcium phosphate as a scaffold for bone tissue engineering, *Biomaterials.* 29 (2008) 2608–2615. doi:10.1016/j.biomaterials.2008.02.021.
- [251] R. Guo, A.R. Merkel, J.A. Sterling, J.M. Davidson, S.A. Guelcher, Substrate modulus of 3D-printed scaffolds regulates the regenerative response in subcutaneous implants through the macrophage

- phenotype and Wnt signaling, *Biomaterials*. 73 (2015) 85–95.
doi:10.1016/j.biomaterials.2015.09.005.
- [252] and I.J.S.C. Fermeiro, J. B. L., M. R. A. Calado, State of the art and challenges in bioprinting technologies , contribution of the 3D bioprinting in Tissue Engineering, *Bioeng. (ENBENG)*, 2015 IEEE 4th Port. Meet. on. IEEE, 2015. (2015) 26–28.
doi:10.1109/ENBENG.2015.7088883.
- [253] D. Eggbeer, R. Bibb, P. Evans, L. Ji, Evaluation of direct and indirect additive manufacture of maxillofacial prostheses, *Proc. Inst. Mech. Eng. Part H-Journal Eng. Med.* 226 (2012) 718–728.
doi:10.1177/0954411912451826.
- [254] D. Ibrahim, T.L. Broilo, C. Heitz, M.G. de Oliveira, H.W. de Oliveira, S.M.W. Nobre, J.H.G. dos Santos Filho, D.N. Silva, Dimensional error of selective laser sintering, three-dimensional printing and PolyJet™ models in the reproduction of mandibular anatomy, *J. Cranio-Maxillofacial Surg.* 37 (2009) 167–173.
doi:10.1016/j.jcms.2008.10.008.
- [255] M. Salmi, K.S. Paloheimo, J. Tuomi, J. Wolff, A. M??kitie, Accuracy of medical models made by additive manufacturing (rapid manufacturing), *J. Cranio-Maxillofacial Surg.* 41 (2013) 603–609.
doi:10.1016/j.jcms.2012.11.041.
- [256] J. Asaumi, N. Kawai, Y. Honda, H. Shigehara, T. Wakasa, K. Kishi, Comparison of three-dimensional computed tomography with rapid prototype models in the management of coronoid hyperplasia, *Dentomaxillofacial Radiol.* 30 (2001) 330–335.
doi:10.1038/sj.dmfr.4600646.
- [257] H.-J. Yen, C.-S. Tseng, S. Hsu, C.-L. Tsai, Evaluation of chondrocyte growth in the highly porous scaffolds made by fused deposition manufacturing (FDM) filled with type II collagen, *Biomed. Microdevices.* 11 (2009) 615–624. doi:10.1007/s10544-008-9271-7.
- [258] J.Y. Kim, D.W. Cho, Blended PCL/PLGA scaffold fabrication using multi-head deposition system, *Microelectron. Eng.* 86 (2009) 1447–1450. doi:10.1016/j.mee.2008.11.026.
- [259] E.Y. Teo, S.Y. Ong, M.S. Khoon Chong, Z. Zhang, J. Lu, S.

- Moochhala, B. Ho, S.H. Teoh, Polycaprolactone-based fused deposition modeled mesh for delivery of antibacterial agents to infected wounds, *Biomaterials*. 32 (2011) 279–287.
doi:10.1016/j.biomaterials.2010.08.089.
- [260] S.-W. Kang, J.-H. Bae, S.-A. Park, W.-D. Kim, M.-S. Park, Y.-J. Ko, H.-S. Jang, J.-H. Park, Combination therapy with BMP-2 and BMSCs enhances bone healing efficacy of PCL scaffold fabricated using the 3D plotting system in a large segmental defect model, *Biotechnol. Lett.* 34 (2012) 1375–1384. doi:10.1007/s10529-012-0900-0.
- [261] J.H. Shim, T.S. Moon, M.J. Yun, Y.C. Jeon, C.M. Jeong, D.W. Cho, J.B. Huh, Stimulation of healing within a rabbit calvarial defect by a PCL/ PLGA scaffold blended with TCP using solid freeform fabrication technology, *J. Mater. Sci. Mater. Med.* 23 (2012) 2993–3002.
doi:10.1007/s10856-012-4761-9.
- [262] J.-H. Shim, J.-S. Lee, J.Y. Kim, D.-W. Cho, Bioprinting of a mechanically enhanced three-dimensional dual cell-laden construct for osteochondral tissue engineering using a multi-head tissue/organ building system, *J. Micromechanics Microengineering*. 22 (2012) 085014. doi:10.1088/0960-1317/22/8/085014.
- [263] S. Van Bael, T. Desmet, Y.C. Chai, G. Pyka, P. Dubruel, J.P. Kruth, J. Schrooten, In vitro cell-biological performance and structural characterization of selective laser sintered and plasma surface functionalized polycaprolactone scaffolds for bone regeneration, *Mater. Sci. Eng. C*. 33 (2013) 3404–3412. doi:10.1016/j.msec.2013.04.024.
- [264] C.E. Corcione, F. Gervaso, F. Scalera, F. Montagna, 3D printing of hydroxyapatite polymer-based composites for bone tissue engineering, (2017) 1–6. doi:10.1515/polyeng-2016-0194.
- [265] C. Esposito, C. Francesca, S. Francesca, G. Francesco, A. Sannino, A. Maffezzoli, One-step solvent-free process for the fabrication of high loaded PLA / HA composite filament for 3D printing, *J. Therm. Anal. Calorim.* 134 (2018) 575–582. doi:10.1007/s10973-018-7155-5.
- [266] J.P. Li, P. Habibovic, M. van den Doel, C.E. Wilson, J.R. de Wijn, C.A. van Blitterswijk, K. de Groot, Bone ingrowth in porous titanium implants produced by 3D fiber deposition, *Biomaterials*. 28 (2007) 2810–2820.

doi:10.1016/j.biomaterials.2007.02.020.

- [267] K. Patryk, M. Tadeusz, R. Rafa, W. Maciej, M. Joanna, W. Piotr, SU 087 E POSTER IN IMPLANT THERAPY OUTCOMES , SURGICAL ASPECTS Clinical application of titanium individual bone scaffold using 3D printing in the reconstruction of alveolar bone ridge, 28 (2012) 2017.
- [268] M. Berger, F. Probst, C. Schwartz, M. Cornelsen, H. Seitz, M. Ehrenfeld, S. Otto, A concept for scaffold-based tissue engineering in alveolar cleft osteoplasty, *J. Cranio-Maxillofacial Surg.* 43 (2015) 830–836. doi:10.1016/j.jcms.2015.04.023.
- [269] K.R. Hixon, A.M. Melvin, A.Y. Lin, A.F. Hall, S.A. Sell, Cryogel scaffolds from patient-specific 3D-printed molds for personalized tissue-engineered bone regeneration in pediatric cleft-craniofacial defects, 32 (2017) 598–611. doi:10.1177/0885328217734824.
- [270] C.P.G. Coelho, M.I. Greenberg, L. Dean, A.M. Guarino, A.J. Haque, B.N. Cronstein, Osteogenic Effects of Dipyridamole Versus rhBMP-2 Using 3D-Printed Bioceramic Scaffolds in a Growing Alveolar Cleft Model Presenter : Christopher D . Lopez , BA Affiliation : NYU Langone Health , New is a safe and useful alternative to SF in the immediate RECONSTRUCTIVE SESSION 2 Retrorectus Mesh Fixation Using Fibrin Glue : Early Outcomes of an Evolving Technique Presenter : Irfan A . Rhemtulla , MD , MS, (2018) 133–134.
- [271] J. Korpela, A. Kokkari, H. Korhonen, M. Malin, T. Närhi, J. Seppälä, Biodegradable and bioactive porous scaffold structures prepared using fused deposition modeling, *J. Biomed. Mater. Res. Part B Appl. Biomater.* 101B (2013) 610–619. doi:10.1002/jbm.b.32863.
- [272] B.S. Chang, C.K. Lee, K.S. Hong, H.J. Youn, H.S. Ryu, S.S. Chung, K.W. Park, Osteoconduction at porous hydroxyapatite with various pore configurations, *Biomaterials.* 21 (2000) 1291–1298. doi:10.1016/S0142-9612(00)00030-2.
- [273] S. Soliman, S. Sant, J.W. Nichol, M. Khabiry, E. Traversa, A. Khademhosseini, Controlling the porosity of fibrous scaffolds by modulating the fiber diameter and packing density, *J. Biomed. Mater. Res. - Part A.* 96 A (2011) 566–574. doi:10.1002/jbm.a.33010.

- [274] D.A. Hollander, M. Von Walter, T. Wirtz, R. Sellei, B. Schmidt-Rohlfing, O. Paar, H.J. Erli, Structural, mechanical and in vitro characterization of individually structured Ti-6Al-4V produced by direct laser forming, *Biomaterials*. 27 (2006) 955–963. doi:10.1016/j.biomaterials.2005.07.041.
- [275] S. Ponader, C. Von Wilmowsky, M. Widenmayer, R. Lutz, P. Heini, C. Körner, R.F. Singer, E. Nkenke, F.W. Neukam, K.A. Schlegel, In vivo performance of selective electron beam-melted Ti-6Al-4V structures, *J. Biomed. Mater. Res. - Part A*. 92 (2010) 56–62. doi:10.1007/s00500-018-3248-0.
- [276] A.A. Zadpoor, Bone tissue regeneration: The role of scaffold geometry, *Biomater. Sci*. 3 (2015) 231–245. doi:10.1039/c4bm00291a.
- [277] H.Y. Cheung, K.T. Lau, T.P. Lu, D. Hui, A critical review on polymer-based bio-engineered materials for scaffold development, *Compos. Part B Eng*. 38 (2007) 291–300. doi:10.1016/j.compositesb.2006.06.014.
- [278] L.S. Nair, C.T. Laurencin, Biodegradable polymers as biomaterials, *32* (2007) 762–798. doi:10.1016/j.progpolymsci.2007.05.017.
- [279] H. Tsuji, K. Ikarashi, In vitro hydrolysis of poly (L -lactide) crystalline residues as extended-chain crystallites III . Effects of pH and enzyme, *85* (2004) 647–656. doi:10.1016/j.polymdegradstab.2004.03.004.
- [280] H. Tsuji, K. Ikarashi, In vitro hydrolysis of poly (l -lactide) crystalline residues as extended-chain crystallites . Part I : long-term hydrolysis in phosphate-buffered solution at 37 C, *25* (2004) 5449–5455. doi:10.1016/j.biomaterials.2003.12.053.
- [281] W.H. De Jong, J.E. Bergsma, J.E. Robinson, R.R.M. Bos, Tissue response to partially in vitro predegraded poly- L -lactide implants, *26* (2005) 1781–1791. doi:10.1016/j.biomaterials.2004.06.026.
- [282] A. Majola, S. Vainionpää, P. Rokkanen, H.M. Mikkola, P. Törmälä, Absorbable self-reinforced polylactide (SR-PLA) composite rods for fracture fixation: strength and strength retention in the bone and subcutaneous tissue of rabbits, *J. Mater. Sci. Mater. Med*. 3 (1992) 43–47. doi:10.1007/BF00702943.
- [283] R.M. Felfel, K.M. Zakir, H. Andrew, C.D. Rudd, I. Ahmed, Accelerated

- in vitro degradation properties of polylactic acid / phosphate glass fibre composites, (2015) 3942–3955. doi:10.1007/s10853-015-8946-8.
- [284] N.A. Weir, F.J. Buchanan, J.F. Orr, G.R. Dickson, Degradation of poly-L-lactide . Part 1 : in vitro and in vivo physiological temperature degradation, (2004) 307–319.
- [285] J.E. Bergsma, W.C. De Bruijn, F.R. Rozema, R.R.M. Bos, G. Boering, Late degradation tissue response to poly (L-lactide) bone plates and screws, 16 (1995) 25–31.
- [286] C. Chen, J. Chueh, H. Tseng, H. Huang, S. Lee, Preparation and characterization of biodegradable PLA polymeric blends, 24 (2003) 1167–1173.
- [287] E.W. Fischer, H.J. Sterzel, G. Wegner, Investigation of the structure of solution grown crystals of lactide copolymers by means of chemical reactions, *Kolloid-Zeitschrift Und Zeitschrift Für Polym.* 251 (1973) 980–990. doi:10.1007/BF01498927.
- [288] M. Lang, W. Wenhui, C. XiaoQi, T. Woodfield, W. Wang, X.Q. Chen, T. Woodfield, Integrated system for 3D assembly of bio-scaffolds and cells, *Autom. Sci. Eng. (CASE)*, 2010 IEEE Conf. (2010) 786–791. doi:10.1109/coase.2010.5584476.
- [289] J.E. Bergsma, F.R. Rozema, R.R.M. Bos, G. Boer, W.C. De Bruijn, A.J. Pennin, In vivo degradation and biocompatibility study of in vitro polylactide particles, 16 (1995) 267–274.
- [290] N.A. Weir, F.J. Buchanan, J.F. Orr, D.F. Farrar, G.R. Dickson, Degradation of poly-L-lactide. Part 2: increased temperature accelerated degradation, *Proc. Inst. Mech. Eng. Part H J. Eng. Med.* 218 (2004) 321–330. doi:10.1243/0954411041932809.
- [291] P. Törmälä, Ultra-high strength, self-reinforced absorbable polymeric composites for applications in different disciplines of surgery, *Clin. Mater.* 13 (1993) 35–40. doi:10.1016/0267-6605(93)90087-N.
- [292] P. Törmälä, Biodegradable self-reinforced composite materials; manufacturing structure and mechanical properties., *Clin. Mater.* 10 (1992) 29–34.
- [293] D. Garlotta, A Literature Review of Poly (Lactic Acid), 9 (2002). doi:10.1023/A:1020200822435.

- [294] H.S. Azevedo, R.L. Reis, *Biodegradable Systems in Tissue Engineering and Regenerative Medicine*, CRC Press, 2005.
- [295] P. Olla, Opening Pandora's 3D Printed Box, *IEEE Technol. Soc. Mag.* (2015) 74–80.
- [296] P. Krawczak, Editorial corner: A personal view Additive manufacturing of plastic and polymer composite parts: Promises and challenges of 3D-printing, *Express Polym. Lett.* 9 (2015) 959.
doi:10.3144/expresspolymlett.2015.86.
- [297] A.M. Forster, *Materials Testing Standards for Additive Manufacturing of Polymer Materials* :, Nist.Ir.8059. (2015).
doi:http://dx.doi.org/10.6028/NIST.IR.8059.
- [298] T. Kasuga, H. Maeda, K. Kato, M. Nogami, K.I. Hata, M. Ueda, Preparation of poly(lactic acid) composites containing calcium carbonate (vaterite), *Biomaterials.* 24 (2003) 3247–3253.
doi:10.1016/S0142-9612(03)00190-X.
- [299] T. Otani, L.A. Whiteside, S.E. White, Strain distribution in the proximal femur with flexible composite and metallic femoral components under axial and torsional loads., *J. Biomed. Mater. Res.* 27 (1993) 575–85.
doi:10.1002/jbm.820270504.
- [300] J. Vander Sloten, L. Labey, R. Van Audekercke, J. Helsen, G. Van Der Perre, The development of a physiological hip prosthesis: The influence of design and materials, *J. Mater. Sci. Mater. Med.* 4 (1993) 407–414. doi:10.1007/BF00122200.
- [301] K. Li, S.C. Tjong, Preparation and Characterization of Isotactic Polypropylene Reinforced with Hydroxyapatite Nanorods, *J. Macromol. Sci. Part B.* 50 (2011) 1983–1995.
doi:10.1080/00222348.2010.549437.
- [302] S.S. Liao, F.Z. Cui, W. Zhang, Q.L. Feng, Hierarchically Biomimetic Bone Scaffold Materials : Nano-HA / Collagen / PLA Composite, (2004) 158–165. doi:10.1002/jbm.b.20035.
- [303] L.C. Hieu, E. Bohez, J. Vander Sloten, H.N. Phien, E. Vatcharaporn, P.H. Binh, P.V. An, P. Oris, Design for medical rapid prototyping of cranioplasty implants, *Rapid Prototyp. J.* 9 (2003) 175–186.
doi:10.1108/13552540310477481.

- [304] E. Pepla, L.K. Besharat, G. Palaia, G. Tenore, G. Migliau, Nano-hydroxyapatite and its applications in preventive, restorative and regenerative dentistry: a review of literature, *Ann. Stomatol.* 5 (2014) 108–114.
- [305] Á. Pereira, P. Oliva, Eficacia de la Hidroxiapatita en la Cicatrización de Injertos Óseos e Implantes Dentales: una Revisión Sistemática de la Literatura Hydroxyapatite Effectiveness in Healing of Bone Grafts and Dental Implants: A Systematic Review of the Literature, *Int. J. Odontostomat.* 8 (2014) 425–432.
- [306] L. Zhang, N. Hanagata, M. Maeda, T. Minowa, T. Ikoma, H. Fan, X. Zhang, Porous hydroxyapatite and biphasic calcium phosphate ceramics promote ectopic osteoblast differentiation from mesenchymal stem cells, *Sci. Technol. Adv. Mater.* 10 (2009) 025003. doi:10.1088/1468-6996/10/2/025003.
- [307] W. Zhu, X. Zhang, D. Wang, W. Lu, Y. Ou, Y. Han, K. Zhou, H. Liu, W. Fen, L. Peng, C. He, Y. Zeng, Experimental study on the conduction function of nano-hydroxyapatite artificial bone, *Micro Nano Lett.* 5 (2010) 19. doi:10.1049/mnl.2009.0049.
- [308] K.H. Prakash, R. Kumar, C.P. Ooi, P. Cheang, K.A. Khor, Apparent solubility of hydroxyapatite in aqueous medium and its influence on the morphology of nanocrystallites with precipitation temperature, *Langmuir.* 22 (2006) 11002–11008. doi:10.1021/la0621665.
- [309] C.J. Wilcock, P. Gentile, P. V Hatton, C.A. Miller, Rapid Mix Preparation of Bioinspired Nanoscale Hydroxyapatite for Biomedical Applications, (2017) 1–7. doi:10.3791/55343.
- [310] S. Mallick, S. Tripathi, P. Srivastava, Advancement in Scaffolds for Bone Tissue Engineering: A Review, *IOSR J. Pharm. Biol. Sci. Ver.* 10 (2015) 2319–7676. doi:10.9790/3008-10143754.
- [311] J.W. Leenslag, A.J. Pennings, R.R.M. Bos, F.R. Rozema, G. Boering, Resorbable materials of poly(l-lactide). VII. In vivo and in vitro degradation, *Biomaterials.* 8 (1987) 311–314. doi:10.1016/0142-9612(87)90121-9.
- [312] J.W. Leenslag, A.J. Pennings, R.R.M. Bos, F.R. Rozema, G. Boering, Resorbable materials of poly(l-lactide). VI. Plates and screws for

- internal fracture fixation, *Biomaterials*. 8 (1987) 70–73.
doi:10.1016/0142-9612(87)90034-2.
- [313] A.-M. Yousefi, M.E. Hoque, R.G.S. V. Prasad, N. Uth, Current strategies in multiphasic scaffold design for osteochondral tissue engineering: A review, *J. Biomed. Mater. Res. Part A*. 103 (2015) 2460–2481. doi:10.1002/jbm.a.35356.
- [314] A. Göpferich, Mechanisms of polymer degradation and erosion, *Biomaterials*. 17 (1996) 103–114. doi:10.1016/0142-9612(96)85755-3.
- [315] D.F. Williams, S.P. Zhong, Biodeterioration / Biodegradation of Polymeric Medical Devices In Situ, *International Biodeterior. Biodegrad.* 95 (1994) 95–130. doi:0964-8305(95)00027-5.
- [316] A. Remes, D.F. Williams, Immune response in biocompatibility, *Biomaterials*. 13 (1992) 731–743. doi:10.1016/0142-9612(92)90010-L.
- [317] PolyVation, Platimer 232 Data Sheet, 2016.
- [318] NatureWorks, Ingeo™ Biopolymer 4043D Technical Data Sheet 3D Printing Monofilament – General Purpose Grade, (n.d.) 1–4.
- [319] R. Suuronen, T. Pohjonen, J. Hietanen, C. Lindqvist, A 5-year in vitro and in vivo study of the biodegradation of polylactide plates, *J. Oral Maxillofac. Surg.* 56 (1998) 604–614. doi:10.1016/S0278-2391(98)90461-X.
- [320] J.C. Middleton, A.J. Tipton, Synthetic biodegradable polymers as orthopedic devices, 21 (2000).
- [321] H. Tsuji, Autocatalytic hydrolysis of amorphous-made polylactides: effects of l-lactide content, tacticity, and enantiomeric polymer blending, *Polymer (Guildf)*. 43 (2002) 1789–1796. doi:10.1016/S0032-3861(01)00752-2.
- [322] S. Lyu, D. Untereker, Degradability of polymers for implantable biomedical devices, *Int. J. Mol. Sci.* 10 (2009) 4033–4065. doi:10.3390/ijms10094033.
- [323] M. Vert, S.M. Li, G. Spenlehauer, P. Guerin, Bioresorbability and biocompatibility of aliphatic polyesters, *J. Mater. Sci. Mater. Med.* 3 (1992) 432–446. doi:10.1007/BF00701240.
- [324] T. Nakamura, S. Hitomi, S. Watanabe, Y. Shimizu, K. Jamshidi, S.H. Hyon, Y. Ikada, Bioabsorption of polylactides with different molecular

- properties., *J. Biomed. Mater. Res.* 23 (1989) 1115–30.
doi:10.1002/jbm.820231003.
- [325] Y. Ikarashi, T. Tsuchiya, A. Nakamura, Effect of heat treatment of poly (L -lactide) on the response of, 21 (2000) 1259–1267.
- [326] P. Törmälä, Biodegradable Self-Reinforced Composite Materials, *Clin. Mater.* 10 (1992) 29–34.
- [327] P. Tjirmdii, Ultra-high Strength , Self-Reinforced Absorbable Polymeric Composites for Applications in Wounds of Surgery, *Biomaterials.* 3 (1993) 35–40.
- [328] International Standards Organization, ISO 10993-13:2010. Biological evaluation of medical devices Part 13 : Identification and quantification of degradation products from polymeric, 2010.
- [329] M.F.A. Goosen, Investigation of Poly (lactic acid) Degradation Product Release, *J. Bioact. Compat. Polym.* 9 (1994) 80–100.
- [330] H. Tsuji, Poly(lactide) stereocomplexes: Formation, structure, properties, degradation, and applications, *Macromol. Biosci.* 5 (2005) 569–597. doi:10.1002/mabi.200500062.
- [331] G. Evonik Nutrition & Care, Technical Information. Resomer L 206 S, 2015.
- [332] A.L. Quintanar-Meléndez, C.A. Orozco-Díaz, R. Bustamante-Bello, J.R. Álvarez-Bada, M.K. Muguerza-Jiménez, J. Nava-Rojas, A.L. Quintanar Melendez, C.A. Orozco Diaz, R. Bustamante Bello, J.R. Alvarez Bada, M.K. Muguerza Jimenez, J. Nava Rojas, Concept validation of a MEMS powered, automatic multichannel pipetting device, *Midwest Symp. Circuits Syst.* (2009) 325–328.
doi:10.1109/MWSCAS.2009.5236088.
- [333] R. Landers, R. Mülhaupt, Desktop manufacturing of complex objects, prototypes and biomedical scaffolds by means of computer-assisted design combined with computer-guided 3D plotting of polymers and reactive oligomers, *Macromol. Mater. Eng.* 282 (2000) 17–21.
doi:10.1002/1439-2054(20001001)282:1<17::AID-MAME17>3.0.CO;2-8.
- [334] G. Wei, P.X. Ma, Structure and properties of nano-hydroxyapatite/polymer composite scaffolds for bone tissue

- engineering, *Biomaterials*. 25 (2004) 4749–4757.
doi:10.1016/j.biomaterials.2003.12.005.
- [335] J. Ahmed, S.K. Varshney, J. Ahmed, S.K. Varshney, *Poly lactides — Chemistry , Properties and Green Packaging Technology : A Review* POLYLACTIDES — CHEMISTRY , PROPERTIES AND GREEN PACKAGING TECHNOLOGY : A REVIEW, 2912 (2011).
doi:10.1080/10942910903125284.
- [336] R.R.M. Bos, F.B. Rozema, G. Boering, A.J. Nijenhuis, A.J. Pennings, A.B. Verwey, P. Nieuwenhuis, H.W.B. Jansen, *Degradation of and tissue reaction to biodegradable poly(L-lactide) for use as internal fixation of fractures: a study in rats*, *Biomaterials*. 12 (1991) 32–36.
doi:10.1016/0142-9612(91)90128-W.
- [337] Y. Kong, J.N. Hay, *The enthalpy of fusion and degree of crystallinity of polymers as measured by DSC* The enthalpy of fusion and degree of crystallinity of polymers as measured by DSC, (2016).
doi:10.1016/S0014-3057(03)00054-5.
- [338] P. Gill, T.T. Moghadam, B. Ranjbar, *Differential scanning calorimetry techniques: applications in biology and nanoscience.*, *J. Biomol. Tech.* 21 (2010) 167–193.
- [339] K. Isama, T. Tsuchiya, *Enhancing effect of poly (L-lactide) on the differentiation of mouse*, 24 (2003) 3303–3309. doi:10.1016/S0142-9612(03)00216-3.
- [340] M. Vert, S. Li, H. Garreau, *New insights on the degradation of bioresorbable polymeric devices based on lactic and glycolic acids.*, *Clin. Mater.* 10 (1992) 3–8. doi:10.1016/0267-6605(92)90077-7.
- [341] Y. Kong, J.N. Hay, *The enthalpy of fusion and degree of crystallinity of polymers as measured by DSC*, *Eur. Polym. J.* 39 (2003) 1721–1727.
doi:10.1016/S0014-3057(03)00054-5.
- [342] T. Noraihan, A. Tuan, A.M. Abdullah, H. Akil, D. Mohamad, *Preparation and characterization of a newly developed polyamide composite utilising an affordable 3D printer*, (2015).
doi:10.1177/0731684415594692.
- [343] P. Carrotte, *Endodontics: Part 4 Morphology of the root canal system*, *Br. Dent. J.* 197 (2004) 379–383. doi:10.1038/sj.bdj.4811711.

- [344] W. Batwa, F. Alsulaimani, Incisors' proportions in smile esthetics, *J. Orthod. Sci.* 2 (2013) 109. doi:10.4103/2278-0203.119685.
- [345] A. Wiecheć, E. Stodolak-Zych, A. Frączek-Szczypta, M. Błazewicz, W.M. Kwiatek, The study of human osteoblast-like MG 63 cells proliferation on resorbable polymer-based nanocomposites modified with ceramic and carbon nanoparticles, *Acta Phys. Pol. A.* 121 (2012) 546–550.
- [346] F. Wu, Y. Ngothai, J. Wei, C. Liu, B. O'Neill, Y. Wu, Premixed, injectable PLA-modified calcium deficient apatite biocement (cd-AB) with washout resistance, *Colloids Surfaces B Biointerfaces.* 92 (2012) 113–120. doi:10.1016/j.colsurfb.2011.11.037.
- [347] T.A.M. Valente, D.M. Silva, P.S. Gomes, M.H. Fernandes, J.D. Santos, V. Sencadas, Effect of sterilization methods on electrospun poly(lactic acid) (PLA) fiber alignment for biomedical applications, *ACS Appl. Mater. Interfaces.* 8 (2016) 3241–3249. doi:10.1021/acsami.5b10869.
- [348] C.H. Chung, E.E. Golub, E. Forbes, T. Tokuoka, I.M. Shapiro, Mechanism of action of beta-glycerophosphate on bone cell mineralization., *Calcif. Tissue Int.* 51 (1992) 305–311. doi:10.1007/BF00334492.
- [349] M.J. Coelho, M.H. Fernandes, Human bone cell cultures in biocompatibility testing. Part II: Effect of ascorbic acid, ??-glycerophosphate and dexamethasone on osteoblastic differentiation, *Biomaterials.* 21 (2000) 1095–1102. doi:10.1016/S0142-9612(99)00192-1.
- [350] M.A. Yassin, K.N. Leknes, T.O. Pedersen, Z. Xing, Y. Sun, S.A. Lie, A. Finne-Wistrand, K. Mustafa, Cell seeding density is a critical determinant for copolymer scaffolds-induced bone regeneration, *J. Biomed. Mater. Res. - Part A.* 103 (2015) 3649–3658. doi:10.1002/jbm.a.35505.
- [351] S. Shahangian, K.O. Ash, D.E. Rollins, An enzymatic method for the analysis of formate in human plasma, *J. Anal. Toxicol.* 8 (1984) 273–276. doi:10.1093/jat/8.6.273.
- [352] S. Anoopkumar-Dukie, J.B. Carey, T. Conere, E. O'Sullivan, F.N. Van Pelt, A. Allshire, Resazurin assay of radiation response in cultured

- cells, *Br. J. Radiol.* 78 (2005) 945–947. doi:10.1259/bjr/54004230.
- [353] H. Puchtler, S.N. Meloan, M.S. Terry, On the History and Mechanism of Alizarin and Alizarin Red S Stains for Calcium, (2016) 2–3. doi:10.1177/17.2.110.
- [354] L.F. Nielsen, D. Moe, S. Kirkeby, C. Garbarsch, Sirius Red and Acid Fuchsin Staining Mechanisms, *Biotech. Histochem.* 73 (1998) 71–77. doi:10.3109/10520299809140509.
- [355] D.F. Farrar, R.K. Gillson, Hydrolytic degradation of polyglyconate B : the relationship between degradation time , strength and molecular weight, 23 (2002) 3905–3912.
- [356] C.G. Pitt, G. Zhong-wei, Modification of the rates of chain cleavage of poly(ϵ -caprolactone) and related polyesters in the solid state, *J. Control. Release.* 4 (1987) 283–292. doi:10.1016/0168-3659(87)90020-4.
- [357] J. Bergsma, Late degradation tissue response to poly(ϵ -lactide) bone plates and screws, *Biomaterials.* 16 (1995) 25–31. doi:10.1016/0142-9612(95)91092-D.
- [358] J.O. Hollinger, *Biomedical Applications of Synthetic Biodegradable Polymers*, 1st Editio, CRC Press, 1995.
- [359] I.M. Ward, J. Sweeney, *Mechanical Properties of Solid Polymers*, John Wiley & Sons, Ltd, Chichester, UK, 2012. doi:10.1002/9781119967125.
- [360] L. Schedl, Why degradable polymers undergo surface erosion or bulk erosion, 23 (2002) 4221–4231. doi:10.1016/S0142-9612(02)00170-9.
- [361] R.M. Felfel, K.M.Z. Hossain, A.J. Parsons, C.D. Rudd, I. Ahmed, Accelerated in vitro degradation properties of polylactic acid/phosphate glass fibre composites, *J. Mater. Sci.* (2015) 3942–3955. doi:10.1007/s10853-015-8946-8.
- [362] J. Siewerdsen, P.J. La Riviere, W.A. Kalender, Anniversary Paper : Development of x-ray computed tomography : The role of Medical Physics and AAPM from the 1970s to present, (2008) 3728–3739. doi:10.1118/1.2952653.
- [363] P. Education, *X-ray computed tomography*, (2001).
- [364] R. Datta, S. Datta, W.D. McDavid, R.G. Waggener, Electron beam

- depth dose scaling by means of effective atomic number reconstructed from CT scans, 526 (2013). doi:10.1118/1.594644.
- [365] C.E.J. Carraher, Seymour/Carraher's Polymer Chemistry, 6th ed., Marcel Dekker, Inc, New York, 2007.
- [366] S.P. Lyu, J. Schley, B. Loy, D. Lind, C. Hobot, R. Sparer, D. Untereker, Kinetics and time-temperature equivalence of polymer degradation, *Biomacromolecules*. 8 (2007) 2301–2310. doi:10.1021/bm070313n.
- [367] A. Kantaros, N. Chatzidai, D. Karalekas, 3D printing-assisted design of scaffold structures, *Int. J. Adv. Manuf. Technol.* 82 (2016) 559–571. doi:10.1007/s00170-015-7386-6.
- [368] L.D. Harris, B.S. Kim, D.J. Mooney, Open pore biodegradable matrices formed with gas foaming, *J. Biomed. Mater. Res.* 42 (1998) 396–402. doi:10.1002/(SICI)1097-4636(19981205)42:3<396::AID-JBM7>3.0.CO;2-E.
- [369] J. Kadkhodapour, H. Montazerian, A.C. Darabi, A.P. Anaraki, S.M. Ahmadi, A.A. Zadpoor, S. Schmauder, Failure mechanisms of additively manufactured porous biomaterials: Effects of porosity and type of unit cell, *J. Mech. Behav. Biomed. Mater.* 50 (2015) 180–191. doi:10.1016/j.jmbbm.2015.06.012.
- [370] R. Bibb, D. Thompson, J. Winder, Computed tomography characterisation of additive manufacturing materials, *Med. Eng. Phys.* 33 (2011) 590–596. doi:10.1016/j.medengphy.2010.12.015.
- [371] D. Garlotta, A Literature Review of Poly (Lactic Acid), 9 (2002).
- [372] M. Hakkarainen, A.C. Albertsson, S. Karlsson, Weight losses and molecular weight changes correlated with the evolution of hydroxyacids in simulated in vivo degradation of homo- and copolymers of PLA and PGA, *Polym. Degrad. Stab.* 52 (1996) 283–291. doi:10.1016/0141-3910(96)00009-2.
- [373] K. Koskikare, E. Hirvensalo, H. Patiala, P. Rokkanen, T. Pohjonen, P. Tormala, G. Lob, Intraosseous plating with absorbable self-reinforced poly-L-lactide plates in the fixation of distal femoral osteotomies on rabbits, *J. Biomed. Mater. Res.* 30 (1996) 417–421. doi:10.1002/jbm.820300402.
- [374] B.J.R. Millar, D.G. Smith, W.E. Marr, T.R.E. Kressman, Solvent-

- modified Polymer Networks. Part I. The Preparation and Characterisation of Expanded -network and Macroporous Styrene-Divinylbenzene Copolymers and their Sulphonates., *J. Chem. Soc.* (1963).
- [375] C.S. Proikakis, N.J. Mamouzelos, P.A. Tarantili, A.G. Andreopoulos, Swelling and hydrolytic degradation of poly(d,l-lactic acid) in aqueous solutions, *Polym. Degrad. Stab.* 91 (2006) 614–619. doi:10.1016/j.polymdegradstab.2005.01.060.
- [376] S. Li, H. Garreau, M. Vert, Structure-property relationships in the case of the degradation of massive poly (α -hydroxy acids) in aqueous media, Part 3: Influence of the morphology of poly (L-lactic acid), *J. Mater. Sci. Mater. Med.* 1 (1990) 198–206. doi:10.1007/BF00701077.
- [377] J.A. Leenheer, Comprehensive approach to preparative isolation and fractionation of dissolved organic carbon from natural waters and wastewaters, *Environ. Sci. Technol.* 15 (1981) 578–587. doi:10.1021/es00087a010.
- [378] H. Song, O. Orr, Y. Hong, T. Karanfil, Isolation and fractionation of natural organic matter: Evaluation of reverse osmosis performance and impact of fractionation parameters, *Environ. Monit. Assess.* 153 (2009) 307–321. doi:10.1007/s10661-008-0357-8.
- [379] R. Suuronen, M.J. Manninen, T. Pohjonen, O. Laitinen, C. Lindqvist, Mandibular osteotomy fixed with biodegradable plates and screws: An animal study, *Br. J. Oral Maxillofac. Surg.* 35 (1997) 341–348. doi:10.1016/S0266-4356(97)90407-1.
- [380] R. Suuronen, T. Pohjonen, R. Taurio, P. Törmälä, L. Wessman, K. Rönkkö, S. Vainionpää, Strength retention of self-reinforced poly-L-lactide screws and plates: an in vivo and in vitro study, *J. Mater. Sci. Mater. Med.* 3 (1992) 426–431. doi:10.1007/BF00701239.
- [381] J.J. Li, C.R. Dunstan, in sheep tibiae Additive manufacturing of polymer melts for implantable medical devices and scaffolds, (n.d.).
- [382] P. Mainil-Varlet, R. Curtis, S. Gogolewski, Effect of in vivo and in vitro degradation on molecular and mechanical properties of various low-molecular-weight polylactides., *J. Biomed. Mater. Res.* 36 (1997) 360–380. doi:10.1002/(sici)1097-4636(19970905)36:3<360::aid-

jbm11>3.0.co;2-i.

- [383] Y. Hattori, Y. Haruna, M. Otsuka, Dissolution process analysis using model-free Noyes-Whitney integral equation, *Colloids Surfaces B Biointerfaces*. 102 (2013) 227–231. doi:10.1016/j.colsurfb.2012.08.017.
- [384] F. Heidari, M. Razavi, M. Ghaedi, M. Forooghi, M. Tahriri, L. Tayebi, Investigation of mechanical properties of natural hydroxyapatite samples prepared by cold isostatic pressing method, *J. Alloys Compd.* 693 (2017) 1150–1156. doi:10.1016/j.jallcom.2016.10.081.
- [385] J.I. Goldstein, D.E. Newbury, P. Echlin, D.C. Joy, C.E. Lyman, E. Lifshin, L. Sawyer, J.R. Michael, *Scanning Electron Microscopy and X-ray Microanalysis*, Springer US, Boston, MA, 2003. doi:10.1007/978-1-4615-0215-9.
- [386] J.H. Butler, D.C. Joy, G.F. Bradley, S.J. Krause, Low-voltage scanning electron microscopy of polymers, *Polymer (Guildf)*. 36 (1995) 1781–1790. doi:10.1016/0032-3861(95)90924-Q.
- [387] P. Science, Effect of solvent on glass transition temperature in chemically modified polyvinyl chloride (PVC) The chemical modification of PVC allows one, 167 (1994) 159–167. doi:10.1007/BF00658842.
- [388] A. Yoshioka, K. Tashiro, Solvent effect on the glass transition temperature of syndiotactic polystyrene viewed from time-resolved measurements of infrared spectra at the various temperatures and its simulation by molecular dynamics calculation, *Macromolecules*. 37 (2004) 467–472. doi:10.1021/ma035505z.
- [389] G.W. Ehrenstein, R.P. Thieriault, *Polymeric Materials: Structure, Properties, Applications, Illustrate*, Hanser Publishers, Cincinnati, 2001.
- [390] S. Bose, S. Dasgupta, S. Tarafder, A. Bandyopadhyay, Microwave-processed nanocrystalline hydroxyapatite: Simultaneous enhancement of mechanical and biological properties, *Acta Biomater.* 6 (2010) 3782–3790. doi:10.1016/j.actbio.2010.03.016.
- [391] Y.J. Hong, J.S. Chun, W.K. Lee, Association of collagen with calcium phosphate promoted osteogenic responses of osteoblast-like MG63

- cells, *Colloids Surfaces B Biointerfaces*. 83 (2011) 245–253.
doi:10.1016/j.colsurfb.2010.11.028.
- [392] S. Lossdörfer, Z. Schwartz, C.H. Lohmann, D.C. Greenspan, D.M. Ranly, B.D. Boyan, Osteoblast response to bioactive glasses in vitro correlates with inorganic phosphate content, *Biomaterials*. 25 (2004) 2547–2555. doi:10.1016/j.biomaterials.2003.09.094.
- [393] Y. Takagishi, T. Kawakami, Y. Hara, M. Shinkai, T. Takezawa, T. Nagamune, Bone-Like Tissue Formation by Three-Dimensional Culture of MG63 Osteosarcoma Cells in Gelatin Hydrogels Using Calcium-Enriched Medium, *Tissue Eng.* 12 (2006) 927–937.
doi:10.1089/ten.2006.12.927.
- [394] M.E. Hoque, Y.L. Chuan, I. Pashby, M. Enamul Hoque, Y. Leng Chuan, *Ian Pashby*, 97 (2011) 83–93. doi:10.1002/bip.21701.
- [395] O. Laitinen, P. Törmälä, R. Taurio, K. Skutnabb, K. Saarelainen, T. Iivonen, S. Vainionpää, Mechanical properties of biodegradable ligament augmentation device of poly(L-lactide) in vitro and in vivo, *Biomaterials*. 13 (1992) 1012–1016. doi:10.1016/0142-9612(92)90152-E.
- [396] G. Bonuccelli, S. Avnet, G. Grisendi, M. Salerno, D. Granchi, M. Dominici, K. Kusuzaki, N. Baldini, Role of mesenchymal stem cells in osteosarcoma and metabolic reprogramming of tumor cells, *Oncotarget*. 5 (2014) 7575–88. doi:10.18632/oncotarget.2243.
- [397] D. Hu, D. Wu, L. Huang, Y. Jiao, L. Li, L. Lu, C. Zhou, 3D bioprinting of cell-laden scaffolds for intervertebral disc regeneration, *Mater. Lett.* 223 (2018) 219–222. doi:10.1016/j.matlet.2018.03.204.
- [398] J.E. Brown, B.P. Partlow, A.M. Berman, M.D. House, D.L. Kaplan, Injectable silk-based biomaterials for cervical tissue augmentation: An in vitro study, *Am. J. Obstet. Gynecol.* 214 (2016) 118.e1-118.e9. doi:10.1016/j.ajog.2015.08.046.
- [399] H. Seyednejad, D. Gawlitta, R. V. Kuiper, A. De Bruin, C.F. Van Nostrum, T. Vermonden, W.J.A. Dhert, W.E. Hennink, In vivo biocompatibility and biodegradation of 3D-printed porous scaffolds based on a hydroxyl-functionalized poly(ϵ -caprolactone), *Biomaterials*. 33 (2012) 4309–4318. doi:10.1016/j.biomaterials.2012.03.002.

- [400] J. An, J.E.M. Teoh, R. Suntornnond, C.K. Chua, Design and 3D Printing of Scaffolds and Tissues, *Engineering*. 1 (2015) 261–268. doi:10.15302/J-ENG-2015061.
- [401] W.M. Lam, H.B. Pan, M.K. Fong, W.S. Cheung, K.L. Wong, Z.Y. Li, K.D.K. Luk, W.K. Chan, C.T. Wong, C. Yang, W.W. Lu, In Vitro characterization of low modulus linoleic acid coated strontium-substituted hydroxyapatite containing PMMA bone cement, *J. Biomed. Mater. Res. - Part B Appl. Biomater.* 96 B (2011) 76–83. doi:10.1002/jbm.b.31741.
- [402] A.E. Porter, N. Patel, J.N. Skepper, S.M. Best, W. Bonfield, Effect of sintered silicate-substituted hydroxyapatite on remodelling processes at the bone-implant interface, *Biomaterials*. 25 (2004) 3303–3314. doi:10.1016/j.biomaterials.2003.10.006.
- [403] C.R. Gautam, S. Kumar, S. Biradar, S. Jose, V.K. Mishra, Synthesis and enhanced mechanical properties of MgO substituted hydroxyapatite: A bone substitute material, *RSC Adv.* 6 (2016) 67565–67574. doi:10.1039/c6ra10839c.
- [404] M.M. Germaini, R. Detsch, A. Grünewald, A. Magnaudeix, F. Lalloue, A.R. Boccaccini, E. Champion, Osteoblast and osteoclast responses to A/B type carbonate-substituted hydroxyapatite ceramics for bone regeneration, *Biomed. Mater.* 12 (2017). doi:10.1088/1748-605X/aa69c3.
- [405] G. Ciobanu, A.M. Bargan, C. Luca, New Bismuth-Substituted Hydroxyapatite Nanoparticles for Bone Tissue Engineering, *Jom*. 67 (2015) 2534–2542. doi:10.1007/s11837-015-1467-8.
- [406] A.A. Noyes, W.R. Whitney, The rate of solution of solid substances in their own solutions, *J. Am. Chem. Soc.* 19 (1897) 930–934. doi:10.1021/ja02086a003.
- [407] M.A. Liebert, M. Montjovent, L. Mathieu, B. Hinz, L.E.E.L. Applegate, P. Bourban, P. Zambelli, Biocompatibility of Bioresorbable Poly(L-lactic acid) Composite Scaffolds Obtained by Supercritical Gas Foaming with Human Fetal Bone Cells, 11 (2005) 1640–1649.